CONTROL AND BLACK START RESTORATION OF ISLANDED MICROGRIDS

A Dissertation

by

OGBONNAYA BASSEY

Submitted to the Office of Graduate and Professional Studies of
Texas A&M University
in partial fulfillment of the requirements for the degree of

DOCTOR OF PHILOSOPHY

Chair of Committee, Karen L. Butler-Purry
Committee Members, Pierce Cantrell
Mehrdad Ehsani
Jianxin Zhou
Head of Department, Miroslav M. Begovic

December 2020

Major Subject: Electrical Engineering

ABSTRACT

Electric power systems face the risk of outages due to extreme weather events, cyber-attack, human errors, and other unforeseen circumstances. A power grid that is resilient to these unfortunate events has become a consistent theme in literature and media. One approach to improve the grid's resilience is by decentralizing the grid into smaller controllable units called microgrids. This dissertation focuses on the control and operation of islanded microgrids for black start restoration (BSR).

Two operation modes were identified based on islanded microgrids' primary control for BSR. These modes are the single master operation (SMO) and multi-master operation (MMO) modes. These two control approaches were used to develop two sequential multi-step BSR methods for islanded microgrids.

The first part of this dissertation presents the BSR formulation for SMO microgrids. The restoration problem was formulated as a mixed-integer linear programming (MILP) problem. The frequency response of the isochronous synchronous-machine based generator (ISMG) was derived and validated through transient simulation. The frequency response was then used to characterize the ramp rate and the settling time of the ISMG. With these characterizations, the BSR can minimize total restoration time and maximize energy restored. The developed BSR method was studied on a modified IEEE 123 node test feeder.

The second part of this dissertation provides studies of the use of MMO microgrids for BSR. The MMO microgrids were assumed to be operating with conventional droop

control. Before developing the BSR method, two novel linear power flow (LPF) formulations for islanded droop-controlled microgrids were derived. These two LPF formulations were extended to develop optimal power flow (OPF) formulations as a quadratic programming (QP) and a mixed-integer quadratic programming (MIQP) problem to minimize cost. These formulations were followed by a MILP formulation to realize a novel BSR method for MMO microgrids with the derived LPF equations incorporated as the power flow constraint. Extensive case studies were used to validate and verify the developed BSR method.

Because the MMO microgrid can have multiple master DGs per microgrid, they are expected to improve islanded microgrids' resilience compared to SMO microgrids which have one master DG per microgrid.

DEDICATION

To my family and friends

ACKNOWLEDGEMENTS

I would like to thank my advisor, Dr. Karen Butler-Purry, for her patience, guidance, and support throughout my Ph.D. program. I have learned a lot from her experience and knowledge. I am thankful to my committee members, Dr. Pierce Cantrell, Dr. Mehrdad Ehsani, and Dr. Jianxin Zhou, for their feedback and time. I had the opportunity to learn about computer networks from Dr. Cantrell's class and optimization from Dr. Zhou's class; these classes were very interesting and helpful. I also want to thank Dr. Overbye for his time and feedback during my preliminary exam.

I am thankful to my colleagues at the Argonne National Lab, particularly Dr. C. Chen and Dr. B. Chen for their time, supervision, and guidance during my internship. Parts of section 5 of this dissertation was completed during my internship at Argonne. I am thankful to my supervisor, Dr. Y. Sharon, at S&C Electric Company. During my internship at S&C, I learned a lot from Dr. Sharon.

I would like to thank my friends and colleagues in the ECE department and the Power System Automation Lab: Joseph, Eavin, Ammar, Abhijeet, Sophia, Amara, Peter, Tania, and Iyke for their discussions and friendship. I want to thank Iyke for his help during my preliminary and final exams prep.

Many persons have been very supportive during this period. I am grateful to Kara for his friendship. Thanks to my mentor and friend, Dr. G. Nwosu, for his useful advice. I am grateful to my cousin, Uchenna, for his mentorship and support during my undergrad studies, and for helping me when I first came to Texas. Thanks to all my friends in the

College Station area and beyond: Chuks, André, Ifedi, Wisdom, Ugo, Anderson, Kevin, Udoka, Chinedu, Uchechi, Afam, the Kios, Sami, Emeka, Tolu, and Ibrahim.

I want to specially thank my mum, Mercy Chidi Bassey, for her encouragement, love, and support. Without her sacrifice and hard work, I would not be where I am today. Thanks to my siblings, Amaechi, Arukwe, and Nne for their love and support. Finally, thanks to my sweetheart, Tomi, for her love and support. I am, indeed, very lucky to have Tomi in my life.

CONTRIBUTORS AND FUNDING SOURCES

Contributors

This work was supervised by a dissertation committee consisting of Professor Karen Butler-Purry (advisor), Professor Pierce Cantrell, and Professor Mehrdad Ehsani of the Electrical and Computer Engineering department, and Professor Jianxin Zhou of the Mathematics department.

All works conducted for this dissertation was completed by the student independently.

Funding Sources

This work was supported in part by the Alpha Kappa Alpha Graduate Merit Scholarship.

This work was supported in part by the department of Electrical and Computer Engineering Thomas W. Powell ’62 and Powell Industries Inc. Fellowship at Texas A&M University.

This work was supported in part by the Graduate Teaching Fellowship from the College of Engineering at Texas A&M University.

This work was supported in part by the department of Electrical and Computer Engineering Summer Research Scholarship at Texas A&M University.

TABLE OF CONTENTS

Page

LIST OF FIGURES

Page

LIST OF TABLES

Page

1. INTRODUCTION

1.1. Background and Motivation

The U.S. Department of Energy defines a microgrid as “a group of interconnected loads and distributed energy resources within clearly defined electrical boundaries that act as a controllable entity with respect to the grid. A microgrid can connect and disconnect from the grid to enable it to operate in both grid-connected or island mode” [1]. From this definition, it is important to highlight that what makes a microgrid different from most electrical systems with loads and distributed energy resources (DERs) is being a controllable entity. This controllability makes it possible for a microgrid to operate in grid-connected or islanded mode.

Figure 1.1 shows a simple depiction of a microgrid with decentralized local controllers (microsource controllers, load controllers) and a central controller called microgrid central controller (MGCC). The controllers form a network through the communication link. The higher-level coordination of the system is implemented by the MGCC [2].

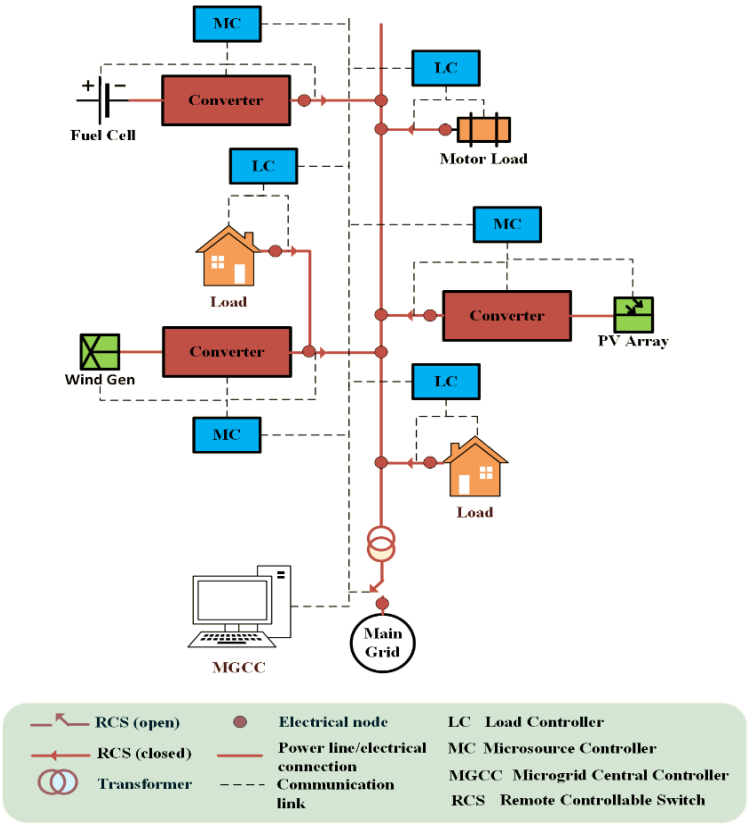

Figure 1.1 Typical Architecture of a Simple Microgrid

The microgrid has been identified as one of the ways to improve the resilience of the power system through its ability to island and operate autonomously during disruptive situations [3]. Because of a microgrid's ability to operate in island mode, it can significantly improve power system resilience during a blackout by providing electricity to critical loads. In August 2020, for instance, hot weather and wildfire led to a shortage of electricity supply in California; this caused the utilities to implement a rolling blackout. Several microgrids operated in island mode and freed up energy for other grid-connected customers, while other microgrids remained grid-connected and served as generating

resources [4]. In several real-life scenarios, microgrids have been utilized to provide electricity in times of emergencies [5-7].

When an emergency occurs, which leads to the unavailability of the power from the bulk grid, microgrids in distribution systems will have to rely on their local energy resources to restore electricity. The process of electricity restoration using a microgrid as a standalone (or island) system without relying on the bulk grid is called microgrid black start. The black start of an islanded microgrid is made possible by the availability of local energy dispatchable resources and remote-controlled switches (RCS) in the distribution system.

As discussed in [8], the island operation of a microgrid is more challenging compared to its grid-connected operation. Some challenges of microgrid island operation highlighted in [8] include smaller system size, higher penetration of distributed generators (DGs), higher uncertainty, lower system inertia, unbalanced three-phase loading issues, and the inability to use traditional system analysis approach for unbalanced microgrid systems. These challenges call for a systematic and efficient black start methodology of the distribution system using an islanded microgrid.

The aim of the dissertation research reported herein was to develop a black start restoration framework for islanded microgrids. Characterization of the participating resources (inertial and non-inertial generators, storage systems, renewable energy sources, loads, smart switches, lines) into simplified modules that are being integrated into the restoration framework was developed. These modules ensure that the framework is generalized to a reasonable extent. Two microgrid control architectures were studied for

use in black start: microgrids operating isochronously and those operating in droop control mode.

Microgrids, due to their modular nature, can be used for faster power restoration as opposed to depending on the main grid which might take more time to fix during an outage caused by a severe occurrence. Apart from power restoration applications, microgrid restoration strategies can be applied to newly built islanded or grid-connected microgrids for black start and optimal network configuration during the initial system build-up. Though this work focused on applying microgrids in islanded mode to black start, many of the considerations and control operations of microgrids developed in this work apply to the normal operation of islanded microgrid systems.

1.2. Contributions

As highlighted in section 2.2, which is a survey of literature review on microgrid restoration, most of the microgrid and distribution system restoration work in the literature focus on energy optimization and reconfiguration without proper consideration of the control philosophy adopted in the microgrid to be restored (especially primary control). The goal of this dissertation is to address these gaps. The key contributions of this dissertation are as follows:

1. Formulated sequential black start restoration of islanded single master microgrids controlled isochronously with consideration of operational and dynamic stability constraints, primary control, and frequency response characteristics.

2. Proposed linear power flow formulations for optimal operation of droop-controlled multi-master microgrids.
3. Formulated sequential black start restoration of islanded droop-controlled multi-master microgrids with considerations of operational and dynamic stability constraints.

1.3. Organization

This dissertation is organized into sections. Section 2 contains a review of related literature. Section 3 consists of the problem description and solution methodology. Section 4 consists of the black start restoration formulation for single master isochronous microgrids operating in island mode. Section 5 proposes linear power flow equations and accompanying optimal power flow formulations for droop-controlled multi-master microgrids. Section 6 consists of the black start restoration formulation for multi-master droop-controlled microgrids in island mode. Section 7 consists of extensive case studies and performance verification of the restoration formulation in section 6. In section 8, conclusions are presented and future work is identified.

2. LITERATURE REVIEW

In this section, we start by introducing the microgrid control philosophies available in the literature as this is essential in the coordination of distributed energy resources for restoration purposes.

We also summarize some of the literature on restoration methodologies for distribution systems and microgrids. Finally, we introduce some stability issues in autonomous microgrids, distributed energy resources (DERs) classification, and linear power flow formulations in distribution systems and microgrids.

2.1. Microgrid Control Philosophy

Identifying the control strategy for the operation of a microgrid is crucial in realizing a well-coordinated and stable system. The concept of hierarchical control of microgrids has become popular and it enables a modular approach to microgrid control [9-11]. Summarily, it entails grouping the control into layers, namely: primary, secondary, and tertiary control as shown in Figure 2.1.

In microgrids, the primary control is responsible for local voltage control and local power balance among the distributed generators and controllable loads and should give an almost instantaneous response to varying system conditions. The secondary control is responsible for dispatching setpoints for the distributed resources in the system through the communication network. The tertiary control runs high-level algorithms to optimize system performance and then send the optimized setpoints to the secondary control for implementation.

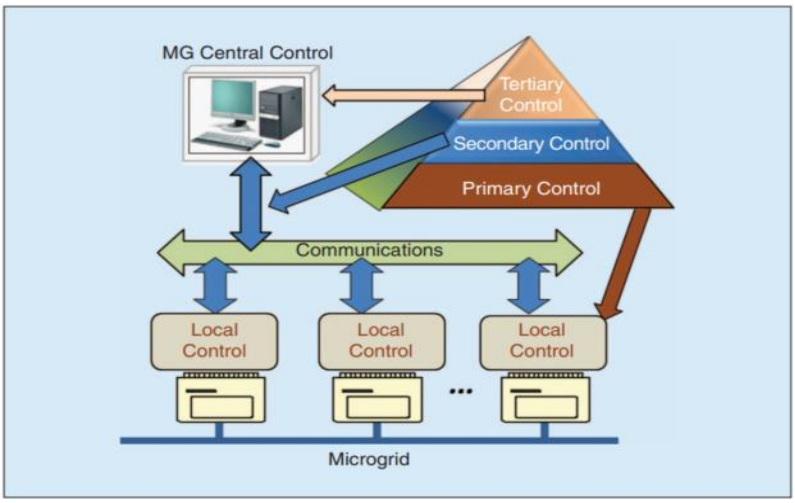

Figure 2.1 Hierarchical Control of Microgrids [11]

In microgrid black start operation, the type of primary control adopted goes a long way in determining system topology as well as essential considerations for safe and stable operation. In the section that follows, we will highlight two major classifications of microgrids based on the primary control that will be referenced in many parts of this dissertation.

2.1.1. Microgrid Classification Based on Primary Control

Microgrids can be classified based on the functionality of interest considered. They can be classified as isolated grid (IG), grid-connected, or may be designed to transition between the isolated and the grid-connected mode [12]. The latter classification could be grouped based on the point of disconnection from the area electric power system (EPS) during islanding operation. This is classified in [13] as local EPS island (facility island), secondary island, lateral island, circuit island, substation bus island, substation island, and

an adjacent circuit island. Details of these island systems and illustrative diagrams are discussed in [13].

Microgrids can also be classified based on frequency and the voltage control technique utilized when operated as isolated grids. The authors in [14] provided a thorough discussion of control strategies for microgrid island operation and they categorized these operational modes as single master operation (SMO) and multi-master operation (MMO). This categorization is reviewed below.

2.1.1.1. Single Master Operation (SMO)

In the SMO mode, as the name implies, the microgrid system is equipped with a single master distributed generator (DG) [14]. The role of the master DG is to provide voltage and frequency references for the other grid-feeding (or grid-following) DGs interfaced in the system. The grid-following DGs are operated in PQ mode – that is, they are given active and reactive power setpoints and are typically not set to respond to changes in the system's frequency, whereas the master DG acts to balance the energy in the system, and thus drives the frequency error to zero. Figure 2.2 shows a block diagram of SMO implementation in isolated microgrids. In the context of power restoration, the communication link transmits switching times for the remote controllable switch (RCS), switch on/off times, and PQ setpoints for the DGs.

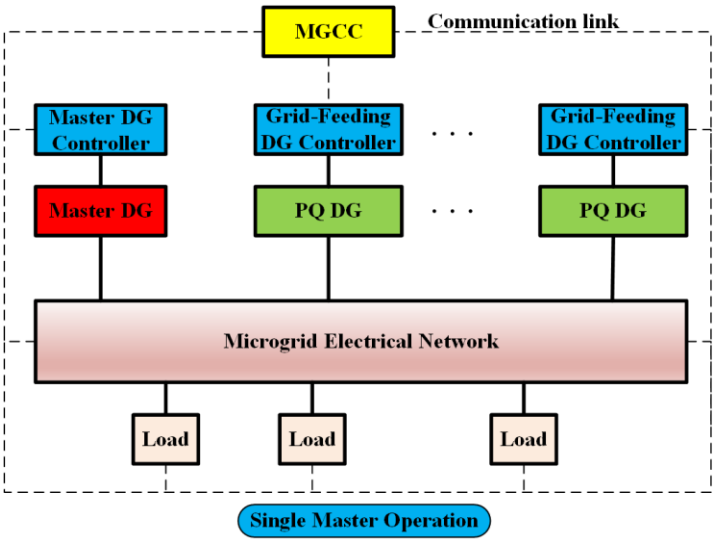

Figure 2.2 Single Master Operation Scheme in Islanded Microgrid

2.1.1.2. Multi-Master Operation (MMO)

In the MMO mode, more than one DG can be operated as a master [14]. There may be other DGs operating in grid-feeding mode. Each of the master DGs will be given an active and reactive power setpoint and also will also have droop control implemented in their power controllers. This droop option means that the master generators share the energy imbalance arising in the microgrid, thereby helping to regulate the frequency in the meantime before new setpoints are communicated to the DGs from the microgrid central controller (MGCC) which would eventually drive the frequency error to zero. Using MGCC to determine and communicate new setpoints for the DGs is one way of implementing secondary frequency control. Another way of implementing secondary frequency control is with the use of storage devices to inject or absorb power to drive the frequency error to zero [14]. Figure 2.3 shows the block diagram implementation of the MMO control scheme in an isolated microgrid.

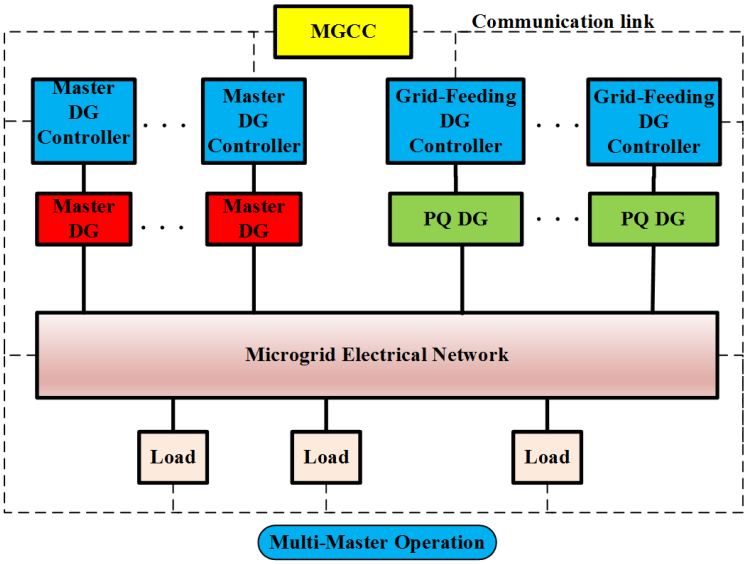

Figure 2.3 Multi-Master Operation Scheme in Islanded Microgrid

2.2. Distribution System and Microgrid Restoration

2.2.1. Restoration Methodology in Distribution Systems and Microgrids

Earlier works in distribution service restoration were formulated as network reconfiguration problems. Reconfiguration techniques in shipboard power distribution systems were formulated as a mixed-integer linear programming problem (MILP) in [15-17]. In [18], the authors proposed a mixed-integer linear programming (MILP) method for a look-ahead reconfiguration of the distribution system with distributed generators. In [19], the author presented an algorithm that combined integer programming, a heuristic method, fuzzy logic, and operator's expertise to arrive at optimal load reconfiguration in the distribution system in the event of a fault. The authors in [20] presented an optimal method for reconfiguration in distribution systems with microgrids in the event of a fault. They divided the problem into capacity sub-problem and reconfiguration sub-problem. In

[21], the authors proposed an integrated approach that explored both microgrid load dispatch and reconfiguration problem considering the stochastic nature of load and energy resources. They made use of four bio-inspired optimization schemes.

Some algorithms that have been used in the formulation of the distribution systems and microgrid restoration include heuristic approach [22], dynamic programming [23], genetic algorithm [24-26], mixed-integer non-linear programming (MINLP) [27], MILP [28-36], mixed-integer second-order cone programming (MISOCP) [37] , and mixed-integer semi-definite programming [38]. A combined service restoration and crew dispatch framework based on a universal routing model was presented in [32].

2.2.2. Dynamic Studies of Islanded Microgrid Black Start

Most of the works that considered the transient simulation of microgrid emergency operation (including the black start) and control philosophy for microgrids have not attempted to formulate the operation of the studied microgrids systematically but rather were mostly rule-based and for concept verification through transient simulation and experimental studies [14, 39-43]. As the size of the system and constraints/considerations increases, the rule-based approach to black start restoration is no longer sufficient in realizing optimal restoration solutions.

Table 2.1 shows a summary of some of the distribution system and microgrid restoration methodology and dynamic studies of islanded microgrid black start available in the literature.

Table 2.1 Summary of Restoration Methodology in Distribution Systems and Microgrids

Ref	Method	Summary
[24]	Parallel Genetic Algorithm (GA)	The method was applied to maximize loads restored in out of service area
[25]	Hybrid GA	The problem was formulated to minimize energy not served using a hybrid GA and considered optimal switching sequence as well
[26]	Two-stage GA	The goal is to minimize expected energy not supplied by the use of 2 stage GA. The first stage solves for the radial network while the second stage searches for an optimal sequence of switching action
[27]	Mixed-integer non-linear programming (MINLP)	Proposes a self-healing strategy for distribution by sectionalizing the system into microgrids
[28-32, 36]	Mixed-integer linear programming (MILP)	Formation of multiple microgrids for service restoration in the distribution system
[37]	Mixed-integer second-order cone programming (MISOCP)	Formation of multiple microgrids for service restoration in distribution system considering demand-side management
[14]	Time-domain transient simulation	The paper defined control methods for islanded operation of microgrid and grouped them mainly as single-master operation (SMO) and multi-master operation (MMO)
[41]	Time-domain transient simulation	Investigates microgrid operation in autonomous mode for preplanned and fault-initiated islanding.
[42, 43]	Time-domain transient simulation	Investigates the use of microgrid for restoration during a fault-initiated islanding and reconnection to the grid

What is lacking in these works is an integrated approach that considers the primary, secondary, and tertiary control into the microgrid restoration formulation, especially the primary control of distributed generators (DGs). As discussed in [8], operation of a microgrid in island mode is more challenging than grid-connected operation due to smaller system size, higher penetration of distributed generators (DGs), higher uncertainty, lower system inertia, unbalanced three-phase loading issues, and the inability to use traditional system analysis approach for unbalanced microgrid systems. Primary control consideration is particularly important for islanded microgrids given that it is the control layer that is expected to respond in real-time to changes in the microgrid operating point.

The integration of microgrid control layers into black start formulation can be done based on proper consideration of the control philosophy used in a given microgrid and

also characterizing the dynamic behavior of the resources available for restoration. A more realistic restoration approach for microgrids should include extended transient simulation studies for method validation, some aspects of DG controller characteristics (mostly primary control), and system-level optimization (tertiary control). The purpose of this dissertation is to integrate these considerations to develop a more holistic and effective black start restoration formulation for islanded microgrids.

2.3. Microgrid Stability

The work in this dissertation is focused on microgrids operating in islanded mode. Stability considerations should be necessary constraints during microgrid black start. The operation of a microgrid in islanded mode is more challenging than when connected to the bulk grid due to the microgrid facing stability and system adequacy problems [8, 44].

Many of the papers on microgrid stability approach the work from a small-signal stability approach [45-47]. However, small-signal stability and eigenvalue analysis approaches are solved by linearizing the system around an operating point and are cumbersome calculations for a microgrid with changing topology and operating point. Such an approach may be difficult to incorporate into a restoration method as stability constraints. An elegant characterization of the stability of the microgrid is necessary.

Still, small-signal stability analysis can help one understand and gain intuition on the direction of parameter changes that influence the microgrid's stability margin negatively or positively. Figure 2.4 and Figure 2.5 show the eigenvalue trajectory of low-frequency modes as a function of active and reactive power droop coefficients respectively of a case study droop controlled autonomous microgrid in [45]. Both trajectories move to

the unstable right-hand plane as the droop coefficients are increased. Intuitively, this is expected since higher droop co-efficients imply a higher sensitivity of the droop inverters to changes in active and reactive power demand, and this sensitivity will be reflected as higher transients in frequency and voltage. Such high transients in frequency can create large-angle swings which might cause the DERs to lose synchronism with each other.

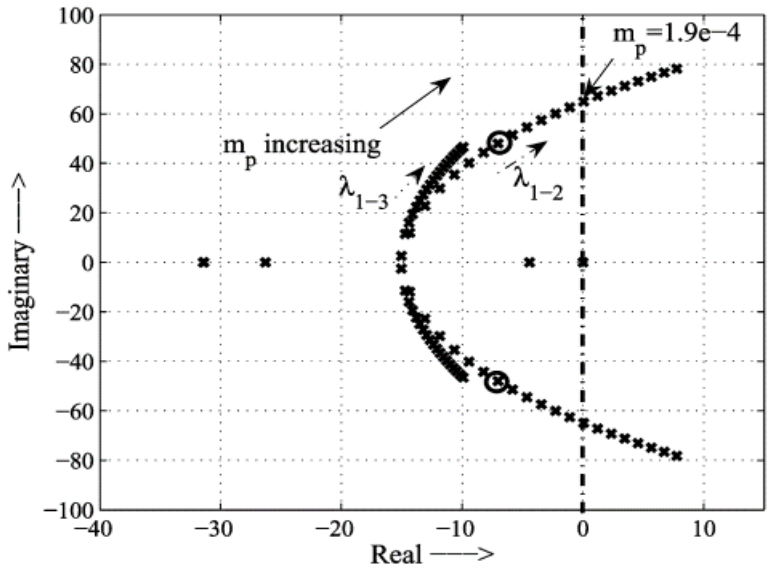

Figure 2.4 Trace of Low-Frequency Modes as a Function of the Active Power Droop Co-efficient, m_p [45]

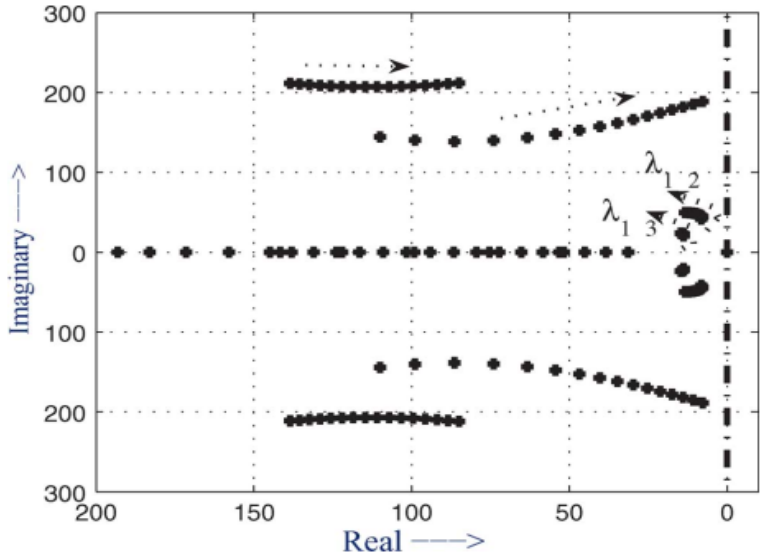

Figure 2.5 Trace of Low-Frequency Modes as a Function of the Reactive Power Droop Co-efficient [45]

In [46], Majumder argued for the case of angle droop, which was demonstrated to show lesser frequency transients and variation when compared to the conventional frequency droop method of active power sharing. However, the angle droop requires a common clock (possibly through the installation of a GPS device at each DER) to enable common phase reference for all droop controlled DERs in the system. Consideration of angle droop for restoration is out of the scope of this dissertation.

In [48, 49], Simpson-Porco et al showed that droop-controlled inverter-based microgrids can be cast as the Kuramoto model of phase-coupled oscillators. The Kuramoto model is a theory of coupled oscillators first developed by Japanese Physicist, Yoshiki Kuramoto, in 1975 [50]. Simpson-Porco attempted to characterize the necessary and sufficient conditions for the existence of an exponential synchronized solution for the system under the special network condition of a purely inductive microgrid. The condition

that was presented, simply interpreted, means that the power flow should be feasible. However, this does not identify the modes in the system and does not characterize the system's behavior under large step changes in load (which is to be expected during restoration) and changes to droop coefficient settings.

During the restoration of islanded microgrids, the sequential pick-up of loads can be considered "large" changes due to the relatively small size of the system, and thus, small-signal stability may not be sufficient. Large signal stability analysis utilizes a non-linear model of the microgrid, thereby, making it more accurate than small-signal stability [51]. A detailed review of large-signal Lyapunov-based stability studies of microgrids is presented in [51]; the authors noted that Lyapunov-based microgrid stability studies are scarce and highlighted necessary gaps which ought to be studied. Most of the microgrid large-signal stability studies are focused on a droop-controlled system using the Lyapunov stability approach [52-54] to estimate the domain of attraction. As the size of the microgrid increases, the model order also increases and model order reduction may be necessary to get approximate models whose analysis is doable. A detailed hierarchy of microgrid models have been developed in [55, 56]. Generally, a large-signal stable system is small-signal stable [51].

In the distribution system and microgrid restoration literature, or rather particularly islanded microgrid restoration literature as this is the most affected by stability issues [8, 44], stability has not been given much attention. Since most stability analysis methods do not offer closed-form equations that can be easily incorporated as constraints into distribution systems and microgrid restoration formulation, stability constraints become

difficult to characterize. In the isochronous/single-master microgrid restoration that is formulated in section 4, we devised a way to incorporate stability constraints through extended transient simulation. For multi-master/droop-controlled restoration presented in section 6, we highlighted the stability considerations in the post-optimization processing subsections (section 6.5) and introduced into the restoration formulation a low transient smooth synchronization approach for the master DGs.

2.4. Classification and Abstraction of Distributed Energy Resources

According to the North American Electric Reliability Corporation (NERC), a distributed energy resource (DER) is any resource on the distribution system that produces electricity and is not otherwise included in the formal NERC definition of the bulk electric system (BES) [57]. Also, NERC's definition of BES [58] is given as: "… all transmission elements operated at 100 kV or higher and real power and reactive power resources connected at 100 kV or higher. This does not include facilities used in the local distribution of electric energy." In these definitions, the term DER is reserved for electricity sources in distribution systems. This includes traditional sources like fuel cells, photovoltaics, wind generators, microturbines, diesel generator, and not so obvious ones like controllable loads with demand response capability [59] [60].

2.4.1. Dispatchable and Non-Dispatchable DERs

DERs can be classified based on how dispatchable their output can be serviced. Dispatchable DERs are those electricity sources whose output setpoints can be adjustable at will and can as well be turned on and off. Examples include fossil fuel-based DGs, diesel engine generators, and storage systems.

On the other hand, non-dispatchable DERs are those electricity sources whose output cannot be adjusted at will, but rather depends on a combination of predictable and unpredictable factors. Examples include wind turbines and photovoltaics. Non-dispatchable DGs could be made dispatchable by interfacing them with energy storage systems to buffer against the uncertainties in their output.

2.4.2. Converter Interfaced DERs

Many DERs in distribution systems are interfaced with intelligent power electronics. This helps to enhance their controllability and power quality. There are three major modes that inverter interfaced DERs can operate in, namely, grid-forming, grid-feeding, and grid-supporting modes [61]. As the semantic of these terms can slightly differ when compared with other literature, in this dissertation, the terms grid-forming, grid-feeding, and grid-supporting modes are based on the definition in [61] and are explained as follows.

2.4.2.1. Grid-Forming Mode

Inverters operating in grid-forming mode are modeled to follow a given voltage amplitude and frequency [61, 62]. Grid-forming inverters could be likened to the behavior of synchronous generators with an isochronous governor whereby the isochronous governor integrates the frequency error in the system to zero. Inverters operating in this mode are not suited for paralleling with other inverters operating in grid-forming and grid-supporting mode since they are configured to work as a voltage source with fixed output values and as such, a precise synchronization system is needed to enable parallel operation [61]. This mode is best suited for the islanded operation and can work with other grid-

feeding inverters. Since this inverter is configured to pick up the active and reactive power slack in the system, the microsource interfaced with it should be dispatchable and in most cases should be relatively large compared to other microsources in the system operating in grid-feeding mode. The master DG in single-master operation microgrids are typically operated in this mode.

Figure 2.6 shows a simple block diagram of the grid-forming inverter modeled as a voltage-controlled source. Microgrids operated with a central grid-forming DG have simpler primary and secondary controls compared with other modes, and this is because the central grid-forming DG will be responsible for restoring the voltage (at least on the DG node) and frequency of the system to the nominal value.

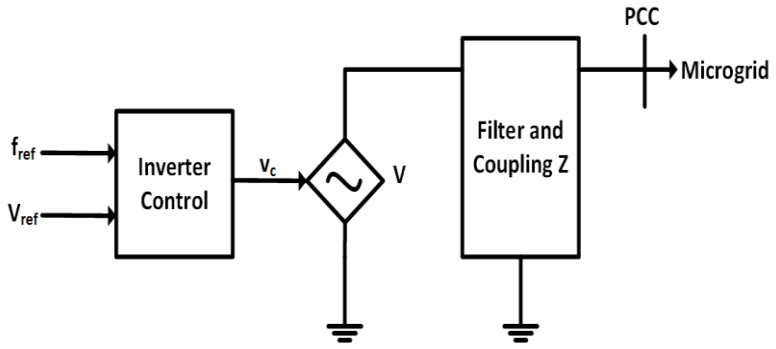

Figure 2.6 Block Diagram of Grid-Forming Inverter

2.4.2.2. Grid-Feeding Mode

The grid-feeding mode is also called grid-following mode. The grid-feeding inverters are controlled such that they serve a set active and reactive power output, and thus, could also be called PQ inverters. In this mode, the voltage reference is supplied by

the distribution or microgrid system, and then the inverter controls its current output to match the values required for the set active and reactive power. Thus, a grid-feeding converter cannot operate as the only DG in the system; rather it needs at least one grid-forming or supporting source to provide a reference voltage for its operation.

Most of the interfaced power inverters in distribution systems and microgrids operate in grid-feeding mode [61, 63]. Its utility is based on the idea that it can be used for both dispatchable and non-dispatchable DG sources. For dispatchable DG sources, a setpoint could be given to it from the secondary control layer, and for non-dispatchable DG sources, the setpoint could be allowed to follow the maximum power tracking. Figure 2.7 shows a simple block diagram of the grid-feeding inverter depicted as a voltage-controlled current source.

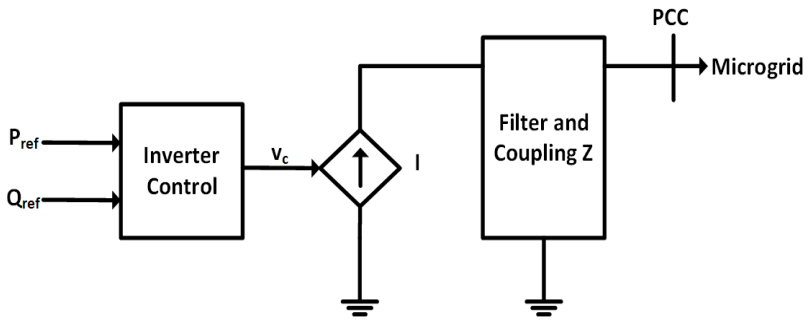

Figure 2.7 Block Diagram of Grid-Feeding Inverter

2.4.2.3. Grid-Supporting Mode

Grid-supporting inverters are designed to emulate the working of droop controlled synchronous generators used in bulk power systems. In this mode, more than one grid-supporting DG (master DGs) can coorporate to provide the voltage and frequency

references for the microgrid; and all other DGs, if any, are typically operating in grid-feeding mode (or grid-following mode). In certain literature (e.g. [11]), grid-supporting DGs are called grid-forming because they actually form voltage reference for the microgrid, except that unlike the definition of grid-forming in section 2.4.2.1, multiple grid-supporting DGs can coorporate together to form the grid. Each of the master DGs would typically have droop implemented in their power controllers. This droop option ensures that the master generators share the active and reactive power load changes arising in the microgrid thereby helping to regulate the voltage and frequency in the system. The block diagram of a droop-controlled grid-supporting source is shown in Figure 2.8.

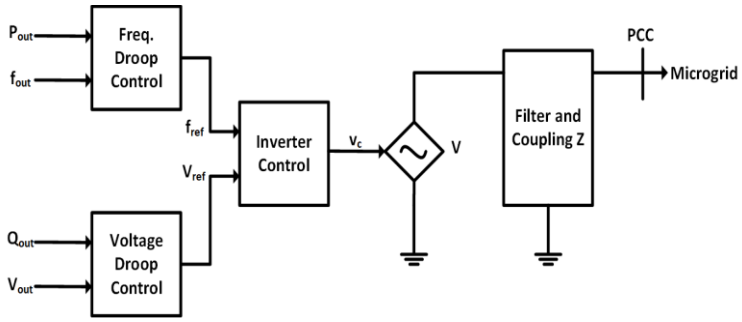

Figure 2.8 Block Diagram of Grid-Supporting Inverter

2.4.3. Energy Storage Systems (ESS)

Energy storage systems (ESS) include battery systems, flywheel, compressed air, and supercapacitors. ESS can act as power supplies to the microgrid when discharging and as load when charging. ESS can be made to contribute to the regulation of the system's frequency by incorporating the needed primary and secondary control into the ESS [14].

2.4.4. Controllable Loads

Controllable loads are loads whose value can be controlled or shedded by the MGCC. Having controllable loads is essential for the safe operation of the microgrid, especially in island condition when there is no stiff source or an approximate slack bus in the system. Automatic shedding of aggregated loads or adjusting aggregate load values can help to restore the frequency during contingencies when a supply node or branch is lost [9].

2.5. Linear Power Flow Formulation in Distribution Systems and Microgrid

Simplified DistFlow branch equations were introduced in [64] for optimal network reconfiguration in distribution systems. The simplified DistFlow is based on a single-phase system and is linear if the square of voltage magnitudes is considered as the unknown variable. The unbalanced three-phase equivalence was proposed in [65] and has been applied to develop service restoration algorithms for distribution systems and microgrids [29, 30].

For single-master/isochronous microgrid restoration, the power flow constraints are formulated by assuming that each formed microgrid has a DG operating isochronously. The node at which the isochronous DG is connected is approximated as a slack bus and thus, conventional DistFlow can be applied in the formulation of such a microgrid restoration problem.

However, when the microgrid is droop-controlled (multi-master microgrid), conventional DistFlow and other linear power flow methods cannot be easily incorporated into the microgrid optimization and restoration problem. In section 5, this dissertation

provides new closed-form formulations of linear power flow that can be incorporated into the droop-controlled microgrid optimization problem.

2.6. Section Summary

In this section, the microgrid control philosophy was introduced. A review of the existing work in distribution systems and the microgrid's black start restoration was presented. An overview of microgrid stability and distributed energy resources was discussed. Finally, power flow considerations and challenges in microgrid optimization and restoration problems were presented. The subsections, while providing a review of the materials in the literature, also highlighted some of the existing problems which this dissertation attempts to solve.

3. PROBLEM DESCRIPTION AND SOLUTION METHODOLOGY

For the successful implementation of a microgrid restoration solution, there are several considerations. Some of these considerations include: inherent unbalance present in distribution systems, control methods required for the successful operation of distributed generators within each microgrid, consideration of the microgrid's interaction and interconnection for reliability and utilization improvement, and necessary constraints required for safe system restoration. In this section, we begin with a statement of the problem, followed by hypothetical black start examples, and finally the new solution methodology.

3.1. Statement of Problem

The restoration methodology discussed in this dissertation is the black start of distribution systems with the use of islanded microgrids. The restoration method is implemented centrally in a MGCC. Two major microgrid control architecture are considered during black start: single master operation (SMO) and multi-master operation (MMO) microgrids. Figure 3.1 shows the framework of the microgrid with black start capability. The microgrid black start framework consists of the central processor engine, which is called the "microgrid black start control application" in Figure 3.1. This processor engine can access necessary data via communication links to the renewable energy forecast application, load forecast application, and distribution management system (DMS) database. It can also communicate to the local controllers in the system such as microsource controllers (MCs), load controllers (LCs), and the remote controlled switches (RCSs) to ascertain their status and to send out setpoint settings.

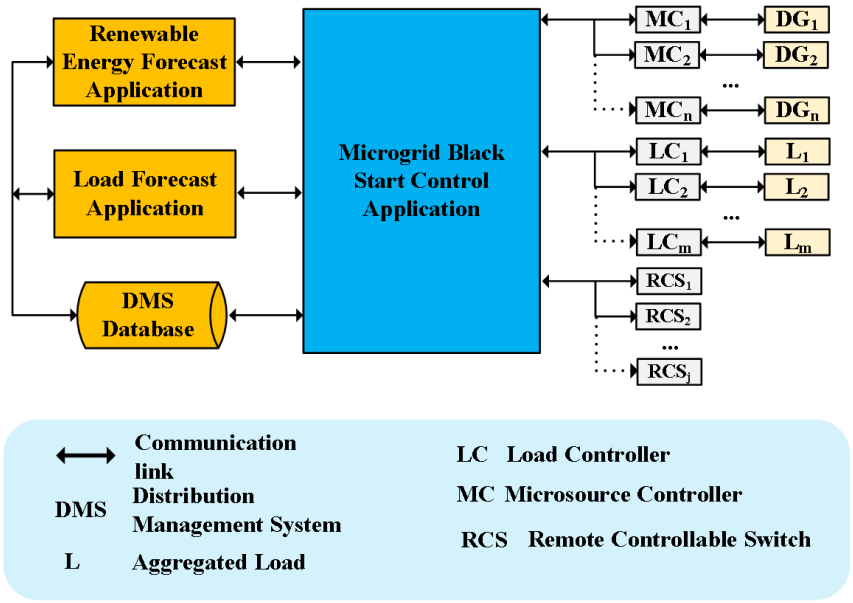

Figure 3.1 Islanded Microgrid Black Start Framework

The first part of the problem is to identify the control philosophy that should be used for the black start restoration. This depends on the class of DGs available in the system. As mentioned before, we considered two control philosophies in this work: single-master and multi-master operation.

For the single-master operation black start approach, the restoration is expected to form multiple microgrids. The number of formed microgrids is equal to the number of DGs in the system with black start capability and operate in grid-forming mode operation. The restoration is performed sequentially. The restoration problem is to determine optimal energy dispatch for the DGs, optimal restoration sequence, and if possible, the actual switching times of the remote controlled switches (RCS) while satisfying the system's operational constraints.

The restoration control for the multi-master approach is more complicated than the single master approach. This is because multiple DGs, operating in grid-supporting mode, are expected to be controlled optimally to support the system's voltage and to share loads appropriately. This approach has the potential to form a larger microgrid (instead of multiple microgrids) which could potentially enhance system resilience, DG utilization, and energy optimization.

3.2. A Simple Black Start Example

In this section, we present simple examples to discuss microgrid topology choice and other considerations necessary during restoration. We identify three DG operating modes in these examples: grid-feeding mode (or grid-following mode), grid-forming mode (master mode), and grid-supporting mode (an alternative master mode) [62].

DGs operating in grid-feeding mode are set to follow the reference voltage and frequency provided by the system, and the voltage and current of these DGs are controlled such that it gives out a set power. DGs operating in grid-forming mode are set to operate as a voltage source and sets its voltage magnitude, phase, and frequency while other DGs in the system would be set to follow in grid-feeding mode. It is not advisable to have more than one grid-forming mode in the system since there is no primary control for reference negotiation between master DGs operating in this mode. Lastly, DGs operating in grid-supporting mode are set to operate in droop which allows paralleling with other similar DGs to form a voltage reference.

3.2.1. Single Master Operation Example

In the single master approach, each microgrid formed would comprise a single DG operating in grid-forming mode and any number of DGs operating in grid-feeding mode. Consider the 14-node distribution system in Figure 3.2 that needs to be restored after a blackout.

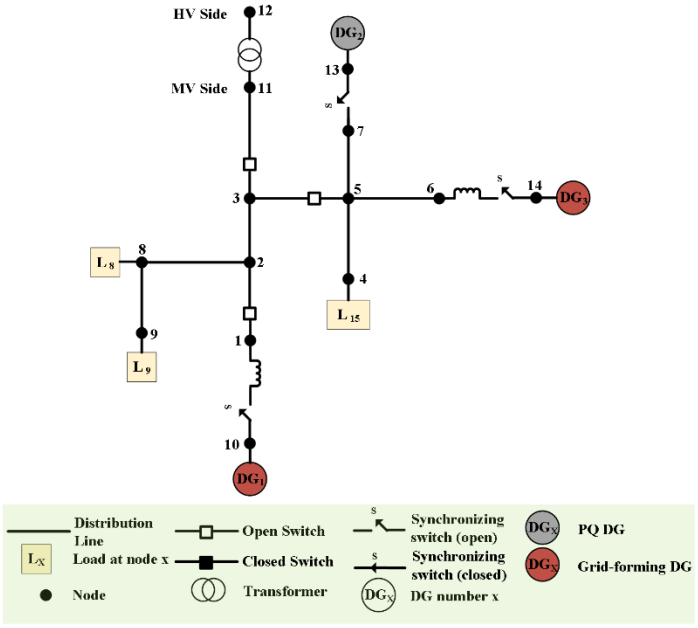

Figure 3.2 14-Node Distribution System Waiting to be Restored

As shown in Figure 3.3, two build-up nodes are identified at nodes 10 and 14, and the build-up should have an isochronous grid-forming DG (or at least a grid-supporting DG) with black start capability. Two microgrids restored in parallel, starting from these two nodes, can be formed at the end of the black start restoration as depicted in Figure 3.3. The switch on the line between nodes 3 and 5 was left open so as not to connect the two microgrids.

To connect the two systems would probably require changing the modes of operation of the grid-forming DGs to grid-supporting DGs and also implementing some synchronization algorithm. This synchronization algorithm may require implementing additional secondary and primary control into the open switch between nodes 3 and 5 of Figure 3.3. Since in our proposed method, the formed microgrid topology is dynamic, it would be difficult to know ahead of time where this sophisticated switch is to be placed. There have been studies on sectionalizing distribution systems into multiple microgrids during restoration [27-30], however, interconnecting the multiple microgrids may become a challenge due to synchronization requirements which we will discuss later. Interconnected microgrids or forming a larger microgrid will likely offer better reliability, load balancing, and energy coordination. The multi-master approach addresses this issue by building the network up to the DG connected nodes and then synchronizing with these DGs at their connection nodes since DGs are expected to have synchronization ability implemented in their hardware.

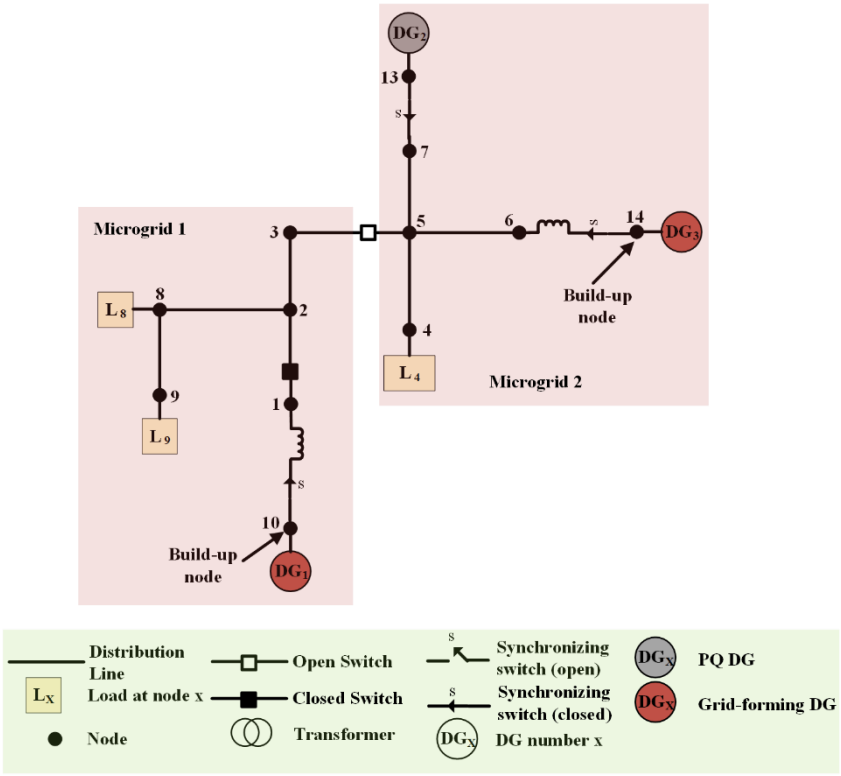

Figure 3.3 Final Restoration Step of an Example Restoration with Single Master Approach

3.2.2. Multi-Master Operation Example

In multi-master mode, one or more grid-supporting DGs operating in droop mode are controlled to provide voltage reference for the system. Consider the 14-node distribution system in Figure 3.2 that needs to be restored after a blackout. Assume that the two grid-forming DGs in Figure 3.2 have been replaced with two grid-supporting DGs to enable voltage and frequency reference negotiation through droop control.

The two three-phase grid-supporting DGs at nodes 10 and 14 can act as master for the system. Let us assume that the entire system starts expanding from one node called "build-up" node with a grid-supporting DG and then connects with the other DGs as the

build-up gets to the respective DG nodes. The following steps show an example build-up of the above 14-node islanded system for a black start restoration.

Step 1, 2, and 3: From Figure 3.2, nodes 10 and 14 are the nodes that are connected to a droop-controlled DG, therefore one of these two nodes can be chosen as a start-up node since the islanded system needs at least one master DG at any given time. Consider Figure 3.4 below. Let us assume that the central controller for the restoration chooses bus 10 as the build-up node after solving for the optimal system restoration sequence. Thus, the DG at node 10 is energized at the first restoration step as shown in Figure 3.4.

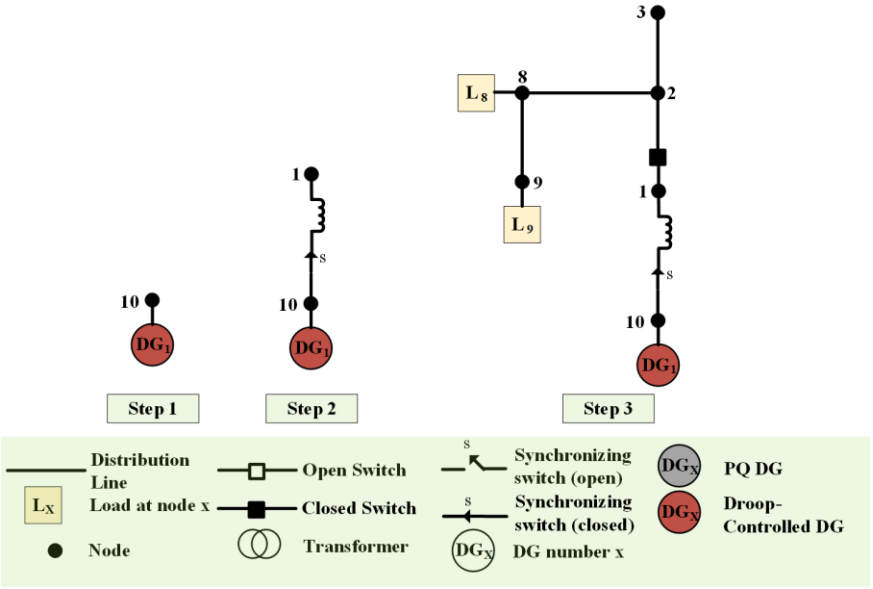

Figure 3.4 Step 1, 2 & 3 of an Example Restoration Process with Multi-Master Approach

In step 2, the synchronizing switch of DG 1 is closed and node 1 becomes energized (in this step, the synchronizing switch is connected to an unenergized system, therefore, there is no need for a synchronization check).

In step 3, the switch on the distribution line between nodes 1 to 2 is energized, leading to nodes 2, 3, 8, and 9 becoming energized automatically since lines 2 to 3, 2 to 8, and 8 to 9 are non-switchable lines. Also loads L8 and L9 are energized as well.

Step 4: In step 4, the line between nodes 3 and 5 is energized which automatically energizes nodes 4, 5, 6, and 7. Also, DG 2 is synchronized to the system and load L4 is energized too. The topology of the microgrid in this step is shown in Figure 3.5.

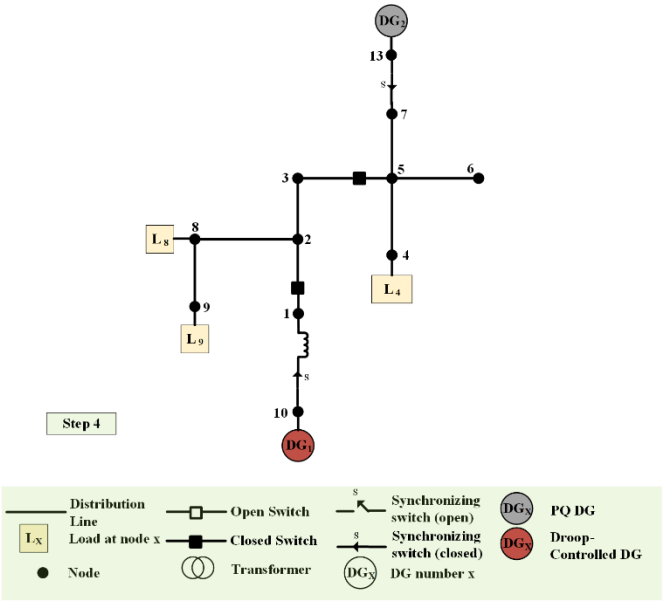

Figure 3.5 Step 4 of the Example Restoration Process with Multi-Master Approach

Step 5: Finally, in step 5, the droop-controlled DG at node 14 is synchronized to the system as shown in Figure 3.6. For a stable connection, a precise synchronization method should be implemented in this droop-controlled DG. Even though the PQ DG needs to be synchronized as well, the synchronization of a droop-controlled DG is more critical since it is responsive to changes in the frequency and voltage of the microgrid.

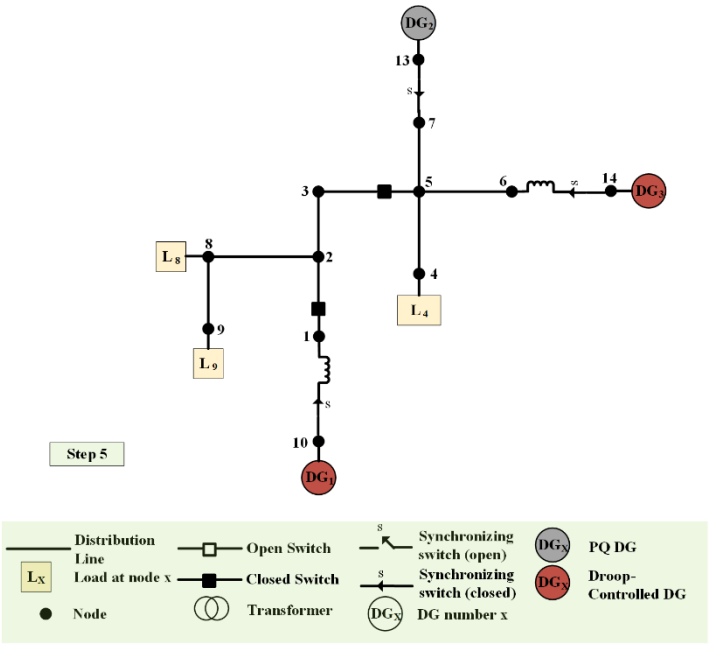

Figure 3.6 Step 5 of the Example Restoration Process

However, if two microgrids were restored in parallel with each droop-controlled DG acting as a master for each microgrid, interconnecting both microgrids can be an issue. This is depicted in Figure 3.7. The boundary switch between the two microgrids at nodes 3 and 5 will not be able to adjust the frequency, voltage magnitude, and phase of both nodes for smooth synchronization. This is the motivation for building the microgrid from a single build-up node and then synchronizing each DG to the microgrid at their respective nodes since each DG is expected to have synchronization check capability.

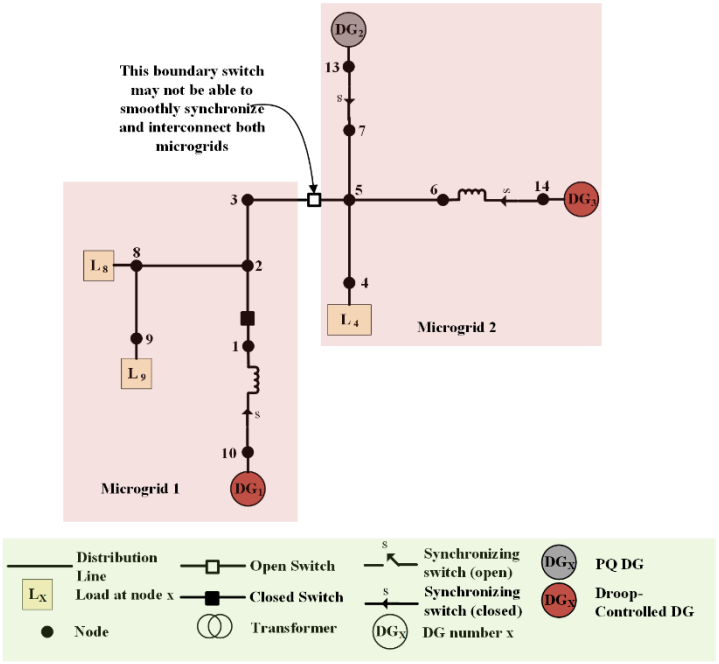

Figure 3.7 Parallel Restoration with Master DG and Problem with Synchronizing and Interconnecting the restored Microgrids

Table 3.1 shows a comparison of the single master approach versus the multi-master approach for islanded microgrid restoration.

Table 3.1 Comparison of Single Master and Multi-Master Restoration Approach for Islanded Microgrids

Single Master Approach	Multi-Master Approach
Multiple smaller microgrids are restored in parallel	A single larger microgrid can be restored
Each restored microgrid has one grid-forming DG (one master DGs)	The restored microgrid can have one or more grid-supporting DGs (one or more master DGs). Generally, would be more resilient since it can have more than one master DG
Can have one or more grid-feeding DGs	Can have one or more grid-feeding DGs
The grid-forming DGs are typically operated in isochronous mode and therefore, do not support real-time power-sharing	The grid-supporting DGs are typically operated in droop mode and therefore, supports real-time power-sharing among the master DGs
Control is simpler and can enable faster parallel microgrids restoration	Coordinating droop control and its setting is more complicated, larger microgrid might enhance better DG utilization and load balancing

3.3. Solution Methodology

Two black start restoration methodologies are proposed in this dissertation. The first one is the single master microgrid approach presented in section 4, and the second is the multi-master microgrid approach presented in section 6. In both formulations, the mathematical model of the distribution system is developed and linearized using novel and existing approaches to realize mixed-integer linear programming (MILP) problems. The resulting MILP problems can then be solved using an off-the-shelf solver. To showcase the dynamic characteristics of the DGs in the single master approach, extended PSCAD simulations are carried out and incorporated into the restoration formulation. In both approaches, the restoration solutions are validated using detailed transient simulation in PSCAD.

Section 5 proposes two novel linear power flow formulations for multi-master droop-controlled microgrids. These linear power flow formulations are extended to develop optimal power flow (OPF) formulations to realize a quadratic programming (QP) and a mixed-integer quadratic programming (MIQP) problem. These OPF formulations can be solved using the appropriate off-the-shelf solver. While section 5 has an example application of the developed OPF to minimize cost in islanded droop-controlled microgrids, the linear power flow constraints of the multi-master restoration formulation in section 6 is based on one of the linear power flow formulations of section 5.

More details about the solution methodology for each section are provided in the respective sections of this dissertation.

4. BLACK START RESTORATION IN ISOCHRONOUS MICROGRID*

4.1. Section Abstract

This section presents a methodology for generating restoration sequences in distribution systems and microgrids, with emphasis on deriving optimal switching times for remote control switches (RCS). The method assumes the microgrid architecture is operating in islanded single master/isochronous mode. Control methods for handling the unbalance inherent in distribution systems using single-phase controlled PQ inverters were developed and incorporated in the proposed method. The problem of considering simultaneously both energy optimization and dynamic stability of the system, which is lacking in existing methods, was addressed by studying the transient behavior of microgrids based on extended EMTP simulations and then approximating and incorporating these behaviors into the optimization formulation for restoration. The approach is based on multi-objective optimization of final restored loads and total restoration time. The methodology was studied on a modified IEEE 123 node test feeder. An EMTP simulation in PSCAD of the formed microgrids was used to validate the accuracy of the dynamic and steady-state characteristics of the resulting systems. By

*Parts of this section are reprinted with permission from O. Bassey and K. L. Butler-Purry, "Modeling Single-Phase PQ Inverter for Unbalanced Power Dispatch in Islanded Microgrid," *2019 IEEE Texas Power and Energy Conference (TPEC)*, College Station, TX, USA, 2019, pp. 1-6, doi: 10.1109/TPEC.2019.8662149 © 2019 IEEE

Parts of this section are reprinted with permission from O. Bassey, K. L. Butler-Purry and B. Chen, "Dynamic Modeling of Sequential Service Restoration in Islanded Single Master Microgrids," in *IEEE Transactions on Power Systems*, vol. 35, no. 1, pp. 202-214, Jan. 2020, doi: 10.1109/TPWRS.2019.2929268 © 2019 IEEE

considering the transient behavior of DGs during restoration, a better restoration sequence that does not trigger protection relays could be realized.

4.2. Introduction

Microgrid technologies could be designed as 'plug-and-play' modules and thus could be immediately deployed during emergencies. However, to ensure optimal system reconfiguration and that safety is not compromised, it is necessary to plan and study the use of microgrids for this purpose. In this section, we present a framework for the sequential restoration in a fully automated distribution system by the formation of multiple microgrids after system blackout. Microgrid architecture considered in the restoration formulation of this section is assumed to be operating in an islanded single master mode.

In earlier work in [29, 30] developed by Chen et al at the Power System Automation Lab, Texas A&M University, the restoration problem was formulated as a MILP formulation by linearizing the system model and operational constraints. The method generates sequences of control actions for the remote-control switches (RCS) that facilitates the sequential formation of the system into multiple microgrids. The formulation is inherently quasi-dynamic: it considers steady-state operating points of the system at different time steps without considering the dynamic characteristics due to primary control adopted in each microgrid system and the time interval between switching steps.

The formulation in this work follows from Chen's earlier work in [29, 30] and has the following additional contributions:

1. Shows how a simplified dynamic characteristic of inertial DGs with isochronous governor can be derived and linearized for restoration purposes.

2. Formulates the restoration problem such that actual switching times of the RCS can be incorporated and optimized.

3. Explores the use of the single master operation (SMO) microgrid control strategy to form multiple isolated microgrids for black start restoration using both inertial and non-inertial DGs.

4. Develops a platform for validation of the restoration solution using EMTP simulation studies in PSCAD.

The work presented in this section attempts to characterize and curtail the transients in low inertia systems used for restoration from the sequential build-up of microgrids. As highlighted in [66-68], the ability to curtail the frequency transients within acceptable limits could determine if a microgrid survives or collapses during large disturbances. By minimizing the microgrid build-up time, critical loads can be restored quickly after the occurrence of an outage and the cold load pickup issue can be avoided. The method introduced in this section could potentially be used in advanced distribution systems and microgrids to affect fast and safe emergency restoration.

4.3. Methodology

The proposed distribution system restoration (DSR) method is modeled to generate switching sequences and times for remote controlled switches (RCS) for use in advanced distribution systems (ADS). The method can be divided into three operations: 1) planning and resource characterization, 2) system monitoring, and 3) restoration execution.

The first operation, planning and resource characterization, are typically occasional recurring actions to make feasible restoration plans ahead and identify resources in the system. Distributed energy resources (DERs) that are available in the distribution system are identified. DERs are classified based on the control modes (isochronous, droop, charge/discharge, and PQ modes) in which they can be operated. The dynamic characteristics of these DERs are then estimated through experimentation, if possible, simulation, or from the manufacturer's datasheet. For the ADS, this operation is expected to be performed through a manual process and then the required information is updated in the distribution management system (DMS) database. This should probably be done when a new DER is installed in the system or an old one is removed. Figure 4.1a is a flow chart of the planning and resource characterization process.

The system monitoring operation is based on information obtained by the distribution system supervisory control and data acquisition (SCADA) system. The status of network branches, RCS, bus aggregated loads, and DERs are inferred from the SCADA data and are updated in the DMS database. During the system monitoring process, if an outage is detected then the restoration algorithm is called upon for execution. Figure 4.1b is a flow chart of the system monitoring operation.

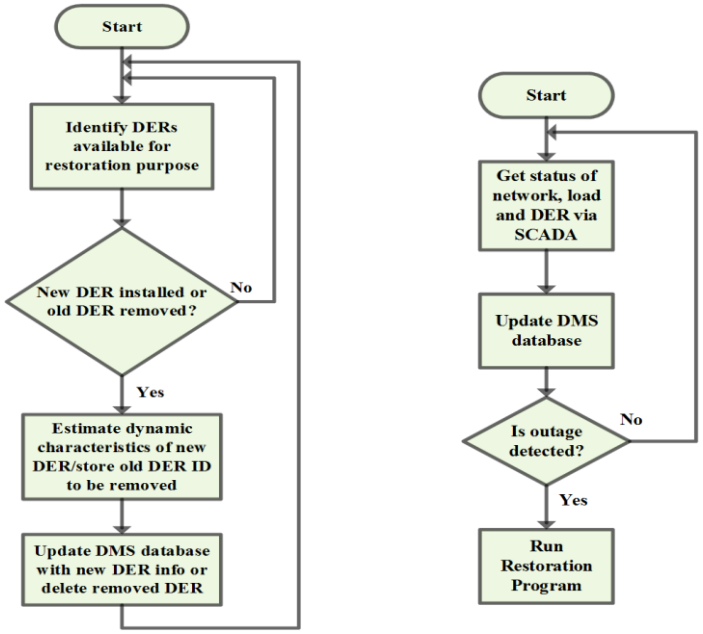

(a) (b)

Figure 4.1 Flow Chart of (a) Planning and Resource Characterization (b) System Monitoring
(© 2020 IEEE)

The restoration execution is activated when the system monitoring operation detects an outage in the system. The restoration program uses the current status of the network, forecasted aggregate loads at the buses, DGs, and other distributed energy resources, and determines the sequence of restoration actions. Since the time interval between sequences is modeled in this method, the switching times are ordered in ascending order of command times, and each command is sent one at a time from the microgrid control center (MGCC). Figure 4.2 is a flowchart of the sequential service restoration process.

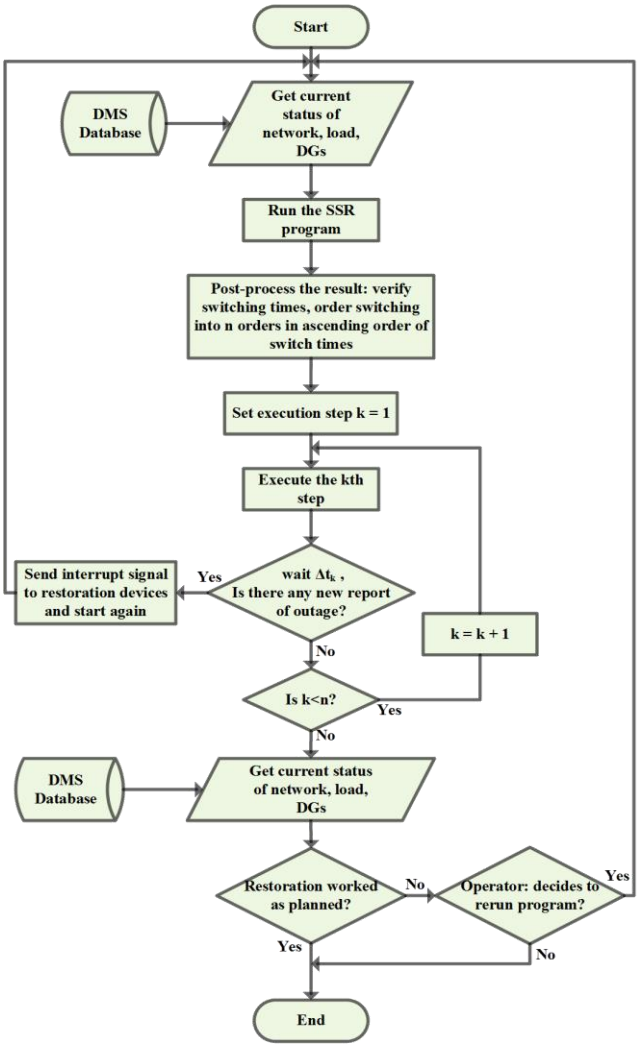

Figure 4.2 Flow Chart of the Proposed Restoration Process
(© 2020 IEEE)

4.4. DG Characteristics and Control Method

The control philosophy for multi-microgrid black start used in the rest of section 4 is presented, frequency response characteristics for diesel generators are derived and validated, and finally, control of non-inertial inverter-based DGs in grid-feeding mode is also presented.

4.4.1. Control for Black Start Energy Balance

In this section, we assume that each microgrid formed is operated in SMO mode as discussed in [14, 69]. Each microgrid system is equipped with a single master DG which provides a voltage reference for the system and all other energy sources, if any, are operated in grid-following mode. This ensures that we do not have significant steady-state frequency deviation as a consequence of droop since a master DG for SMO mode is operated in an isochronous mode to integrate the frequency error to zero. We assume that there is a three-phase synchronous generator acting as the master DG in each microgrid formed.

4.4.2. Frequency Response Characteristics of Diesel Generators with Isochronous Governor

Figure 4.3 shows a simplified block diagram of a diesel engine generator with an isochronous governor.

The relationship between ΔP_{valve} (differential change in mechanical power input in per unit) and $\Delta\omega$ (differential change in rotor speed in per unit) can be written mathematically as.

$$\Delta P_{valve} = -K_I \int_0^t \Delta\omega \, dt - K_P \Delta\omega \tag{4.1}$$

K_I and K_P are the gains of the integral and proportionate controller respectively. Using a classical generator model [70], the rotor dynamics can be written as (all quantities are in pu).

$$d\omega/dt = \frac{\omega_s}{2H}(T_m - T_e - T_{fw}) \tag{4.2}$$

T_m is the mechanical torque, T_e is the electrical torque, ω_s is the synchronous speed, H is the generator inertia constant in seconds and T_{fw} is the loss and dampening term. Ignoring T_{fw} and assuming little speed deviation, we can write the mechanical (P_m) and electrical power (P_e) thus: $P_m = \omega T_m \approx \omega_s T_m, P_e = \omega T_e \approx \omega_s T_e$ and (4.2) could be simplified and linearized as shown below.

$$d\omega/_{dt} = \frac{1}{2H}(P_m - P_e) \tag{4.3}$$

$$d\Delta\omega/_{dt} = \frac{-1}{2H}\Delta P_e + \frac{1}{2H}\Delta P_m \tag{4.4}$$

Ignoring the prime mover transmission dynamics and assuming perfect transmission, we can assume that $\Delta P_m = \Delta P_{valve}$ and then substituting (4.1) into (4.4) and taking the Laplace transform of the resulting equation gives the transfer function:

$$\frac{\Delta\omega(s)}{\Delta P_e(s)} = \frac{\frac{-1}{2H}}{s + \frac{1}{2H}\frac{K_I}{s} + \frac{1}{2H}K_P} = \frac{\frac{-s}{2H}}{s^2 + \frac{1}{2H}K_P s + \frac{1}{2H}K_I} \tag{4.5}$$

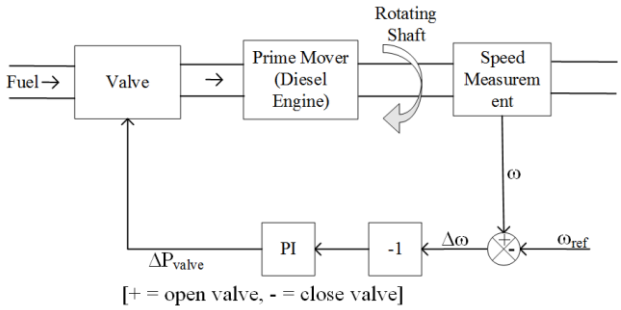

Figure 4.3 Block Diagram of the Isochronous Governor (adapted from [71])

Rearranging the denominator of (4.5) to look like the standard second-order system ($s^2 + 2\zeta\omega_n s + \omega_n{}^2$), we get.

$$\zeta = \frac{K_P}{4H}\sqrt{\frac{2H}{K_I}} = \frac{K_P}{\sqrt{8HK_I}}\,, \omega_n = \sqrt{\frac{2H}{K_I}} \tag{4.6}$$

Equation (4.5) is a typical transfer function of the second-order system and can yield a step response of undamped ($\zeta = 0$), under-damped ($0 < \zeta < 1$), overdamped ($\zeta > 1$) or critically damped ($\zeta = 1$) [72]. By careful choice of the PI parameters using (4.6), we can get the desired frequency response characteristics.

Since the stator transient is relatively much faster than the mechanical transient [70], we can assume that when an incremental load is added to the generator that the electrical power steps up instantly while the mechanical dynamics in the diesel engine responds relatively slow to changes in load.

Hence, for an instantaneous change in P_e(t) to $P_e(t) + \Delta P_e(t)$ at $t = 0$, where $\Delta P_e(t) = \Delta P_k$, a constant in pu (note that $\Delta P_e(s) = \frac{\Delta P_k}{s}$), then:

$$\Delta\omega(s) = \frac{\frac{-\Delta P_k}{2H}}{s^2 + 2\zeta\omega_n s + \omega_n{}^2} \tag{4.7}$$

We can get an approximate frequency response of an isochronous generator by substituting the actual values of the parameters in (4.7) and taking inverse Laplace transform. As an example, the synchronous generators used in the case study of section 4.6 each has the following parameters: $H = 3.117\ sec, K_P = 8.8, K_I = 2.5 \rightarrow \zeta = 1.1145$ (over-damped), $\omega_n = 0.6333$. Substituting these values into (4.7) and taking the inverse Laplace transform gives the result:

$$\Delta\omega(t) = -0.51474\Delta P_k e^{-0.7058t} sin\, h(0.3116t)\, pu \qquad (4.8)$$

From (4.8), it is obvious that minimum frequency deviation is directly proportional to the step loading, ΔP_k. The settling time characteristics with step loading can be found through numerical method or graphical method. To validate this analytical result, we then compare it with the result obtained with the detailed model through simulation. Both are plotted in Figure 4.4. Note that (4.8) gives the frequency deviation in pu and ΔP_k is step loading in pu.

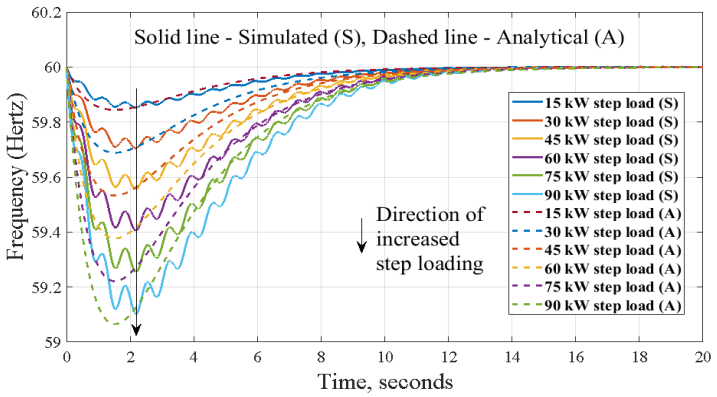

Figure 4.4 Comparison of the Frequency Response of Isochronous Generator by Simulation and Analytical Method
(© 2020 IEEE)

By analyzing the response plot of Figure 4.4 and assuming that the transient has settled when the frequency deviation falls within ±0.01 Hz, we obtain the two relationships: a linear relationship for the minimum (or maximum) frequency versus incremental loading (or negative loading) whose slope determines the frequency response rate (FRR) and a cubic relationship for the settling time versus incremental loading used

to determine safe switching times. We will discuss the linearization of this cubic relationship in section 4.5.4.6. Both the FRR and settling time characteristics were used in deriving the sequential restoration method under the maximum load step constraints (section 4.5.4.5), and energy and time change constraints (section 4.5.4.6) respectively.

4.4.3. PQ Control of Inverters

Interfacing microsources (MSs) with inverters enhance their controllability and power quality. For an inverter to operate successfully when interfaced, adequate control mode should be identified and implemented. These inverter control philosophies for integration in a microgrid are discussed in [14, 73, 74].

Most of the work on microgrid dynamic studies with inverter interfaced microsources assume a three-phase balanced system [14, 39, 40], however, to account for the inherent unbalance in distribution systems, we assumed that a few single-phased decoupled PQ controlled inverters are installed at strategic points across the distribution system. This ensures that the burden of serving the system unbalance is dispatched to the single-phase controlled inverter interfaced MSs and not to the master DG which provides three-phase voltage reference points for the distribution system. Using three-phase controlled inverters to supply unbalanced power can introduce significant unbalance in the three-phase voltage of the MG system [75], a similar outcome goes for three-phase grid-forming synchronous generators [76]. These inverter-interfaced MSs could be fuel cells, photovoltaics, wind generators, microturbines, or other sources.

To reduce complexity and to realize a fast dynamic simulation model, the inverter model used in this work consists only of the control model with the output approximated

as a voltage-controlled source [76]. Hence, power semiconductor models, fast switching transients, losses, and harmonics are neglected. This is in accordance with the simplified approach adopted in many other dynamic studies of inverter interfaced MSs used in ADS (advanced distribution systems) and MG systems [14, 39, 40].

The PQ decoupled single-phase inverter control model was designed based on control ideas for DQ frame controlled single-phase inverters derived from [77-81]. Detailed derivation and simulation of this PQ inverter model can be found in our previous work [76, 82]. The per-phase block diagram of the PQ inverter control model implemented in PSCAD is shown in Figure 4.5.

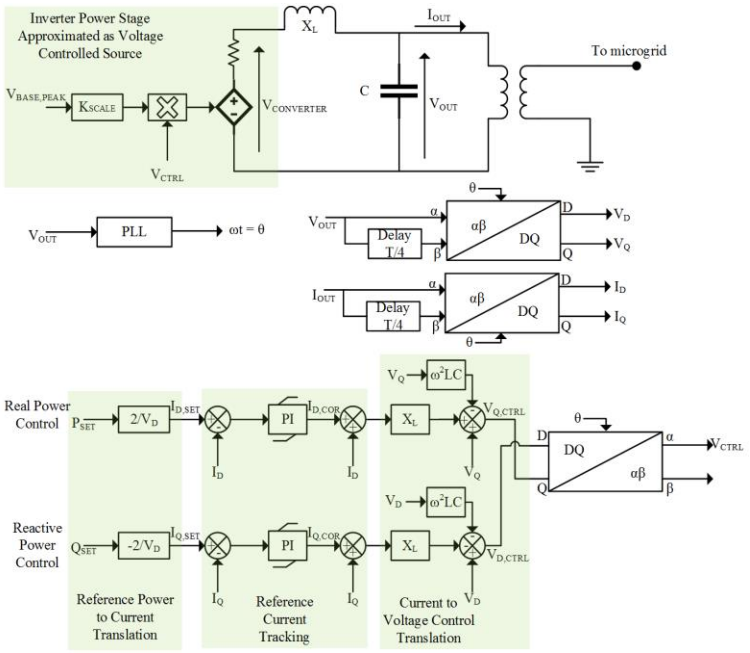

Figure 4.5 One Phase PQ Inverter Control Diagram in the DQ Frame with the Power Stage approximated as a Voltage-Controlled Source
(© 2019 IEEE)

4.5. Dynamic Restoration Modelling of Isochronous Microgrids

4.5.1. Model Description

The symbols and parameters used in this section are summarized in Table 4.1. The distribution system and microgrids can be represented as a graph, $G(N, B)$, made up of $n(N)$ nodes and $n(B)$ lines/edges with aggregated loads and DGs connected at different nodes in the system.

Table 4.1 Symbols and Parameters of the Restoration Model (© 2020 IEEE)

Sets	
$n(A)$	The number of elements in set A
B, B^S, B^F, C	Set of transmission lines, switchable lines, damaged transmission lines, and switchable lines between bus blocks
G, G^{BS}, G^F	Set of DGs, subset of black start DGs, subset of damaged DGs
L	Set of loads
T	Set of time steps $\{1,2, \dots, N_T\}$ and $n(T) = N_T$
N, N^F, K	Set of nodes, subset of damaged nodes, and set of bus blocks, $n(K) \leq n(N)$
Binary Decision Variables (1 – Energized, 0 – Not Energized)	
$\hat{S}^N_{i,t}, \hat{S}^K_{j,t}$	Energization status of node i/bus block j at time step t
$\hat{x}^G_{g,t}, \hat{x}^L_{l,t}$	Energization status of DG g/load l at time step t
$\hat{x}^{BR}_{ij,t}, \hat{x}^K_{ij,t}$	Energization status of a line (i,j) at time step t, where $(i,j) \in B, K$ respectively
Continuous Decision Variables	
$a, b, or\ c$	Used as subscript or superscript to denote variable or parameter in phase a, b or c respectively
$\hat{P}^{BR}_{ij,t}, \hat{Q}^{BR}_{ij,t}$	Active and reactive power flowing from node i to j at step t
$\hat{P}^G_{g,t}, \hat{Q}^G_{g,t}$	Active and reactive power output of DG g at step t
$\hat{P}^{\emptyset}_{l,t}, \hat{Q}^{\emptyset}_{l,t}$	Active and reactive power demand of load $l \in L$ at time step t, for phase $\emptyset \in \{a, b, c\}$
$\Delta\hat{t}^G_{g,t}$	Time interval from step t to $t+1$ for each microgrid formed, i.e. $\forall g \in G^{BS}$

Table 4.1 Continued

Parameters	
FRR_g^G	The frequency response rate for DG g measured in Hz/KW
M	A large number chosen deliberately to manipulate the constraint equations
$P_g^{G,MLS}$	Maximum absolute value of differential load of DG g for each time step (maximum load step)
$S_g^{G,max}$	Rated capacity of DG g based on the maximum allowable current that a given DG could produce
$S_{ij,t}^{max}$	Maximum allowable apparent power through line $(i,j) \in B$
P_g^{min}, P_g^{max}	Minimum & maximum active power output of DG g
Q_g^{min}, Q_g^{max}	Minimum & maximum reactive power output of DG g
$\lvert\Delta P_g^{max}\rvert, \lvert\Delta Q_g^{max}\rvert$	Maximum allowable active and reactive power difference between phases of DG g

An edge represents the distribution line between two nodes in the system. The restoration algorithm proceeds in such a way that no loops are formed, and each microgrid system formed is a tree and the entire system is a forest. The model presented builds on an earlier model proposed by Chen et al at PSAL, Texas A&M University in [12, 13] with improvements to account for DG dynamic characteristics and switching times of the remote controlled switches (RCS).

4.5.2. Assumptions

The following assumptions were made in the implementation of the proposed restoration algorithm:

1. There is an elaborate communication infrastructure in the ADS.
2. The load models are assumed as constant PQ load in the restoration model; this is justified given that the restoration time is optimized and coordinated to complete in seconds or a couple of minutes such that load variation within this short time frame can be neglected. For the dynamic simulation, a constant impedance load model is adopted for

simplicity. As highlighted in the section summary (section 4.7), modeling a constant PQ load in a dynamic simulation environment can present some challenges in isolated power systems.

3. Black start DGs are assumed to be diesel engine generators and operable in isochronous mode. The isochronous mode of operation is necessary for DGs operating as masters in islanded microgrids.

4. Non-black start DGs are assumed to be dispatchable single-phased controlled PQ inverters operating in grid-following mode. These DGs are assumed to have a battery interface between their microsources and their inverters, thus the battery serves as a buffer for the dynamics and uncertainties associated with the microsources. With this assumption, we can ignore the dynamics of the microsources.

4.5.3. Overview of the Optimization Formulation

The optimization problem is formulated as a mixed-integer linear programming (MILP) and is presented in the next two subsections with constraint equations described in section 4.5.4 and objective function described in section 4.5.5.

As presented in Table 4.1, the decision variables include the following binary variables: energization status of nodes and bus blocks, $\hat{S}^N_{i,t}, \hat{S}^K_{i,t}$, energization status of DGs and loads, $\hat{x}^G_{g,t}, \hat{x}^G_{l,t}$, and energization status of lines, $\hat{x}^{BR}_{ij,t}, \hat{x}^K_{ij,t}$; and the following continuous variables: active and reactive power flowing across branches, $\hat{P}^{BR}_{ij,t}, \hat{Q}^{BR}_{ij,t}$, active and reactive power output of DGs, $\hat{P}^G_{g,t}, \hat{Q}^G_{g,t}$, active and reactive power demand of loads, $\hat{P}^{\varphi}_{l,t}, \hat{Q}^{\varphi}_{l,t}$, and time interval between sequences of restoration, $\Delta\hat{t}^G_{g,t}$. Note that these decision variables are dependent and coupled by the constraint

equations; for instance, the energization status of a given DG will determine if the power output is zero or not. Decision variables are denoted with a hat.

The objective function presented in section 4.5.5 is a weighted multi-objective approach set to maximize total restored active power and minimize total restoration time with priority set on the former. The objective function is described mathematically in terms of these decision variables: load demands and time interval between sequences of restoration. Though not all decision variables are present in the objective function, they each influence the resultant objective value since the constraint equations provide the dependency and coupling.

4.5.4. Constraint Equations

4.5.4.1. Transformer and Line Ampacity Constraint

Equation (4.9) is the transformer and line ampacity constraint. $S_{ij,t}^{max}$ could be seen as the radius of the constraining circle. This type of constraint was linearized and applied in [30] with details of the derivation in the appendix of [83]. This is accomplished by approximating the constraining circle with the sides of a regular convex polygon.

$$(\hat{P}_{ij,t}^{BR})^2 + (\hat{Q}_{ij,t}^{BR})^2 \leq (S_{ij,t}^{max})^2, (i,j) \in B, t \in T \tag{4.9}$$

4.5.4.2. DG Current Unbalance (CUF) Constraint

Current unbalanced factor (CUF) is a measure of the unbalanced loading on a DG and is quantitatively measured as the absolute ratio of the negative sequence current, $I_2^{(1)}$, to the positive sequence current, $I_1^{(1)}$ at first harmonic [29].

$$\left|I_2^{(1)}\right| / \left|I_1^{(1)}\right| \leq CUF_g, g \in G \tag{4.10}$$

Equation (4.10) can be written in terms of each DG's output power and details of its linearization in terms of output power variables are covered in the appendix of [29].

4.5.4.3. DG Power Unbalance Constraint

Considering that CUF is majorly influenced by the relative angular position and magnitude of the three-phase current phasors, the current phasors can have a low CUF without affecting reasonable active and reactive power balance in the three phases of the DG; thus, may induce significant voltage unbalance among the phases due to the differing apparent power amongst the phases. This voltage unbalance would further increase the current unbalance and can in turn adversely affect the CUF linearization which was realized with the assumption that the voltage is balanced. To ensure that each black start DG (or any DG acting to provide a reference voltage in the microgrid) maintain a reasonable power balance between the phases, constraints (4.11) and (4.12) are implemented as shown below.

$$-\left|\Delta P_g^{max}\right| \leq \hat{P}_{g,t}^{G,i} - \hat{P}_{g,t}^{G,j} \leq \left|\Delta P_g^{max}\right|, i,j \in \{a,b,c\}, i \neq j, g \in G^{BS} \backslash G^F, t \in T \quad (4.11)$$

$$-\left|\Delta Q_g^{max}\right| \leq \hat{Q}_{g,t}^{G,i} - \hat{Q}_{g,t}^{G,j} \leq \left|\Delta Q_g^{max}\right|, i,j \in \{a,b,c\}, i \neq j, g \in G^{BS} \backslash G^F, t \in T \quad (4.12)$$

For best balance condition during restoration, $\left|\Delta P_g^{max}\right|$ and $\left|\Delta Q_g^{max}\right|$ should be made as close to zero as possible. However, the cost for a lower allowable phase power difference is that lesser loads are likely to be restored.

4.5.4.4. DG Output Constraint

Equations (4.13) and (4.14) are the DG output constraints [29, 30] and ensure that each DG stays within its allowable minimum and maximum power when it is operating and also forces the power output to zero if it is not operating. P_g^{min} and P_g^{max} will most

likely be determined by how much power the battery interface can safely supply or how much power the prime mover can supply for non-battery interfaced microsources.

$$\hat{x}_{g,t}^{G}.P_{g}^{min} \leq \hat{P}_{g,t}^{G} \leq \hat{x}_{g,t}^{G}.P_{g}^{max}, g \in G, t \in T \tag{4.13}$$

$$\hat{x}_{g,t}^{G}.Q_{g}^{min} \leq \hat{Q}_{g,t}^{G} \leq \hat{x}_{g,t}^{G}.Q_{g}^{max}, g \in G, t \in T \tag{4.14}$$

The current carrying capacity of the inverter module or stator coils in the case of wound generators should also be taken into consideration and is shown in (4.15). Equation (4.15) ensures that the apparent power of the DG at any step is within the current carrying capacity of the DG's inverter interface or armature in the case of a wound generator, and its linearization follows the polygon approach discussed earlier as presented in [30, 83].

$$(\hat{P}_{g,t}^{G})^2 + (\hat{Q}_{g,t}^{G})^2 \leq \left(S_{g}^{G,max}\right)^2, g \in G, t \in T \tag{4.15}$$

4.5.4.5. Maximum Load Step (MLS) Constraint

The MLS is the maximum differential load that a DG can pick or drop at a given time. This ensures that the frequency response of the DG does not exceed a given limit. The maximum load step ($P_{g}^{G,MLS}$) for each DG can be derived from the frequency response rate (FRR_{g}^{G}) and maximum allowable frequency deviation for the system ($|\Delta f|_{max}$) as as follows (also refer to section 4.4.2 for more explanation on FRR).

$$P_{g}^{G,MLS} = |\Delta f|_{max} / \left|FRR_{g}^{G}\right|, g \in G \tag{4.16}$$

$$-\hat{x}_{g,t}^{G}.P_{g}^{G,MLS} \leq \hat{P}_{g,t}^{G} - \hat{P}_{g,t-1}^{G} \leq \hat{x}_{g,t}^{G}.P_{g}^{G,MLS}, g \in G, t \in T \tag{4.17}$$

4.5.4.6. Energy and Time Change Constraint

Under this restoration scheme as earlier stated, the number of expected microgrids formed at the end of the restoration for the multi-microgrid approach is $n(G^{BS})$. Defining

the incremental power for each step for an $n(T)$ time step process as (these are the incremental power of the black start DGs).

$$\Delta P_{g,t}^{G} = \left|\hat{P}_{g,t}^{G} - \hat{P}_{g,t-1}^{G}\right|, \qquad t \in T, g \in G^{BS} \tag{4.18}$$

Based on the simulation studies carried out on the isochronous generators (assuming the black start DGs are of the isochronous type), the settling time could be approximated as a cubic function [69]. The cubic function can be linearized by the use of two conservative linear functions which are simply support tangents to the cubic fit and a third linear function passing through the origin (to ensure that settling time is set to zero when there is no incremental loading for a given time step) as shown in Figure 4.6.

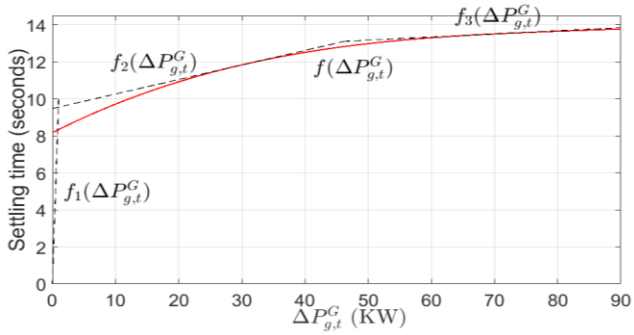

Figure 4.6 Linearization of Settling Time Fit Function
(© 2020 IEEE)

The time interval between time steps could be defined as

$$\Delta \hat{t}_{g,t}^{G} = f\left(\Delta P_{g,t}^{G}\right), \quad t \in T, g \in G^{BS} \tag{4.19}$$

$f\left(\Delta P_{g,t}^{G}\right)$ is the cubic function approximation for the settling time. Using the three linear function approximations in Figure 4.6, the following settling time constraints will be realized.

$$\Delta\hat{t}_{g,t}^{G} \geq f_1\left(\Delta P_{g,t}^{G}\right) - x_{g,t}^{f1} M, \;\; t \in T, g \;\in\; G^{BS} \tag{4.20}$$

$$\Delta\hat{t}_{g,t}^{G} \geq f_2\left(\Delta P_{g,t}^{G}\right) - x_{g,t}^{f2} M, \;\; t \in T, g \;\in\; G^{BS} \tag{4.21}$$

$$\Delta\hat{t}_{g,t}^{G} \geq f_3\left(\Delta P_{g,t}^{G}\right) - x_{g,t}^{f3} M, \;\; t \in T, g \;\in\; G^{BS} \tag{4.22}$$

$$x_{g,t}^{f1} + x_{g,t}^{f2} + x_{g,t}^{f3} = 2, \;\; t \in T, g \;\in\; G^{BS} \tag{4.23}$$

$x_{g,t}^{f1}, x_{g,t}^{f2}, x_{g,t}^{f3}$ are artificial binary variables that help in choosing the function with the lowest value for the inequality constraints and M is a large number chosen to manipulate the constraint equations. Since total time is minimized in the objective function to be introduced soon (section 4.5.5), the above constraints will resolve to the equality of the function (f_1, f_2, or f_3) with lowest value for any given $\Delta P_{g,t}^{G}$ as desired.

A cumulative time interval for each microgrid is defined in (4.24) and represents the total time needed for each microgrid to complete its restoration process.

$$\Delta t_{g}^{G,total} = \sum_{k=1}^{N_T} \Delta\hat{t}_{g,k}^{G}, k \in T, g \;\in\; G^{BS} \tag{4.24}$$

4.5.4.7. Topology and Sequencing Constraints

We first introduce the concept of a bus block described in [29, 30]. A bus block is a group of nodes connected by non-switchable lines. Grouping the system into a set of bus blocks, K, reduces the size of the distribution system graph with edges represented by a set of switchable lines between bus blocks, C. The following constraints adapted from [29] then follows.

4.5.4.7.1. Topology Constraints

Topology constraints ensure that each formed microgrid remains isolated from each other and that each maintains a tree topology and are summarized below [29].

$$\hat{S}_{i,t}^{N} = \hat{S}_{k,t}^{K}, \forall\, k \in K, t \in T \tag{4.25}$$

$$(\hat{S}_{i,t}^{K} - \hat{S}_{i,t-1}^{K}) + (\hat{S}_{j,t}^{K} - \hat{S}_{j,t-1}^{K}) \geq \hat{x}_{ij,t}^{K} - \hat{x}_{ij,t-1}^{K}, (i,j) \in C, t \in T, t > 1 \tag{4.26}$$

$$\sum_{i:(i,j)\in C} (\hat{x}_{ij,t}^{K} - \hat{x}_{ij,t-1}^{K}) + \sum_{i:(k,i)\in C} (\hat{x}_{ki,t}^{K} - \hat{x}_{ki,t-1}^{K}) \leq 1 + M.\hat{S}_{i,t-1}^{K}, \quad i \in K, t \in T, t > 1 \tag{4.27}$$

Equation (4.25) ensures that the status of each bus within a bus block is the same as the status of the bus block. Equation (4.26) ensures that if two bus blocks at both terminals of a switchable line are already energized in the previous step, then this line cannot be energized to maintain the tree topology. Equation (4.27) ensures that if a bus block is not energized at a previous step, then it can only be energized by at most one switchable line.

4.5.4.7.2. Sequencing Constraints

Sequencing constraints ensure that a reasonable switching sequence is realized and are summarized below [29]:

$$\hat{S}_{i,t}^{K} \leq \sum_{i:(i,j)\in C} \hat{x}_{ij,t}^{K} + \sum_{i:(k,i)\in C} \hat{x}_{ij,t}^{K}, i \in K, t \in T, i \cap G^{BS} = \emptyset \tag{4.28}$$

$$\hat{x}_{ij,t}^{K} \leq \hat{S}_{i,t-1}^{K} + \hat{S}_{j,t-1}^{K}, (i,j) \in C, t \in T, t > 1 \tag{4.29}$$

Equation (4.28) ensures that if a bus block does not contain any black start node then it can only be energized by a switchable line. Equation (4.29) ensures that a

switchable line can only be energized when one of its end's bus block is energized in the previous step.

4.5.4.8. Other Constraints

There are a few other constraints required for the successful operation of the single master microgrids that were not reported here. These constraints are broadly classified as: linear power flow constraints which are based on the DistFlow [64, 65] – help to ensure energy balance and application of Kirchhoff's voltage law across branches in the system; and connectivity constraints – help to ensure adequate interconnection between elements in the system [29, 30].

4.5.5. Objective Function

To keep the objective function linear, we make use of a weighted multi-objective optimization approach that maximizes the final total restored active power in the system and minimizes the total time interval for the restoration.

$$min -\sum_{l\in L}\sum_{\emptyset\in\{a,b,c\}} w_l \hat{P}^{\emptyset}_{l,N_T} - \sum_{t=1}^{N_T-1} \alpha_t \sum_{l\in L}\sum_{\emptyset\in\{a,b,c\}} w_l \hat{P}^{\emptyset}_{l,t} + \beta \sum_{g\epsilon G^{BS}} \sum_{k=1}^{N_T} \Delta\hat{t}^{G}_{g,k}, 0 < \beta \ll 1, 0 < \alpha_t \ll 1 \tag{4.30}$$

Subject to the constraint equations described in section 4.5.4 subsections 1 to 8. Where $N_T = n(T)$ denotes the last time step.

The decision variables are the binary and continuous variables described in Table 4.1 and determine the status of the DGs, branches, switches, and loads for all time steps. The constraints provide the dependency and coupling between the decision variables (both those present and those not present in the objective function).

The weights in (4.30) can be seen as translating the base units of power and time into cost quantities and are assigned based on the importance of each term. All loads are assumed to be weighted by the priority factor w_l though for simplicity in the case study that follows, all loads are assumed to have an equal priority of $w_l = 1$. The first term is the summation of the final restored power and it has a combined weight of 1 as it is the most important. The second term is a weighted summation of power from the first step to the penultimate step and has a combined weight of α_t for each time step excluding the final time step; this term was intentionally added to the objective function to enhance the selection of sequences that restores the loads sooner. The third term is the summation of the total restoration time for each of the microgrids formed and its weight is the lowest and ensures that the objective function does not prioritize minimizing time, instead of maximizing the final restored load, which could eventually lead to a sub-optimal solution. The weights are chosen heuristically to ensure the final restored load is optimum and prioritized.

4.6. Case Study

In this subsection, we used the proposed method to solve the black start restoration problem on a modified IEEE 123 node test feeder. Afterward, we validated the restoration solution with PSCAD simulation.

4.6.1. SSR Solution for Modified IEEE 123 Node Test Feeder

4.6.1.1. Description of the Case Study System

The single line diagram of a modified IEEE 123 node test system is shown in Figure 4.7 and was adapted from [84] with the line impedance and phase information kept

the same as the original system. The four voltage regulators in the original system have been replaced with RCS.

Four faults as shown in Figure 4.7 were assumed to have occurred in the test system which resulted in a total blackout. A few lines around the faulted regions were manually or remotely disconnected to isolate the faulted area before the start of power restoration.

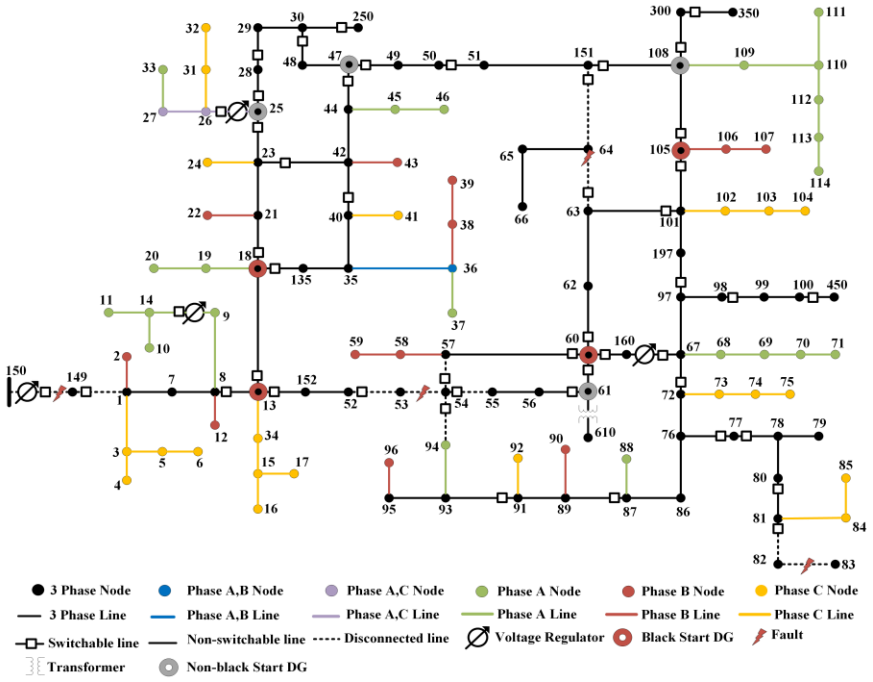

Figure 4.7 Modified IEEE 123 Node Test Feeder
(© 2020 IEEE)

The modified test system consists of eight DGs – four black start DGs and four non-black start dispatchable DGs. The DG parameters are shown in Table 4.2. The type column is the mode in which the DG is operated and is classified as either 1 or 2, where 1

means black start DG and 2 means non-black start DG. The capacity column is the rating of the electrical interface part of the DG in KVA.

$Pmax$ and $Pmin$ are the allowable maximum and minimum real power output from the DG. $Qmax$ and $Qmin$ are the allowable maximum and minimum reactive power output from the DG. MLS, maximum load step, is measured as a fraction of the rated capacity of the DG, i.e., a DG, rated at 500 KVA, with a MLS of 0.1, can pick or drop a maximum of $0.1 \times 500 = 50KW/step$. MLS is calculated such that the maximum allowable frequency deviation is within $\pm 1\ Hz$ (frequency constraint).

CUF is the maximum allowable current unbalance factor for each of the DGs. The CUF for the black start DGs have been set to a low value of 0.05 compared to the CUF of non-black start DGs which was set to 1. PUC is the power unbalance constraint parameter for each of the black start DG. For this case study, the power unbalance constraint between any two phases is set to have a maximum difference of 5KW/5KVAr for the active/reactive power respectively. The inverter-based non-black start DGs do not have the power unbalanced constraint (set as NA – not applicable, in Table 4.2); thus it can be seen as acting as an “unbalance compensator”.

Table 4.2 DG Parameters used for the Case Study
(© 2020 IEEE)

DG Node	Type	Capacity (KVA)	Pmax (KW)	Pmin (KW)	Qmax (KVAr)	Qmin (KVAr)	MLS	CUF	PUC (KW/KVAr)
13	1	500	500	0	300	-200	0.2	0.05	5/5
18	1	500	500	0	300	-200	0.2	0.05	5/5
25	2	200	200	0	200	0	1	1	NA
47	2	300	300	0	300	0	1	1	NA
60	1	500	500	0	300	-200	0.2	0.05	5/5
61	2	400	400	0	300	0	1	1	NA
105	1	500	500	0	300	-200	0.2	0.05	5/5
108	2	400	400	0	300	0	1	1	NA

The frequency response and settling time characteristics used for each of the 4 black start DGs are the same characteristics derived in our earlier work [69]. The 4 black start DGs are assumed to be identical and each is a 4.16 KV L-L 500 KVA diesel engine synchronous generator with AC1A exciter and isochronous governor models. Each of the four black start DGs has the following parameters: $H = 3.117\ sec, K_P = 8.8, K_I = 2.5$, where H is the inertia constant, K_I and K_P are the gains of the governor's integral and proportionate controller respectively.

The load profile is shown in Table 4.3. There is a total of 85 loads in the system. The load profile is comparable to the ones in the original test system. All the loads are assumed to be switchable and wye connected. There are four switchable capacitors in the test system and their values are the same as those of the original IEEE test system.

Each load is represented by its node location under the node columns and its three-phase active and reactive power values under the P(A/B/C) and Q(A/B/C) columns respectively. Phases with non-existent loads are represented with 0. For example, in node 1, P(A/B/C) is given as 20/0/20 meaning that phases A, B, and C have active load values of 20, 0, and 20 KW, respectively.

Table 4.3 Load Values used for the Case Study (© 2020 IEEE)

Node	P(a/b/c) kW	Q(a/b/c) kvar	Node	P(a/b/c) kW	Q(a/b/c) kvar	Node	P(a/b/c) kW	Q(a/b/c) kvar
1	20/0/20	10/0/10	43	0/40/0	0/20/0	79	40/0/0	20/0/0
2	0/20/0	0/10/0	45	20/0/0	10/0/0	80	0/40/0	0/20/0
4	0/0/20	0/0/10	46	20/0/0	10/0/0	82	40/0/0	20/0/0
5	0/0/20	0/0/10	47	35/35/35	25/25/25	83	0/0/20	0/0/10
6	0/0/20	0/0/10	48	70/70/70	50/50/50	84	0/0/20	0/0/10
7	0/20/0	0/10/0	49	35/35/35	25/25/25	85	0/0/40	0/0/20
9	20/0/0	10/0/0	50	0/0/40	0/0/20	86	0/20/0	0/10/0
10	20/0/0	10/0/0	51	20/0/0	10/0/0	87	0/40/0	0/20/0
11	25/0/0	10/0/0	52	30/0/0	15/0/0	88	20/0/0	10/0/0
12	0/20/0	0/10/0	53	30/0/0	15/0/0	90	0/40/0	0/20/0
16	0/0/15	0/0/5	55	20/0/0	10/0/0	92	0/0/40	0/0/20
17	0/0/20	0/0/10	56	0/20/0	0/10/0	94	20/0/0	10/0/0
19	20/0/0	10/0/0	58	0/20/0	0/10/0	95	0/30/0	0/15/0
20	20/0/0	10/0/0	59	0/20/0	0/10/0	96	0/30/0	0/15/0
22	0/40/0	0/20/0	60	20/0/0	10/0/0	98	20/0/0	15/0/0
24	0/0/40	0/0/20	62	0/0/40	0/0/20	99	0/40/0	0/20/0
28	20/0/0	10/0/0	63	20/0/0	10/0/0	100	0/0/40	0/0/20
29	20/0/0	10/0/0	64	0/75/0	0/35/0	102	0/0/20	0/0/10
30	0/0/40	0/0/20	65	35/35/35	25/25/25	103	0/0/40	0/0/20
31	0/0/20	0/0/10	66	0/0/75	0/0/35	104	0/0/40	0/0/20
32	0/0/20	0/0/10	68	20/0/0	10/0/0	106	0/40/0	0/20/0
33	20/0/0	10/0/0	69	40/0/0	20/0/0	107	0/40/0	0/20/0
34	0/0/40	0/0/20	70	20/0/0	10/0/0	109	40/0/0	20/0/0
35	20/0/0	10/0/0	71	40/0/0	20/0/0	111	20/0/0	10/0/0
37	20/0/0	10/0/0	73	0/0/40	0/0/20	112	20/0/0	10/0/0
38	0/20/0	0/10/0	74	0/0/40	0/0/20	113	30/0/0	15/0/0
39	0/20/0	0/10/0	75	0/0/40	0/0/20	114	20/0/0	10/0/0
41	0/0/20	0/0/10	76	70/70/70	50/50/50			
42	20/0/0	10/0/0	77	0/40/0	0/20/0	Total	1060/920/1075	585/510/585

4.6.1.2. Case Study Solution

The proposed method was implemented in MATLAB and utilized the YALMIP [85] MATLAB toolbox to interface the Gurobi [86] 7.5.2 optimization solver and was solved in a Windows computer with Intel Core i7 2.80 GHz CPU, 8 GB of RAM, and 64-

bit operating system. The system was solved for a total of 8-time steps with a computation time of 354.71 seconds. The solution resulted in the formation of four microgrids. Figure 4.8 shows the partitioning of the distribution system into four microgrids at the last time step.

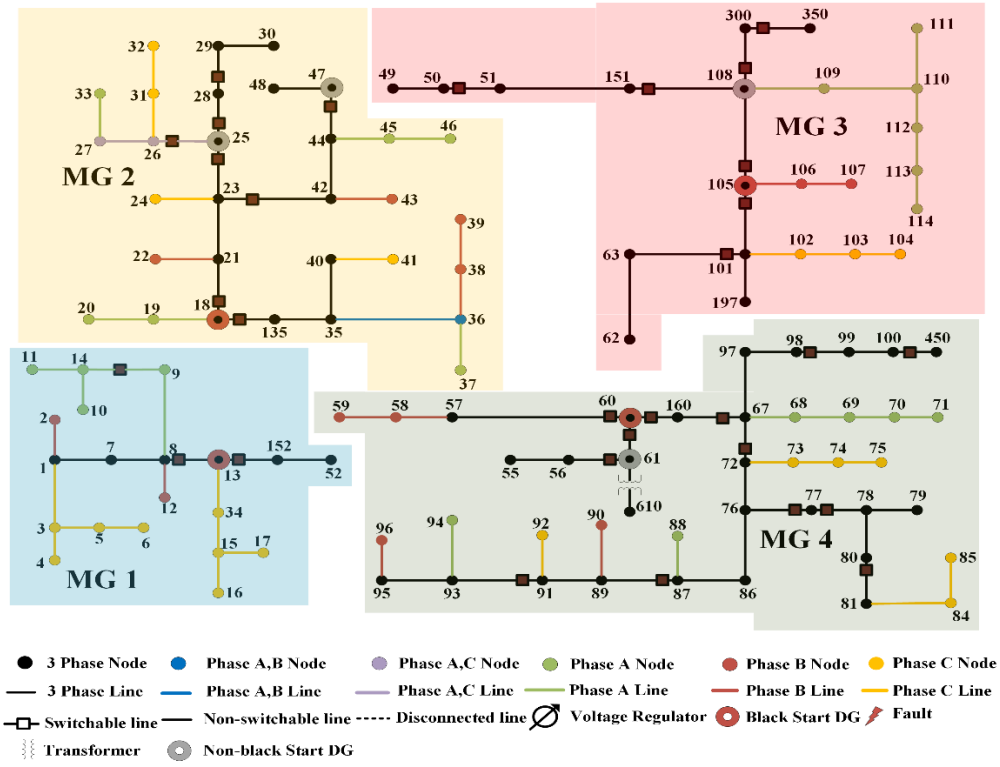

Figure 4.8 Graphical Representation and Legend of the Formed Microgrid at the Last Step
(© 2020 IEEE)

Figure 4.9 to Figure 4.12 show the sequences of formation of microgrid 1 to microgrid 4 with the graphical representation of the microgrids at each time step. $\Delta T_1, \Delta T_2$, and so on represent the variable time interval between restoration steps. Recall that the time interval between restoration steps have been modeled as continuous variables in

section 4.5.4.6. Steps in which the formed microgrids remained the same as previous steps were considered redundant and thus were omitted. Examples of such redundant steps can be found in microgrid 1 from steps 5 to 8.

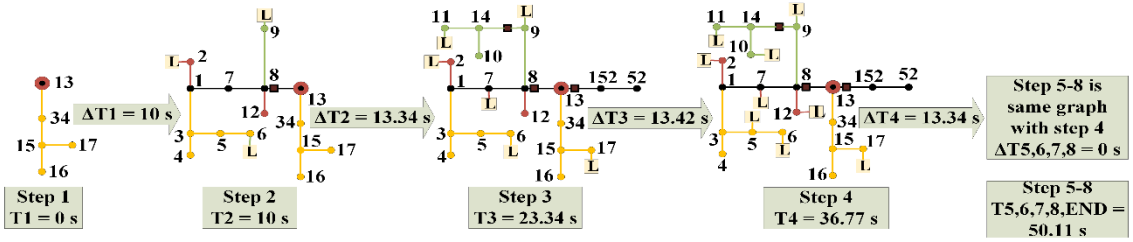

Figure 4.9 Restoration Sequence of Microgrid 1
(© 2020 IEEE)

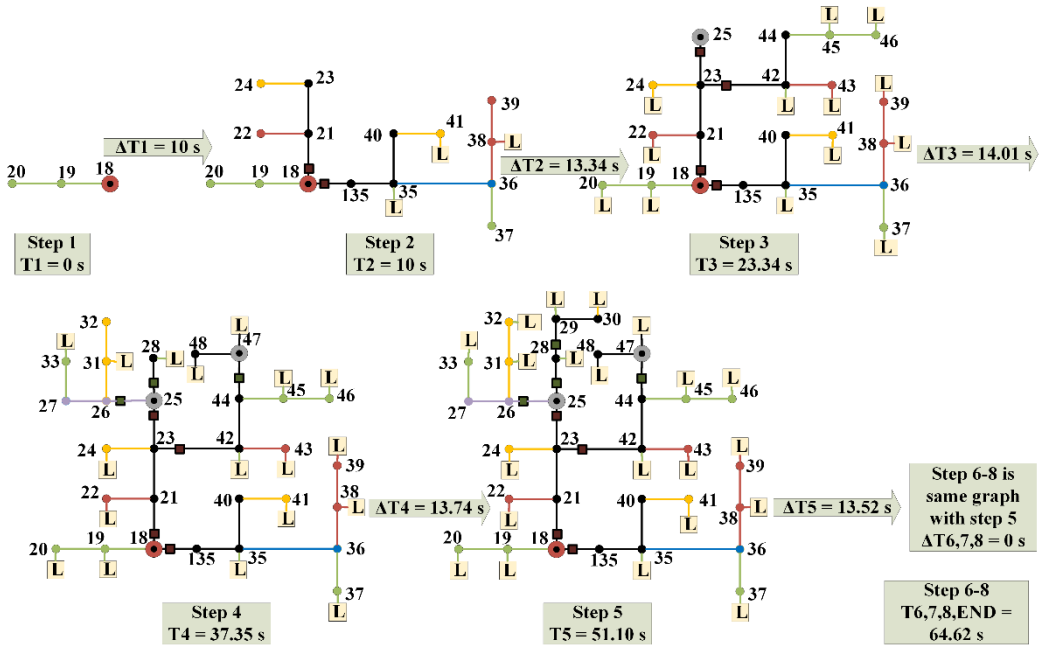

Figure 4.10 Restoration Sequence of Microgrid 2
(© 2020 IEEE)

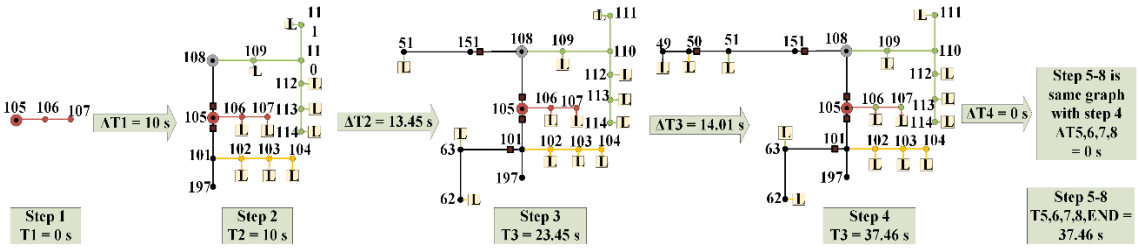

Figure 4.11 Restoration Sequence of Microgrid 3

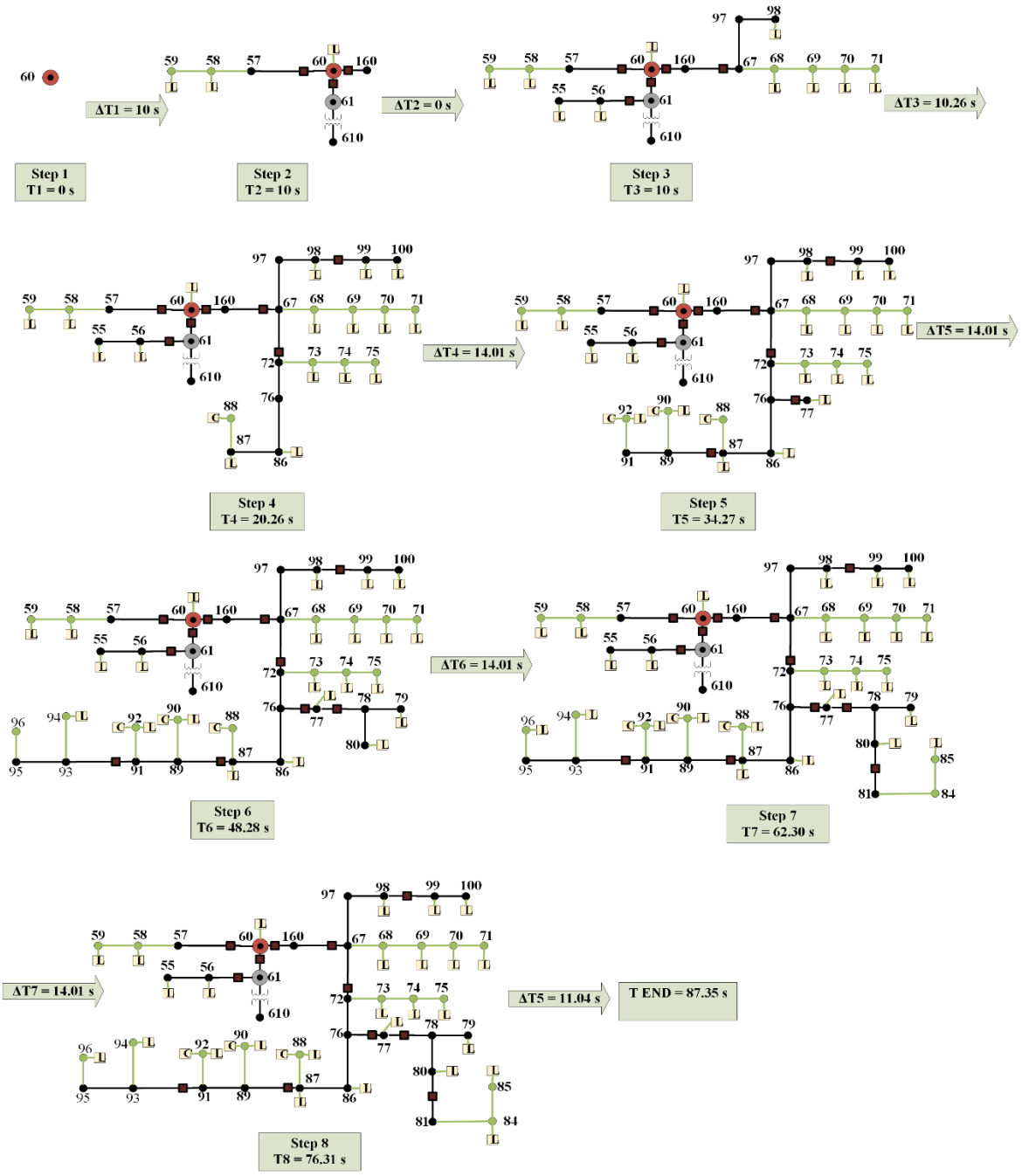

Figure 4.12 Restoration Sequence of Microgrid 4

4.6.2. Solution Validation by PSCAD Simulation

The 4-microgrid solution obtained from solving the proposed method as discussed in the previous section was set up in PSCAD for EMTP simulation. The black start DGs were modeled as three-phase synchronous generators with isochronous governor and the non-black start DGs were modeled as three-phase PQ inverters with independent control in each phase. The lines were modeled with their impedance parameters as obtained from the original IEEE test feeder model. For simplicity, each load was modeled as a constant impedance load. Some results from the simulation are shown in Figure 4.13 to Figure 4.16.

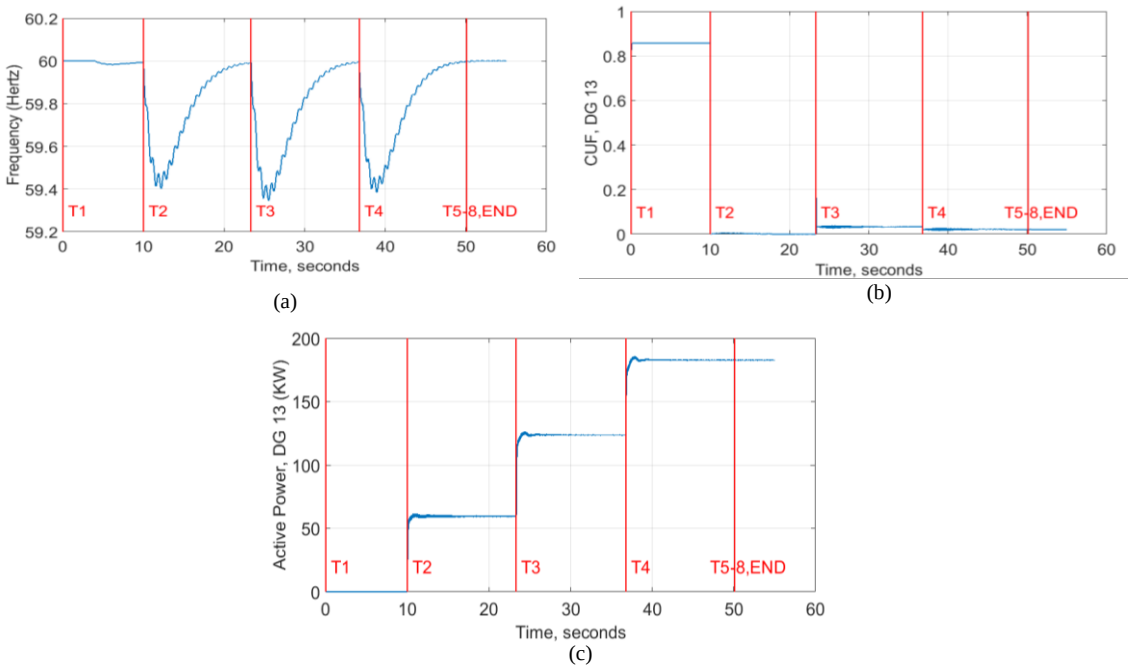

Figure 4.13 Graphs of Dynamic Responses of some Variables in Microgrid 1 (a) Frequency Response (b) Current Unbalance Factor (CUF) and (c) Three-Phase Active Power Output from Black Start DG at Node 13
(© 2020 IEEE)

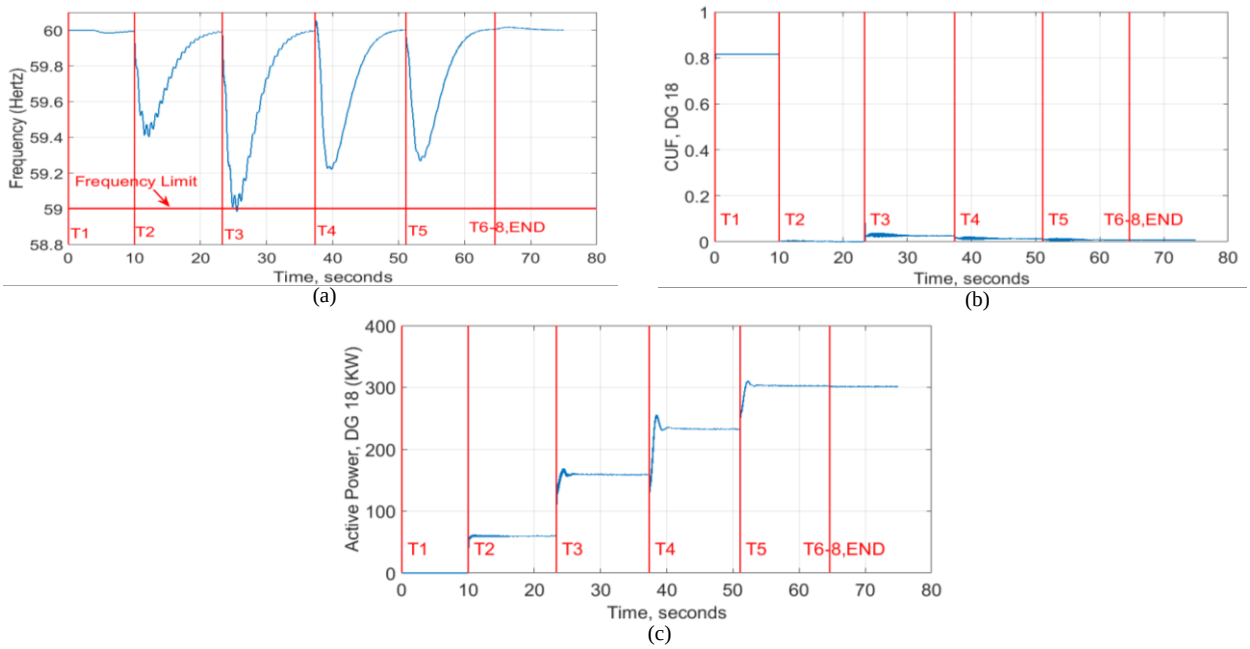

Figure 4.14 Graphs of Dynamic Responses of some Variables in Microgrid 2 (a) Frequency Response (b) Current Unbalance Factor (CUF) and (c) Three-Phase Active Power Output from Black Start DG at Node 18
(© 2020 IEEE)

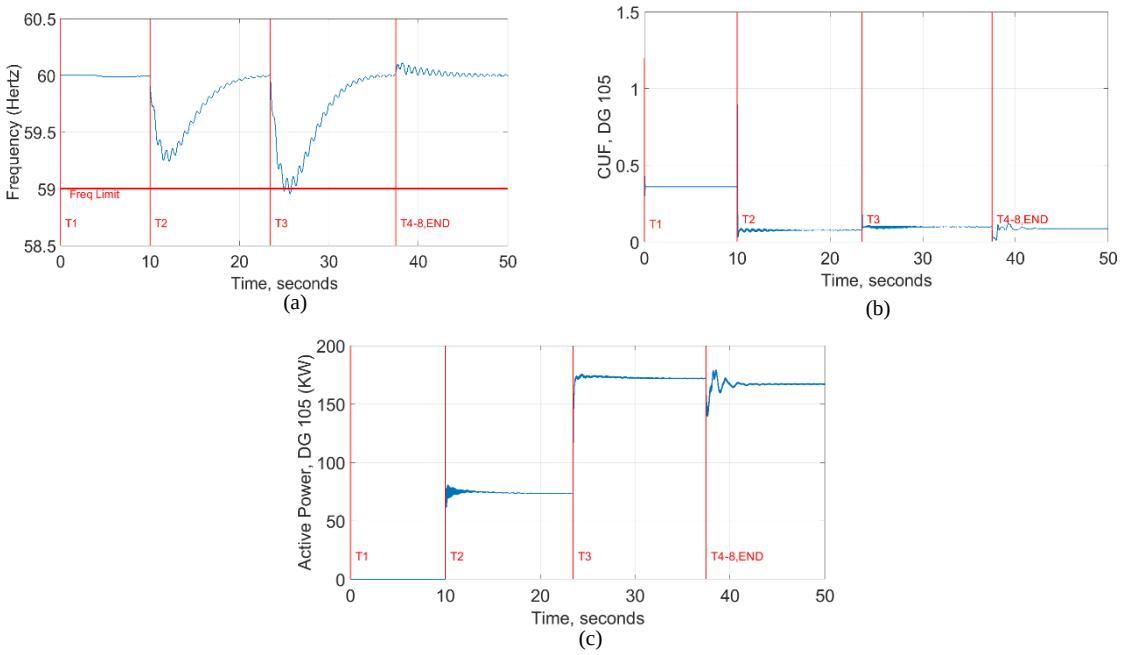

Figure 4.15 Graphs of Dynamic Responses of some Variables in Microgrid 3 (a) Frequency Response (b) Current Unbalance Factor (CUF) and (c) Three-Phase Active Power Output from Black Start DG at Node 105

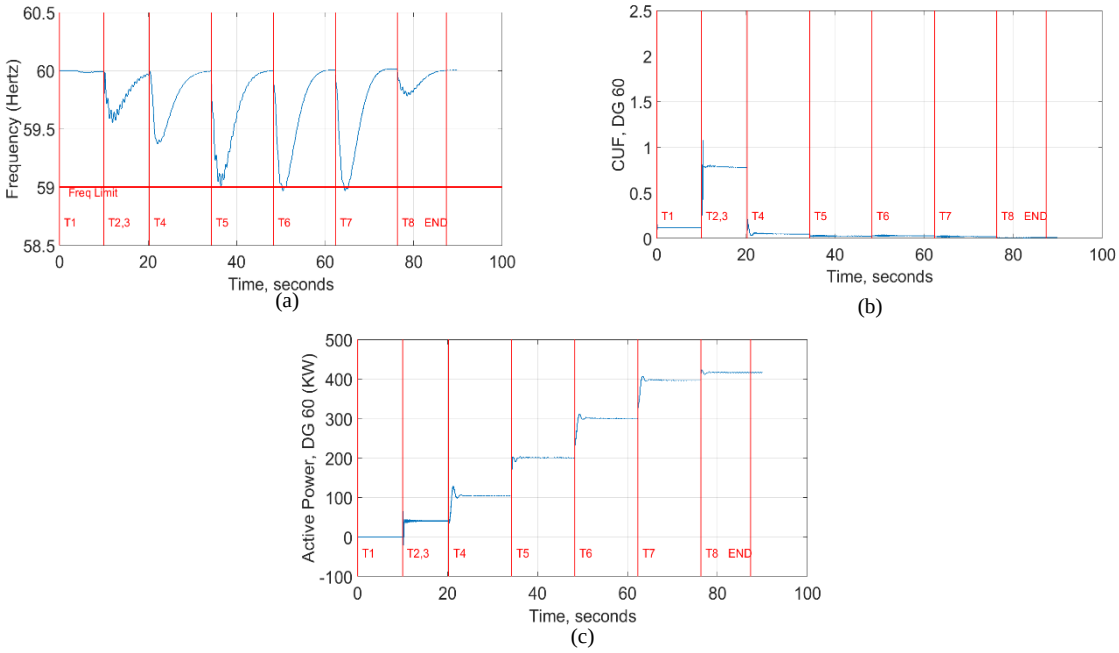

Figure 4.16 Graphs of Dynamic Responses of some Variables in Microgrid 4 (a) Frequency Response (b) Current Unbalance Factor (CUF) and (c) Three-Phase Active Power Output from Black Start DG at Node 60

4.6.3. Discussion of Results

At the end of the restoration process, four microgrids were formed as shown in Figure 4.8 and a total of 72 aggregate loads and 3 capacitors were restored in the system. Expectedly, regions of the system with three-phase PQ DGs acting as an "unbalanced compensator" restored more loads than other regions. For instance, all loads within microgrid 2 were restored since it has two three-phase PQ DGs. However, microgrid 1 with no three-phase PQ DG restored the least loads and its black start DG was poorly utilized due to its inability to pick up loads that would cause it to experience an unbalance beyond allowable unbalance constraints.

A total of 13 aggregate loads and 1 capacitor were not restored and are distributed as such: loads at nodes 1, 4, 16, 34, and 52 were not restored and these nodes belong to microgrid 1. Loads at nodes 53, 64, 65, 66, 82, and 83 were not restored and these nodes belong to the isolated regions due to fault. Loads at nodes 76 and 95 belonging to microgrid 4 were not restored as well. The capacitor at node 83 in the faulted isolated region was not reconnected.

Looking at the graphs in Figure 4.13b and Figure 4.14b, the CUF constraints set to under 0.05 (Table 4.2) were violated during the first interval and were maintained within its limit for the rest of the intervals. The reason for the first interval violation is explained as follows.

In restoring the microgrids, between time steps 1 and 2, the results showed a high CUF of a little more than 0.8 (Figure 4.13b and Figure 4.14b), the reason being that in step 1 (refer to Figure 4.9 and Figure 4.10), only one phase lateral lines were connected to the black start DG with no load. This one-phase lateral will give rise to a small leakage current due to line capacitance in only one phase of the generator which will eventually give rise to a high CUF; meanwhile, the SSR algorithm estimated zero current in all three phases since it did not take into account leakage current due to line capacitance. Though the CUF is high in this interval, it does not present any safety concerns since the leakage current due to the capacitance of the line is very small.

From the results for the frequency response graph in Figure 4.13 to Figure 4.16, we see that the methodology can maintain the frequency within allowable limits and effectively estimate the settling time while minimizing the total restoration time.

There are several other characteristics of the DGs that were difficult to incorporate into the SSR methodology. The PI controller used in the PQ inverter does not yield an instant change in the power output of the inverter as the power setpoint changes. It is somewhat a critically damped response as shown for phase A power output of the PQ DG at node 61 in Figure 4.17. Because the dispatched power from the PQ inverter is not available instantaneously at the moment of a setpoint step change, the black start DG may respond to the energy imbalance of the system during the rise time of the PQ DG response. With a better tuning of the PQ DG PI controllers, a much faster rise time could be achieved.

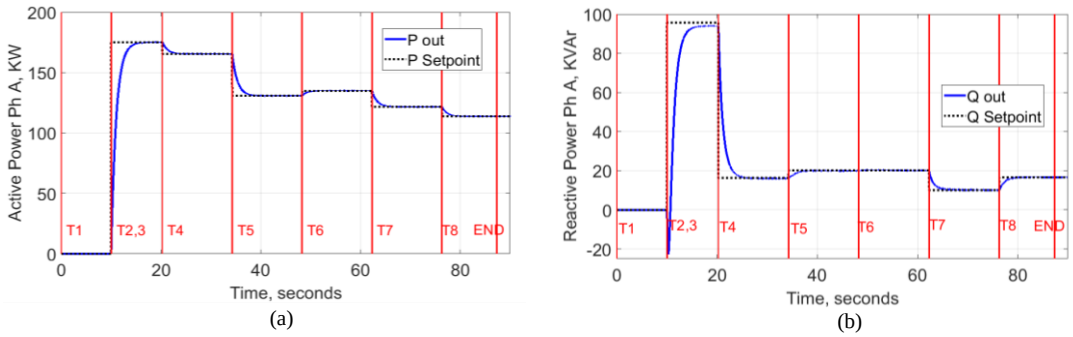

Figure 4.17 An Example of Dispatch Tracking of the PQ Inverter in Phase A of DG 61 for (a) Active Power (b) Reactive Power
(© 2020 IEEE)

4.7. Section Summary

In this section, we presented a sequential service restoration formulation with emphasis on switch timing derivation and optimization for use in black start restoration of single master operation microgrids. We derived the frequency response of synchronous machine DGs with isochronous governor and incorporated this response into optimization

formulation for restoration. The problem of dealing with load unbalance in autonomous microgrids was resolved by the use of single-phase controlled PQ inverter-based DGs for unbalance load compensation. The proposed method was used to generate a restoration solution for the modified IEEE 123 node test feeder.

The restoration solution was validated through dynamic simulation in PSCAD and ensures that the static and dynamic constraints are satisfied while minimizing total restoration time and maximizing total loads restored. The proposed method can be integrated into an automated distribution system for fast emergency restoration.

The constant impedance load model was used in the dynamic simulation of the formed microgrids and is too simple to capture the dynamic behavior of loads in a microgrid. The IEEE 123 node test system [84], on the other hand, implements each of the loads as either constant impedance, constant current or constant power. From the dynamic simulation we performed, the constant current or constant power load model can cause voltage collapse during microgrid black start with non-stiff sources. Developing a constant power load model, for instance, for all values of system voltage would lead to voltage collapse since this model will approximately act as a short circuit at a given node during the instance of voltage build up in the system - the constant power load will try to draw as much current as possible to make up for the low voltage in the system during the build-up. It is expected that no aggregate load, in reality, exhibits completely constant impedance, constant current, or constant power characteristics for all values of system voltage. An approach to dynamic load modeling for autonomous microgrids might be to develop models with changing characteristics as its supply voltage changes. Developing

realistic dynamic load models and incorporating it into dynamic restoration studies will be interesting to explore.

In section 5, we will present linear and optimal power flow formulations for multi-master droop-controlled microgrids. In section 6, we will present a system optimization formulation and control for the black start of multi-master droop-controlled microgrids. With the multi-master approach, one microgrid system can be formed instead of the multiple microgrid systems formed by the single master mode approach discussed. A bigger microgrid may tend to have better reliability, larger system capacity, and more loads balancing each other could potentially result in better utilization of DGs.

5. LINEAR POWER FLOW FORMULATIONS AND OPTIMAL OPERATION OF DROOP-CONTROLLED MICROGRIDS*

5.1. Section Abstract

Linear power flow formulations enable the integration of power flow constraints to linearly constrained power system optimization problems in transmission and distribution systems. Typical examples include the application of DC power flow to optimal power flow and unit commitment and application of DistFlow to distribution system reconfiguration and restoration. The existing linear power flow formulations cannot be directly incorporated into islanded droop-controlled microgrid optimization due to the microgrid's lack of an approximate slack bus, smaller system size/inertia, and dependence of the power flow on the droop settings. To address this need, this section presents two linear power flow approximations for three-phase islanded droop-controlled microgrids. The first approximation was derived based on the current injection method and the second approximation was derived from the three-phase DistFlow formulation. The two approximations were verified using detailed time-domain simulations at steady-state in PSCAD. To demonstrate the application of the proposed power flow formulations, the two approximations were expanded for integration in optimal power flow formulations for islanded droop-controlled microgrids to minimize cost.

---

*Parts of this section are reprinted with permission from O. Bassey, K. L. Butler-Purry and B. Chen, "Active and Reactive Power Sharing in Inverter Based Droop-Controlled Microgrids," *2019 IEEE Power & Energy Society General Meeting (PESGM)*, Atlanta, GA, USA, 2019, pp. 1-5, doi: 10.1109/PESGM40551.2019.8973854.

5.2. Background and Related Work

One of the main motivations for microgrid research and development is the potential to improve power system resilience by delivering power to critical infrastructure during an outage. When an outage occurs, a microgrid that was previously grid-connected will have to operate in island mode. In island operation, the microgrid must regulate its voltage and frequency usually through droop control. Furthermore, the local energy resources have to be optimally operated to meet changing load demands at minimum cost. This optimization challenge requires efficient power flow analysis.

Conventional power flow methods and software like OpenDSS cannot be directly applied to autonomous (i.e. islanded) microgrids due to the presence of droop-controlled distributed generators (DGs) and lack of a stiff node which can be approximated as the slack bus. Although it is possible to simulate the operation of islanded microgrids in software packages such as MATLAB/Simulink and PSCAD, they do not allow closed-form integration of power flow constraints into an islanded microgrid optimization problem.

Non-linear power flow models have been proposed for islanded droop-controlled microgrids in the literature [87-91]. However, incorporating these non-linear models as constraints into the microgrid optimal power flow (OPF) problem will lead to non-convex optimization models which are generally more difficult to solve compared to linearly constrained optimization models. Besides, unlike linear power flow (LPF) models that can

be solved analytically, the power flow solutions of these non-linear models are typically solved using an iterative algorithm.

In this section, two LPF/OPF formulations are derived for islanded droop-controlled microgrids: LPF/OPF based on the current injection method (CIM) and LPF/OPF based on the line flow method (LFM) i.e. DistFlow method.

Different variants of the CIM have been used in LPF formulations [92, 93], optimal reconfiguration [94], and voltage stability analysis of distribution systems [95].

Single-phase simplified DistFlow branch equations were introduced in [64] for optimal network reconfiguration in distribution systems. The unbalanced three-phase equivalence was proposed in [65] and has been applied to develop service restoration algorithms for distribution systems and microgrids [29, 30].

Droop control of islanded microgrids enables power-sharing and regulation of frequency and voltage of microgrids [14, 96]. To leverage the benefit of droop-control, it is the purpose of this section to present two LPF/OPF models for islanded droop-controlled microgrids. The main contributions of this section are as follows:

1. Present derivation of two sets of LPF equations based on the current injection method (CIM) and the DistFlow method which can be solved analytically using non-iterative linear matrix operation.
2. Demonstrate the application of the two afore-mentioned LPF equations using two OPF formulations which are linearly constrained by the derived LPF equations to minimize cost while adjusting the frequency and voltage of the microgrid to reference value.

The mean error of the nodal voltage results from the linear power flow formulations when compared to detailed PSCAD time-domain simulation at a steady state is under 1% and can be considered fair enough accuracy for estimating the operating point of the microgrid.

The rest of section 5 is organized as follows. Section 5.3 presents a brief review of conventional droop-control as applied to autonomous microgrids. Section 5.4 presents the active and reactive power sharing paradigms in islanded droop-controlled microgrids. In sections 5.5 and 5.6, the LPF formulations are derived. Section 5.7 consists of the power flow verification with simulated microgrids in PSCAD, case studies, and discussions. Section 5.8 consists of an optimal power flow extension and application. Section 5.9 concludes section 5.

5.3. Droop Basics

The power flow equations across a predominantly inductive line show an approximate decoupling of active and reactive power [61] controlled by power angle and differential voltage magnitude, respectively. This decoupling enables separate control of the active and reactive power output of synchronous generators in the bulk power system where the transmission lines are predominantly inductive [97]. In the distribution systems, on the other hand, the lines are significantly resistive and several methods have been proposed to realize the power decoupling of the converters used in microgrids. These methods include inductive coupling, power transformation, and virtual impedance [61, 62, 98].

Conventional droop control depends on this active and reactive power decoupling. In this section, we focus on conventional droop control, where the active power output of droop-controlled inverters is dependent on the frequency droop and the reactive power output is dependent on the voltage droop control. This decoupling is realized by adding inductive coupling at the terminal of the droop-controlled inverters. This coupling gives an extra bus per droop-controlled inverter for which to solve for in the power flow formulation. The case of a predominantly resistive microgrid is beyond the scope of this section.

Given a set of inverters in a microgrid, the equations describing the conventional droop control of the i^{th} inverter the given as [99]:

$$f_i = f^{ref} - n_{f,i}(P_i - P_i^{ref}) \tag{5.1}$$

$$|\bar{V}_i| = |\bar{V}_i|^{ref} - n_{v,i}(Q_i - Q_i^{ref}) \tag{5.2}$$

where f^{ref} is the reference frequency in Hz assumed to be equal and set to the nominal value for all droop inverters; P_i^{ref} is the reference power per unit; P_i is the active power output in per unit; $n_{f,i}$ is the frequency droop coefficient in Hz per unit power; $|\bar{V}_i|^{ref}$ is the reference voltage in per unit; Q_i^{ref} is the reference output reactive power in per unit; $|\bar{V}_i|$ is the output per unit RMS voltage in per unit; and $n_{v,i}$ is the voltage droop coefficient in per unit reactive power.

There is another way to express the droop equations in terms of idle frequency and voltage, as presented in [14]. However, the reference value-form of (5.1) and (5.2), though equivalent to the idle form, makes it easier to apply the developed methods for optimal

power flow presented in section 5.8 by setting the reference frequency and voltage of each droop inverter at its reference (i.e., desired) active and reactive power setpoints, respectively.

5.4. Active and Reactive Power Sharing in Droop-Controlled Microgrids

This subsection presents active and reactive power sharing paradigms in islanded microgrids and offers insight into the choice of droop settings to realize good frequency and voltage regulation.

5.4.1. Power Transfer through Inductive Coupling

Figure 5.1 shows the connection of an inverter to a microgrid via inductive coupling. $V_c = |V_c|\angle\delta$ is the voltage at the converter terminal and $V_m = |V_m|\angle 0$ is the voltage at the point of common connection (PCC) with the microgrid. I_c is the current output from the converter. All quantities are in per unit. Applying ohms law across the inductor gives the relation below.

$$I_c = \frac{|V_c|\angle\delta - |V_m|\angle 0}{jX} = \frac{|V_c|}{X} e^{j(\delta-\pi/2)} - \frac{|V_m|}{X} e^{j\left(-\frac{\pi}{2}\right)} \tag{5.3}$$

$$S = V_c {I_c}^* = \frac{|V_c|^2}{X} e^{j\pi/2} - \frac{|V_c||V_m|}{X} e^{j\left(\delta+\frac{\pi}{2}\right)} \tag{5.4}$$

$$P = Re(S) = \frac{|V_c||V_m|}{X} sin\delta, \qquad P_{max} = \frac{|V_c||V_m|}{X} \tag{5.5}$$

$$Q = Im(S) = \frac{|V_c|}{X}(|V_c| - |V_m| cos\delta) \tag{5.6}$$

Since δ is typically small, $sin\delta \approx \delta, cos\delta \approx 1$, then (5.5) and (5.6) can be approximated as:

$$P \approx \frac{|V_c||V_m|}{X}\delta, \qquad Q \approx \frac{|V_c|}{X}(|V_c| - |V_m|) \tag{5.7}$$

P_{max} is the maximum power when $\delta = 90°$ and is called the static transmission capacity [97]. Typically, δ is desired to be kept small far below $90°$ such that the power transferred is far less than the transmission capacity. The coupling inductance is inversely proportional to the transmission capacity and has to be carefully chosen such that it is high enough to turn the network to be mostly inductive and low enough not to cause excessive voltage drop and to keep the δ small.

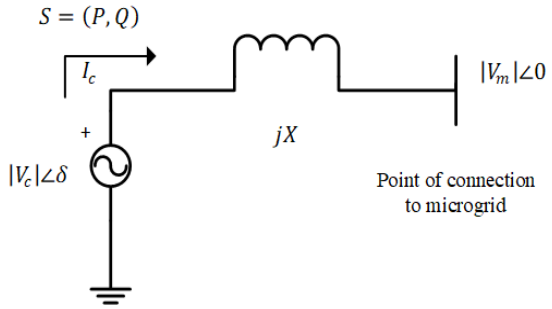

Figure 5.1 Inductive Coupling for Control of Power Transfer
(© 2019 IEEE)

5.4.2. Active Power Sharing

The frequency droop method of sharing active power is a precise power sharing scheme. This is because, though the frequency may differ at various buses in the system during transients, the frequency would usually settle to a common value afterward and can be used for local control by each of the droop controlled DGs without the need for communication. The frequency droop selection presented in this subsection is an extension of the derivations in [48, 49]. For n droop inverter interconnection, let the per unit active

power output of each inverter be $P_i, i \in \{1,2,\dots,n\}$, then clearly P_i should satisfy this inequality:

$$P_i \leq P_{max,i}, \forall\, i \in \{1,2,\dots,n\} \tag{5.8}$$

Where $P_{max,i}$ is the static transmission capacity defined for each inverter based on (5.5) rewritten with subscript i as:

$$P_{max,i} = \frac{|V_c|_i |V_m|_i}{X_i}, i \in \{1,2,\dots,n\} \tag{5.9}$$

$|V_c|_i$ is the per unit RMS voltage at the i^{th} inverter terminal, X_i is the per unit coupling inductive reactance and $|V_m|_i$ is the per unit RMS voltage at the point of connection to the microgrid. Equation (5.8) ensures that the power at each inverter is realistic.

Each droop-controlled inverter i controls its instantaneous frequency, f_i, at its output by the following relations.

$$f_i = f^{ref} - n_{f,i}\left(P_i - P_i^{ref}\right), \;\; i \in \{1,2,\dots,n\} \tag{5.10}$$

Where f^{ref} is the reference frequency in Hz, P_i^{ref} is the reference active power in per unit, P_i is the active power output in per unit, $n_{f,i}$ is the frequency droop co-efficient of the i^{th} inverter in Hz per unit power. Define the frequency deviation by,

$$\Delta f_i = f_i - f^{ref}, i \in \{1,2,\dots,n\} \tag{5.11}$$

For an exponentially stable solution, the frequency deviation will settle to the same constant value for every node in the system, thus, $\Delta f_i = \Delta f$.

In the following subsections 5.4.2.1 and 5.4.2.2, we present two active power sharing paradigms. The paradigm in subsection 5.4.2.1 was derived in [48, 49], however,

we present an alternative perspective and proof of the theorem. In subsection 5.4.2.2, we extend the theorem to load sharing in a microgrid with optimized reference power.

5.4.2.1. Load Sharing Based on Active Power Limit

Assuming the active power constraint is placed by the DC prime mover of each inverter, it can be formulated as,

$$0 \leq P_i \leq \overline{P_i}, i \in \{1,2,\dots,n\} \tag{5.12}$$

The droop coefficients are said to be selected proportionally based on the active power constraint imposed by the DC prime mover if for each $i\epsilon\{1,2,\dots,n\}$ [99],

$$n_{f,i}\overline{P_i} = k_p, a\ constant\ \forall\ i \in \{1,2,\dots,n\} \tag{5.13}$$

Where $\overline{P_i}$ is the maximum allowable active power from the i^{th} inverter's DC prime mover and k_p is a constant. The reference frequency, f^{ref}, is assumed to be the same for all the droop-controlled inverters in the system. The MGCC can be operated in such a way to realize f^{ref} as the system's frequency and as such, P_i^{ref} and $\sum_{i=1}^{n} P_i^{ref}$, the reference power and its summation should be calculated to match closely with the active power output of each inverter P_i and the estimated net total active power of load, $P_{L,total}^{est}$, respectively,

$$\sum_{i=1}^{n} P_i^{ref} = P_{L,total}^{est}, i \in \{1,2,\dots,n\} \tag{5.14}$$

However, due to some uncertainties in load estimation, time-varying load, and losses in the system, there will usually be a mismatch and hence a deviation from the reference frequency. It is desired that any mismatch between $\sum_{i=1}^{n} P_i^{ref}$ and total active

power of loads be shared proportionately according to their DC prime mover active power rating.

5.4.2.1.1. Theorem 1 (Proportional Power Sharing Based on Active Power Limit):

Consider statements (a) and (b) below.

(a) Proportional reference active power

$$P_i^{ref} = k\overline{P_i}, \forall\, i \in \{1,2,\dots,n\} \tag{5.15}$$

$$k = P_{L,total}^{est} / \sum_{i=1}^{n} \overline{P_i} \tag{5.16}$$

Where k $(0 \leq k \leq 1)$ is a constant and same for each droop DG. k is reasonable in this range to ensure that reference power is chosen within the active power constraints.

(b) Proportional droop coefficients of (5.13) are satisfied [99]

If (a) and (b) are true, then the loads are shared proportionately in accordance with the rating of the DC prime mover, that is,

$$P_i/\overline{P_i} = a\ constant, \forall\, i \in \{1,2,\dots,n\} \tag{5.17}$$

Proof:

The proof follows from rearranging (5.10) to,

$$\frac{\Delta f - n_{f,i}P_i^{ref}}{-n_{f,i}} = P_i \tag{5.18}$$

$$P_i/\overline{P_i} = \frac{\Delta f - n_{f,i}P_i^{ref}}{-n_{f,i}\overline{P_i}} \tag{5.19}$$

Substituting (5.13) and (5.15) into (5.19) gives,

$$P_i/\overline{P_i} = \frac{\Delta f - kk_p}{-k_p}, a\ constant, \forall\, i \in \{1,2,\dots,n\} \tag{5.20}$$

5.4.2.2. Load Sharing Based on Optimized Reference Active Power

When the MGCC adds some optimization layer (e.g economic, emission optimization, etc.) to calculate optimal reference power for each droop DG, then the reference power expression in (5.15) may not have the same k for each droop inverter. In such a situation, it may be desired that the power mismatch be shared proportionately to the optimal reference active power calculated by the MGCC. Theorem 2 is motivated by this situation.

5.4.2.2.1. Theorem 2 (Proportional Power Sharing Based on Optimized Reference Active Power):

Consider statements (a) and (b) below.

(a) Optimized reference active power definition:

$$P_i^{ref} = k_i \overline{P_i}, \forall\, i \in \{1,2,\dots,n\} \tag{5.21}$$

Where k_i $(0 \leq k_i \leq 1)$ is a constant and not necessarily the same values for each droop inverter.

(b) Proportional droop coefficients based on optimized reference active power:

$$n_{f,i} P_i^{ref} = k_v, a\ constant\ \forall\, i \in \{1,2,\dots,n\} \tag{5.22}$$

If (a) and (b) are true, then the loads are shared proportionally in accordance with the optimized reference active power, that is,

$$P_i / P_i^{ref} = a\ constant, \forall\, i \in \{1,2,\dots,n\} \tag{5.23}$$

Proof:

Similarly, the proof follows from rearranging (5.10) to get (5.18) and then dividing through by P_i^{ref},

$$P_i/P_i^{ref} = \frac{\Delta f - n_{f,i}P_i^{ref}}{-n_{f,i}P_i^{ref}} = \frac{\Delta f - k_v}{-k_v}, a\ constant \tag{5.24}$$

Assuming little power mismatch, the system operating point may deviate from the optimal dispatch point for a general non-linear relationship between the active power and objective function, however, it would give a reasonably close to optimal dispatch for small active power and reference active power mismatch.

5.4.3. Reactive Power Sharing

5.4.3.1. Voltage Droop

Reactive power sharing is typically accomplished through the voltage droop method represented mathematically as [2],

$$|V_c|_i = |V_c|_i^{ref} - n_{v,i}\left(Q_i - Q_i^{ref}\right), i \in \{1,2,\dots,n\} \tag{5.25}$$

Where $|V_c|_i$ is the output RMS voltage, $|V_c|_i^{ref}$ is the reference output RMS voltage, Q_i is the output reactive power, Q_i^{ref} is the reference output reactive power, all in per unit of the i^{th} inverter. $n_{v,i}$ is the voltage droop co-efficient in per unit reactive power.

Reactive power sharing is not as precise as active power sharing. This is because, unlike that of frequency which eventually settles to a common value for an exponentially stable system, the system does not have uniform voltages at the nodes. Several papers have proposed ways for accurate reactive power sharing like in [100] where the authors proposed a novel droop method that adaptively controls the reference voltage of the inverters and in [101] which argued for increased droop gain. In the following analysis, we present a simple way to coordinate voltage regulation and approximate reactive power

sharing by routine coordination of the conventional voltage droop setpoints and sizing of inductive coupling by the MGCC.

5.4.3.2. Voltage Droop Reference Calculation

As stated in section 5.4.2.1, active power is constrained by the capacity of the DC prime mover. Reactive power, on the hand, could be seen as being constrained by the VI rating of each inverter, $\overline{S_i}$, and the DC prime mover rating, $\overline{P_i}$, by the following relation,

$$0 \leq Q_i \leq \overline{Q_i} \tag{5.26}$$

$$\overline{Q_i} = \sqrt{\overline{S_i}^2 - \overline{P_i}^2}, i \in \{1,2, \dots, n\} \tag{5.27}$$

Equations (5.24) and (5.25) ensure that the VI rating of each inverter is not exceeded. There could be several paradigms for determining the reference reactive power, Q_i^{ref}, for each inverter. It can be chosen proportionately to $\overline{Q_i}$ or based on some optimal network flow considerations. Here we consider the case for inductive type load ($Q_i^{ref}, Q_i > 0$). Thus,

$$Q_i^{ref} = q\overline{Q_i} \tag{5.28}$$

$$q = Q_{L,total}^{est} \Big/ \sum_{i=1}^{n} \overline{Q_i}, \qquad i \in \{1,2, \dots, n\} \tag{5.29}$$

Where q is a constant and $Q_{L,total}^{est}$ is the total estimated reactive power to be shared. Assuming a small power angle for the active power output from each inverter, (5.7) can be rewritten for the reference reactive power output of each inverter as,

$$Q_i^{ref} \approx \frac{|V_c|_i^{ref}}{X_i}\left(|V_c|_i^{ref} - |V_m|_i\right), \qquad i \in \{1,2, \dots, n\} \tag{5.30}$$

Where X_i is the inductive reactance in per unit of the coupling inductor, $|V_m|_i$ is the per unit RMS voltage at the point of connection to the microgrid network for each inverter. One of the goals is to ensure that we have close to 1 per unit at the point of connection to the network. Assuming $|V_m|_i = 1pu$, then (5.30) becomes,

$$\frac{|V_c|_i^{ref\,2}}{X_i} - \frac{|V_c|_i^{ref}}{X_i} - Q_i^{ref} \approx 0 \tag{5.31}$$

Solving for $|V_c|_i^{ref}$ in (5.31) and discarding the negative non-physical result,

$$|V_c|_i^{ref} = \frac{1}{2} + \frac{1}{2}\sqrt{1 + 4Q_i^{ref}X_i} \tag{5.32}$$

If X_i is chosen such that, $0 < 4Q_i^{ref}X_i \ll 1$, and therefore, we can apply binomial approximation to (5.32) to get,

$$|V_c|_i^{ref} \approx \frac{1}{2} + \frac{1}{2}\left(1 + \frac{1}{2} * 4Q_i^{ref}X_i\right) = 1 + Q_i^{ref}X_i \tag{5.33}$$

Equations (5.28), (5.29), and (5.33) can be used by the MGCC to calculate Q_i^{ref} and $|V_c|_i^{ref}$ for each of the inverter's voltage droop controller. If there is a good estimation of the total reactive power in the system, the inverter's output voltage, $|V_c|_i$, and reactive power, Q_i, will closely match the calculated reference values $|V_c|_i^{ref}$ and Q_i^{ref} respectively, and $|V_m|_i \approx 1$.

5.4.3.3. Approximate Reactive Power Sharing by Choice of Inductive Coupling

Assuming that there is a small deviation in total reactive power served from the estimated total reactive power, this deviation is usually manifested as small deviations in

bus voltages. Define the new $|V_m|_i = 1 + \Delta|V_m|_i$, then the reactive power output can be written as,

$$Q_i = \frac{|V_c|_i}{X_i}(|V_c|_i - 1 - \Delta|V_m|_i) \tag{5.34}$$

For a relatively small voltage droop coefficient, $|V_c|_i \approx |V_c|_i^{ref}$, then,

$$Q_i - Q_i^{ref} \approx -\frac{\Delta|V_m|_i|V_c|_i^{ref}}{X_i} \approx -\frac{\Delta|V_m|_i}{X_i}\left(1 + Q_i^{ref}X_i\right) \approx -\frac{\Delta|V_m|_i}{X_i} \tag{5.35}$$

We assume that the coupling inductor was chosen to dominate over the line impedance and thus voltage drops significantly only across the coupling inductor, therefore, the drop across the network can be assumed relatively small. This leads to the approximation,

$$\Delta|V_m|_i = \Delta|V_m|_j = \Delta|V_m|, \qquad \forall\, i,j \in \{1,2,\dots,n\} \tag{5.36}$$

$$\Delta Q_i = Q_i - Q_i^{ref} \approx -\frac{\Delta|V_m|}{X_i} \tag{5.37}$$

$$|\Delta Q_i| : \left|\Delta Q_j\right| \approx \frac{1}{X_i} : \frac{1}{X_j}, \qquad \forall\, i,j \in \{1,2,\dots,n\} \tag{5.38}$$

$$\frac{1}{X_i} : \frac{1}{X_j} = \overline{Q_i} : \overline{Q_j}, \qquad \forall\, i,j \in \{1,2,\dots,n\} \tag{5.39}$$

The implication of (5.38) is that deviations from the reference reactive power can be shared by the inverse proportion of the coupling inductive reactance. Other reactive power sharing paradigm may require varying X_i according to some optimal reactive power reference. In such a case, an inverter control with virtual impedance would offer more flexibility than the physical coupling inductance used here.

5.5. Power Flow based on the Linearized Current Injection Approach

5.5.1. Basics of the Current Injection Method (CIM)

Most of the conventional power flow approach is based on expressing the system physics equations as in (5.40) [97],

$$\bar{Y}\bar{V} = \bar{I} \tag{5.40}$$

where $\bar{Y}$ is the complex admittance matrix of the network, $\bar{V}$ is the complex bus voltage vector, and $\bar{I}$ is the complex bus injection current vector including all present phases at each branch and node. We use a bar on a variable to specify that it is complex. We can separate (5.40) into real and imaginary parts:

$$\begin{bmatrix} G & -B \\ B & G \end{bmatrix} \begin{bmatrix} V^{re} \\ V^{im} \end{bmatrix} = \begin{bmatrix} I^{re} \\ I^{im} \end{bmatrix} \tag{5.41}$$

where $\bar{Y} = G + jB$ and superscripts re and im represent the real and imaginary parts of a complex vector, respectively.

The current injection at each bus can be expressed as a nonlinear function of the nodal voltages. In the following sections, we discuss how to linearize the right-hand side of (5.41).

5.5.2. Linearized Current Injection at Droop, PQ, and Load Bus

5.5.2.1. Current Injection at Droop Bus

Because the formulation is three-phase, the current injection at each droop-controlled bus should be derived per phase. We can approximate the droop characteristics by decoupling equations (5.1) and (5.2) (which are implicitly assumed to model the droop control for three-phase balanced operation) into per-phase equations, as shown below:

$$f_{ph,k} = f^{ref} - n_{f,k}(P_{ph,k} - P_{ph,k}^{ref}) \tag{5.42}$$

$$\left|\bar{V}_{ph,k}\right| = \left|\bar{V}_{ph,k}\right|^{ref} - n_{v,k}(Q_{ph,k} - Q_{ph,k}^{ref}) \tag{5.43}$$

Variables remain as described earlier, except that the subscript ph represents phases a, b, or c at the k^{th} bus. Note that (5.42) and (5.43) are per-phase approximations and can introduce some errors into the droop characterization as the current and power unbalance rate as seen from each droop inverter terminal increase. The per-phase reference settings are the same with the three-phase balance settings in per unit, as long as the base values are changed to their one-phase equivalent (e.g., single-phase base value for power is 1/3 of its three-phase value). Rearranging (5.42) and (5.43) in terms of power injection,

$$P_{ph,k} = \frac{f_{ph,k} - f^{ref}}{-n_{f,k}} + P_{ph,k}^{ref} = \frac{\Delta f_{ph,k}}{-n_{f,k}} + P_{ph,k}^{ref} \tag{5.44}$$

$$Q_{ph,k} = \frac{\left|\bar{V}_{ph,k}\right| - \left|\bar{V}_{ph,k}\right|^{ref}}{-n_{v,k}} + Q_{ph,k}^{ref} \tag{5.45}$$

where $\Delta f_{ph,k}$ is the frequency deviation from nominal at each phase of each bus and can be assumed equal for all nodes in the system. Thus, let $\Delta f_{ph,k} = \Delta f$. In section VI, we demonstrate how $\Delta f_{ph,k}$ can be controlled to zero in the optimal power flow formulation. At each phase ph and bus k, with power injections $P_{ph,k} + jQ_{ph,k}$, the current injection per phase can be written as follows:

$$\bar{I}_{ph,k} = I_{ph,k}^{re} + jI_{ph,k}^{im} = \frac{P_{ph,k} - jQ_{ph,k}}{V_{ph,k}^{re} - jV_{ph,k}^{im}} \tag{5.46}$$

$$I_{ph,k}^{re} = \frac{P_{ph,k}V_{ph,k}^{re} + Q_{ph,k}V_{ph,k}^{im}}{\left|V_{ph,k}^{re}\right|^2 + \left|V_{ph,k}^{im}\right|^2} \tag{5.47}$$

$$I_{ph,k}^{im} = \frac{P_{ph,k}V_{ph,k}^{im} - Q_{ph,k}V_{ph,k}^{re}}{\left|V_{ph,k}^{re}\right|^2 + \left|V_{ph,k}^{im}\right|^2} \tag{5.48}$$

Note that $\left|\bar{V}_{ph,k}\right|^2 = \left|V_{ph,k}^{re}\right|^2 + \left|V_{ph,k}^{im}\right|^2$. Substituting (5.44) and (5.45) into (5.47) and (5.48) gives the nonlinear current injection in terms of rectangular voltages, droop coefficient, and reference settings as shown in (5.49) and (5.50),

$$I_{ph,k}^{re} = \frac{\Delta f}{-n_{f,k}} \frac{V_{ph,k}^{re}}{\left|V_{ph,k}^{re}\right|^2 + \left|V_{ph,k}^{im}\right|^2} + P_{ph,k}^{ref} \frac{V_{ph,k}^{re}}{\left|V_{ph,k}^{re}\right|^2 + \left|V_{ph,k}^{im}\right|^2} + \frac{1}{-n_{v,k}} \frac{V_{ph,k}^{im}}{\sqrt{\left|V_{ph,k}^{re}\right|^2 + \left|V_{ph,k}^{im}\right|^2}} + \frac{\left|\bar{V}_{ph,k}\right|^{ref}}{n_{v,k}} \frac{V_{ph,k}^{im}}{\left|V_{ph,k}^{re}\right|^2 + \left|V_{ph,k}^{im}\right|^2} + Q_{ph,k}^{ref} \frac{V_{ph,k}^{im}}{\left|V_{ph,k}^{re}\right|^2 + \left|V_{ph,k}^{im}\right|^2} \tag{5.49}$$

$$I_{ph,k}^{im} = \frac{\Delta f}{-n_{f,k}} \frac{V_{ph,k}^{im}}{\left|V_{ph,k}^{re}\right|^2 + \left|V_{ph,k}^{im}\right|^2} + P_{ph,k}^{ref} \frac{V_{ph,k}^{im}}{\left|V_{ph,k}^{re}\right|^2 + \left|V_{ph,k}^{im}\right|^2} + \frac{1}{n_{v,k}} \frac{V_{ph,k}^{re}}{\sqrt{\left|V_{ph,k}^{re}\right|^2 + \left|V_{ph,k}^{im}\right|^2}} - \frac{\left|\bar{V}_{ph,k}\right|^{ref}}{n_{v,k}} \frac{V_{ph,k}^{re}}{\left|V_{ph,k}^{re}\right|^2 + \left|V_{ph,k}^{im}\right|^2} - Q_{ph,k}^{ref} \frac{V_{ph,k}^{re}}{\left|V_{ph,k}^{re}\right|^2 + \left|V_{ph,k}^{im}\right|^2} \tag{5.50}$$

5.5.2.2. Current Injection at PQ DG and Load Bus

At each phase of a grounded wye-connected ZIP load bus, assuming a nominal voltage of $1pu$, we can write the power injections as follows:

$$P_{ph,k} = P_{ph,k}^{N}[\alpha_k^Z\left(\left|\bar{V}_{ph,k}\right|\right)^2 + \alpha_k^I\left(\left|\bar{V}_{ph,k}\right|\right) + \alpha_k^P) \tag{5.51}$$

$$Q_{ph,k} = Q_{ph,k}^{N}[\alpha_k^Z\left(\left|\bar{V}_{ph,k}\right|\right)^2 + \alpha_k^I\left(\left|\bar{V}_{ph,k}\right|\right) + \alpha_k^P) \tag{5.52}$$

where the superscript N denotes nominal power of load per phase; α_k^Z, α_k^I, and α_k^P are the ZIP load coefficients for the constant impedance, current, and power component of the load and numerically sum to unity. Note that the nominal power should be negated to signify that the current is injected in the reverse direction into the network for ZIP load

elements. For DG operating in PQ mode, only α_k^P is set to unity and the other power coefficients are set to zero and nominal power is not negated.

Substituting (5.51) and (5.52) into (5.47) and (5.48) gives the following current injection equations for the ZIP load bus per phase (also valid for the PQ DG bus):

$$I_{ph,k}^{re} = \alpha_k^Z\left(P_{ph,k}^N V_{ph,k}^{re} + Q_{ph,k}^N V_{ph,k}^{im}\right) + \alpha_k^I\left(\frac{P_{ph,k}^N V_{ph,k}^{re} + Q_{ph,k}^N V_{ph,k}^{im}}{\sqrt{\left|V_{ph,k}^{re}\right|^2 + \left|V_{ph,k}^{im}\right|^2}}\right) + \alpha_k^P\left(\frac{P_{ph,k}^N V_{ph,k}^{re} + Q_{ph,k}^N V_{ph,k}^{im}}{\left|V_{ph,k}^{re}\right|^2 + \left|V_{ph,k}^{im}\right|^2}\right) \quad (5.53)$$

$$I_{ph,k}^{im} = \alpha_k^Z\left(P_{ph,k}^N V_{ph,k}^{im} - Q_{ph,k}^N V_{ph,k}^{re}\right) + \alpha_k^I\left(\frac{P_{ph,k}^N V_{ph,k}^{im} - Q_{ph,k}^N V_{ph,k}^{re}}{\sqrt{\left|V_{ph,k}^{re}\right|^2 + \left|V_{ph,k}^{im}\right|^2}}\right) + \alpha_k^P\left(\frac{P_{ph,k}^N V_{ph,k}^{im} - Q_{ph,k}^N V_{ph,k}^{re}}{\left|V_{ph,k}^{re}\right|^2 + \left|V_{ph,k}^{im}\right|^2}\right) \quad (5.54)$$

5.5.2.3. Linearization of Current Injection & Power Flow Equations

Equations (5.49), (5.50), (5.53), and (5.54) present four non-linear terms in voltages (assuming all the other parameters are known), which are the same nonlinear terms derived by the authors of [92] for the LPF using CIM for grid-connected distribution systems. These four non-linear terms are:

$$g_{1,ph} = \frac{V_{ph,k}^{re}}{\left|V_{ph,k}^{re}\right|^2 + \left|V_{ph,k}^{im}\right|^2}, g_{2,ph} = \frac{V_{ph,k}^{im}}{\left|V_{ph,k}^{re}\right|^2 + \left|V_{ph,k}^{im}\right|^2},$$
$$g_{3,ph} = \frac{V_{ph,k}^{re}}{\sqrt{\left|V_{ph,k}^{re}\right|^2 + \left|V_{ph,k}^{im}\right|^2}}, g_{4,ph} = \frac{V_{ph,k}^{im}}{\sqrt{\left|V_{ph,k}^{re}\right|^2 + \left|V_{ph,k}^{im}\right|^2}} \quad (5.55)$$

We adopted the technique used in [92] where each of the above functions is linearized for each phase around a compact set of expected operating regions in terms of rectangular voltages. The compact set for each phase is set such that the rectangular

voltages, when expressed in polar form, vary within ±10% from $1pu$ magnitude and the angles within ±10° from 0°, –120°, and 120° for phases *a*, *b*, and *c*, respectively. The linearization for each of the functions was solved as a least-square estimation problem around the compact set to get the following linear form in rectangular voltages:

$$\tilde{g}_{i,ph} = C_{1i,ph}V_{ph}^{re} + C_{2i,ph}V_{ph}^{im} + C_{3i,ph}, i \in \{1,2,3,4\} \tag{5.56}$$

where $C_{1i,ph}$, $C_{2i,ph}$, and $C_{3i,ph}$ are solved constants per phase for each of the four functions.

With the current linearization in terms of rectangular voltages described above, (5.41) can then be written as,

$$\begin{bmatrix} G & -B \\ B & G \end{bmatrix} \begin{bmatrix} V^{re} \\ V^{im} \end{bmatrix} = [M] \begin{bmatrix} V^{re} \\ V^{im} \end{bmatrix} + [K] \tag{5.57}$$

where $[M]$ and $[K]$ are constant matrix and vector respectively realized from the current linearization in terms of rectangular voltages. We can then solve for the voltages:

$$\begin{bmatrix} V^{re} \\ V^{im} \end{bmatrix} = \left[\begin{bmatrix} G & -B \\ B & G \end{bmatrix} - [M] \right]^{-1} [K] \tag{5.58}$$

5.5.3. Estimating Frequency Deviation

In (5.49) and (5.50), it was implicitly assumed that the frequency deviation variable, Δf, is known when we linearized in terms of rectangular voltages. An estimate of the frequency deviation is necessary for the above linearization to be usable.

We can get a ballpark estimate of the frequency deviation by ignoring the losses in the system and assuming that every element is operating at its nominal voltage. Thus, the sum of the bus power injection should give a zero-sum for the system:

$$\sum_{k\in N}\sum\nolimits_{ph\in\{a,b,c\}}\left(\frac{-\Delta f}{n_{f,k}}+P_{ph,k}^{ref}+P_{ph,k}^{N}\right)=0 \tag{5.59}$$

Equation (5.59) is the sum of the droop power injection for all buses with droop DG (from (5.44)) and the nominal power/power setpoints of all ZIP load/PQ DG elements (from (5.51)). Rearranging (5.59) gives,

$$\Delta f=\frac{\sum_{k\in N}\sum_{ph\in\{a,b,c\}}\left(P_{ph,k}^{ref}+P_{ph,k}^{N}\right)}{\sum_{k\in N}\sum_{ph\in\{a,b,c\}}\frac{1}{n_{f,k}}} \tag{5.60}$$

The frequency deviation in (5.60) is calculated with the assumption that the droop coefficient and reference power is the same for each phase of a droop-controlled DG.

After the voltages, currents, and power injections are calculated from the LPF, a better frequency deviation estimate that considers losses can be obtained by replacing the summation of $P_{ph,k}^{N}$ in (5.60) with the negative sum of power injection at the droop DG nodes.

5.6. Power Flow based on the Modified DistFlow (Line Flow) Approach

5.6.1. Three-Phase DistFlow Equations

This second LPF is derived from the DistFlow [64, 65]. We call this adaptation LPF based on the line flow method (LFM).

Consider a microgrid network formulated as a directed graph, G, with N being the set of nodes and B the set of branches. The direction of each branch is an assumed direction of the line power flow. For any given branch (assuming a power flow from node i to j), we have by Kirchhoff's law [29, 30, 65],

$$\bar{V}_j = \bar{V}_i - \bar{Z}_{ij}\bar{I}_{ij} \tag{5.61}$$

$$\bar{I}_{ij} = \bar{S}_{ij}^* \oslash \bar{V}_i^* \tag{5.62}$$

$$\bar{V}_j \odot \bar{V}_j^{\,*} = \bar{V}_i \odot \bar{V}_i^{\,*} - \bar{Z}_{ij}(\bar{S}_{ij}^* \oslash \bar{V}_i^*) \odot \bar{V}_i^* - \bar{Z}_{ij}^*(\bar{S}_{ij} \oslash \bar{V}_i) \odot \bar{V}_i + c_{ij}(\bar{S}_{ij}, \bar{V}_i, \bar{Z}_{ij}) \tag{5.63}$$

where $\bar{V}_i$, $\bar{V}_j$ is a vector of the three-phase complex voltages for each phase in node i, j. $\bar{Z}_{ij} = r_{ij} + jx_{ij}$ is the phase impedance matrix of the branch between nodes i and j. $\bar{I}_{ij}$ is a vector of three-phase complex branch current flowing from nodes i to j. $\bar{S}_{ij}$ is a vector of three-phase complex power flowing from node i to j; $\odot$ and $\oslash$ represent the element-wise multiplication and division, respectively. $c_{ij}(\bar{S}_{ij}, \bar{V}_i, \bar{Z}_{ij})$ is the high-order term. A superscript asterisk represents the complex conjugate operation of a complex variable.

All quantities are per unit. Equation (5.63) was approximated in [29, 30] by neglecting $c_{ij}(\bar{S}_{ij}, \bar{V}_i, \bar{Z}_{ij})$ and assuming nearly balanced voltages to get the following:

$$U_j = U_i - \tilde{Z}_{ij}\bar{S}_{ij}^* - \tilde{Z}_{ij}^*\bar{S}_{ij} \tag{5.64}$$

where U_i, U_j are vectors of square voltage magnitude at node i, j, respectively. $\tilde{Z}_{ij} = \alpha \odot \bar{Z}_{ij}$, and α is defined as,

$$\alpha = \begin{bmatrix} 1 & e^{-j2\pi/3} & e^{j2\pi/3} \\ e^{j2\pi/3} & 1 & e^{-j2\pi/3} \\ e^{-j2\pi/3} & e^{j2\pi/3} & 1 \end{bmatrix} \tag{5.65}$$

Equation (5.64) can be simplified to give,

$$U_i - U_j = 2\left(\tilde{r}_{ij}.P_{ij}^{BR} + \tilde{x}_{ij}.Q_{ij}^{BR}\right) \tag{5.66}$$

where $\tilde{r}_{ij} = re(\tilde{Z}_{ij})$, $\tilde{x}_{ij} = im(\tilde{Z}_{ij})$, $\bar{S}_{ij} = P_{ij}^{BR} + jQ_{ij}^{BR}$.

From graph theory, the node-edge incidence matrix, A, for a directed graph, $G(N,B)$, is an $n(N)$ by $n(B)$ matrix (or n_N by n_B for short denoting the number of elements in sets N and B) where the rows represent the node indices and columns represent the branch indices. A component of A, given by $A_{ij} = 1$, if node i is a sink node of branch j, $A_{ij} = -1$, if node i is a source node of branch j, and $A_{ij} = 0$, if node i is not an edge of branch j.

To account for the three phases of each node, we redefine each component A_{ij} to be a diagonal 3 × 3 submatrix with diagonal components of present phases set to be all 1, -1, or 0, depending on whether it is a sink, source, or unconnected to the given branch. Thus, A is a $3n_N \times 3n_B$ matrix, assuming all three phases are present for all nodes. Let the power-flow direction of each branch be defined according to the assumed direction of the directed graph G. Then, power balance at every bus gives the following matrix equations:

$$-A * [P^{BR}] = \left[P^{inj}\right], -A * [Q^{BR}] = [Q^{inj}] \tag{5.67}$$

where $[P^{BR}]$ and $[Q^{BR}]$ are vectors of active and reactive power flow across the branch with an assumed direction the same as the graph. $\left[P^{inj}\right]$ and $[Q^{inj}]$ are vectors of active and reactive power injection at the nodes. Equation (5.66) can be written in terms of A for all nodes (assuming three phases for each node):

$$\begin{bmatrix} A \\ 2diag(\left[\tilde{r}_{ij}\right]_{n=1}^{n=n_B})^T \\ 2diag(\left[\tilde{x}_{ij}\right]_{n=1}^{n=n_B})^T \end{bmatrix}^T \begin{bmatrix} [U]_{3n_N \times 1} \\ [P^{BR}]_{3n_B \times 1} \\ [Q^{BR}]_{3n_B \times 1} \end{bmatrix} = [0] \tag{5.68}$$

Equation (5.68) is linear in terms of the square of voltage magnitude and branch power flow. To linearize (5.67), the right-hand side of the two equations, which is the power injection, must be linearized in terms of the square of voltage magnitude.

5.6.2. Linearization of Power Injection

For the power injection at droop bus, (5.44) and (5.45) can be rewritten as follows:

$$P_{ph,k} = \frac{\Delta f_{ph,k,i}}{-n_{f,k}} + P_{ph,k}^{ref}, Q_{ph,k} = \frac{\sqrt{U_{ph,k}} - \left|\bar{V}_{ph,k}\right|^{ref}}{-n_{v,k}} + Q_{ph,k}^{ref} \tag{5.69}$$

Equations (5.51) and (5.52) which gives the power injection per phase at the ZIP load and PQ DG bus can be rewritten as

$$P_{ph,k} = P_{ph,k}^{N}[\alpha_k^Z U_{ph,k} + \alpha_k^I \sqrt{U_{ph,k}} + \alpha_k^P] \tag{5.70}$$

$$Q_{ph,k} = Q_{ph,k}^{N}[\alpha_k^Z U_{ph,k} + \alpha_k^I \sqrt{U_{ph,k}} + \alpha_k^P] \tag{5.71}$$

The non-linear term in (5.69)–(5.71) is $\sqrt{U_{ph,k}}$. It can be linearized using a Taylor expansion about $U_{ph,k} = 1$:

$$\sqrt{U_{ph,k}} \approx 0.5 + 0.5U_{ph,k} \tag{5.72}$$

Equation (5.72) can be substituted into (5.69)–(5.71) to produce linear expressions of the bus power injections in terms of the square of node voltage magnitude. With this linearization, (5.67) can be rewritten in linear form as,

$$\begin{bmatrix} -A & [0] \\ [0] & -A \end{bmatrix} \begin{bmatrix} [P^{BR}]_{3n_B \times 1} \\ [Q^{BR}]_{3n_B \times 1} \end{bmatrix} = \begin{bmatrix} M_P \\ M_Q \end{bmatrix} \left[[U]_{3n_N \times 1} \right] + [K] \tag{5.73}$$

where M_P and M_Q are constant matrices and K is a constant vector, obtained from linearizing the bus power injections. Combining (5.68) and (5.73) gives

$$\underbrace{\begin{bmatrix} A^T & 2diag([\tilde{r}_{ij}]_{n=1}^{n=n_B}) & 2diag([\tilde{x}_{ij}]_{n=1}^{n=n_B}) \\ -M_P & \begin{bmatrix} -A & [0] \\ [0] & -A \end{bmatrix} & \\ -M_Q & & \end{bmatrix}}_{A_{sys}} \begin{bmatrix} [U]_{3n_N \times 1} \\ [P^{BR}]_{3n_B \times 1} \\ [Q^{BR}]_{3n_B \times 1} \end{bmatrix} = \begin{bmatrix} [0] \\ K \end{bmatrix} \tag{5.74}$$

The coefficient matrix of (5.74), A_{sys}, has a dimension of $3n_B + 6n_N$ by $6n_B + 3n_N$, assuming all three phases are present per bus. For a microgrid network with tree topology, $n_N > n_B$ i.e. $n_N = n_B + 1$, which makes (5.74) overdetermined.

To solve (5.74) for a microgrid with tree topology, unavailable phase nodes and branch phases are removed from the matrix equation. Then we solve for $[U]$, $[P^{BR}]$, $[Q^{BR}]$ using least-square estimation. Initial and subsequent frequency deviation estimates are calculated similarly as presented previously in section 5.5.3.

5.7. Power Flow Verification, Case Study, and Discussion

5.7.1. Verification Approach

The verification approach is based on solving the power flow of an autonomous microgrid using the two proposed methods and comparing the results with detailed PSCAD simulation with DG control models at a steady state. We introduce the following two metrics which are referred to in the case studies and discussion.

5.7.1.1. Nominal System Load Unbalance Index (NSLUI)

We introduce $NSLUI$ below to quantify the unbalance presented by load demand. Let the total nominal active or reactive power demand ($P_{ph,T}^N$ or $Q_{ph,T}^N$) be defined for each phase as the sum of the nominal active or reactive power load plus the sum of active or reactive power supplied from the PQ inverter. Essentially, the total nominal power demand

is the net power demand that the three-phase droop DGs are meant to share. We define the active power $NSLUI$, denoted $NSLUI_P$, as,

$$\frac{max_{|x|}\left(\{P_{a,T}^N, P_{b,T}^N, P_{c,T}^N\} - avg\left(\{P_{a,T}^N, P_{b,T}^N, P_{c,T}^N\}\right)\right)}{\left|avg(\{P_{a,T}^N, P_{b,T}^N, P_{c,T}^N\})\right|} \times 100\% \tag{5.75}$$

where $max_{|x|}$ and avg denote the absolute maximum and average value of a set, respectively. The $NSLUI_P$ quantifies the unbalanced active power demand by evaluating the maximum deviation from the average phase power. The reactive power $NSLUI$, denoted $NSLUI_Q$, is defined similarly with $P_{ph,T}^N$ replaced with $Q_{ph,T}^N$.

5.7.1.2. Relative Error

The relative error, ε_x, of calculated quantity, x, with respect to its reference value, x_{ref}, is defined as,

$$\varepsilon_x = \frac{\left|x - x_{ref}\right|}{\left|x_{ref}\right|} \times 100\% \tag{5.76}$$

The mean relative error, $\bar{\varepsilon}_x$, of a set of calculated quantity is the average of the relative errors of each element of the set.

5.7.2. Modified 4-Node Test Feeder

The first test case study is based on a modified IEEE 4 node test feeder [84], as shown in Figure 5.2.

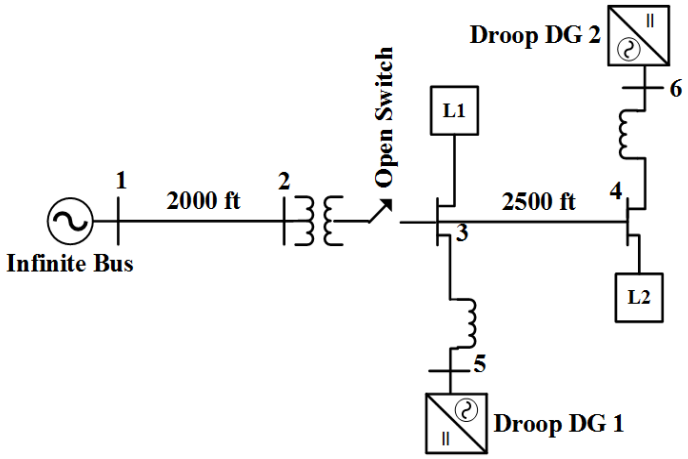

Figure 5.2 Autonomous Microgrid built from Modified 4-node Test Feeder

The line information is the same as the three-wire phase impedance matrix released in the original 4-node test feeder. The modified system has been isolated from the high-voltage infinite bus supply side.

The DG parameters are presented in Table 5.1. Each DG outputs a base line to line voltage of 0.48 kV and then a matching transformer is used to match the voltage to the distribution network level of 4.16 kV line to line. The matching transformer leakage reactance is assumed negligible compared to the reactance of the coupling inductor and thus is not considered in the power flow. The load parameters are shown in Table 5.2.

Table 5.1 Droop DG Parameters for Modified 4-Node Test Feeder

Node	Type	3-Phase P_{ref} (kW)	3-Phase Q_{ref} (kVAr)	n_f (Hz/unit power)	n_v (1/unit power)	f_{ref}, f^* (Hz)	V_{ref} (pu)	Per phase coupling X (pu)	Per phase basekV	Per phase baseMVA
5	Droop	320	150	0.75	0.1875	60	1.03255	0.651	2.4018	1
6	Droop	160	75	1.5	0.1875	60	1.03255	1.302	2.4018	1

Table 5.2 Load Parameters for Modified 4-Node Test Feeder

Node	Type	P^N(A/B/C) kW	Q^N(A/B/C) kVAr	$\alpha^Z/\alpha^I/\alpha^P$
3	Y-ZIP	95/110/100	45/48/55	0.33/0.33/0.33
4	Y-ZIP	105/90/100	55/52/45	0.33/0.33/0.33
$NSLUI$		0.00	0.00	

The power flow results are shown in Table 5.3 to Table 5.5. From Table 5.5, we see that due to the assumption of the lossless line used in the line flow approach (equation (5.67)), the reactive power injection at the droop bus is poorly estimated because the coupling inductance constitutes a significant reactive power loss.

Table 5.3 Power Flow Result Using Linearized Droop Power Flow by CIM for Modified 4-Node Test Feeder (f = 59.9821 Hz)

Node	V_a	V_b	V_c	P^{inj}(A/B/C) kW	Q^{inj}(A/B/C) kVAr
3	0.9791 ∠ 0.00˚	0.9788 ∠ -120.03˚	0.9789 ∠ 120.00˚	-93.1/-107.7/ -98.0	-43.9/-46.7/ -53.6
4	0.9770 ∠ -0.10˚	0.9777 ∠ -120.06˚	0.9774 ∠ 119.90˚	-102.7/-88.1/ -97.8	-53.5/-50.6/ -43.7
5	1.0247 ∠ 4.89˚	1.0246 ∠ -115.15˚	1.0246 ∠ 124.89˚	131.3/131.2 /131.3	77.3/77.8 /77.6
6	1.0266 ∠ 4.71˚	1.0267 ∠ -115.25˚	1.0267 ∠ 124.71˚	64.5/64.6 /64.5	41.8/41.3 /41.6

Table 5.4 Power Flow Result Using Linearized Droop Power Flow by LFM for Modified 4-Node Test Feeder (f = 59.9813 Hz)

Node	$\|V_a\|$	$\|V_b\|$	$\|V_c\|$	P^{inj}(A/B/C) kW	Q^{inj}(A/B/C) kVAr
3	0.9881	0.9877	0.9878	-93.9/-108.6/ -98.8	-44.5/-47.4/ -54.3
4	0.9860	0.9866	0.9863	-103.5/-88.8/ -98.6	-54.2/-51.3/ -44.4
5	1.0295	1.0294	1.0294	133.3/133.3 /133.3	64.2/64.6 /64.4
6	1.0303	1.0304	1.0304	66.7/66.7 /66.7	34.4/33.9 /34.1

Table 5.5 Results from PSCAD Simulation at Steady State for Modified 4-Node Test Feeder

Node	V_a	V_b	V_c	P^{inj}(A/B/C) kW	Q^{inj}(A/B/C) kVAr
3	0.9826 ∠ 0.00˚	0.9815 ∠ -120.06˚	0.9810 ∠ 119.97˚	-93.3/-108.1/ -98.1	-44.3/-47.1/ -54.0
4	0.9806 ∠ -0.09˚	0.9805 ∠ -120.09˚	0.9795 ∠ 119.88˚	-102.9/-88.3/ -98.0	-54.0/-51.0/ -44.1
5	1.0290 ∠ 4.79˚	1.0278 ∠ -115.27˚	1.0273 ∠ 124.77˚	129.3/129.4 /129.1	77.9/77.8 /78.0
6	1.0306 ∠ 4.88˚	1.0304 ∠ -115.14˚	1.0291 ∠ 124.85˚	67.1/67.0 /67.0	42.2/42.2 /42.0

Figure 5.3 shows the percentage relative error of voltage for both the CIM and LFM approaches compared to the result from PSCAD. The CIM, LFM, and PSCAD results gave a frequency of 59.982, 59.981, and 59.981 Hz, respectively. A PSCAD plot of the droop frequency dynamics of the two DGs until steady-state is shown in Figure 5.4. The small steady-state error of the droop frequencies in Figure 5.4 is due to the sensitivities of the droop controllers. Sensitivity can be improved by increasing the droop co-efficient at the cost of a reduced stability margin [102]. The method was also verified and tested with modified IEEE 13 and 123 node test feeders.

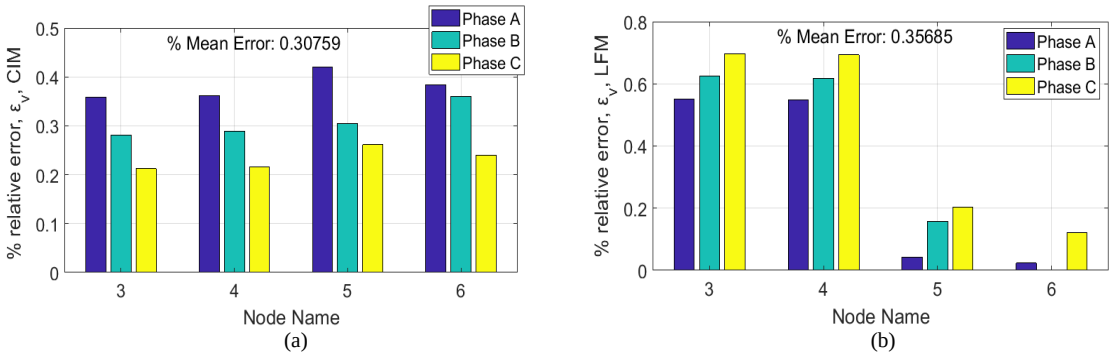

Figure 5.3 Percent Relative Error of Voltage of LPF Solutions with PSCAD result used as a Benchmark for Modified 4-Node Test System using (a) CIM and (b) LFM

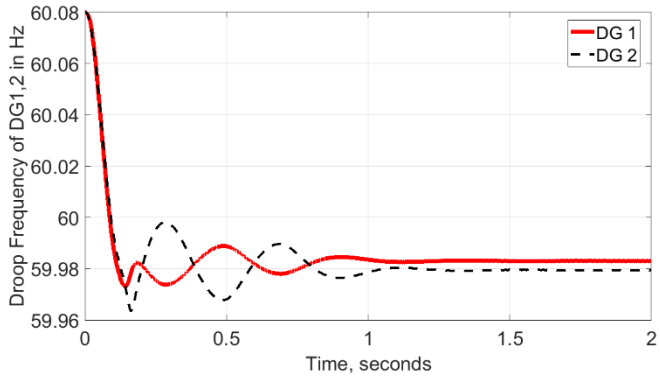

Figure 5.4 Plot of Droop Frequency for DG 1 and 2 of the Modified 4-Node Test Case

5.8. Application: Optimal Power Flow in Islanded Droop-Controlled Microgrid

As a recap, the preceding parts of section 5 present linear power flow equations in which given network states, droop and PQ DG settings, and load details, the operating point of the system can be determined. When the system is operating sub-optimally, it is important to find the optimal droop settings that will optimize a certain objective. In this section, we present an optimization formulation based on the preceding linearized power

flow derivations for the optimal choice of droop parameters and PQ DG setpoints that minimizes the system cost and achieves a certain phase load balancing. For phase load balancing, the dispatchable single-phase PQ DGs setpoints are controlled to reduce the load unbalance in the system. The economic dispatch is formulated as a mixed-integer quadratic programming (MIQP) and a quadratic programming (QP) problem for the current injection and line flow methods, respectively. All decision variables are denoted with a hat and variables with a hat remain the same as described in the power flow derivations.

5.8.1. Objective Function

The objective function is to minimize the cost of power in the system by dispatching power to each DG based on their cost function. A general quadratic cost function, which consists of maintenance and fuel cost, is assumed for each DG [103] and expressed as,

$$min \sum_{k \in G^{DG}} \alpha_k + \beta_k \hat{P}_k + \gamma_k \hat{P}_k^2 \tag{5.77}$$

Subject to constraints in sections 5.8.2 to 5.8.7 except that sections 5.8.4 and 5.8.5 are constraints specific to the current injection method and the line flow method respectively. Where G^{DG} is the set of all DG nodes and P_k is the sum of each DG's output power for all phases present.

5.8.2. Droop Reference Active Power Constraint

It is desired that the frequency be restored to reference (nominal) frequency each time the microgrid is optimized globally from the tertiary control layer, that is, $\Delta f = 0$.

This requires that the output of each droop-controlled DGs should match the reference power according to (5.42):

$$\hat{P}_{ph,k} = \hat{P}_{ph,k}^{ref} \tag{5.78}$$

5.8.3. Droop Reference Reactive Power Constraint

Similarly, for the voltage droop, the following is enforced to restore voltage at each droop node to the droop reference voltage.

$$\hat{Q}_{ph,k} = \hat{Q}_{ph,k}^{ref} \tag{5.79}$$

5.8.4. System Model/Power Flow Constraints (Current Injection Approach)

5.8.4.1. Droop Node

At each droop DG bus, $k \in G^{DG}$, the real and imaginary part of the current injection per phase can be derived in summation form from the network admittance matrix and equations (5.41), (5.49), (5.50), (5.78), and (5.79) to get,

$$\sum_{n \in N_{ph}} (G_{k_{ph},n} \hat{V}_n^{re} - B_{k_{ph},n} \hat{V}_n^{im}) = \hat{I}_{ph,k}^{re} \left(\hat{V}_{k_{ph}}^{re}, \hat{V}_{k_{ph}}^{im} \right) \tag{5.80}$$

$$\sum_{n \in N_{ph}} (B_{k_{ph},n} \hat{V}_n^{re} + G_{k_{ph},n} \hat{V}_n^{im}) = \hat{I}_{ph,k}^{im} \left(\hat{V}_{k_{ph}}^{re}, \hat{V}_{k_{ph}}^{im} \right) \tag{5.81}$$

where N_{ph} is a set of all nodes counting each phase as a node, and k_{ph} is the node index of the phase ph of bus k. The RHS of (5.80) and (5.81) is expressed by substituting (5.78) and (5.79) to (5.49) and (5.50) to get,

$$\hat{I}_{ph,k}^{re} = \hat{P}_{ph,k}^{ref} \frac{\hat{V}_{ph,k}^{re}}{\left|\hat{V}_{ph,k}^{re}\right|^2 + \left|\hat{V}_{ph,k}^{im}\right|^2} + \hat{Q}_{ph,k}^{ref} \frac{\hat{V}_{ph,k}^{im}}{\left|\hat{V}_{ph,k}^{re}\right|^2 + \left|\hat{V}_{ph,k}^{im}\right|^2} \tag{5.82}$$

$$\hat{I}_{ph,k}^{im} = \hat{P}_{ph,k}^{ref} \frac{\hat{V}_{ph,k}^{im}}{\left|\hat{V}_{ph,k}^{re}\right|^2 + \left|\hat{V}_{ph,k}^{im}\right|^2} - \hat{Q}_{ph,k}^{ref} \frac{\hat{V}_{ph,k}^{re}}{\left|\hat{V}_{ph,k}^{re}\right|^2 + \left|\hat{V}_{ph,k}^{im}\right|^2} \tag{5.83}$$

The two voltage quotient terms above have been previously linearized (see equations (5.55) and (5.56)) and substitution of the linearized terms to (5.82) and (5.83) gives,

$$\hat{I}_{ph,k}^{re} = \hat{P}_{ph,k}^{ref} \tilde{g}_{1,ph}\left(\hat{V}_{k_{ph}}^{re}, \hat{V}_{k_{ph}}^{im}\right) + \hat{Q}_{ph,k}^{ref} \tilde{g}_{2,ph}\left(\hat{V}_{k_{ph}}^{re}, \hat{V}_{k_{ph}}^{im}\right) \tag{5.84}$$

$$I_{ph,k}^{im} = \hat{P}_{ph,k}^{ref} \tilde{g}_{2,ph}\left(\hat{V}_{k_{ph}}^{re}, \hat{V}_{k_{ph}}^{im}\right) - \hat{Q}_{ph,k}^{ref} \tilde{g}_{1,ph}\left(\hat{V}_{k_{ph}}^{re}, \hat{V}_{k_{ph}}^{im}\right) \tag{5.85}$$

where $\tilde{g}_{1,ph}$ and $\tilde{g}_{2,ph}$ are linear functions of the rectangular voltages. Notice that (5.84) and (5.85) present a new linearization challenge previously unencountered in the power flow formulation. This is because the droop reference active and reactive power are now decision control variables (previously they were both considered known control parameters in the power flow formulation). The non-linear terms in (5.84) and (5.85) are each product of two continuous variables and are defined as follows:

$$\hat{P}_{ph,k}^{vr} = \hat{P}_{ph,k}^{ref} \hat{V}_{k_{ph}}^{re}, \hat{P}_{ph,k}^{vi} = \hat{P}_{ph,k}^{ref} \hat{V}_{k_{ph}}^{im} \tag{5.86}$$

$$\hat{Q}_{ph,k}^{vr} = \hat{Q}_{ph,k}^{ref} \hat{V}_{k_{ph}}^{re}, \hat{Q}_{ph,k}^{vi} = \hat{Q}_{ph,k}^{ref} \hat{V}_{k_{ph}}^{im} \tag{5.87}$$

Linearization of the product of two bounded continuous variables is accomplished by piecewise linearization [104] and details can be found in Appendix B. The *integer part of this formulation* is a consequence of the piecewise approach employed for this linearization.

5.8.4.2. Load Node

The current balance at the load node can be written in the same way as (5.80) and (5.81). The difference is in the expression of the RHS which is the current injection term. The real and imaginary part of the current injection for the ZIP load bus, k, per phase, ph, is derived by linearizing (5.53) and (5.54) using (5.56):

$$\hat{I}_{ph,k}^{re} = \alpha_k^Z\left(P_{ph,k}^N \hat{V}_{ph,k}^{re} + Q_{ph,k}^N \hat{V}_{ph,k}^{im}\right) + \alpha_k^I\left[P_{ph,k}^N \tilde{g}_{3,ph}\left(\hat{V}_{k_{ph}}^{re}, \hat{V}_{k_{ph}}^{im}\right) + Q_{ph,k}^N \tilde{g}_{4,ph}\left(\hat{V}_{k_{ph}}^{re}, \hat{V}_{k_{ph}}^{im}\right)\right] + \alpha_k^P\left[P_{ph,k}^N \tilde{g}_{1,ph}\left(\hat{V}_{k_{ph}}^{re}, \hat{V}_{k_{ph}}^{im}\right) + Q_{ph,k}^N \tilde{g}_{2,ph}\left(\hat{V}_{k_{ph}}^{re}, \hat{V}_{k_{ph}}^{im}\right)\right] \tag{5.88}$$

$$\hat{I}_{ph,k}^{im} = \alpha_k^Z\left(P_{ph,k}^N \hat{V}_{ph,k}^{im} - Q_{ph,k}^N \hat{V}_{ph,k}^{re}\right) + \alpha_k^I\left[P_{ph,k}^N \tilde{g}_{4,ph}\left(\hat{V}_{k_{ph}}^{re}, \hat{V}_{k_{ph}}^{im}\right) - Q_{ph,k}^N \tilde{g}_{3,ph}\left(\hat{V}_{k_{ph}}^{re}, \hat{V}_{k_{ph}}^{im}\right)\right] + \alpha_k^P\left[P_{ph,k}^N \tilde{g}_{2,ph}\left(\hat{V}_{k_{ph}}^{re}, \hat{V}_{k_{ph}}^{im}\right) - Q_{ph,k}^N \tilde{g}_{1,ph}\left(\hat{V}_{k_{ph}}^{re}, \hat{V}_{k_{ph}}^{im}\right)\right] \tag{5.89}$$

Note that the ZIP coefficients, $P_{ph,k}^N$, and $Q_{ph,k}^N$ are known parameters.

5.8.4.3. PQ DG Node

This node has a similar current balance expression of (5.80) and (5.81) with modifications to the RHS. The current injection for the PQ DG node is written as follows similar to that of the load node with $\alpha_k^Z, \alpha_k^I = 0$ and $\alpha_k^P = 1$:

$$\hat{I}_{ph,k}^{re} = \hat{P}_{ph,k}^{N,dg}\,\hat{g}_{1,ph}\left(\hat{V}_{k_{ph}}^{re}, \hat{V}_{k_{ph}}^{im}\right) + \hat{Q}_{ph,k}^{N,dg}\,\hat{g}_{2,ph}\left(\hat{V}_{k_{ph}}^{re}, \hat{V}_{k_{ph}}^{im}\right) \tag{5.90}$$

$$I_{ph,k}^{im} = \hat{P}_{ph,k}^{N,dg}\,\hat{g}_{2,ph}\left(\hat{V}_{k_{ph}}^{re}, \hat{V}_{k_{ph}}^{im}\right) - \hat{Q}_{ph,k}^{N,dg}\,\hat{g}_{1,ph}\left(\hat{V}_{k_{ph}}^{re}, \hat{V}_{k_{ph}}^{im}\right) \tag{5.91}$$

In this case, $\hat{P}_{ph,k}^{N,dg}$ and $\hat{Q}_{ph,k}^{N,dg}$ is the power setpoints for the PQ DG and thus, a decision variable. Hence (5.90) and (5.91) presents the previously encountered challenge of linearizing the product of two bounded continuous variables.

5.8.5. System Model/Power Flow Constraints (DistFlow Approach)

The second power flow method, which was derived from DistFlow [64, 65], can be incorporated as an alternative as follows.

5.8.5.1. Kirchhoff's Voltage Law across each Branch

Given the set of branches, B, Kirchhoff's voltage law is applied to each branch (i, j) according to (5.66):

$$\widehat{U}_i - \widehat{U}_j = 2\left(\tilde{r}_{ij}.\hat{P}_{ij}^{BR} + \tilde{x}_{ij}.\hat{Q}_{ij}^{BR}\right) \tag{5.92}$$

5.8.5.2. Power Balance Constraint

The power balance constraints are written according to (5.67):

$$-A * \left[\hat{P}^{BR}\right] = \left[\hat{P}^{inj}\right], -A * \left[\hat{Q}^{BR}\right] = [\hat{Q}^{inj}] \tag{5.93}$$

5.8.5.3. Power Injection Constraints

The active and reactive power injection for the droop bus is equated to the reference active and reactive power variables as represented in (5.78) and (5.79). The power injection terms for the ZIP load bus per phase (can be modified for the PQ DG bus too) are represented by substituting (5.72) into equations (5.70) and (5.71):

$$\hat{P}_{ph,k} = P_{ph,k}^{N}[\alpha_k^Z \widehat{U}_{ph,k} + \alpha_k^I(0.5 + 0.5\widehat{U}_{ph,k}) + \alpha_k^P] \tag{5.94}$$

$$\hat{Q}_{ph,k} = Q_{ph,k}^{N}[\alpha_k^Z \widehat{U}_{ph,k} + \alpha_k^I(0.5 + 0.5\widehat{U}_{ph,k}) + \alpha_k^P] \tag{5.95}$$

For the PQ DG bus, $\alpha_k^Z, \alpha_k^I = 0$ and $\alpha_k^P = 1$, and equations (5.94) and (5.95) are modified as follows.

$$\hat{P}_{ph,k} = \hat{P}_{ph,k}^{N,dg} \tag{5.96}$$

$$\hat{Q}_{ph,k} = \hat{Q}_{ph,k}^{N,dg} \tag{5.97}$$

where $\hat{P}_{ph,k}^{N,dg}$ and $\hat{Q}_{ph,k}^{N,dg}$ are decision variables to be determined.

5.8.6. DG Limits and Power Balance Constraints

The active and reactive power limit constraints for each of the droop controlled DGs, $k \in G^{DG}$, can be written as,

$$P_k^{min} + P_k^{offset} \leq \sum\nolimits_{ph\in\{a,b,c\}} \hat{P}_{ph,k}^{ref} \leq P_k^{max} - P_k^{offset} \tag{5.98}$$

$$Q_k^{min} + Q_k^{offset} \leq \sum\nolimits_{ph\in\{a,b,c\}} \hat{Q}_{ph,k}^{ref} \leq Q_k^{max} - Q_k^{offset} \tag{5.99}$$

where P_k^{offset} and Q_k^{offset} are fractions of the power limits P_k^{max} and Q_k^{max} respectively. Both are used to offset and shrink the power limit such that reference dispatch power for each droop-controlled DG does not hit the limit and makes allowance for power-sharing when the load demand deviates from its value at the dispatch moment. For the PQ DG, (5.98) and (5.99) are modified to the following equation where the summation only considers the present phase(s),

$$P_k^{min} \leq \sum\nolimits_{ph\in\{a,b,c\}} \hat{P}_{ph,k}^{N,dg} \leq P_k^{max} \tag{5.100}$$

$$Q_k^{min} \leq \sum\nolimits_{ph\in\{a,b,c\}} \hat{Q}_{ph,k}^{N,dg} \leq Q_k^{max} \tag{5.101}$$

Since the droop-controlled DGs are three-phase controlled, it is desired that the output power is balanced,

$$\hat{P}_{a,k}^{ref} = \hat{P}_{b,k}^{ref} = \hat{P}_{c,k}^{ref}, \hat{Q}_{a,k}^{ref} = \hat{Q}_{b,k}^{ref} = \hat{Q}_{c,k}^{ref} \tag{5.102}$$

To ensure that (5.102) is properly enforced while maintaining an acceptable voltage profile and balance across the system, the following complementary constraint is included to limit the nominal system load unbalance index (NSLUI). To constrain the NSLUI to be less than or equal a given percentage, say ρ%, (5.75) is rewritten in the following linear inequality form for each phase, ph.

$$\hat{P}_{avg,T}^{N} = \frac{1}{3}\sum\nolimits_{ph\in\{a,b,c\}} \hat{P}_{ph,T}^{N} \tag{5.103}$$

$$\frac{\rho}{100}\hat{P}_{avg,T}^{N} \leq \hat{P}_{ph,T}^{N} - \hat{P}_{avg,T}^{N} \leq \frac{-\rho}{100}\hat{P}_{avg,T}^{N} \tag{5.104}$$

A similar equation can be written for reactive power NSLUI.

5.8.7. Voltage Limit Constraints

The voltage limit constraint for each node can be expressed as follows.

$$V^{min} \leq \sqrt{\hat{V}_{k_{ph}}^{re\ 2} + \hat{V}_{k_{ph}}^{im\ 2}} \leq V^{max}, \rightarrow V^{min} \leq \tilde{g}_{5,ph}\left(\hat{V}_{k_{ph}}^{re}, \hat{V}_{k_{ph}}^{im}\right) \leq V^{max} \tag{5.105}$$

where $\tilde{g}_{5,ph}\left(\hat{V}_{k_{ph}}^{re}, \hat{V}_{k_{ph}}^{im}\right)$ is the linearization of the non-linear square root function of (5.105) and is linearized around a compact set of an expected operating region similar to how (5.55) was linearized. When the system model constraint is incorporated using the method derived from DistFlow, the constraint is updated as follows,

$$V^{min^2} \leq \hat{U}_{ph,k} \leq V^{max^2} \tag{5.106}$$

To limit voltage unbalance at the droop (or voltage source) bus, to say within a difference of μ per unit between the phases, the following constraint is incorporated for each droop bus.

$$-\mu \leq \tilde{g}_{5,ph_1}\left(\hat{V}_{k_{ph}}^{re}, \hat{V}_{k_{ph}}^{im}\right) - \tilde{g}_{5,ph_2}\left(\hat{V}_{k_{ph}}^{re}, \hat{V}_{k_{ph}}^{im}\right) \leq \mu \tag{5.107}$$

where $ph_1, ph_2 \in \{a, b, c\}, ph_1 \neq ph_2$.

5.8.8. Post-Optimization Processing

Based on the power-sharing paradigm adopted, we can determine the required frequency droop selection ratio for all the droop DGs. One simple power-sharing paradigm selects the droop coefficients in the inverse proportion of their optimized reference active power as derived in section 5.4.2.2. This ensures that changes in system loading are shared in the proportion of the reference active power calculated by the optimization algorithm. That is for each droop DG, i, the $n_{f,i}$ is selected as follows,

$$\hat{n}_{f,i} P_{ph,i}^{ref} = constant \tag{5.108}$$

Also, the minimum frequency deviation rate in Hz per unit power, Δf_{dev}^{min}, can be constrained by considering the expression in the denominator of (5.60) as follows.

$$\left(\sum_{k \in N} \sum\nolimits_{ph \in \{a,b,c\}} \frac{1}{\hat{n}_{f,k}}\right)^{-1} = \left(3 \sum_{k \in N} \frac{1}{\hat{n}_{f,k}}\right)^{-1} \leq \Delta f_{dev}^{min} \tag{5.109}$$

Equations (5.108) and (5.109) can guide in heuristically choosing the frequency droop coefficients. For the voltage droop coefficient, the same value is assumed for all the droop DGs.

5.8.9. Optimal Power Flow Example Case

The two proposed methods were used to solve the optimal power flow of a microgrid built from the modified IEEE 13-node test system. The one-line diagram of the modified system is shown in Figure 5.5. The capacitor and load profiles are shown in

Table 5.6. The DG parameters are shown in Table 5.7.

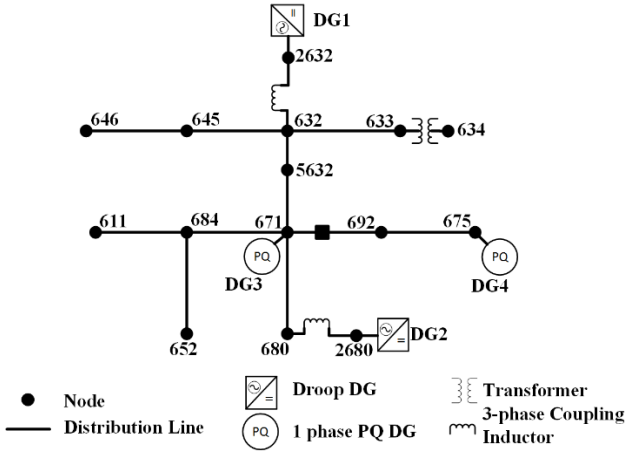

Figure 5.5 One Line Diagram of Autonomous Microgrid built from the Modified IEEE 13-Node Test Feeder

The droop DG outputs were constrained with an offset of 5% of the acceptable power range. The offset was to enable power-sharing when the load profile gradually changes. The voltage was constrained within 0.99 to 1.1 PU. The NSLUI for the active and reactive power loading was constrained to less than or equal to 0.5% by dispatching the balancing power from the PQ DGs.

Table 5.6 Load and Capacitor Parameters for Modified 13-Node Test Feeder

Node	Type	P^N(A/B/C) kW	Q^N(A/B/C) kVAr	$\alpha^Z/\alpha^I/\alpha^P$
634	Y-ZIP	83/60/60	55/45/45	0.4/0.3/0.3
645	Y-ZIP	0/82/0	0/62.5/0	0.4/0.3/0.3
646	Δ-ZIP	0/115/0	0/66/0	0.4/0.3/0.3
652	Y-ZIP	64/0/0	43/0/0	0.4/0.3/0.3
671	Δ-ZIP	192.5/192.5/192.5	110/110/110	0.4/0.3/0.3
5632	Y-ZIP	5.67/22/39	3.34/12.67/22.65	0.4/0.3/0.3
671	Y-ZIP	2.84/11/19.5	1.67/6.34/11.35	0.4/0.3/0.3
675	Y-ZIP	242.5/34/145	95/30/106	0.4/0.3/0.3
692	Δ-ZIP	0/0/85	0/0/75.5	0.4/0.3/0.3
611	Y-ZIP	0/0/85	0/0/40	0.4/0.3/0.3
675	Y-CAP	0/0/0	-100/-100/-50	1/0/0
611	Y-CAP	0/0/0	0/0/-50	1/0/0
$\%NSLUI$		17.24	33.57	

Table 5.7 DG Parameters for Modified 13-Node Test Feeder

Node	Type	Phase	P^{min}/P^{max} kW	Q^{min}/Q^{max} kVAr	Per Phase coupling X (PU)	$\alpha_k/\beta_k/\gamma_k$
680	Droop	ABC	900/0	400/-100	0.7	2/2/10
632	Droop	ABC	900/0	400/-100	0.35	1/1/5
671	PQ	C	300/0	200/-50	NA	1/1/5
675	PQ	A	300/0	200/-50	NA	2/2/10

The optimization results are summarized for both the MIQP and QP approach in

Table 5.8 to Table 5.10. The reverse calculation of the power flow using the resulting control parameters shows that the frequency was regulated to 60 Hz for both methods.

Table 5.8 Droop Setting from Optimization Result

	Node	Type	V_{ref} PU	3-phase P_{ref} (kW)	3-phase Q_{ref} (kVAr)	n_f/n_v
MIQP (CIM)	680	Droop	1.0611	525.4	314.3	0.1839/0.12
	632	Droop	1.0351	855	375	0.113/0.12
QP (LF)	680	Droop	1.0288	577.3	120.5	0.1737/0.12
	632	Droop	1.0442	855	375	0.1173/0.12

Table 5.9 PQ DG Setpoint from Optimization Result

	Node	Type	Phase	P_{set} (kW)	Q_{set} (kVAr)
MIQP (CIM)	671	PQ	C	168.8	149.6
	675	PQ	A	137.2	104.5
QP (LF)	671	PQ	C	163.1	148.3
	675	PQ	A	131.3	104.1

Table 5.10 Optimization Summary

	Obj Value	Solution Time (sec)	$\%NSLUI_P$	$\%NSLUI_Q$
MIQP (CIM)	15.095	41.2057	0.5	0.5
QP (LF)	15.728	1.2357	0.31	0.07

5.9. Section Conclusion

In this section, we presented two new linear power flow (LPF) methods for droop-controlled autonomous microgrids: LPF based on the current injection method (CIM) and LPF based on the line flow method (LFM). The two methods were verified through

detailed time-domain simulation in PSCAD at steady-state and used to solve the power flow of sample microgrids. The proposed linear power flow formulations were expanded to formulate optimal power flow methods to minimize cost while maintaining a given load phase balancing, and restoring frequency and voltage to their reference values.

In section 6, the black start restoration for multi-master droop-controlled microgrids is formulated. The power flow constraints of this formulation are based on LPF by CIM that was presented in this section.

6. BLACK START RESTORATION IN AUTONOUMOUS MULTI-MASTER MICROGRIDS

6.1. Introduction

In section 4.5, we presented black start restoration formulation for isochronous microgrids in which for each formed microgrid, one DG is operated in isochronous mode (grid-forming mode) and other DGs in the same microgrid are operated in grid-following mode. Given a system with more than one isochronous DG, this led to the restoration of multiple microgrids to keep the isochronous mode DGs isolated from each other.

To restore a larger microgrid, there should be a control that enables reference forming DGs to cooperate together to form the grid. In the literature, droop-control is the most common method to ensure interoperability of multiple master (that is multiple reference forming) DGs [61, 62, 98, 99]. Given that the droop control enables real-time power sharing, it is considered the primary control [11].

Because of changing system operating points as loads are restored during a black start, it is necessary to occasionally re-set the primary control to ensure that the system is operating within the desired region and that power is being shared rightly. This resetting of the primary control is done by sending updated control parameter settings (like droop, load and PQ DG settings) to the elements in the system. These updated settings are sent from the secondary and tertiary control layers which are housed in the microgrid central controllers (MGCC) [11]. The MGCC, as an essential aspect of a microgrid, is expected

to balance generation and load, coordinate load shedding when necessary, and regulate voltage and frequency [2].

In this section, the formulation of the sequential restoration approach for multi-master microgrids is presented. The multi-master microgrids considered are assumed to be operating in droop-control mode. To the best of the author's knowledge, this is the first black start formulation for microgrid restoration considering droop-controlled inverter based DGs.

6.2. Description of System To be Restored

The system is assumed to be an advanced distribution network (ADN) disconnected from the main grid with remote controllable switches (RCSs), conventional droop-controlled inverter based DGs (grid-supporting DGs), dispatchable PQ inverter based DGs (grid-feeding DGs), non-dispatchable PQ DGs, controllable (demand response) loads and/or switchable/non-switchable aggregated loads. Before the islanded microgrid is restored, we assume that an unforeseen emergency situation leads the system to be in a blackout state and thus, all resources in the system are de-energized to OFF state. In this completely de-energized state, the system would need to be black-started.

An abstraction of the islanded distribution microgrid is shown in Figure 6.1.

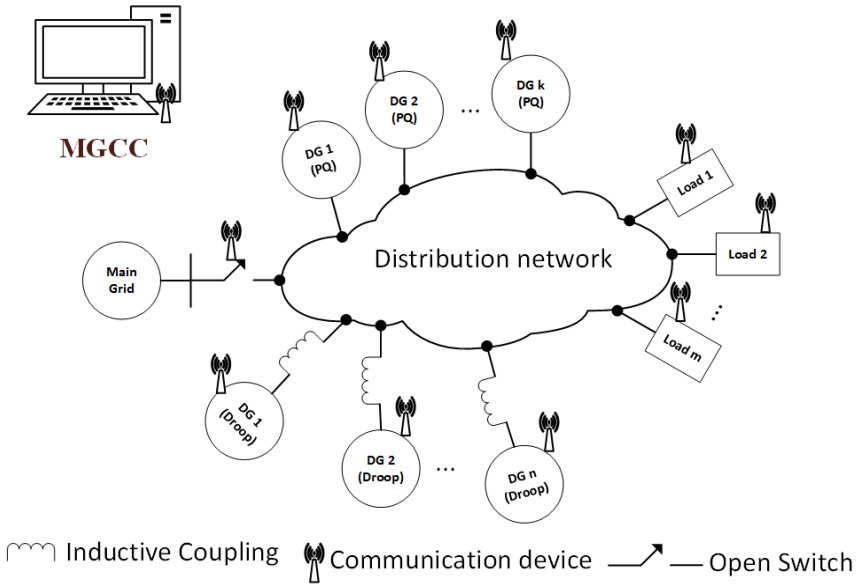

Figure 6.1 Islanded Microgrid Representation with Loads, Droop Controlled DGs, and PQ DGs

Figure 6.1 shows the key elements in the system to be restored. These elements include three-phase droop-controlled DGs, dispatchable and non-dispatchable PQ DGs, and loads. The distribution network is assumed to be equipped with remote controllable switches (RCS) which help in the sequential reconfiguration of the system for black start restoration.

A two-way communication network is assumed to exist between the MGCC and the various elements in the system to facilitate status probing and setpoint corrections by the MGCC. To decouple the active and reactive power control, each of the droop-controlled DGs is coupled to the microgrid through an inductor. The higher-level control (secondary and tertiary levels) are assumed to be executed by the MGCC which sends set points for the DGs via a communication network.

6.3. Formulation of the Restoration Method for Multi-Master Microgrids

In this subsection, we introduce the formulation of the restoration method. The symbols and parameters used in this formulation are summarized in Table 6.1; decision variables are denoted with a hat. This subsection starts by introducing the objective function followed by all the constraint equations. The constraint equations are broadly categorized as initial sequencing constraints, connectivity constraints, synchronization enhancing constraints, power flow constraints, DG and system operation constraints, and lastly, topology and sequencing constraints. The objective function, constraint equations and computation engine are expected to be stored and executed in the MGCC.

Table 6.1 Symbols and Parameters of the Proposed Restoration Formulation

Sets	
$n(A)$	The number of elements in set A
B, B^S, B^F, C	Set of branches, switchable and damaged branches, set of switchable branches between bus blocks
$G, G^{BS}, G^{Dr}, G^F, G^{PQ}$	Set of all DERs, subset of black start DGs, subset of droop-controlled DGs, subset of damaged DGs, subset of PQ DGs
L, L^S, L^C, L^F	Set of loads, subset of switchable loads, subset of controllable load (with demand response) and subset of damaged load
T	Set of time steps $\{1,2, \dots, N_T\}$ and $n(T) = N_T$
N_p, N, K	Set of phase nodes, nodes, bus blocks, $n(N_p) \geq n(N) \geq n(K)$
Binary Decision Variables (1 – Energized, 0 – Not Energized)	
$\hat{x}^N_{i,t}, \hat{x}^K_{j,t}$	Energization status of node i at time step t, energization status of bus block j at time step t
$\hat{x}^G_{g,t}$	Energization status of DG g at time step t
$\hat{x}^{BR}_{ij,t}, \hat{x}^K_{ij,t}$	Energization status of line (i,j) at time step, t, where $(i,j) \in B, C$ respectively
$\hat{x}^L_{l,t}$	Energization status of load l at time step t

Table 6.1 Continued

Continuous Decision Variables	
$a, b, or\ c$	Used as subscript or superscript to denote variable or parameter in phase a, b or c respectively
$\hat{P}^{dg}_{ph,k,t}, \hat{Q}^{dg}_{ph,k,t}$	Active and reactive power output of PQ DG k at step t and phase $ph \in \{a, b, c\}$
$\hat{V}^{re}_{n,t}, \hat{V}^{im}_{n,t}$	Real and imaginary part of three-phase nodal voltage vector of node n at step t
$\hat{V}^{re,ph}_{n,t}, \hat{V}^{im,ph}_{n,t}$	Real and imaginary part of nodal voltage of node n at step t and phase ph
$n_{v,g,t}$	Voltage droop co-efficient of DG g, $g \in G^{Dr}$ at step t
$n_{f,g,t}$	Frequency droop co-efficient of DG g, $g \in G^{Dr}$ at step t
$\hat{P}^{ref}_{ph,k,t}, \hat{Q}^{ref}_{ph,k,t}$	Droop reference active and reactive power output of DG k at step t, $k \in G^{Dr}$
$\hat{P}_{ph,l,t}, \hat{Q}_{ph,l,t}$	Nominal active and reactive power demand of load l, phase ph, at time step t
Parameters	
M	A large number chosen deliberately to manipulate the constraint equations
Δt	time interval between restoration steps and is assumed to be a constant value for all intervals
$P^{G,ramp}_{g}, Q^{G,ramp}_{g}$	Maximum absolute value of differential active and reactive power output of DG g for each time step (DG ramp rate)
P^{min}_{g}, P^{max}_{g}	Minimum and maximum active power output of DG g
Q^{min}_{g}, Q^{max}_{g}	Minimum and maximum reactive power output of DG g
$P_{ph,l,t}, Q_{ph,l,t}$	Nominal active and reactive power value of load l, phase ph, at time step t (fixed to the same value for all time steps and is independent of whether the load has been restored or not)
$z_{i,j} = r_{i,j} + jx_{i,j}$	Impedance of line between nodes i and j, and $y_{i,j} = \frac{1}{z_{i,j}} = g_{i,j} + jb_{i,j}$
$y^{sh}_{i,j} = g^{sh}_{i,j} + jb^{sh}_{i,j}$	Shunt admittance between nodes i and j
$P^{fc}_{ph,k,t}, Q^{fc}_{ph,k,t}$	Active and reactive power output from forecast of non-dispatchable PQ DG k at step t and phase ph

6.3.1. Objective Function

The objective function is to maximize the energy restored in the time horizon under consideration while maintaining system operational constraints.

$$min - \sum_{t \in T} \sum_{l \in L} \sum_{ph \in \{a,b,c\}} \hat{P}_{ph,l,t}.\Delta t \tag{6.1}$$

Where $\hat{P}_{ph,l,t} = \hat{x}^{L}_{l,t} P_{ph,l,t}$. As defined in the symbols and parameters table, Table 6.1, $\hat{x}^{L}_{l,t}$ is a binary variable which represents the energization status of the load l at time step t, and $P_{ph,l,t}$ is the nominal value of load l at time step t for phase ph, Δt is the time interval between steps and is assumed to be a constant value for all intervals. For demand response loads, $\hat{P}_{ph,l,t}$ is defined differently to vary over a range as follows: $x^{L}_{g,t} P^{min}_{l} \leq \hat{P}_{ph,l,t} \leq x^{L}_{g,t} P^{max}_{l}$, where P^{min}_{l}/P^{max}_{l} is the minimum/maximum of the range that the demand response load is allowed to vary.

The objective function of (6.1) is subject to the following operating constraints: initial sequencing constraints (equations (6.2) to (6.4)), connectivity constraints (equations (6.5) to (6.12)), synchronization enhancing constraints (equations (6.17) to (6.24)), power flow constraints (equations (6.32), (6.33), (6.39), (6.40), (6.43) to (6.48)), DG and system operation constraints (equations (6.49) to (6.70)), and topology and sequencing constraints (equations (6.71) to (6.75)).

6.3.2. Initial Sequencing Constraints

The sequencing constraints ensure that the system builds up in the desired way. In section 3.2.2, under the MMO black start example, we considered the method to restoring the system sequentially, by identifying a build-up or start-up node.

One node is selected as the build-up node by the dynamic optimization algorithm. These initial start-up conditions are expressed in equations (6.2)-(6.4) below.

$$\sum\nolimits_{g \in \{G^{Dr} n G^{BS}\}} \hat{x}^{G}_{g,t} = 1, \sum\nolimits_{g \in \{G \setminus (G^{Dr} n G^{BS})\}} \hat{x}^{G}_{g,t} = 0, t = 1 \tag{6.2}$$

$$\hat{x}^{BR}_{ij,t} = 0, (i,j) \in B^{S} \setminus B^{F}, t = 1 \tag{6.3}$$

$$\hat{x}_{ij,t}^{BR} = 0, \hat{x}_{g,t}^{G} = 0, \hat{x}_{l,t}^{L} = 0, (i,j) \in B^F, g \in G^F, l \in L^F, t \in T \quad (6.4)$$

The first sum in equation (6.2) ensures that one black start droop-controlled DG is started at time step 1 at the build-up node and the second sum ensures that all other DGs are not connected. Recall that $x_{g,t}^{G}$ is the energization status of DG g at time step t, G^{Dr} and G^{BS} are the set of all droop-controlled DGs and black start DGs, respectively, and G is the set of all DGs.

Equation (6.3) ensures that all switchable lines are turned off at time step 1. $x_{ij,t}^{BR}$ is a binary variable that represents the energization status of the branch $(i,j) \in B^S \backslash B^F$, where B^S is the set of all switchable branches, and B^F is the set of all failed branches.

Equation (6.4) ensures that the status of all damaged resources are de-energized by setting them to 0 for all time steps. As reiterated above $x_{ij,t}^{BR}$ and $x_{g,t}^{G}$ represent energization status of the branches and DGs, respectively. $x_{l,t}^{L}$ is a binary variable that represents the status of the load l. B^F, G^F, and L^F represent sets of failed branches, failed DGs, and failed loads, respectively.

6.3.3. Connectivity Constraints

Connectivity constraints help to ensure acceptable interconnection between elements in the system. The concepts of these connectivity constraints were adapted from Chen's work in [29, 30] to suit the multi-master microgrid architecture. In general, we consider the following interconnection acceptable for each step of the restoration:

1. Whenever a DG is energized, then that DG node must have been energized in the same or previous time step as the DG energization time step
2. Once any DG, branch or load is energized, it cannot be de-energized

3. Both nodes of an energized branch must be energized

4. A load can only be energized once its node is energized

These interconnection requirements are enforced according to the constraint equations below:

$$\hat{x}_{g,t}^{G} \leq \hat{x}_{g,t}^{N}, g \in \mathrm{G}, t \in T \tag{6.5}$$

$$\hat{x}_{g,t}^{G} - \hat{x}_{g,t-1}^{G} \geq 0, g \in G, t \in T \tag{6.6}$$

$$\hat{x}_{ij,t}^{BR} \leq \hat{x}_{i,t}^{N}, \hat{x}_{ij,t}^{BR} \leq \hat{x}_{j,t}^{N}, (i,j) \in B^{S} \backslash B^{F}, t \in T\ , i,j\ \in N \tag{6.7}$$

$$\hat{x}_{ij,t}^{BR} = \hat{x}_{i,t}^{N}, \hat{x}_{ij,t}^{BR} = \hat{x}_{j,t}^{N}, (i,j) \in B \backslash B^{S} \backslash B^{F}, t \in T\ , i,j\ \in N \tag{6.8}$$

$$\hat{x}_{ij,t}^{BR} - \hat{x}_{ij,t-1}^{BR} \geq 0, (i,j) \in B^{S} \backslash B^{F}, t \in T\ , i,j\ \in N \tag{6.9}$$

$$\hat{x}_{n,t}^{L} \leq \hat{x}_{n,t}^{N}, n \in L^{S} \backslash L^{F}, t \in T \tag{6.10}$$

$$\hat{x}_{n,t}^{L} = \hat{x}_{n,t}^{N}, n \in L \backslash L^{S} \backslash L^{F}, t \in T \tag{6.11}$$

$$\hat{x}_{n,t}^{L} - \hat{x}_{n,t-1}^{L} \geq 0, n \in L^{S} \backslash L^{F}, t \in T \tag{6.12}$$

The less than or equal to sign in equation (6.5) ensures that the network builds up such that a DG can only be turned on and synchronized to an energized node. Recall $\hat{x}_{g,t}^{G}$ and $\hat{x}_{g,t}^{N}$ are the DG and node energization status, respectively.

Equation (6.6) ensures that a DG stays on after it is turned on. This is enforced by ensuring that the difference of each DG's energization status between current and previous time step is greater than or equal to zero.

Equation (6.7) ensures that once a switchable line is energized then its two nodes must be energized too. This is enforced by the ≤ sign. Recall that $\hat{x}_{ij,t}^{BR}$ and $\hat{x}_{i,t}^{N}$ represents the status of the branch and node respectively.

Equation (6.8) ensures that the status of a non-switchable line and its nodes are equal and that they all get energized together. This is enforced by the $=$ sign.

Equation (6.9) ensures that an energized line cannot be turned off. This is enforced by ensuring that the difference of each branch's energization status between current and previous time step is greater than or equal to zero.

Equation (6.10) ensures that a switchable load can only be turned on when its node is energized. (6.11) ensures that non-switchable loads are automatically turned on when its node is energized. Equation (6.12) ensures that a switchable load remains energized after it has been turned on. Recall that $\hat{x}_{n,t}^{L}$ represents the energization status of load $n \in L$.

6.3.4. Synchronization Enhancing Constraints

Connecting a grid-supporting DG to an already operating islanded microgrid is a complex interplay of all the controllers in the system and because of the low inertia of the system, this can easily lead the system to instability. Detailed analysis of all the controllers' interaction and their stability analysis is beyond the scope of this dissertation.

Based on the islanded microgrid simulation studies we conducted, we made reasonable observations on system conditions that enhance smooth synchronization of grid-supporting DGs for stable connection to an already operating islanded microgrid. We describe these conditions by looking at the DG synchronization to microgrid and analyzing the droop equations. The droop-controlled DG synchronization is more critical than those of PQ DG because unlike PQ DGs, droop-controlled DGs contribute to forming voltage

reference and respond by varying their frequency and voltage to changes in system operation point [61, 62, 98, 99].

Synchronizing the droop DGs to the islanded microgrid is done using a similar synchronization philosophy as those of the bulk power system, that is, match frequency, voltage magnitude and close the breaker as close to zero angle difference as possible [105, 106]. The block diagram of the synchronization control implemented for matching the frequency, voltage magnitude and phase for the three-phase droop-controlled DGs is shown in Figure 6.2. This synchronization controller was implemented for each droop-controlled DG in the time domain simulation of the restoration solution of section 7.4.6.

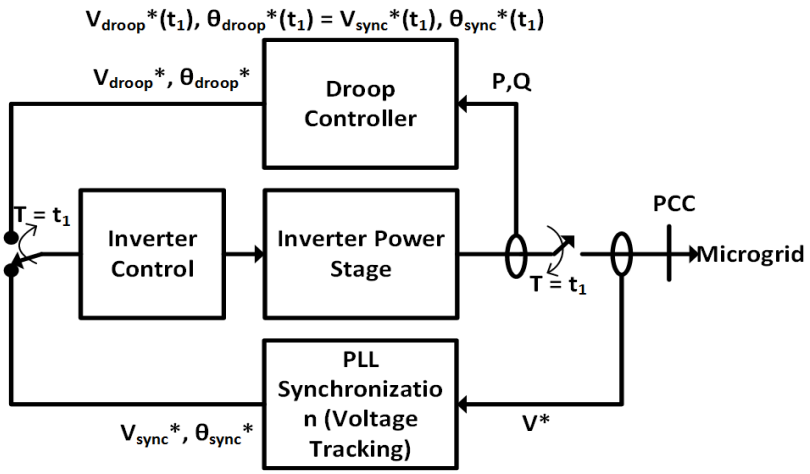

Figure 6.2. Block diagram of Droop DG Synchronization implemented in PSCAD for time domain simulation

Figure 6.2 has four blocks: the PLL synchronization, the droop controller, inverter control, and the inverter power stage blocks. The PLL synchronization block tracks the voltage at the point of common connection (PCC) and sends this voltage (denoted

$V_{sync}^{*}, \theta_{sync}^{*}$) to the inverter control block which will use it as input signal to control the inverter power stage block. In Figure 6.2, prior to the closing the breaker at time $T = t_1$, the frequency, voltage magnitude and phase at the point of common connection (PCC) to the microgrid is tracked by the PLL block and fed into the inverter control block. The inverter control block will then control the inverter power stage to match its terminal voltage with the voltage of the PCC. At $T = t_1$, the inverter is connected to the PCC and simultaneously the inverter control block is switched over to the droop control block. The droop control block takes as input the inverter's active and reactive power output (denoted P, Q) to output reference control voltage for the inverter control block. A look at the droop equations at the time of inverter connection to microgrid can offer insight to what droop settings enhance smoother and more stable synchronization for a low inertia system.

Consider the droop equations of the i^{th} droop-controlled inverter-based DG for a hypothetical three-phase balanced distribution system in per phase equivalent equations as follows:

$$f_i = f^{ref} - n_{f,i}(P_i - P_i^{ref}) \tag{6.13}$$

$$|\bar{V}_i| = |\bar{V}_i|^{ref} - n_{v,i}(Q_i - Q_i^{ref}) \tag{6.14}$$

where f^{ref} is the reference frequency in Hz assumed to be equal and set to the nominal value for all droop inverters; P_i^{ref} is the reference power in per unit; P_i is the active power output in per unit; $n_{f,i}$ is the frequency droop coefficient in Hz per unit power; $|\bar{V}_i|^{ref}$ is the reference voltage in per unit; Q_i^{ref} is the reference output reactive power in per unit;

$|\bar{V}_i|$ and f_i are the output per unit RMS voltage and output frequency in Hz; and $n_{v,i}$ is the voltage droop coefficient in per unit power.

Consider equation (6.13). At the point of synchronizing this arbitrary i^{th} inverter to the microgrid, the droop frequency of this inverter will decide to a larger extent the angle stability of the synchronizing inverter since frequency is the time rate of change of angle, $\frac{d\theta_i(t)}{dt}$. Assuming that the angle of the microgrid is θ_{sys} and its frequency is f^{ref} (nominal frequency), then we express the rate of change of angle difference as follows,

$$\frac{d\theta_i(t)}{dt} - \frac{d\theta_{sys}(t)}{dt} = f_i - f^{ref} = -n_{f,i}(P_i - P_i^{ref}) \tag{6.15}$$

Therefore, the angle difference for $t \geq t_1$ can be expressed as follows:

$$\begin{aligned} \theta_{diff}(t) &= \theta_i(t) - \theta_{sys}(t) \\ &= \int_{t_1}^{t} -n_{f,i}\left(P_i - P_i^{ref}\right)dt + \theta_i(t_1) - \theta_{sys}(t_1) \end{aligned} \tag{6.16}$$

If the PLL block tracks the PCC voltage accurately prior to inverter connection to microgrid, then $\theta_i(t_1) - \theta_{sys}(t_1) = 0$. This means that the dynamics of $\theta_{diff}(t)$ is mostly dependent on $P_i - P_i^{ref}$ where P_i^{ref} is reference power setting of the droop controller.

At $t = t_1$, which is when the connection is made, assuming accurate voltage tracking between inverter terminal and PCC, then the inverter output active power, P_i, will be approximately equal to 0. Thus setting P_i^{ref} to 0 can help minimize angle transients. This is a zero-dispatch synchronizing condition. Since this is a multi-time step restoration methodology, in the next time step following this zero-dispatch synchronization, the droop settings of the synchronized DG can be changed to have non-zero reference active power.

A similar argument can be made for the voltage droop equation of (6.14). Assuming accurate voltage tracking between inverter terminal and PCC, then the inverter output reactive power, Q_i, will be approximately equal to 0. Thus setting Q_i^{ref} to 0 and $|\bar{V}_i|^{ref}$ to the PCC voltage can help ensure voltage stability for the inverter during the synchronizing time step.

From the above analysis, we can minimize system disturbance and enhance stability during synchronization and connection of grid-supporting DGs by employing this zero-dispatch synchronizing condition according to the following constraints:

1. At most one droop-controlled DG can be newly connected to the system per time step (equation (6.17))
2. 'Freeze' the status/settings of every other element at any time step that a droop-controlled DG is synchronized to the system. This means that,
    a. No additional load is restored at a synchronization time step (equation (6.18))
    b. The status and dispatch settings of PQ DGs should remain the same as the previous time step just before the synchronization step (equations (6.19)-(6.21))
    c. The active and reactive power reference settings of all droop DGs should remain the same as the previous time step just before the synchronization step and the DG that is about to be synchronized to the system should do at zero power reference settings (equations (6.22) & (6.23)). Equations (6.22) & (6.23) also ensure that the synchronized

DG is connected with a zero reference power since its reference power at the previous step would be set to zero according to the DG operation constraints.

d. The status of all branches should remain the same as the previous time step just before the synchronization step except for one branch that can connects the synchronizing DG to the system, that is, only the branch that connects the DG to the system is allowed to change from "OFF" to "ON" (equation (6.24)) if it was not already energized.

$$\sum_{g\in\{G^{Dr}\}} \hat{x}^{G}_{g,t+1} - \sum_{g\in\{G^{Dr}\}} \hat{x}^{G}_{g,t} \leq 1, t \in T \tag{6.17}$$

$$\hat{x}^{L}_{n,t+1} - \hat{x}^{L}_{n,t} \leq M\left(1 - \sum_{g\in\{G^{Dr}\}} \left(\hat{x}^{G}_{g,t+1} - \hat{x}^{G}_{g,t}\right)\right), n \in L, t \in T \tag{6.18}$$

$$\hat{x}^{G}_{g,t+1} - \hat{x}^{G}_{g,t} \leq M\left(1 - \sum_{g\in\{G^{Dr}\}} \left(\hat{x}^{G}_{g,t+1} - \hat{x}^{G}_{g,t}\right)\right), g \in G^{PQ}, t \in T \tag{6.19}$$

$$\begin{aligned} -M\left(1 - \sum_{g\in\{G^{Dr}\}} \left(\hat{x}^{G}_{g,t+1} - \hat{x}^{G}_{g,t}\right)\right) &\leq \hat{P}^{dg}_{ph,k,t+1} - \hat{P}^{dg}_{ph,k,t} \\ &\leq M\left(1 - \sum_{g\in\{G^{Dr}\}} \left(\hat{x}^{G}_{g,t+1} - \hat{x}^{G}_{g,t}\right)\right), k \in G^{PQ}, t \in T \end{aligned} \tag{6.20}$$

$$\begin{aligned} -M\left(1 - \sum_{g\in\{G^{Dr}\}} \left(\hat{x}^{G}_{g,t+1} - \hat{x}^{G}_{g,t}\right)\right) &\leq \hat{Q}^{dg}_{ph,k,t+1} - \hat{Q}^{dg}_{ph,k,t} \\ &\leq M\left(1 - \sum_{g\in\{G^{Dr}\}} \left(\hat{x}^{G}_{g,t+1} - \hat{x}^{G}_{g,t}\right)\right), k \in G^{PQ}, t \in T \end{aligned} \tag{6.21}$$

$$-M\left(1-\sum_{g\in\{G^{Dr}\}}\left(\hat{x}_{g,t+1}^{G}-\hat{x}_{g,t}^{G}\right)\right)\leq \hat{P}_{ph,k,t+1}^{ref}-\hat{P}_{ph,k,t}^{ref} \leq M\left(1-\sum_{g\in\{G^{Dr}\}}\left(\hat{x}_{g,t+1}^{G}-\hat{x}_{g,t}^{G}\right)\right), k\in G^{Dr}, t\in T \quad (6.22)$$

$$-M\left(1-\sum_{g\in\{G^{Dr}\}}\left(\hat{x}_{g,t+1}^{G}-\hat{x}_{g,t}^{G}\right)\right)\leq \hat{Q}_{ph,k,t+1}^{ref}-\hat{Q}_{ph,k,t}^{ref} \leq M\left(1-\sum_{g\in\{G^{Dr}\}}\left(\hat{x}_{g,t+1}^{G}-\hat{x}_{g,t}^{G}\right)\right), k\in G^{Dr}, t\in T \quad (6.23)$$

$$\sum_{(i,j)\in B}\hat{x}_{ij,t+1}^{BR}-\sum_{(i,j)\in B}\hat{x}_{ij,t}^{BR}\leq 1+M\left(1-\sum_{g\in\{G^{Dr}\}}\left(\hat{x}_{g,t+1}^{G}-\hat{x}_{g,t}^{G}\right)\right), t\in T \quad (6.24)$$

The difference in the sum of droop DG status between any two adjacent time steps in equation (6.17) ensures that no more than one droop-controlled DG is synchronized to the system per time step. Recall that $\hat{x}_{g,t}^{G}$ represents the status of DG g at time step t and G^{Dr} is the set of all droop-controlled DGs.

Equation (6.18) ensures that no additional load is energized at each synchronization step by using the large number M. For every time step in which a droop-controlled DG is synchronized to the microgrid, the summation term in (6.18) will be equal to 1 and thus rendering the right hand side to zero; this will prevent the status of each load from changing in the synchronization step. Recall that $\hat{x}_{n,t}^{L}$ is the status of load n at time step t.

Just like in (6.18), equations (6.19)-(6.21) uses the large number M to ensure that the status and dispatch settings of PQ DGs remain as they were in the previous step for

every synchronization step. G^{PQ} is the set of all PQ DGs, $\hat{P}^{dg}_{ph,k,t}$ and $\hat{Q}^{dg}_{ph,k,t}$ are the active and reactive power dispatch settings for DG $k \in G^{PQ}$ at phase ph and time step t.

Equations (6.22) & (6.23) also use the large number M to ensure that droop reference active and reactive power settings during a synchronization time is the same as the previous step. $\hat{P}^{ref}_{ph,k,t}$ and $\hat{Q}^{ref}_{ph,k,t}$ are the active and reactive power droop reference settings for DG $k \in G^{Dr}$ at phase ph and time step t.

Lastly, equation (6.24) uses the large number M to ensure that at most only one branch is energized at a synchronization step. Recall that $\hat{x}^{BR}_{ij,t}$ represents the status of branch $(i,j) \in B$ at time step t.

6.3.5. Power Flow Constraints

The power flow constraints for a microgrid with droop-controlled inverters are a bit tricky to derive. First, there is no bus to approximate as a slack bus. The frequency has to be considered in the power flow since for such a small grid there is likely to be a significant deviation in frequency as the loads change. Also, there are additional nodes at the droop-controlled DGs' nodes before the inductor coupling which have to be considered in the power flow formulation. Detailed derivation of the droop-controlled linear power flow can be found in section 5.5 of this dissertation. In this subsection, we adapt the linear power flow derivation using current injection approach of section 5.5 for a multi-time step restoration with switchable and non-switchable branches.

6.3.5.1. KCL at Each Node

For balanced three-phase systems, the power flow is usually represented in terms of balanced single-phase per unit equivalence as in [97]:

$$\bar{Y}\bar{V} = \bar{I} \tag{6.25}$$

Where $\bar{Y}$ is the complex bus admittance matrix, $\bar{V}$ is the complex bus voltage vector and $\bar{I}$ is the complex current injection vector. Equation (6.25) is derived by application of KCL at each node. For three-phase unbalanced systems, the $\bar{Y}$ is computed considering each phase as a node (each phase node) and the unbalanced branch and shunt admittances. Let $\bar{Y} = G + jB$, $\bar{V} = V^{re} + jV^{im}$, and $\bar{I} = I^{re} + jI^{im}$, then (6.25) can be separated into real and imaginary parts:

$$\begin{bmatrix} G & -B \\ B & G \end{bmatrix} \begin{bmatrix} V^{re} \\ V^{im} \end{bmatrix} = \begin{bmatrix} I^{re} \\ I^{im} \end{bmatrix} \tag{6.26}$$

Ideally (6.26) would represent the system physics for a single time step solution where the status of the branches is known. However, in the case of mult-time step restoration, the status of the branches is not known ahead of time until after the restoration solution is returned by the optimization solver. Therefore, the bus admittance matrix, $\bar{Y} = G + jB$, has to be modified to include branch energization status which would determine whether a given branch admittance should be included (or not included) in the bus admittance matrix.

First, we show how to include the energization status of branches into equations (6.25) and (6.26) using a simple three-node power system and then generalize to an arbitrary number of nodes. Consider Figure 6.3 below,

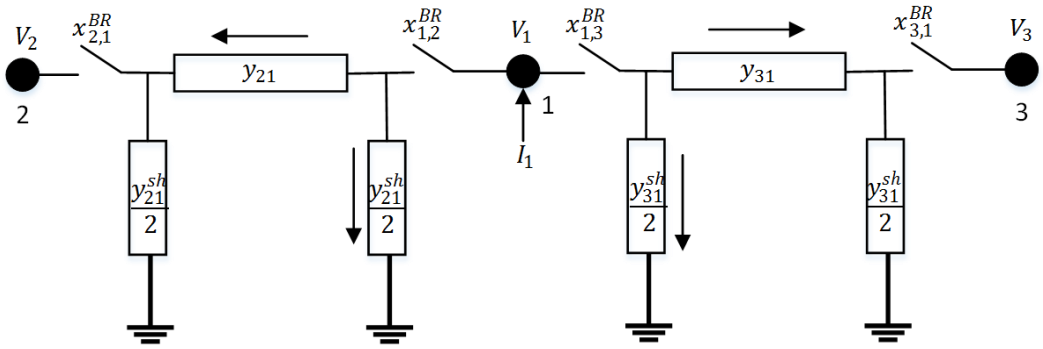

Figure 6.3 Three-Node example to illustrate Power Flow Constraints for Droop-Controlled Microgrid

In Figure 6.3, there are three nodes labeled 1, 2, and 3, and each node is assumed to be a three-phase node. This means that the voltage of each node labeled V_1, V_2, and V_3 are each complex vectors of length equal to three as well as the current injections. y_{21} and y_{21}^{sh} are each a 3 by 3 complex branch admittance matrix and shunt admittance matrix respectively between nodes 2 and 1. y_{31} and y_{31}^{sh} are each a 3 by 3 complex branch admittance matrix and shunt admittance matrix respectively between nodes 3 and 1. $x_{2,1}^{BR} = x_{1,2}^{BR}$, and is considered the binary energization status of the branch between nodes 2 and 1. Likewise, $x_{3,1}^{BR} = x_{1,3}^{BR}$, and is considered binary energization status of the branch between nodes 3 and 1.

Application of Kirchhoff's current law at node 1 will depend on the energization status of $x_{1,2}^{BR}$ and $x_{1,3}^{BR}$, and can be written following the assumed current direction indicated by the arrows in Figure 6.3 as follows.

$$x_{1,2}^{BR} y_{21}(V_1 - V_2) + x_{1,2}^{BR} \frac{y_{21}^{sh}}{2} V_1 + x_{1,3}^{BR} y_{31}(V_1 - V_3) + x_{1,3}^{BR} \frac{y_{31}^{sh}}{2} V_1 = I_1 \qquad (6.27)$$

Note that in (6.27), the multiplication of energization status and a matrix or vector is a scalar multiplication. Equation (6.27) can be rearranged as follows.

$$\left(x_{1,2}^{BR}y_{21} + x_{1,3}^{BR}y_{31} + x_{1,3}^{BR}\frac{y_{31}^{sh}}{2}\right)V_1 + \left(-x_{1,2}^{BR}y_{21}\right)V_2 + \left(-x_{1,3}^{BR}y_{31}\right)V_3 = I_1 \tag{6.28}$$

Similar KCL equations as (6.28) can be written for nodes 2 and 3. Equation (6.28) can be written in matrix form where X has been used to represent equivalent elements for the KCL at nodes 2 and 3.

$$\underbrace{\begin{bmatrix} x_{1,2}^{BR}y_{21} + x_{1,3}^{BR}y_{31} + x_{1,3}^{BR}\frac{y_{31}^{sh}}{2} & -x_{1,2}^{BR}y_{21} & -x_{1,3}^{BR}y_{31} \\ X & X & X \\ X & X & X \end{bmatrix}}_{Y(x^{BR})}\begin{bmatrix} V_1 \\ V_2 \\ V_3 \end{bmatrix} = \begin{bmatrix} I_1 \\ X \\ X \end{bmatrix} \tag{6.29}$$

Notice that the coefficient matrix, which is the complex Y bus admittance matrix is now a function of branch energization status. Note that $y_{nm} = g_{nm} + jb_{nm}$, $y_{nm}^{sh} = g_{nm}^{sh} + jb_{nm}^{sh}$, $V_n = V_n^{re} + jV_n^{im}$, $I_n = I_n^{re} + jI_n^{im}$. Without the energization status, the off-diagonal term of the bus admittance matrix is given by $Y_{nm} = -y_{nm}$. Note that $Y_{nm} = G_{nm} + jB_{nm}$, $\therefore G_{nm} = -g_{nm}$, $B_{nm} = -b_{nm}$. Substituting $y_{nm} = g_{nm} + jb_{nm}$, $y_{nm}^{sh} = g_{nm}^{sh} + jb_{nm}^{sh}$, $V_n = V_n^{re} + jV_n^{im}$, $I_n = I_n^{re} + jI_n^{im}$ into (6.28) and separating the resulting expression into real and imaginary gives the following:

$$\begin{aligned} &\sum_{\substack{k:k\in\{1,2,3\} \\ k\neq 1}}(G_{1,k}V_k^{re} - B_{1,k}V_k^{im})x_{1,k}^{BR} + \sum_{\substack{k:k\in\{1,2,3\} \\ k\neq 1}}(-G_{1,k}V_1^{re} + \frac{g_{1,k}^{sh}}{2}V_1^{im})x_{1,k}^{BR} \\ &\qquad - \sum_{\substack{k:k\in\{1,2,3\} \\ k\neq 1}}(-B_{1,k}V_1^{re} + \frac{b_{n,k}^{sh}}{2}V_1^{im})x_{1,k}^{BR} = I_n^{re} \end{aligned} \tag{6.30}$$

$$\sum_{\substack{k:k\in\{1,2,3\}\\k\neq 1}}(B_{1,k}V_k^{re}+G_{1,k}V_k^{im})x_{1,k}^{BR}+\sum_{\substack{k:k\in\{1,2,3\}\\k\neq 1}}(-B_{1,k}\,V_1^{re}+\frac{b_{1,k}^{sh}}{2}V_1^{im})x_{1,k}^{BR}$$
$$+\sum_{\substack{k:k\in\{1,2,3\}\\k\neq 1}}(-G_{1,k}V_1^{re}+\frac{g_{1,k}^{sh}}{2}V_1^{im})x_{1,k}^{BR}=I_n^{im} \quad (6.31)$$

Equation (6.30) and (6.31) are the real and imaginary parts of equation (6.28) in expanded form. The first summation terms in equations (6.30) and (6.31) are the product terms due to the off-diagonal Y bus terms written in rectangular coordinate. The next two terms in equations (6.30) and (6.31) are the product terms due to the leading diagonal terms of the Y bus matrix. Similar equations can be written for the KCL at nodes 2 and 3 of Figure 6.3.

We can generalize equations (6.30) and (6.31) for an arbitrary node n of a microgrid with sets of nodes N as follows with additional step subscript for the time step indicated by t as follows:

$$\sum_{\substack{k:k\in N\\k\neq n}}(G_{n,k}\hat{V}_{k,t}^{re}-B_{n,k}\hat{V}_{k,t}^{im})\hat{x}_{n,k,t}^{BR}+\sum_{\substack{k:k\in N\\k\neq n}}(-G_{n,k}\,\hat{V}_{n,t}^{re}+\frac{g_{n,k}^{sh}}{2}\hat{V}_{n,t}^{re})\hat{x}_{n,k,t}^{BR}$$
$$-\sum_{\substack{k:k\in N\\k\neq n}}(-B_{n,k}\hat{V}_{n,t}^{im}+\frac{b_{n,k}^{sh}}{2}\hat{V}_{n,t}^{im})\hat{x}_{n,k,t}^{BR}=\hat{I}_{n,t}^{re}(\hat{V}_{n,t}^{re},\hat{V}_{n,t}^{im}) \quad (6.32)$$

$$\sum_{\substack{k:k\in N\\k\neq n}}(B_{n,k}\hat{V}_{k,t}^{re}+G_{n,k}\hat{V}_{k,t}^{im})\hat{x}_{n,k,t}^{BR}+\sum_{\substack{k:k\in N\\k\neq n}}(-B_{n,k}\hat{V}_{n,t}^{re}+\frac{b_{n,k}^{sh}}{2}\hat{V}_{n,t}^{re})\hat{x}_{n,k,t}^{BR}$$
$$+\sum_{\substack{k:k\in N\\k\neq n}}(-G_{n,k}\hat{V}_{n,t}^{im}+\frac{g_{n,k}^{sh}}{2}\hat{V}_{n,t}^{im})\hat{x}_{n,k,t}^{BR}=\hat{I}_{n,t}^{im}(\hat{V}_{n,t}^{re},\hat{V}_{n,t}^{im}) \quad (6.33)$$

Where $G_{n,k}=-g_{n,k}$ ($g_{n,k}$ is a matrix that represents the real part of the branch admittance between nodes n and k) and $B_{n,k}=-b_{n,k}$ ($b_{n,k}$ is a matrix that represents the

imaginary part of the branch admittance between nodes n and k). Note that $\hat{V}_{n,t}^{re} = \left[\hat{V}_{n,t}^{re,a}\ \hat{V}_{n,t}^{re,b}\ \hat{V}_{n,t}^{re,c}\right]^T$, $\hat{V}_{n,t}^{im} = \left[\hat{V}_{n,t}^{im,a}\ \hat{V}_{n,t}^{im,b}\ \hat{V}_{n,t}^{im,c}\right]^T$, $\hat{I}_{n,t}^{re}$ and $\hat{I}_{n,t}^{im}$ are similarly defined as three-phase current vectors.

To specify the power flow constraint for the microgrid to be restored, (6.32) and (6.33) have to be defined as constraints for every node and every step of the restoration. Just like in (6.30) and (6.31), the first summation terms in equations (6.32) and (6.33) are the product terms due to the off-diagonal Y bus terms written in rectangular coordinate. The next two terms in equations (6.32) and (6.33) are the product terms due to the leading diagonal terms of the Y bus matrix. The RHS terms are the sum of the three-phase current injection vector at each node. The LHS of equations (6.32) and (6.33) present bilinear vector terms which are products of rectangular voltage vectors (continuous) and branch energization status (binary) – these terms are linearized by introducing new variables for each bilinear term. Details of this linearization is discussed in Appendix A.

6.3.5.2. Current Injection for Each Node

According to the expression for the current injection at each node derived in section 5.5 (in this context, each node is assumed to be three-phase thereby giving a three-phase vector for its corresponding variables like nodal voltages and injection current with unavailable phase(s) replaced with zero), the current injections for all node types are described in this subsection.

At any given generic phase ph and node n, with power injections $P_{ph,n,t}^{inj} + jQ_{ph,n,t}^{inj}$, the current injection per phase can be written as follows in terms of the phase power injection and phase node voltage:

$$\bar{I}_{ph,n,t} = \hat{I}_{n,t}^{re,ph} + j\hat{I}_{n,t}^{im,ph} = \frac{P_{ph,n,t}^{inj} - jQ_{ph,n,t}^{inj}}{\hat{V}_{n,t}^{re,ph} - j\hat{V}_{n,t}^{im,ph}} \tag{6.34}$$

Equation (6.34) is derived from the complex power equation which gives that the current is equal to the complex conjugate of complex power divided by the complex conjugate of voltage [97]. Separating the RHS of (6.34) into real and imaginary part gives the following:

$$\hat{I}_{n,t}^{re,ph} = \frac{P_{ph,n,t}^{inj}\hat{V}_{n,t}^{re,ph} + Q_{ph,n,t}^{inj}\hat{V}_{n,t}^{im,ph}}{\left|\hat{V}_{n,t}^{re,ph}\right|^2 + \left|\hat{V}_{n,t}^{im,ph}\right|^2} \tag{6.35}$$

$$\hat{I}_{n,t}^{im,ph} = \frac{P_{ph,n,t}^{inj}\hat{V}_{n,t}^{im,ph} - Q_{ph,n,t}^{inj}\hat{V}_{n,t}^{re,ph}}{\left|\hat{V}_{n,t}^{re,ph}\right|^2 + \left|\hat{V}_{n,t}^{im,ph}\right|^2} \tag{6.36}$$

Note that $\left|\hat{V}_{n,t}^{ph}\right|^2 = \left|\hat{V}_{n,t}^{re,ph}\right|^2 + \left|\hat{V}_{n,t}^{im,ph}\right|^2$.

The current injection for the droop-controlled DG, PQ DG, and load nodes are expressed as follows.

6.3.5.2.1. Droop Node

At each phase of the node of a droop-controlled DG, the RHSs of equations (6.32) and (6.33) can be expressed by substituting the power injection terms in (6.35) and (6.36) with the reference power variables of the droop DGs as follows,

$$\hat{I}_{n,t}^{re,ph} = \hat{P}_{n,t}^{ref,ph}\frac{\hat{V}_{n,t}^{re,ph}}{\left|\hat{V}_{n,t}^{re,ph}\right|^2 + \left|\hat{V}_{n,t}^{im,ph}\right|^2} + \hat{Q}_{n,\mathrm{t}}^{ref,ph}\frac{\hat{V}_{n,t}^{im,ph}}{\left|\hat{V}_{n,t}^{re,ph}\right|^2 + \left|\hat{V}_{n,t}^{im,ph}\right|^2} \tag{6.37}$$

$$\hat{I}_{n,t}^{im,ph} = \hat{P}_{n,t}^{ref,ph}\frac{\hat{V}_{n,t}^{im,ph}}{\left|\hat{V}_{n,t}^{re,ph}\right|^2 + \left|\hat{V}_{n,t}^{im,ph}\right|^2} - \hat{Q}_{n,t}^{ref,ph}\frac{\hat{V}_{n,t}^{re,ph}}{\left|\hat{V}_{n,t}^{re,ph}\right|^2 + \left|\hat{V}_{n,t}^{im,ph}\right|^2} \tag{6.38}$$

Notice that the power injection for each phase of the droop-controlled DG node have been set equal to their reference power variables which implicitly enforces the droop reference active and reactive power constraints of section 5.8.2 and 5.8.3. The droop reference active and reactive power constraints ensure that the control variables are set such that the droop DGs' output power and their reference power settings are the same. The two voltage quotient terms in equations (6.37) and (6.38) have been previously linearized in section 5.5.2; (6.37) and (6.38) can be rewritten with the linearized functions for the voltage quotient terms as follows,

$$\hat{I}_{n,t}^{re,ph} = \hat{P}_{n,t}^{ref,ph}\tilde{g}_{1,ph}\left(\hat{V}_{n,t}^{re,ph}, \hat{V}_{n,t}^{im,ph}\right) + \hat{Q}_{n,\mathrm{t}}^{ref,ph}\tilde{g}_{2,ph}\left(\hat{V}_{n,t}^{re,ph}, \hat{V}_{n,t}^{im,ph}\right) \quad (6.39)$$

$$\hat{I}_{n,t}^{im,ph} = \hat{P}_{n,t}^{ref,ph}\tilde{g}_{2,ph}\left(\hat{V}_{n,t}^{re,ph}, \hat{V}_{n,t}^{im,ph}\right) - \hat{Q}_{n,t}^{ref,ph}\tilde{g}_{1,ph}\left(\hat{V}_{n,t}^{re,ph}, \hat{V}_{n,t}^{im,ph}\right) \quad (6.40)$$

Where $\tilde{g}_{1,ph}$ and $\tilde{g}_{2,ph}$ are linear functions of the rectangular voltages. Notice that (6.39) and (6.40) contain the product of two continuous bounded variables and these products have to be linearized. These products are results of the droop reference powers and rectangular voltages being considered as decision control variables. The linearization of the product of two continuous bounded variables using piecewise linearization approach is discussed in Appendix B.

The piecewise linearization approach presented in Appendix B introduces several variables and constraints including special order set of type 2 (SOS2) constraints. These additional variables and constraints typically increase the computation burden and numerical issues for the model. An alternative to the piecewise linearization approach is to approximate the rectangular voltage variables to constants equal to their nominal values as presented in Appendix C. This alternative approach has been observed from the case

studies we ran to have less numerical issues than those of piecewise linearization especially for larger system size. Depending on the case study system discussed in section 7, a mix of the piecewise linearization and the alternative approach or only the alternative approach is used in the formulation of the restoration model before being fed to the MILP solver.

6.3.5.2.2. Load Node and Load Models (switchable & non-switchable loads):

The loads are assumed to be single, double-phase, and three-phase ZIP loads connected in wye or delta to the system. The Z stands for constant impedance, I for constant current and P for constant power components of the load. At each phase of a grounded wye-connected ZIP load node, assuming a nominal voltage of $1pu$, we can write the power injections as follows [107]:

$$P_{ph,n,t}^{inj} = P_{ph,n,t}[\alpha_n^Z(|\hat{V}_{n,t}^{ph}|)^2 + \alpha_n^I(|\hat{V}_{n,t}^{ph}|) + \alpha_n^P)] \quad (6.41)$$

$$Q_{ph,n,t}^{inj} = Q_{ph,n,t}[\alpha_n^Z(|\hat{V}_{n,t}^{ph}|)^2 + \alpha_n^I(|\hat{V}_{n,t}^{ph}|) + \alpha_n^P) \quad (6.42)$$

α_n^Z, α_n^I, and α_n^P are the ZIP load coefficients for the constant impedance, current, and power components of the load and numerically sum to unity. $P_{ph,n,t}$ and $Q_{ph,n,t}$ are the nominal active and reactive power rating of load n at phase ph. Note that the current injection should be negated to signify that the current is injected in the reverse direction into the network for ZIP load elements.

The derivation for the current injection at the load node follows similar steps as the current injection derived for the load nodes in section 5.5.2. This derivation is simply

plugging the ZIP load expressions of (6.41) and (6.42) into (6.35) and (6.36) and then linearizing the resulting voltage quotients to get the following,

$$-\hat{I}_{n,t}^{re,ph} = x_{n,t}^{L}\alpha_n^{Z}\left(P_{ph,n,t}\hat{V}_{n,t}^{re,ph} + Q_{ph,n,t}\hat{V}_{n,t}^{im,ph}\right) +$$

$$x_{n,t}^{L}\alpha_n^{I}\left[P_{ph,n,t}\tilde{g}_{3,ph}\left(\hat{V}_{n,t}^{re,ph}, \hat{V}_{n,t}^{im,ph}\right) + Q_{ph,n,t}\tilde{g}_{4,ph}\left(\hat{V}_{n,t}^{re,ph}, \hat{V}_{n,t}^{im,ph}\right)\right] + \tag{6.43}$$

$$x_{n,t}^{L}\alpha_n^{P}\left[P_{ph,n,t}\tilde{g}_{1,ph}\left(\hat{V}_{n,t}^{re,ph}, \hat{V}_{n,t}^{im,ph}\right) + Q_{ph,n,t}\tilde{g}_{2,ph}\left(\hat{V}_{n,t}^{re,ph}, \hat{V}_{n,t}^{im,ph}\right)\right]$$

$$-\hat{I}_{n,t}^{im,ph} = x_{n,t}^{L}\alpha_n^{Z}\left(P_{ph,n,t}\hat{V}_{ph,k}^{im} - Q_{ph,n,t}\hat{V}_{ph,k}^{re}\right) +$$

$$x_{n,t}^{L}\alpha_n^{I}\left[P_{ph,n,t}\tilde{g}_{4,ph}\left(\hat{V}_{n,t}^{re,ph}, \hat{V}_{n,t}^{im,ph}\right) - Q_{ph,n,t}\tilde{g}_{3,ph}\left(\hat{V}_{n,t}^{re,ph}, \hat{V}_{n,t}^{im,ph}\right)\right] + \tag{6.44}$$

$$x_{n,t}^{L}\alpha_n^{P}\left[P_{ph,n,t}\tilde{g}_{2,ph}\left(\hat{V}_{n,t}^{re,ph}, \hat{V}_{n,t}^{im,ph}\right) - Q_{ph,n,t}\tilde{g}_{1,ph}\left(\hat{V}_{n,t}^{re,ph}, \hat{V}_{n,t}^{im,ph}\right)\right]$$

$\tilde{g}_{1,ph}$ to $\tilde{g}_{4,ph}$ are linear functions of the rectangular voltages derived for each phase. Note that the products of $x_{n,t}^{L}$ and $\hat{V}_{n,t}^{re,ph}$ or $\hat{V}_{n,t}^{im,ph}$ in (6.43) and (6.44) give bilinear terms which were linearized according to the approach discussed in Appendix A.

For delta-connected loads, equations (6.41)–(6.44) are expressed similarly, with the phase voltages replaced by phase-to-phase voltages (i.e., the differences between the phase voltages). Given that (6.41) and (6.42) are implicitly written in per-phase base values, their equivalent expression for delta-connected loads in per phase base values should have correction factors of $1/3$ and $1/\sqrt{3}$ for the constant impedance and current terms, respectively. The current realized from the delta-connected loads using the equations above is then transformed to per-phase injection current using the relation below,

$$\begin{bmatrix} \hat{I}_{n,t}^{re,a} \\ \hat{I}_{n,t}^{re,b} \\ \hat{I}_{n,t}^{re,c} \end{bmatrix} = \begin{bmatrix} 1 & 0 & -1 \\ -1 & 1 & 0 \\ 0 & -1 & 1 \end{bmatrix} \begin{bmatrix} \hat{I}_{n,t}^{re,ab} \\ \hat{I}_{n,t}^{re,bc} \\ \hat{I}_{n,t}^{re,ca} \end{bmatrix} \tag{6.45}$$

A similar equation can be written for the imaginary current components as follows:

$$\begin{bmatrix} \hat{I}_{n,t}^{im,a} \\ \hat{I}_{n,t}^{im,b} \\ \hat{I}_{n,t}^{im,c} \end{bmatrix} = \begin{bmatrix} 1 & 0 & -1 \\ -1 & 1 & 0 \\ 0 & -1 & 1 \end{bmatrix} \begin{bmatrix} \hat{I}_{n,t}^{im,ab} \\ \hat{I}_{n,t}^{im,bc} \\ \hat{I}_{n,t}^{im,ca} \end{bmatrix} \tag{6.46}$$

6.3.5.2.3. PQ DG Nodes (Dispatchable DG, non-dispatchable DG, controllable load with demand response)

The current injection for the PQ DG node is expressed similarly to those of load nodes with α_n^Z, $\alpha_n^I = 0$ and $\alpha_n^P = 1$. Also, the injection direction for the PQ node is opposite to those of load node injections. This injection is expressed as follows for each PQ DG's phase node:

$$\hat{I}_{n,t}^{re,ph} = \hat{P}_{ph,k,t}^{dg} \tilde{g}_{1,ph}\left(\hat{V}_{n,t}^{re,ph}, \hat{V}_{n,t}^{im,ph}\right) + \hat{Q}_{ph,k,t}^{dg} \tilde{g}_{2,ph}\left(\hat{V}_{n,t}^{re,ph}, \hat{V}_{n,t}^{im,ph}\right) \tag{6.47}$$

$$\hat{I}_{n,t}^{im,ph} = \hat{P}_{ph,k,t}^{dg} \tilde{g}_{2,ph}\left(\hat{V}_{n,t}^{re,ph}, \hat{V}_{n,t}^{im,ph}\right) - \hat{Q}_{ph,k,t}^{dg} \tilde{g}_{1,ph}\left(\hat{V}_{n,t}^{re,ph}, \hat{V}_{n,t}^{im,ph}\right) \tag{6.48}$$

Equations (6.47) and (6.48) convey the challenge of linearizing the product of two continuous bounded variables. This linearization can be accomplished by using the piecewise linearization approach in Appendix B or by using the alternative approach in Appendix C which is based on approximating the rectangular voltages to nominal values. In the method implementation, there is an option to use both or only the alternative approach to solve the system to be restored. More details about choice of linearization is provided in section 7.2.7.2.

Equations (6.47) and (6.48) are used to express the current injections for dispatchable PQ DGs, non-dispatchable PQ DGs, and controllable load with demand response. The difference in the model of the PQ DGs is that the $\hat{P}_{ph,k,t}^{dg}$ and $\hat{Q}_{ph,k,t}^{dg}$ are constrained within a given operating range for the dispatchable DGs when energized and fixed to forecasted values for the non-dispatchable DGs when energized which is similar to the work in [34]. The $\hat{P}_{ph,k,t}^{dg}$ and $\hat{Q}_{ph,k,t}^{dg}$ for demand response loads has an opposite injection to the system since they are loads and constrained within the range that the respective demand response load can operate. More details about the $\hat{P}_{ph,k,t}^{dg}$ and $\hat{Q}_{ph,k,t}^{dg}$ constraints are presented in section 6.3.6.

6.3.6. DG and System Operating Constraints

6.3.6.1. Phase Voltage Unbalance Rate Constraint (PVUR)

According to the IEEE standard test procedure for polyphase induction motors and generators 112-2017 [108], the percent voltage unbalance equals 100 times the maximum voltage deviation from the average voltage divided by the average voltage. This standard stipulates that voltage unbalance shall not exceed 0.5%. When we make use of the phase voltages to calculate the voltage unbalance, it is called a phase voltage unbalance rate ($\%PVUR$) [109]. To avoid the issue with linearizing the quotient in the voltage unbalance definition, we constrain the voltage across any two pair of phases of a droop node to say within a difference of μ per unit between the phases similar to what we did in section 5.8.7.

$$
\begin{aligned}
&-\mu - \left(1 - x_{i,t}^{N}\right)M \\
&\qquad \leq \tilde{g}_{5,ph_1}\left(\hat{V}_{n,t}^{re,ph}, \hat{V}_{n,t}^{im,ph}\right) - \tilde{g}_{5,ph_2}\left(\hat{V}_{n,t}^{re,ph}, \hat{V}_{n,t}^{im,ph}\right) \\
&\qquad \leq \mu + (1 - x_{i,t}^{N})M
\end{aligned}
\tag{6.49}
$$

Where $ph_1, ph_2 \in \{a, b, c\}, ph_1 \neq ph_2$ and $\tilde{g}_{5,ph}\left(\hat{V}_{n,t}^{re,ph}, \hat{V}_{n,t}^{im,ph}\right)$ is the linearization of the non-linear square root function for converting rectangular coordinate to magnitude and follows from the same linearization of square root function around a compact set discussed in section 5.5.2. Equation (6.49) ensures that for an energized node that the phase unbalance rate stays within an acceptable value; and binary value, $x_{i,t}^{N}$, representing the energization state of a node ensures that (6.49) is disabled for the unenergized node.

6.3.6.2. Voltage Limit Constraint

The voltage limit constraint for each node can be expressed as

$$
\begin{aligned}
V^{min} - \left(1 - x_{i,t}^{N}\right)M &\leq \tilde{g}_{5,ph}\left(\hat{V}_{n,t}^{re,ph}, \hat{V}_{n,t}^{im,ph}\right) \\
&\leq V^{max} + (1 - x_{i,t}^{N})M
\end{aligned}
\tag{6.50}
$$

This limit maintains the voltage magnitude across an energized node to be within a certain limit which is $[V^{min}\ V^{max}]$. The term, $\left(1 - x_{i,t}^{N}\right)M$, is used to disable this constraint for an unenergized node, where M is a large number. For an unenergized node, $x_{i,t}^{N} = 0$, thereby making (6.50) to be bounded between two large negative and positive numbers, $-M$ and $+M$; this large bound effectively disables this constraint.

6.3.6.3. DG Power Unbalance Constraints

These constraints apply to only the droop-controlled DGs. The droop-controlled DGs are three-phase controlled and unbalanced loading negatively affects their controller and hence can lead to significant voltage unbalance in the system [75, 76]. Therefore, it is desired that the output power of the three phases are approximately balanced. This can be realized by constraining power differences between each of the two phases within tight margins as follows:

$$-\varepsilon_P \leq \begin{bmatrix} \hat{P}^{ref}_{a,k,t} - \hat{P}^{ref}_{b,k,t} \\ \hat{P}^{ref}_{b,k,t} - \hat{P}^{ref}_{c,k,t} \\ \hat{P}^{ref}_{c,k,t} - \hat{P}^{ref}_{a,k,t} \end{bmatrix} \leq \varepsilon_P \tag{6.51}$$

$$-\varepsilon_Q \leq \begin{bmatrix} \hat{Q}^{ref}_{a,k,t} - \hat{Q}^{ref}_{b,k,t} \\ \hat{Q}^{ref}_{b,k,t} - \hat{Q}^{ref}_{c,k,t} \\ \hat{Q}^{ref}_{c,k,t} - \hat{Q}^{ref}_{a,k,t} \end{bmatrix} \leq \varepsilon_Q \tag{6.52}$$

Where ε_P and ε_Q are very small fractions of the active and reactive power limits.

6.3.6.4. Nominal System Load Unbalance Index (NSLUI) Constraints

Similar to the unbalance constraint of section 5.8.6, we include a complementary set of constraints to (6.51) and (6.52) to limit the NSLUI to within a given percentage, say ρ%, as follows. These constraints ensure that the net load minus the power generated by the PQ DGs are balanced within a certain limit to minimize the unbalance loads served by the three-phase grid-supporting DGs.

$$\hat{P}^{N}_{avg,t} = \frac{1}{3}\sum_{l\in L}\sum_{ph\in\{a,b,c\}} \hat{P}_{ph,l,t} - \frac{1}{3}\sum_{k\in G^{PQ}}\sum_{ph\in\{a,b,c\}} \hat{P}^{dg}_{ph,k,t} \tag{6.53}$$

$$\hat{Q}^{N}_{avg,t} = \frac{1}{3}\sum_{l\in L}\sum_{ph\in\{a,b,c\}}\hat{Q}_{ph,l,t} - \frac{1}{3}\sum_{k\in G^{PQ}}\sum_{ph\in\{a,b,c\}}\hat{Q}^{dg}_{ph,k,t} \tag{6.54}$$

$$\frac{-\rho}{100}\hat{P}^{N}_{avg,t} \le \sum_{l\in L}\hat{P}_{ph,l,t} - \sum_{k\in G^{PQ}}\hat{P}^{dg}_{ph,k,t} - \hat{P}^{N}_{avg,t} \le \frac{\rho}{100}\hat{P}^{N}_{avg,t} \tag{6.55}$$

$$\frac{-\rho}{100}\hat{Q}^{N}_{avg,t} \le \sum_{l\in L}\hat{Q}_{ph,l,t} - \sum_{k\in G^{PQ}}\hat{Q}^{dg}_{ph,k,t} - \hat{Q}^{N}_{avg,t} \le \frac{\rho}{100}\hat{Q}^{N}_{avg,t} \tag{6.56}$$

Equations (6.53) and (6.54) represent average active and reactive power per phase served by the three-phase droop-controlled DGs. These equations are formed by simple energy balance by subtracting the sum of PQ DG dispatch from the sum of loads restored per time step and dividing by 3 to get the average power per phase served by the droop DGs.

Equations (6.55) and (6.56) ensure that net power per phase served by the droop-controlled DGs are close to the average power values calculated in (6.53) and (6.54). Essentially, (6.55) and (6.56) ensure that the NSLUI, defined in section 5.7.1.1, should be less than or equal to a certain ρ%. The NSLUI helps to constrain the search space and ensure that the unbalance loads are well compensated for by the PQ DGs so that the droop-controlled three-phase DGs see approximately balanced loads at its terminal.

6.3.6.5. DG Output Constraints

The active and reactive power limit constraints for each of the droop controlled DGs, $k \in G^{Dr}$, can be written as,

$$\hat{x}^{G}_{g,t}P^{min}_{k} \le \sum\nolimits_{ph\in\{a,b,c\}}\hat{P}^{ref}_{ph,k,t} \le \hat{x}^{G}_{g,t}P^{max}_{k} \tag{6.57}$$

$$\hat{x}_{g,t}^{G} Q_k^{min} \leq \sum_{ph\in\{a,b,c\}} \hat{Q}_{ph,k,t}^{ref} \leq \hat{x}_{g,t}^{G} Q_k^{max} \tag{6.58}$$

For dispatchable DGs operating in PQ mode, (6.57) and (6.58) are modified to the following equation for the PQ DGs (the PQ DGs are assumed to be single-phase in this formulation).

$$\hat{x}_{g,t}^{G} P_k^{min} \leq \hat{P}_{ph,k,t}^{dg} \leq \hat{x}_{g,t}^{G} P_k^{max}, t \in T, ph \in \{a,b,c\} \tag{6.59}$$

$$\hat{x}_{g,t}^{G} Q_k^{min} \leq \hat{Q}_{ph,k,t}^{dg} \leq \hat{x}_{g,t}^{G} Q_k^{max}, t \in T, ph \in \{a,b,c\} \tag{6.60}$$

For non-dispatchable renewable DGs operating in PQ mode, the power output is fixed to the forecasted value, $P_{ph,k,t}^{fc}$ and $Q_{ph,k,t}^{fc}$, when it is energized.

$$\hat{x}_{g,t}^{G} P_{ph,k,t}^{fc} \leq \hat{P}_{ph,k,t}^{dg} \leq \hat{x}_{g,t}^{G} P_{ph,k,t}^{fc} \tag{6.61}$$

$$\hat{x}_{g,t}^{G} Q_{ph,k,t}^{fc} \leq \hat{Q}_{ph,k,t}^{dg} \leq \hat{x}_{g,t}^{G} Q_{ph,k,t}^{fc} \tag{6.62}$$

Notice that equations (6.61) and (6.62) have the same upper and lower bounds and thus are equivalent to an equality constraint but have been left in the bound form of (6.59) and (6.60). Equations (6.57) to (6.62) ensure that each DG stays within its allowable minimum and maximum power during operation and also force the power output to zero when it is not operating.

6.3.6.6. Demand Response Loads Constraint

Demand response (DR) loads are loads that can participate in demand response and can be varied over the time horizon of interest. The demand response model utilized are assumed to be incentive-based DR with direct load control (DLC) program [110, 111]. The DLC program enables the MGCC to directly control the DR loads for each time step. This direct control of loads can be considered the most suitable form of demand response

program for black start restoration since the loads can be varied quickly by the MGCC to meet generation balance needs without customer interference. The following constraints are included for each controllable load:

$$\hat{x}_{g,t}^{G} P_l^{min} \leq \hat{P}_{ph,l,t} \leq \hat{x}_{g,t}^{G} P_l^{max} \tag{6.63}$$

$$\hat{x}_{g,t}^{G} Q_l^{min} \leq \hat{Q}_{ph,l,t} \leq \hat{x}_{g,t}^{G} Q_l^{max} \tag{6.64}$$

$$\frac{\hat{P}_{ph,l,t}}{P_l^{max}} = \frac{\hat{Q}_{ph,l,t}}{Q_l^{max}}, l \in L^C \tag{6.65}$$

$$\hat{P}_{ph,l,t+1} \geq \hat{P}_{ph,l,t}, \hat{Q}_{ph,l,t+1} \geq \hat{Q}_{ph,l,t}, l \in L^C \tag{6.66}$$

Equations (6.63) and (6.64) ensures that the loads are controlled within their allowable boundaries and assumes a continuous control range. Equation (6.65) is a constraint that maintains the active and reactive load settings ratio which is equivalent to the assumption that the load's power factor remains the same as it is varied. Equation (6.66) ensures that the demand response works such that the load curtailment doesn't increase with time step but rather is forced to decrease or leave the curtailment as it was in the previous step; this is to ensure that specific loads within the DR aggregate load stay on after the DLC program commands it to energize. In other words, (6.66) ensures that any specific load within each aggregate load participating in demand response will stay on after it has been energized instead of flipping on and off over the restoration time steps.

6.3.6.7. Ramp Rate Constraints

While inverter interfaced DGs can ramp up their power almost instantly, it could place significant stress on the DC prime mover of the DG. How much load can be picked up per step depends on a prime mover's response [112]. Also, changing active and reactive

reference power settings can affect frequency/angle and voltage stability, respectively according to the droop control. Determining what would be the best allowable step change in active and reactive power settings of the DGs is beyond the scope of this work. Hence, we specify the maximum absolute change in the active and reactive power settings of the DGs for any two adjacent time steps by the constraints:

$$-\hat{x}^{G}_{g,t}.P^{G,ramp}_{g} \leq \hat{P}^{dg}_{ph,k,t} - \hat{P}^{dg}_{ph,k,t-1} \leq \hat{x}^{G}_{g,t}.P^{G,ramp}_{g}, g \in G/G^{Dr}, t \in T \tag{6.67}$$

$$-\hat{x}^{G}_{g,t}.Q^{G,ramp}_{g} \leq \hat{Q}^{dg}_{ph,k,t} - \hat{Q}^{dg}_{ph,k,t-1} \leq \hat{x}^{G}_{g,t}.Q^{G,ramp}_{g}, g \in G/G^{Dr}, t \in T \tag{6.68}$$

$$-\hat{x}^{G}_{g,t}.P^{G,ramp}_{g} \leq \sum_{ph\in\{a,b,c\}} \hat{P}^{ref}_{ph,k,t} - \sum_{ph\in\{a,b,c\}} \hat{P}^{ref}_{ph,k,t-1} \leq \hat{x}^{G}_{g,t}.P^{G,ramp}_{g}, g \in G^{Dr}, t \in T \tag{6.69}$$

$$-\hat{x}^{G}_{g,t}.Q^{G,ramp}_{g} \leq \sum_{ph\in\{a,b,c\}} \hat{Q}^{ref}_{ph,k,t} - \sum_{ph\in\{a,b,c\}} \hat{Q}^{ref}_{ph,k,t-1} \leq \hat{x}^{G}_{g,t}.Q^{G,ramp}_{g}, g \in G^{Dr}, t \in T \tag{6.70}$$

Equations (6.67) and (6.68) specify the ramp limits for the PQ DGs while (6.69) and (6.70) specify the ramp limits for the three-phase droop-controlled DGs.

6.3.7. Topology and Sequencing Constraint

We first introduce the concept of bus block described in [29, 30]. A bus block is a group of nodes connected by non-switchable lines. Grouping the distribution system into a set of bus blocks, K, reduces the size of the graph in which edges are represented by a

set of switchable branches between bus blocks, C. Figure 6.4 shows an example of forming a graph from a distribution system using bus blocks.

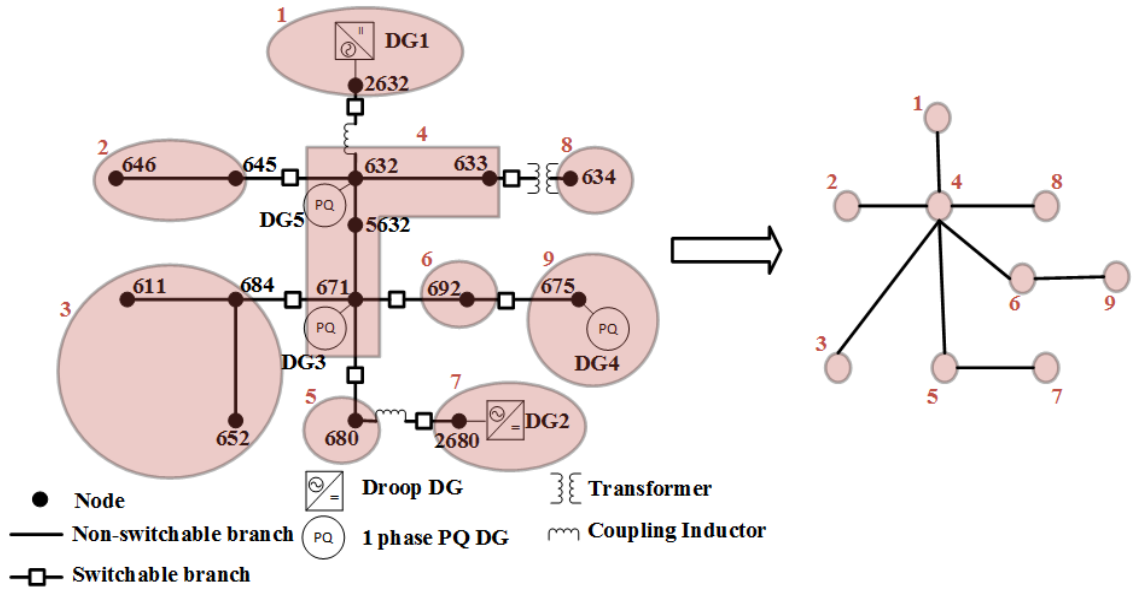

Figure 6.4 Illustration of Bus Block Reduction using Modified IEEE 13 Node Test Feeder

The topology and sequencing constraints ensure that the system maintains a tree topology for all restoration step and are summarized below. While a tree topology has the same graphical characteristics as radial topology, we use tree here to mean that there is no restriction on the power flow direction. The following constraints, (6.71) to (6.75), adapted from [29] and [113] are given below.

$$\hat{x}_{i,t}^{N} = \hat{x}_{j,t}^{K}, i\epsilon N, j\epsilon K, t\epsilon T \tag{6.71}$$

Equation (6.71) ensures that the energization status of each node, i, within a bus block is the same as the status of the bus block.

$$\left(\hat{x}_{i,t}^{K} - \hat{x}_{i,t-1}^{K}\right) + \left(\hat{x}_{j,t}^{K} - \hat{x}_{j,t-1}^{K}\right) \geq \hat{x}_{ij,t}^{K} - \hat{x}_{ij,t-1}^{K}, (i,j) \in C, t \in T, t > 1, i, j \in K \tag{6.72}$$

Equation (6.72) ensures that if two bus blocks at both terminals on a switchable line are already energized in the previous step, then this line cannot be energized to maintain tree topology.

$$\sum_{i:(i,j)\in C}\left(\hat{x}_{ij,t}^{K} - \hat{x}_{ij,t-1}^{K}\right) + \sum_{i:(k,i)\in C}\left(\hat{x}_{ki,t}^{K} - \hat{x}_{ki,t-1}^{K}\right) \leq 1 + M\hat{x}_{i,t-1}^{K}, i \in K, t \in T, t > 1 \tag{6.73}$$

Equation (6.73) ensures that if a bus block is not energized at a previous step, then it can only be energized by at most one switchable line. Recall that $x_{i,t-1}^{K}$ is the energization status of bus block i at time step $t-1$ and M is a large number. If this bus block is not energized, then $Mx_{i,t-1}^{K} = 0$ and thus forces the RHS of (6.73) to be equal to 1; when the RHS is one, then at most only one switchable branch can energize bus block i. When bus block i becomes energized, then $M\hat{x}_{i,t-1}^{K}$ becomes a large number and disables this constraint.

$$\sum_{i\in N}\hat{x}_{i,t}^{N} - \sum_{(i,j)\in B}\hat{x}_{ij,t}^{BR} = 1, i \in N, t \in T \tag{6.74}$$

Equation (6.74) ensures that a tree topology is maintained for the entire system. The RHS of (6.74) is set to 1 because the goal is to eventually form one microgrid system or else it could be set otherwise. As shown in [113], constraint (6.74) is not sufficient to maintain tree topology; however, combined with (6.72) and (6.73), it can be shown that a tree structure is maintained.

Then lastly,

$$\hat{x}_{ij,t}^{BR} \leq \hat{x}_{i,t-1}^{N} + \hat{x}_{j,t-1}^{N}, (i,j) \in B^{S} \backslash B^{F}, t \in T\ , i,j\ \in N, t > 1 \qquad (6.75)$$

Equation (6.75) ensures that each switchable branch can only be switched on if at least one of its nodes is energized in the previous step.

6.4. Pre-Optimization Processing

The pre-optimization processing are mostly graph based heuristics that analyzes the distribution system to be restored to check for graph connectivity and suggests estimated number of time steps needed as input in the restoration solver.

6.4.1. Network Graph Evaluation

A graph is connected if every vertex is joined to every other vertex by a path. A disconnected graph is a graph that is not connected, that is, not every pair of vertices has a path joining them [114]. Figure 6.5 shows an example of connected and disconnected graphs.

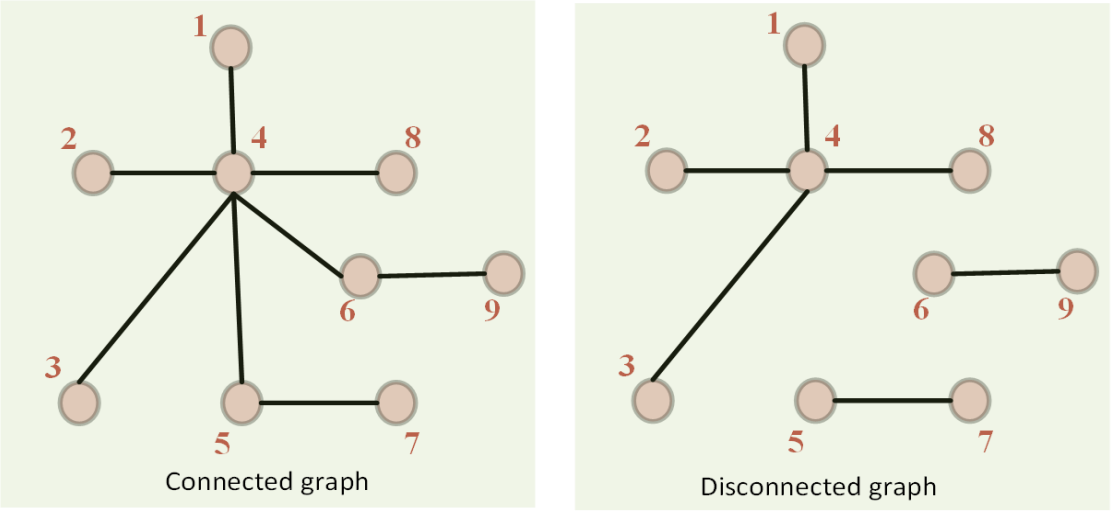

Figure 6.5 An Example of Connected and Disconnected Graphs

To evaluate the system topology for restoration, an undirected graph is generated which includes nodes (or vertices) and edges (or branches) with all damaged branches removed. If the resulting graph is connected, then the system data is used as inputs to the restoration algorithm. However, if the graph is disconnected, then it can be grouped into two or more connected subgraphs with each component subgraph solved separately by the restoration algorithm.

6.4.2. Estimating the Number of Solution Time Steps

To estimate the number of time steps required to restore the entire system, the system is reduced to a set of bus blocks and then we apply the concept of distance and eccentricity from graph theory which is introduced next. Each bus block is regarded as a vertex and each switchable branch between bus blocks is regarded as an edge.

The concept of distance and eccentricity of a vertex/node in a graph as presented in [114, 115] are used. Distance and eccentricity are defined as follows.

6.4.2.1. Distance and Eccentricity

Distance: Let u, v be vertices in a graph G ($u, v \in V(G)$). The distance from u to v is the length of the shortest path from u to v, and is denoted $d(u, v)$ [115].

Eccentricity: The eccentricity, $e(v)$, of a vertex v in a graph G is given by the maximum of all the distances measured from v to every other vertex [115]. That is,

$$e(v) = \max \{d(u, v) | u \in V(G)\} \tag{6.76}$$

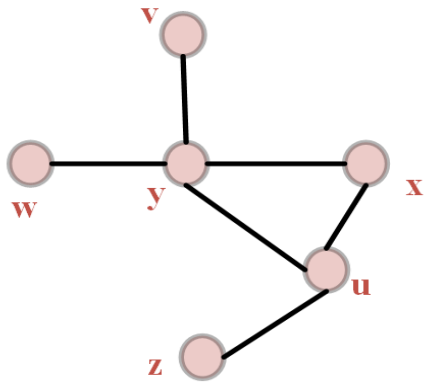

$d(u, v) = 2$
$e(v) = \max\{d(i, v) | i \in [u, w, x, y, z]\} = 3$

Figure 6.6 An Example to illustrate the Concept of Distance and Eccentricity

Figure 6.6 is a simple example to illustrate the concept of distance and eccentricity. From the vertex labeled v to the one labeled u, there are two paths between u and v: 2 edge distance and 3 edge distance paths. Therefore, the distance between u and v is the shortest path and is thus equal to 2. The eccentricity of v is the maximum of all distance from v to every other vertex in the graph. From vertex v to every other vertex in Figure 6.6 has a distance of 2 except for its distance to vertex z, which has a distance of 3. Therefore, the eccentricity of v is equal to 3.

The rationale for using distance and eccentricity is given thus. While the distance gives the minimum number of time steps required to get from vertex v to an arbitrary vertex u, eccentricity gives the maximum of all the required minimum number of time steps required to get from vertex v to every other vertex in the graph. Therefore, if the startup node for the restoration is v, then the eccentricity gives the minimum number of steps required to get to every vertex in the system.

6.4.2.2. Restoration Step Diameter and Radius

We introduce the term *restoration step diameter* (RSD), denoted as $RSD(G)$, which is defined as the maximum of the eccentricities of vertices representing nodes where black start DGs are connected. Let $V_{BS}(G)$ represent the set of vertices with black start DGs. Then, RSD can be written as,

$$RSD(G) = \max\{e(v)|v \in V_{BS}(G)\} \tag{6.77}$$

We also introduce the term *restoration step radius* (RSR), denoted as $RSR(G)$, which is defined as the minimum of the eccentricities of vertices representing nodes where black start DGs are connected. RSR can be written similarly as:

$$RSR(G) = \min\{e(v)|v \in V_{BS}(G)\} \tag{6.78}$$

The RSD gives a generous estimate of the number of time steps required to get from any of the black start vertices to all other vertices in the system. The RSR gives a conservative estimate of the number of time steps required to get from the black start nodes with minimum eccentricity to all other vertices in the system.

6.4.2.3. Conservative and Generous Restoration Steps Estimate

Assuming that the ramp rate of the DGs is sufficiently high, then a generous estimate for the required time steps for the solution method is given as,

$$n_p(T) = RSD(G) + n(G^{BS}) \tag{6.79}$$

The second term of (6.79), $n(G^{BS})$, is the number of black start DGs available for restoration and is added to account for the zero-dispatch synchronization steps when restoration of the branches and loads are paused temporarily for each of the droop-controlled black start DGs.

Similarly, a conservative estimate for the required time steps is calculated by replacing RSD in (6.80) with RSR,

$$n_c(T) = RSR(G) + n(G^{BS}) \tag{6.80}$$

6.4.3. Time Interval Considerations

The time interval between sequences of restoration have to be set for the time domain simulation and verification in PSCAD. Choice of this value is based on system familiarity and inverter fast decaying transients for an exponentially stable system. Detailed analytical procedure for determining the time interval is beyond the scope of this dissertation and will be of interest for future work.

6.5. Post Optimization Processing, Power Sharing and Stability Considerations

Just like we did in post processing of the optimal power flow in section 5.8.8, after the restoration problem is solved, the voltages at each droop node is averaged across the three phases and is taken as the reference voltage setting for each droop inverter.

Notice that because of the reference active and reactive power constraints, the frequency droop co-efficient, $n_{f,g,t}$, and voltage droop co-efficient, $n_{v,g,t}$, do not appear in the optimization formulation as decision variables. The restoration solution is calculated with the goal of setting droop DG's reference active and reactive power to equal its output power, thus making $n_{f,g,t}$ and $n_{v,g,t}$ to not affect its steady-state operating point.

However, the choice of $n_{f,g,t}$ and $n_{v,g,t}$ affect the dynamic stability, power-sharing paradigm, voltage and frequency deviation rate, and sensitivity of the system to changes in the loading. High droop gain increases the sensitivity at the cost of reducing stability margin and increasing frequency and voltage deviation rate [102]. On the other hand, low

droop gain increases the stability margin and decreases frequency and voltage deviation rate at the cost of decreasing the system's sensitivity and response time. Optimal choice of $n_{f,g,t}$ and $n_{v,g,t}$ with consideration of transient stability is, therefore, a trade-off analysis and the range of the choice in this work for the time-domain PSCAD simulation is based on heuristics and system familiarity. A detailed analysis for informed choice of droop co-efficient for each time step will involve large signal stability analysis considering domain of attraction similar to what is done in [52]. Consideration of the domain of attraction between time steps will be of great interest for future work and it is beyond the scope of this dissertation.

Nevertheless, based on the active power-sharing paradigms proposed in section 5.4.2, we can determine the required frequency droop selection ratio for all the droop DGs. One of the power-sharing paradigms presented in section 5.4.2 is selecting the droop coefficients in the inverse proportion of their optimized reference active power. This ensures that changes in system loading are shared in the proportion of the reference active power calculated by the restoration algorithm. That is for each droop DG, i, the $n_{f,i,t}$ is selected as follows,

$$\hat{n}_{f,i,t} P_{ph,i,t}^{ref} = constant \tag{6.81}$$

Recall that equation (5.60) gives the frequency deviation as being equal to the total power mismatch divided by the sum of the inverse frequency droop coefficient. By rearranging (5.60) and a little dimensional analysis, we can see that the inverse of its denominator is the frequency deviation rate in Hz per unit power. Therefore, the minimum

frequency deviation rate in Hz per unit power, Δf_{dev}^{min}, can be constrained using the inverse expression of the denominator of equation (5.60) as follows.

$$\left(\sum_{k\in N}\sum\nolimits_{ph\in\{a,b,c\}}\frac{1}{\hat{n}_{f,k,t}}\right)^{-1}=\left(3\sum_{k\in N}\frac{1}{\hat{n}_{f,k,t}}\right)^{-1}\leq\Delta f_{dev}^{min} \tag{6.82}$$

Equations (6.81) and (6.82) can provide guidance in heuristically choosing the frequency droop coefficients. For the voltage droop coefficient, the same value is assumed for all the droop DGs.

6.6. Implementation of Multi-Master Restoration Methodology

The methodology is implemented as a MATLAB program. The mathematical modeling in MATLAB is written with the YALMIP toolbox [85] and solved using the Gurobi optimizer [86]. A flowchart of the implementation of the proposed methodology is shown below,

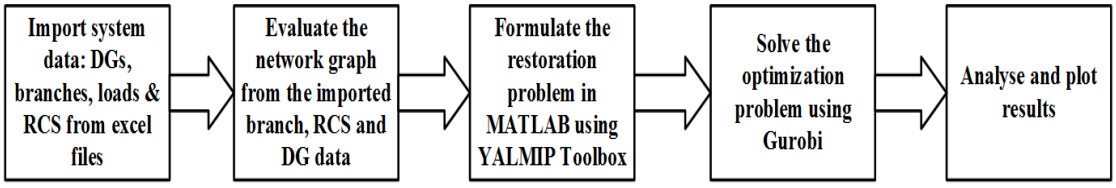

Figure 6.7 Flow Chart Describing the Implementation of the Restoration Methodology

The system data is stored as an Excel file and is imported into MATLAB. The imported data are then evaluated to create the network graph. This graph is evaluated to check for connectivity and then conservative and generous time step estimates are calculated for the network graph. Afterwards, the imported data together with choice of

time steps (a conservative, generous, or a different time step can be selected) are fed as inputs into the restoration algorithm which was developed as a MATLAB function. Within the restoration MATLAB function, YALMIP toolbox is used to create a mathematical model of the system and then Gurobi optimizer is called to solve the mathematical model of the system to be restored. Lastly, the results that are returned from the Gurobi optimizer are organized and plotted.

6.7. Section Conclusion

In this section, we have presented a black start restoration methodology with considerations of droop as the primary control. The objective is to maximize the total energy restored in the chosen restoration time steps while ensuring that operational constraints are not violated. The constraints considered are broadly classified as initial sequencing constraints, connectivity constraints, synchronization enhancing constraints, power flow constraints, DG and system operation constraints, topology and sequencing constraints. The constraints are linearized using existing and novel approaches to realize a mixed-integer linear programming problem. Unlike the restoration formulation in section 4.5 where multiple microgrids are formed, this formulation ensures that a single microgrid is formed, and this is made possible by controlling the grid-supporting DGs in droop mode. Droop control makes it possible for power sharing and voltage reference negotiation among the grid-supporting DGs.

7. CASE STUDIES AND PERFORMANCE VERIFICATION

In this section, we apply the black start methodology developed in section 6 to islanded microgrids built from modified IEEE 13 and 123 node test feeders.

7.1. Test Systems

The microgrids used in the following case studies are derived from the IEEE 13 and 123 node test feeders. General details of the system can be found in Appendix D and Appendix E, respectively. Specific changes to the system for each case study are highlighted in their respective case study sections.

7.2. Performance Metrics and Computation Options

The following performance metrics and computation options are referred to throughout the case study sections.

7.2.1. Total Energy Restored (Objective Function)

The total energy restored, E, is a measure of how much active loads were restored and how fast they were restored in the time horizon under consideration. This is the objective function to be maximized presented in section 6.3.1 and can be written as shown below:

$$E = \sum_{t \in T} \sum_{l \in L} \sum_{ph \in \{a,b,c\}} \hat{P}_{ph,l,t} . \Delta t \tag{7.1}$$

where $\hat{P}_{ph,l,t} = x^L_{l,t} P_{ph,l,t}$. $x^L_{l,t}$ is a binary variable which represents the energization status of the load l at time step t, and $P_{ph,l,t}$ is the nominal value of load l at time step t for phase ph, Δt is the time interval between steps and is assumed to be a constant value for all

intervals (essentially it is factored out and ignored). For demand response loads, $\hat{P}_{ph,l,t}$ is defined differently to vary over a range as follows: $x_{g,t}^{L} P_l^{min} \leq \hat{P}_{ph,l,t} \leq x_{g,t}^{L} P_l^{max}$, where P_l^{min}/P_l^{max} is the minimum/maximum of the range that the demand response load is allowed to vary. E can be seen as having the units of $kW.steps$ In comparative case studies that follow, E will be used as one of the measures to compare performance and load restoration outcomes.

7.2.2. Best Bound

One unique property of mixed-integer programming problems is having a knowledge of a lower or upper bound of the objective function for a minimization or maximization problem respectively. This knowledge usually comes from some form of relaxing the constraints of the problem [116]. For a minimization problem, the solver returns a lower bound for the objective function, which is called the best bound. The best bound gives an idea of how good an optimal solution can be when optimality was not proved for the incumbent solution. The difference between the current best objective value (from the incumbent solution) and the best bound is called the gap and is expressed in Gurobi as a percentage of the current best objective value [116]. When the gap is zero, then optimality has been proved.

7.2.3. Sum of Nominal Active Loads Restored

The sum of the nominal active loads restored is the summation of the nominal active power of all aggregate loads that are energized by the last restoration step.

7.2.4. Total Number of Restored Aggregate Load

The total number of restored aggregate load is an integer count of the number of restored aggregate load.

7.2.5. Computation (Solver) Time

Computation time, or solver time, is the run time in seconds it takes the solver to find the best or optimal solution. In the comparative case studies, different scenarios were run under the same processor capability with the computation time providing insight into the comparative computation burden of each scenario.

7.2.6. Mean Error with PSCAD Simulation as Benchmark

The mean error of different parameters like bus voltages and power injection when compared to detailed time-domain simulation in PSCAD helps to verify the accuracy of the methodology. This was accomplished by using the restoration results such as branch, load and DG turn on sequences to set up a detailed time-domain simulation and then comparing the variable values from the PSCAD simulation to corresponding variables obtained during execution of the proposed methodology.

7.2.7. Computation Options

The computation options are the different choices under which each case study is computed. A model that may be infeasible can be feasible under a different choice of computation option and this gives insight on how the method performs under different computational conditions. These computation options are summarized below.

7.2.7.1. Options.connectGFDGs

The first option is set using the field “Options.connectGFDGs”. Setting this field as “true” ensures that all grid-forming (GF) DGs (or more precisely grid-supporting DGs) are connected at the last step to improve system resilience even if a certain grid-supporting DG is not needed to restore the loads. This option adds a constraint to the problem which enforces that all GF DGs are connected at or before the last step of the restoration. Care has to be taken when this is set as true to ensure that the necessary amount of time steps has been chosen and that the topology can allow for this. If not, it will result in an infeasible solution. When in doubt, this option has been set to “false”.

7.2.7.2. Options.skipPWL

“skipPWL” stands for skip piecewise linearization. Because of the computational burden and numerical issues of the piecewise linearization of the product of two continuous variables (Appendix B), an alternative given in Appendix C can be used instead. Setting this option to false will only use the piecewise linearization at the last time step and use the alternative approximation given in Appendix C for the other time steps. Setting it to true will skip the piecewise linearization for all time steps.

7.2.7.3. Options.ignoreShuntAdmittance

“Options.ignoreShuntAdmittance” determines if the shunt admittance is ignored or not. Selecting true will ignore the shunt admittance of the branches for all time steps. The reason for introducing this option is because the relatively small value of the shunt admittance can increase numerical instability for systems as large as the IEEE 123 node test feeder. Because the distribution lines are relatively shorter compared to the bulk power

system transmission lines, the shunt admittance can be ignored without incurring significant errors. This is similar to the linear power flow approach used in DistFlow in which the shunt admittance is ignored [64, 65].

7.2.7.4. Options.includeShuntAdmittanceForLastStepOnly

This option is a sub-option to the immediate previous option. Selecting false in the previous option and selecting true to this option will cause the method to use the shunt admittance for the last step only.

7.2.7.5. Options.MIPGap

MIPGap stands for the relative MIP (mixed-integer programming) optimality gap. The Gurobi solver used is based on the branch-and-bound search method. For a minimization problem, the branch-and-bound procedure returns lower bound for the objective function, which is called the best bound. The difference between the current best objective value and the best bound is called the gap [116]. In Gurobi, the gap is usually returned as a percentage of the current best objective value. When the gap is zero, then optimality has been proved. The default value of the MIPGap in Gurobi is 1e-4 (that is 0.01%). To use a different MIPGap, this option should be set with the desired MIPGap value.

7.2.7.6. Conservative/Generous Time Step Estimate

Before the method is run, a graphical preprocessing is performed to estimate the number of necessary time steps. The options for the time step after the preprocessing is to choose either conservative, generous, or a different user-entered number of time steps.

7.3. Case Studies

The subsections that follow present various cases that were solved using the proposed black start restoration methodology. In all cases, the proposed method was implemented in MATLAB and utilized the YALMIP [85] MATLAB toolbox to interface the Gurobi [86] 9.0.2 optimization solver, and was solved in a Windows computer with Intel Core i7 2.80 GHz CPU, 8 GB of RAM and 64-bit operating system.

Some of the common computational settings and parameters common across the cases include the following:

- ZIP load coefficient: Without loss of generality, the ZIP load co-efficient for every load has been set to 0.4, 0.3, and 0.3 for constant impedance, current, and power components respectively.
- The node voltage magnitude has been constrained to [0.95 1.05] per unit for all energized nodes except for the droop-controlled DG nodes which are constrained to [0.95 1.1] per unit. The droop-controlled DG nodes have a higher upper limit for the voltage magnitude because of their inductor coupling which can drop the voltage transmitted to the adjacent node.
- The phase voltage magnitude difference between any two phases at a droop-controlled node has been constrained to be less than 0.01 per unit

7.4. Case Studies 1: Case Studies for Validation and Performance Verification using PSCAD Simulation as a Benchmark

The purpose of the case studies categorized under case studies 1 is to validate that the MATLAB program implementing the restoration in autonomous multi-master microgrids performs the basic functionalities stated in the method formulation of section 6.

7.4.1. Case Studies 1 Test System

The islanded microgrid used for the case studies 1 is adapted from the IEEE 13 node test feeder [84]. Details of this test system are available in Appendix D. Because of the bulkiness of the time domain PSCAD modeling of the power electronics and the complexities of multi-interacting low-level controller tuning which is beyond the scope of this dissertation, we limit the PSCAD simulation to IEEE 13 node test feeder only for case studies 1. Some of the other case studies will be adapted from the modified IEEE 123 node test feeder. Case studies 1 is made up of five scenarios and these are summarized as follows:

- Scenario 1: case studies for validation of topology and sequencing constraints (section 6.3.7)
- Scenario 2: case studies for validating the effects of DG ramp rate and ramp rate constraints (section 6.3.6.7)
- Scenario 3: case studies for validating the effects of different DG capacities
- Scenario 4: case studies for validating the effects of different loading conditions

- Scenario 5: verification of steady-state power flow results of the base cases in scenario 1 to 4 above using PSCAD simulation

The computation options for all cases categorized under case 1 section is outlined in Table 7.1 below,

Table 7.1 Computation Settings for Case 1 Studies

Options	Choice
Options.connectGFDGs	True
Options.skipPWL	False
Options.ignoreShuntAdmittance	False
Options.includeShuntAdmittanceForLastStepOnly	True
Options.MIPGap	0.01% (Default)
Conservative/Generous Time Step Estimate	Varies with case

For all cases under case studies 1, the active and reactive power difference between any two phases of a three-phase droop-controlled DG has been constrained to be no more than 0.05% of the values of P_{max} and Q_{max} of the DG. Also, the nominal system load unbalance index (NSLUI) for the active and reactive power load have been constrained and compensated to be no more than 2%.

7.4.2. Scenario 1: Validation of Topology and Sequencing Constraints

7.4.2.1. Description of Test System

Under this scenario, there is a total of 6 cases run numbered scenario 1.1, 1.2, to 1.6 of which scenario 1.1 is considered the base case. Scenario 1.2 to 1.6 is derived from 1.1 by randomly varying which lines are switchable and non-switchable. Validation of the topology and sequencing constraints is by observing the graph of the restored system for every step to ensure that the sequences of restoration are as outlined in sections 6.3.7 and 6.3.2. Topology and sequencing constraints are also observed in other scenario cases

studied later to ensure that the sequences of restoration are as outlined in sections 6.3.7 and 6.3.2.

A one-line diagram of the base test system is shown in Figure 7.1. In the diagram of Figure 7.1, the thickest lines are three-phase branches, the medium-thick lines are two-phase branches, and the least thick lines are single-phase branches. Phase information for the two-phase and single-phase branches have been shown as well. This test system is made up of two three-phase droop-controlled DGs at nodes 2632 and 2680 (these two additional nodes are coupled to their adjacent node through inductor coupling), and three single-phase PQ DGs at nodes 633, 671 and 675. The branch adjacent to a droop-controlled DG node is assumed to be the inductor coupling, for instance, the branch between nodes 632 and 2632 is the inductor coupling. The system is assumed to have experienced a blackout following the failure of the bulk power grid due to a severe occurrence such as a hurricane, and thus, the system was islanded from the bulk system to initiate a black start procedure.

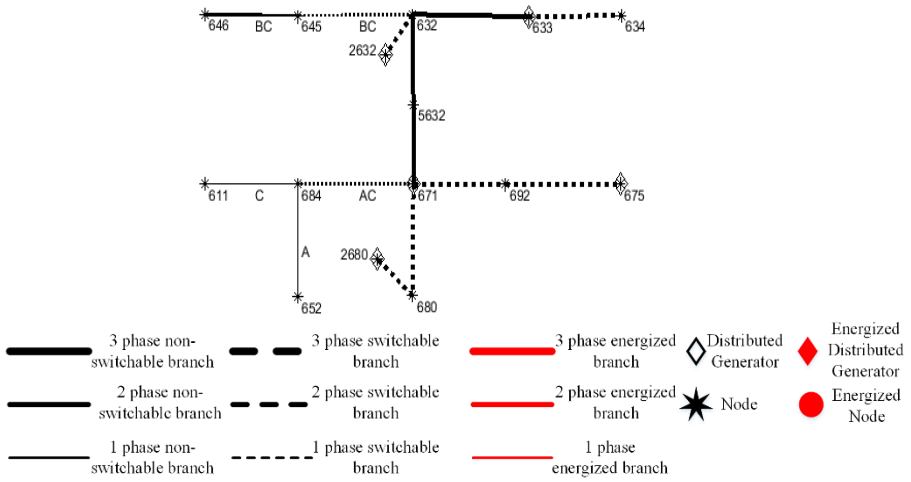

Figure 7.1 One-Line Diagram of the Modified IEEE 13 Node Test Feeder for the Base Case of Case 1 Scenario 1

7.4.2.2. DGs Information

The DGs' information is shown in Table 7.2. The f^{ref} column is the reference frequency for the droop-controlled DGs. The "pu (per unit) coupling X" column is the value of the inductor coupling between the droop-controlled DG's node and its adjacent node in per unit. The pu X is calculated using the "baseMVA" and "baseKVA" columns. "Pmax" and "Pmin" columns contain the maximum and minimum allowable active power for each DG. "Qmax" and "Qmin" columns contain the maximum and minimum allowable reactive power for each DG. The "phase" column is the phase of the node where the DG is connected. Droop-controlled DGs are connected to all three phases while PQ DGs are assumed to be connected to one phase. The "status" column is used to denote whether a DG can participate in the restoration; "1" means that the DG is healthy and can participate while "0" means it cannot participate. The "ramp rate" column gives the

allowable step change in the DG's output active and reactive power expressed as a percentage of the Pmax and Qmax.

Table 7.2 DGs' Information for Case 1 Scenario 1

Label	Node	Type	f^{ref} (Hz)	Per phase BaseMVA	per phase baseKV	pu coupling X	Pmax (KW)	Pmin (KW)	Qmax (KVAR)	Qmin (KVAR)	Phase	Status	Blackstart	Ramp Rate %
DG1	2680	Droop	60	1	2.4018	0.5	500	0	300	-75	ABC	1	1	40
DG2	2632	Droop	60	1	2.4018	0.5	500	0	300	-75	ABC	1	1	40
DG3	671	PQ	NA	NA	2.4018	NA	150	0	100	0	C	1	0	60
DG4	675	PQ	NA	NA	2.4018	NA	150	0	100	0	A	1	0	60
DG5	633	PQ	NA	NA	2.4018	NA	150	0	100	0	B	1	0	60

7.4.2.3. Time Step Estimation using Bus Block Graph

Estimation of the number of the time steps is done as explained in section 6.4.2. To calculate the restoration step distance (RSD), we reduce Figure 7.1 to a graph of bus blocks as follows. The bus blocks are labeled in red from numbers 1 to 9 in Figure 7.2. Bus blocks 1 and 7 are the ones that are connected to black start droop-controlled DGs, thus, $V_{BS}(G) = \{1, 7\}$. Analyzing the eccentricities of the resulting bus block graphs from vertices 1 and 7 gives:

$$RSD(G) = \max\{e(v)|v \in V_{BS}(G)\} = 4 \tag{7.2}$$

$$RSR(G) = \min\{e(v)|v \in V_{BS}(G)\} = 3 \tag{7.3}$$

where RSD is the restoration step diameter and RSR is the restoration step radius.

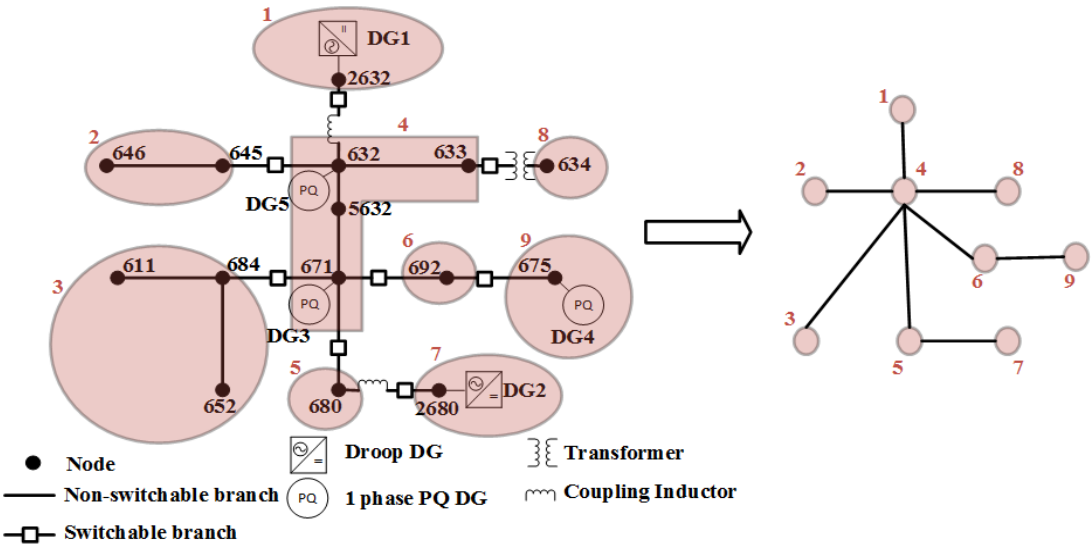

Figure 7.2 Reduction of the Microgrid to Bus Blocks for Case 1

Therefore, the generous restoration step estimate is calculated as follows:

$$n_p(T) = RSD(G) + n(G^{BS}) = 4 + 2 = 6 \tag{7.4}$$

While the conservative restoration step estimated is calculated as:

$$n_p(T) = RSR(G) + n(G^{BS}) = 3 + 2 = 5 \tag{7.5}$$

The generous restoration step estimate of 6 is used for all the cases under this scenario. Note that the above-calculated step estimates were done using the graph of the base case.

7.4.2.4. Restoration Sequence Graph

The one-line diagram of the restoration sequence for the base case is shown in Figure 7.3 (a) to (f). Line thickness as shown in the legend has been used to denote single, double, and three-phase branches.

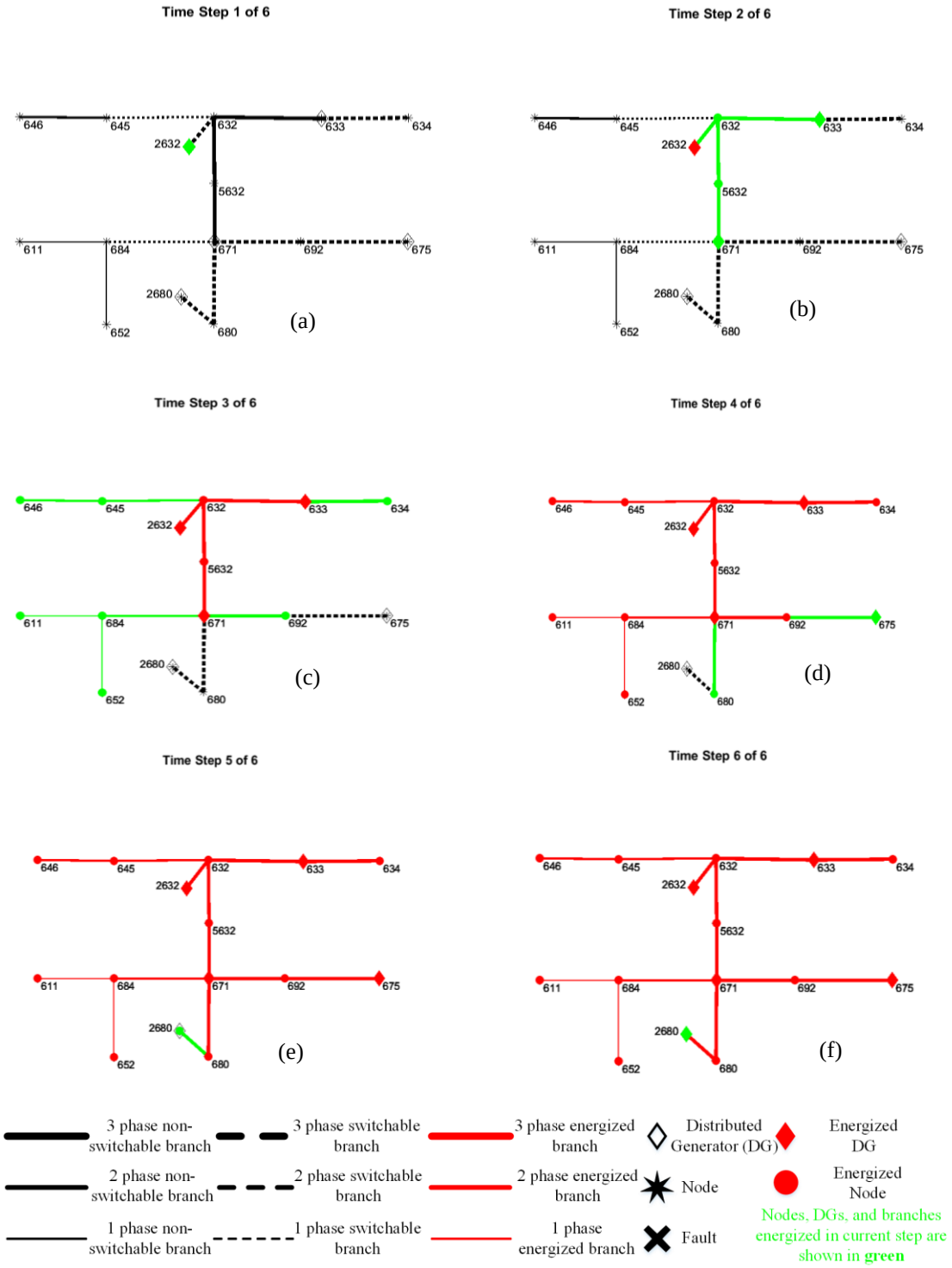

Figure 7.3 Restoration Sequence for Case 1 Scenario 1.1

Figure 7.3(a), which is the first step of the black start restoration, shows that node 2632 is chosen as the start-up node since a droop-controlled DG is connected here. Every other node and branch is still in de-energized state. This is in accordance with the initial sequencing constraints of section 6.3.2.

The concept of a bus block was introduced in the topology and sequencing constraints under section 6.3.7. By considering Figure 7.3(a), nodes 632, 633, 5632, and 671 are classified under the same bus block since they are connected by non-switchable branches. Recall that in section 6.3.7, all elements of a bus block are energized together. Therefore, in step 2, when the branch between nodes 2632 is energized, all the nodes of this bus block (nodes 632, 633, 5632, and 671) are all energized at this step. All the other bus blocks in this island microgrid also follow the same condition of being energized at the same time. Also, notice how the system builds across the restoration steps: a switchable branch is only switched on if at least one of its nodes is energized in the previous step in accordance with the topology and sequencing constraints.

The restoration graph of the first and last steps for scenario 1.2 to 1.6 is shown in Figure 7.4 to Figure 7.8. The same legend in Figure 7.3 was used for Figure 7.4 to Figure 7.8. These derived scenarios also comply with the topology and sequencing constraints just as scenario 1.1.

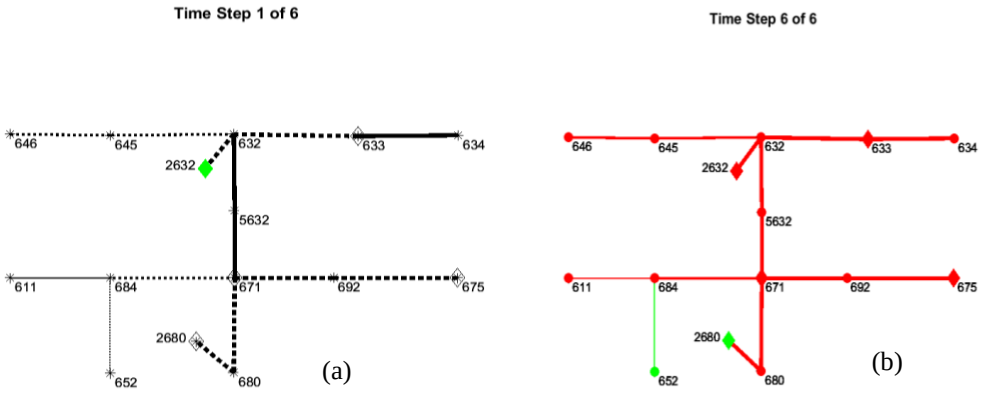

Figure 7.4 Restoration Sequence for Case 1 Scenario 1.2 showing the First and Last Steps

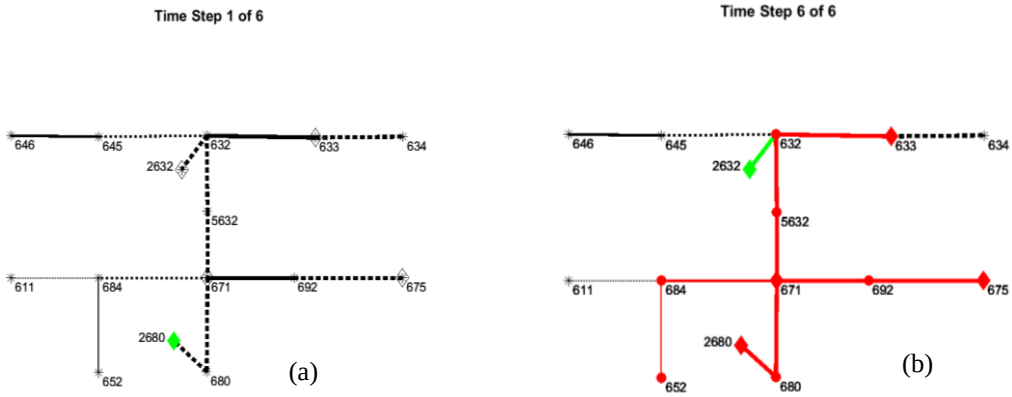

Figure 7.5 Restoration Sequence for Case 1 Scenario 1.3 showing the First and Last Steps

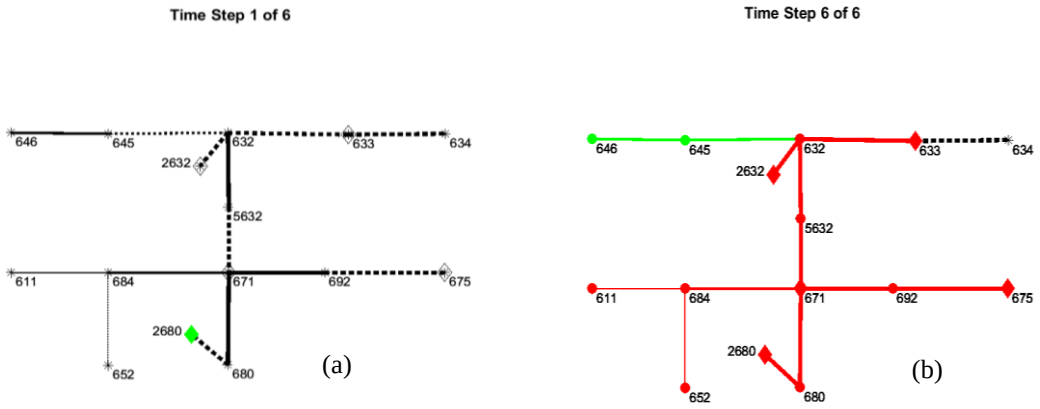

Figure 7.6 Restoration Sequence for Case 1 Scenario 1.4 showing the First and Last Steps

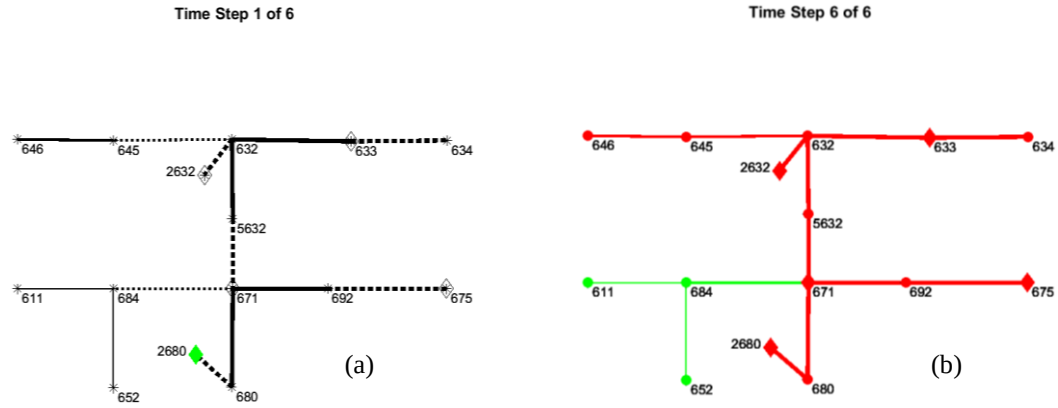

Figure 7.7 Restoration Sequence for Case 1 Scenario 1.5 showing the First and Last Steps

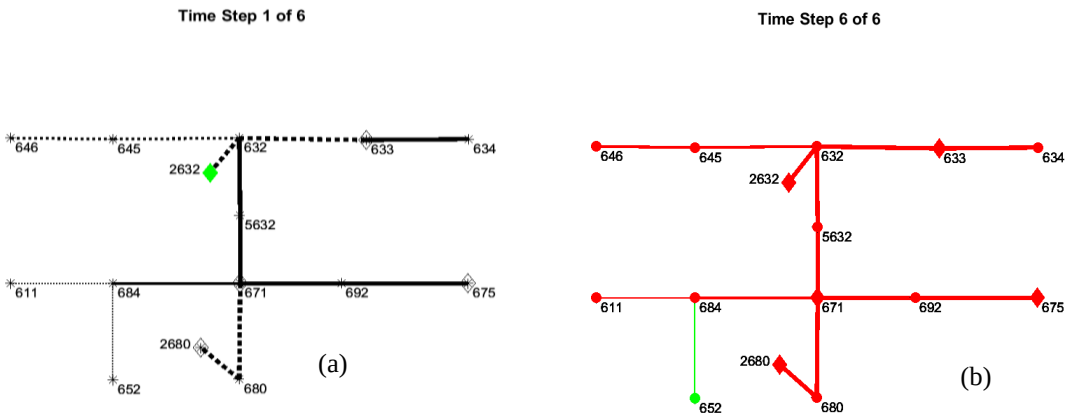

Figure 7.8 Restoration Sequence for Case 1 Scenario 1.6 showing the First and Last Steps

Figure 7.4 to Figure 7.8 show which branches are switchable versus which ones are non-switchable for scenarios 1.2 to 1.6. The intermediate sequences between the first and last steps have been omitted.

7.4.2.5. Load Restoration Results

The load details and restoration steps for each load across scenario 1.1 to 1.6 are shown in Table 7.3. The turn-on steps for the loads in scenario 1.1 to 1.6 have been assigned a column in Table 7.3. All loads are assumed to be switchable and restorable. Table 7.3 shows that the initial state of the topology of scenarios 1.4, 1.5, and 1.6 restored more load. As an aside, there doesn't seem to be a general rule of thumb for the initial state of topology that is more beneficial; however, it is an interplay of DGs' capacity and where they are situated, number of solution steps, and the extent to which the initial state of the topology enhances balancing of the loads as seen from the three-phase droop-controlled DGs.

Table 7.3 Load Details and Restoration Steps for Case 1 Scenarios 1.1 to 1.6

Node	Config	P(a/B/C) KW	Q(A/B/C) KVAR	Turn-On Step, Scenario 1.1	Turn-On Step, Scenario 1.2	Turn-On Step, Scenario 1.3	Turn-On Step, Scenario 1.4	Turn-On Step, Scenario 1.5	Turn-On Step, Scenario 1.6
611	Y	0/0/85	0/0/40	Off	Off	Off	6	Off	Off
634	Y	83/60/30	55/45/15	Off	Off	Off	Off	4	4
645	Y	0/82/0	0/62.5/0	4	4	Off	6	6	6
646	D	0/115/0	0/66/0	Off	Off	Off	6	4	4
652	Y	100/0/0	55/0/0	Off	Off	Off	6	Off	6
671	D	110/90/90	60/50/50	5	5	5	4	3	3
671	Y	2.835/11/19.5	1.665/6.335/11.35	2	3	5	Off	3	3
675	Y	100/34/70	45/30/40	4	4	4	3	6	2
692	D	0/0/85	0/0/75.5	4	4	Off	4	4	Off
5632	Y	5.665/22/39	3.335/12.665/22.65	2	3	4	3	3	2

7.4.2.6. Voltage Magnitude Plot at Last Step

The method ensured that the voltages are constrained within the limits set according to the voltage limit constraints. Because of the linearization that was utilized to convert the rectangular voltages for each node into magnitude form, the voltages at the nodes occasionally violated the constraints bound by as little as 0.01 per unit. Only the last step of the base case is in Figure 7.9.

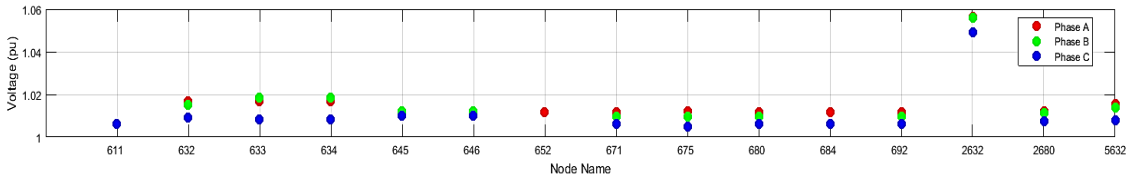

Figure 7.9 Voltage Magnitude across all Nodes for Case 1 Scenario 1 Base Case at Last Step

7.4.2.7. Summary of Case 1 Scenario 1 Results

Table 7.4 shows a summary of the 6 cases run in this scenario. The columns represent the performance metrics outlined in section 7.2.

Table 7.4 Summary of Case 1 Scenario 1.1 to 1.6 Results

	Total Number of Restored Load	Sum of Nominal Active Power of Loads Restored (KW)	Solver Time (Sec)	Objective Value (KW-Steps)	Best Bound (KW-Steps)	Optimality Gap (%)
Scenario 1.1	6 out of 10 loads	761	287	(-)2,193	(-)2,193	0
Scenario 1.2	6 out of 10 loads	761	705	(-)2,093	(-)2,093	0
Scenario 1.3	4 out of 10 loads	594	106	(-)1,459	(-)1,459	0
Scenario 1.4	8 out of 10 loads	1,028	240	(-)2,590	(-)2,590	0
Scenario 1.5	8 out of 10 loads	1,049	204	(-)2,965	(-)2,965	0
Scenario 1.6	8 out of 10 loads	1,064	406	(-)3,693	(-)3,693	0

In all the 6 cases in this scenario, the sequences and topology follow the conditions outlined in sections 6.3.7 and 6.3.2. These conditions can be summarized as: the black start restoration should start from a single start-up node, build sequentially while maintaining tree topology, and all elements in a bus block should have the same status. In the case studies that follow, it is observed that the topology and sequencing process of the restored systems always work as expected.

7.4.3. Scenario 2: case studies for validating the effect of DG ramp rate and ramp rate constraints

7.4.3.1. Description of Test System

Under this scenario, there were a total of 6 cases run numbered scenario 2.1, 2.2, to 2.6 of which scenario 2.1 is considered the base case. Scenarios 2.2 to 2.6 were derived from 2.1 by multiplying the DG ramp rate of 2.1 with a factor of 0.33, 0.67, 1.33, 1.67, and 2, respectively. The purpose of these cases is to evaluate the effects/validation of the DG ramp rate. The DG ramp rate constraints are described in section 6.3.6.7. In practice,

the ramp rate of a DG between two restoration steps would depend on a lot of factors such as time interval between steps, local controller type, and prime mover's dynamics. Determining the practical ramp rate is not in the scope of this work. However, in the cases under this scenario, we assume that the DG ramp rates are known and then test the method for different assumed ramp rate settings.

A one-line diagram of the base test system is shown in Figure 7.10. This test system is made up of two three-phase droop-controlled DGs at nodes 2632 and 2671, and three single-phase PQ DGs at nodes 632, 671 and 675. The system is assumed to have experienced a blackout following the failure of the bulk power grid due to a severe occurrence such as a hurricane, and thus, the system was islanded from the bulk system to initiate a black start procedure.

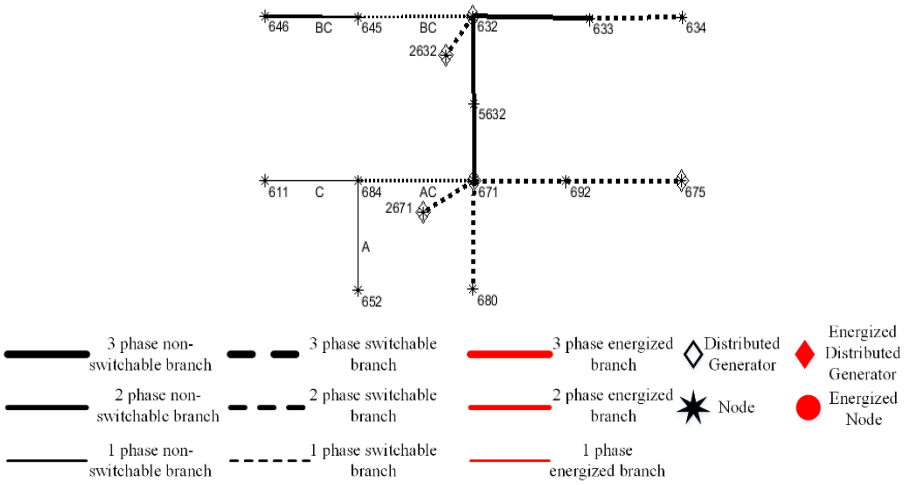

Figure 7.10 One-Line Diagram of Modified IEEE 13 Node Test Feeder for the Base Case of Case 1 Scenario 2

7.4.3.2. DGs Information

The DGs' information is shown in Table 7.5. The DGs' information columns are the same as previously described in section 7.4.2.2.

Table 7.5. DGs' Information for Case 1 Scenario 2

Label	Node	Type	f^{ref} (Hz)	Per phase BaseMVA	per phase baseKV	pu coupling X	Pmax (KW)	Pmin (KW)	Qmax (KVAR)	Qmin (KVAR)	Phase	Status	Blackstart	Ramp Rate %
DG1	2671	Droop	60	1	2.4018	0.5	600	0	300	-50	ABC	1	1	50
DG2	2632	Droop	60	1	2.4018	0.5	600	0	300	-50	ABC	1	1	50
DG3	671	PQ	NA	NA	2.4018	NA	200	0	120	0	C	1	0	50
DG4	675	PQ	NA	NA	2.4018	NA	200	0	120	0	A	1	0	50
DG5	632	PQ	NA	NA	2.4018	NA	200	0	120	0	B	1	0	50

7.4.3.3. Time Step Estimation using Bus Block Graph

Estimation of number of time steps is performed as explained in section 6.4.2. By graphically analyzing the one-line diagram of Figure 7.10, the conservative and generous time steps were estimated to be both 5. The time step of 5 was chosen to solve for the black start restoration of the microgrid system.

7.4.3.4. Restoration Sequence Graph

The one-line diagram of the restoration sequence for the base case is shown in Figure 7.11 (a) to (e). Line thickness is shown in the legend and has been used to denote single, double, and three-phase branches. Just like in the previous scenario, the topology and sequencing features of the microgrid in Figure 7.11 (a) to (e) followed the expected sequence across the restoration steps. The restoration graph of the derivative scenarios, that is scenarios 2.2 to 2.6, have been omitted.

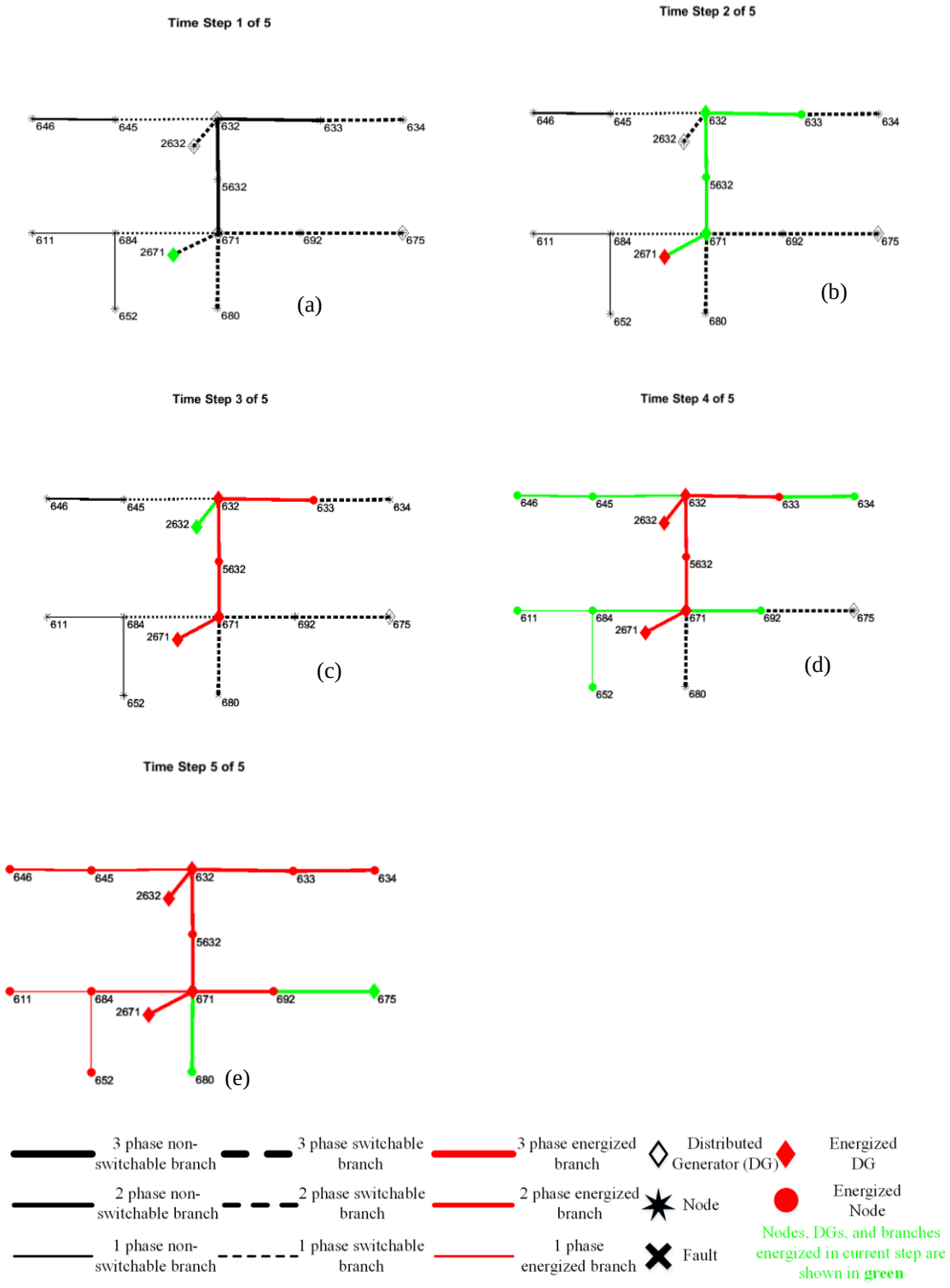

Figure 7.11 Restoration Sequence for Case 1 Scenario 2.1

7.4.3.5. Load Restoration Results

The load details and restoration steps for each load for scenarios 2.1 to 2.6 are shown in Table 7.6. All loads are assumed to be switchable and restorable. As expected, Table 7.6 shows that generally under the same condition, the higher ramp rate leads to more loads being restored. As shown in the next subsection, the DG ramp rate constraints are maintained and loads that would have violated the constraints are not restored. Notice that solving the restoration model using the generous time step estimate does not guarantee that the system will restore as much as it can. If the ramp rate is sufficiently high, then the generous step estimate will be sufficient to restore all the loads that the DGs in the system can afford to.

Table 7.6 Load Details and Restoration Steps for Case 1 Scenario 2.1 to 2.6

Node	Config	P(a/B/C) KW	Q(A/B/C) KVAR	Turn-On Step, Scenario 2.1 (Base Case)	Turn-On Step, Scenario 2.2 (Ramp Factor: × 0.33)	Turn-On Step, Scenario 2.3 (Ramp Factor: × 0.67)	Turn-On Step, Scenario 2.4 (Ramp Factor: × 1.33)	Turn-On Step, Scenario 2.5 (Ramp Factor: × 1.67)	Turn-On, Scenario Step 2.6 (Ramp Factor: × 2)
611	Y	0/0/85	0/0/40	4	Off	5	3	3	3
634	Y	83/60/30	55/45/15	4	Off	5	3	3	3
645	Y	0/82/0	0/62.5/0	4	Off	5	3	3	3
646	D	0/115/0	0/66/0	5	Off	5	3	3	3
652	Y	100/0/0	55/0/0	5	Off	5	5	5	5
671	D	110/90/90	60/50/50	4	5	4	2	2	2
671	Y	2.835/11/19.5	1.665/6.335/11.35	2	2	2	2	2	2
675	Y	100/34/70	45/30/40	5	Off	Off	5	5	5
692	D	0/0/85	0/0/75.5	Off	Off	Off	Off	5	5
5632	Y	5.665/22/39	3.335/12.665/22.65	2	3	2	5	5	5

The ramp factor in Table 7.6 for the derivative cases is a factor that was used to multiply the ramp rates of the base case to get that particular derivative case. For example, each of the DGs in the base case (scenario 2.1) has a ramp rate of 50% per restoration step,

and scenario 2.2 with a ramp rate factor of 0.33 means that each of the DGs in this scenario case are modified to have a ramp rate of $50 \times 0.33 = 16.5\%$ per restoration step.

7.4.3.6. DG Dispatch Result and Ramp Rate Validation

The three-phase power reference settings for the two droop-controlled DGs and power setpoints for the PQ DGs for the base case of scenario 2.1 are shown in Figure 7.12 to Figure 7.15. The legend for the DGs are formed by joining "DG" to the node number where the DG is connected, for instance, the droop DG at node 2671 is called DG2671 in the legend of Figure 7.12. Figure 7.12 (b) to Figure 7.15 (b) show the ramp rates and ramp limits (red horizontal line) for the DGs; for figures with both ramp down and ramp up, the ramp-up and ramp-down limits have been shown, and for those with only ramp up, ramp up limit has been shown (ramp down limit is negative of ramp up limit). The ramp rate for each DG at step n, for instance, is found by subtracting its dispatch power setting at step $n-1$ from its power setting at step n.

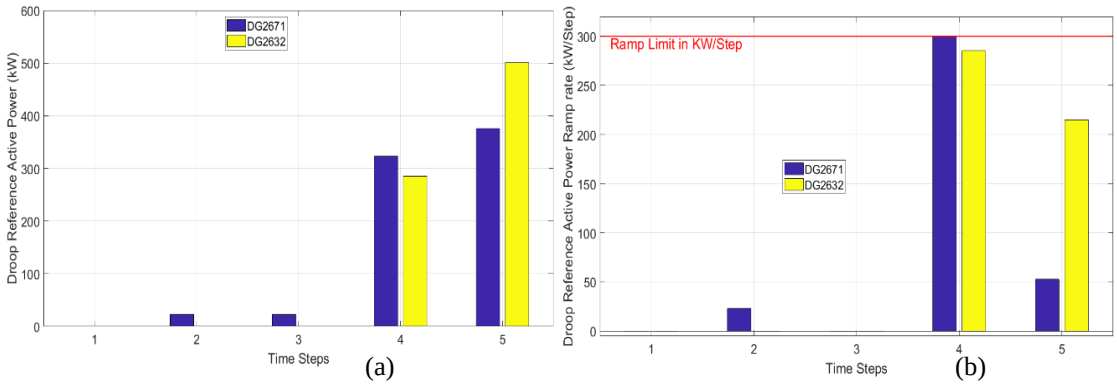

Figure 7.12 (a) Droop Three-Phase Active Power Reference (b) Droop Three-Phase Active Power Ramp Rate per Step for the Base Case

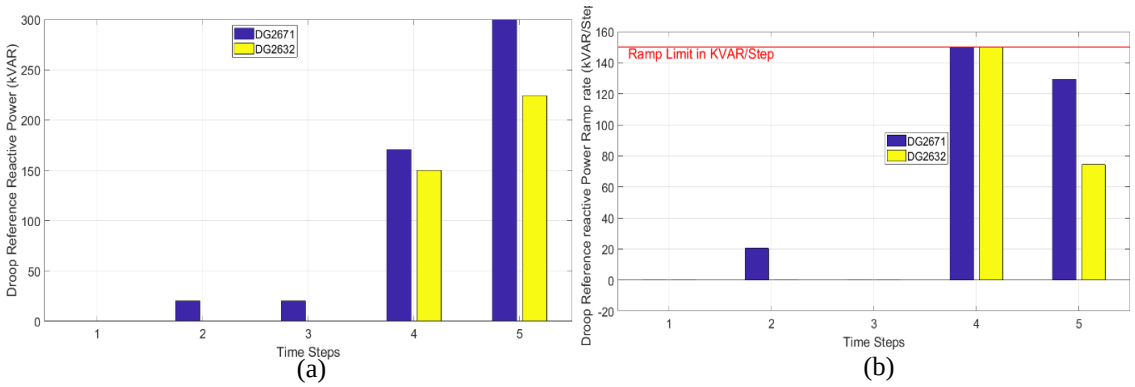

Figure 7.13 (a) Droop Three-Phase Reactive Power Reference (b) Droop Three-Phase Reactive Power Ramp Rate per Step for the Base Case

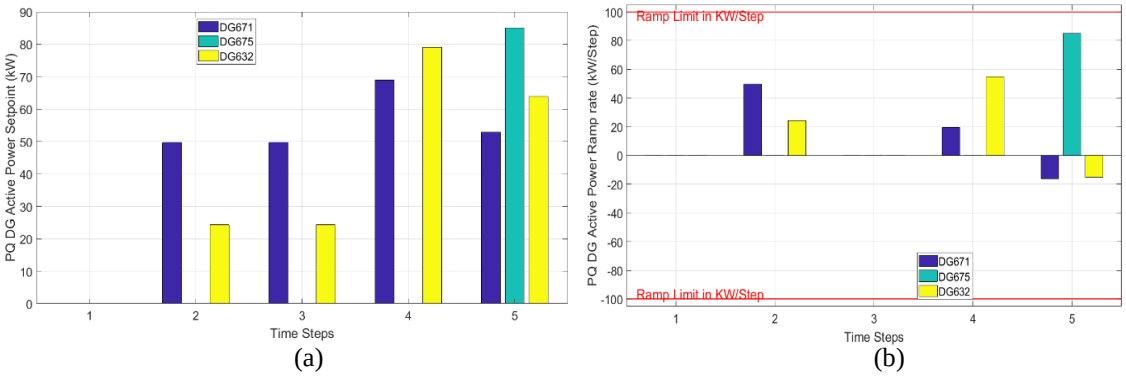

Figure 7.14 (a) PQ DG Active Power Setpoint (b) PQ DG Active Power Ramp Rate per Step for the Base Case

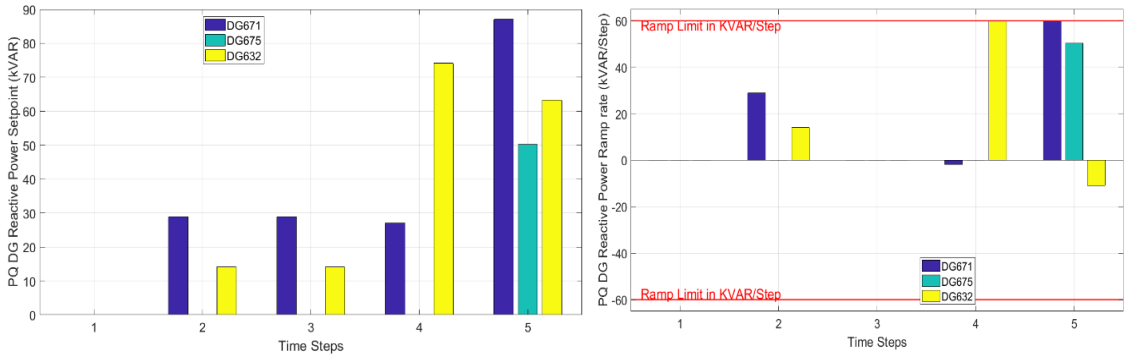

(a) (b)

Figure 7.15 (a) PQ DG Reactive Power Setpoint (b) PQ DG Reactive Power Ramp Rate per Step for the Base Case

Notice that the ramp rate for step 1 is zero for all of Figure 7.12 (b) to Figure 7.15 (b) since this was the first step where the black start DG at node 2671 was energized (compare with sequence graph of Figure 7.11a of the base case). Also notice the ramp rate for step 3 is zero for all of Figure 7.12 (b) to Figure 7.15 (b), since this is the synchronization step for the second droop-controlled DG at node 2632 (compare with sequence graph of Figure 7.11c of the base case). This is following the zero-dispatch and system "freeze" requirement for the synchronization of a droop-controlled DG.

Figure 7.12 (b) to Figure 7.15 (b) show that the DG ramp rate for all time steps is within the ramp rate limits which are denoted by a red horizontal line.

7.4.3.7. Voltage Magnitude Plot at Last Step

The method ensured that the voltage lies within the limits set according to the voltage limit constraints. Only the last step of the base case is shown in Figure 7.16.

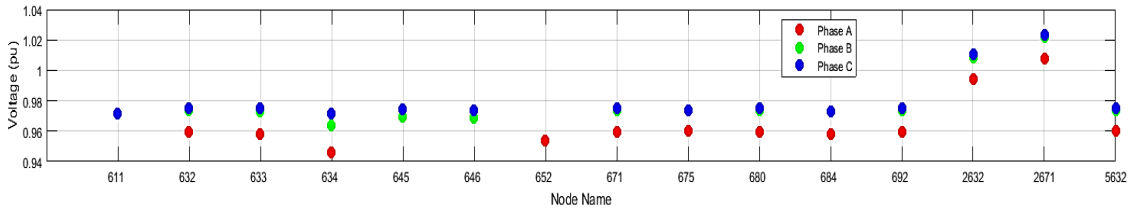

Figure 7.16 Voltage Magnitude across all Nodes for Case 1 Scenario 2 Base Case at Last Step

7.4.3.8. Summary of Case 1 Scenario 2 Results

Table 7.7 shows a summary of the cases studied in this scenario. As expected, a higher ramp rate increases the total loads restored as shown in the two highlighted rows. Lower ramp rate may need an increase in the number of solution time steps to restore more loads with the same DG capacities.

Table 7.7 Summary of Case 1 Scenario 2.1 to 2.6 Results

	Total Number of Restored Load	Sum of Nominal Active Power of Loads Restored (KW)	Solver Time (Sec)	Objective Value (KW-Steps)	Best Bound (KW-Steps)	Optimality Gap (%)
Scenario 2.1 (base case)	9 out of 10 loads	1,149	291	(-)2,079	(-)2,079	0
Scenario 2.2 (Ramp Factor: × 0.33)	3 out of 10 loads	390	272	(-)623.34	(-)623.34	0
Scenario 2.3 (Ramp Factor: × 0.67)	8 out of 10 loads	945	170	(-)1,535	(-)1,535	0
Scenario 2.4 (Ramp Factor: × 1.33)	9 out of 10 loads	1,149	74	(-)3,029	(-)3,029	0
Scenario 2.5 (Ramp Factor: × 1.67)	10 out of 10 loads	1,234	60	(-)3,114	(-)3,114	0
Scenario 2.6 (Ramp Factor: × 2)	10 out of 10 loads	1,234	80	(-)3,114	(-)3,114	0

7.4.4. Scenario 3: case studies for validating the effects of different DG capacities

7.4.4.1. Description of Test System

Under this scenario, there is a total of 6 cases run numbered scenario 3.1, 3.2, to 3.6 of which scenario 3.1 is considered the base case. Scenario 3.2 to 3.6 is derived from 3.1 by multiplying the DG capacity of 3.1 with a factor of 0.33, 0.67, 1.33, 1.67, and 2 respectively. The purpose of these cases is to evaluate the effects/validation of the DG capacity. The DG capacity constraints are described in section 6.3.6 under "DG Output Constraints".

A one-line diagram of the base test system to be restored is shown in Figure 7.17. This test system is made up of two three-phase droop-controlled DGs at nodes 2680 and 2671, and three single-phase PQ DGs at nodes 632, 680, and 675.

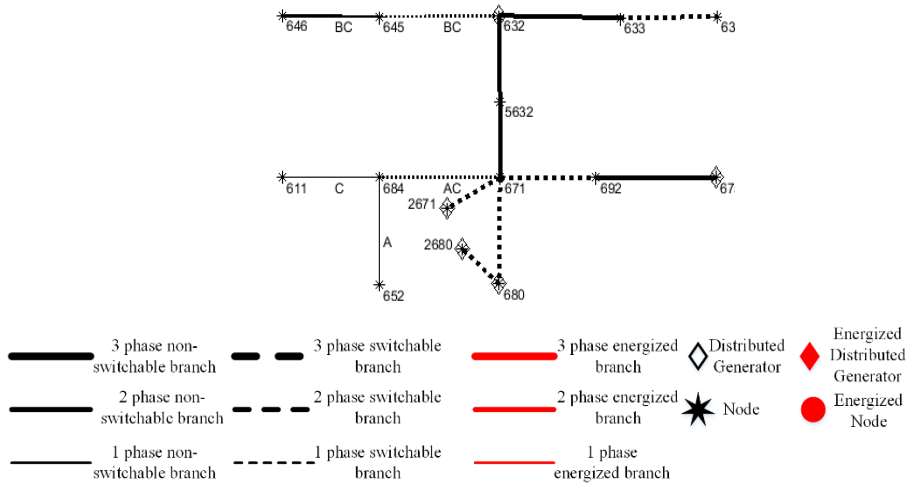

Figure 7.17 One-Line Diagram of Modified IEEE 13 Node Test Feeder for the Base Case of Case Studies 1 Scenario 3

7.4.4.2. DGs Information

The DGs' information is shown in Table 7.8. The DG columns are the same as previously described in section 7.4.2.2.

Table 7.8 DGs' Information for Case 1 Scenario 3

Label	Node	Type	f^{ref} (Hz)	Per phase BaseMVA	per phase baseKV	pu coupling X	Pmax (KW)	Pmin (KW)	Qmax (KVAR)	Qmin (KVAR)	Phase	Status	Blackstart	Ramp Rate %
DG1	2680	Droop	60	1	2.4018	0.6	600	0	300	-50	ABC	1	1	50
DG2	2671	Droop	60	1	2.4018	0.6	600	0	300	-50	ABC	1	1	50
DG3	680	PQ	NA	NA	2.4018	NA	200	0	120	0	C	1	0	50
DG4	675	PQ	NA	NA	2.4018	NA	200	0	120	0	A	1	0	50
DG5	632	PQ	NA	NA	2.4018	NA	200	0	120	0	B	1	0	50

7.4.4.3. Time Step Estimation using Bus Block Graph

Estimation of number of time steps is performed as explained in section 6.4.2. By graphically analyzing the one-line diagram of Figure 7.17, the conservative and generous time steps were estimated to be both 5. The time step of 5 was chosen to solve for the black start restoration of the microgrid system.

7.4.4.4. Restoration Sequence Graph

The one-line diagram of the restoration sequence for the base case is shown in Figure 7.18(a) to (e). Line thickness is shown in the legend and has been used to denote single, double, and three-phase branches.

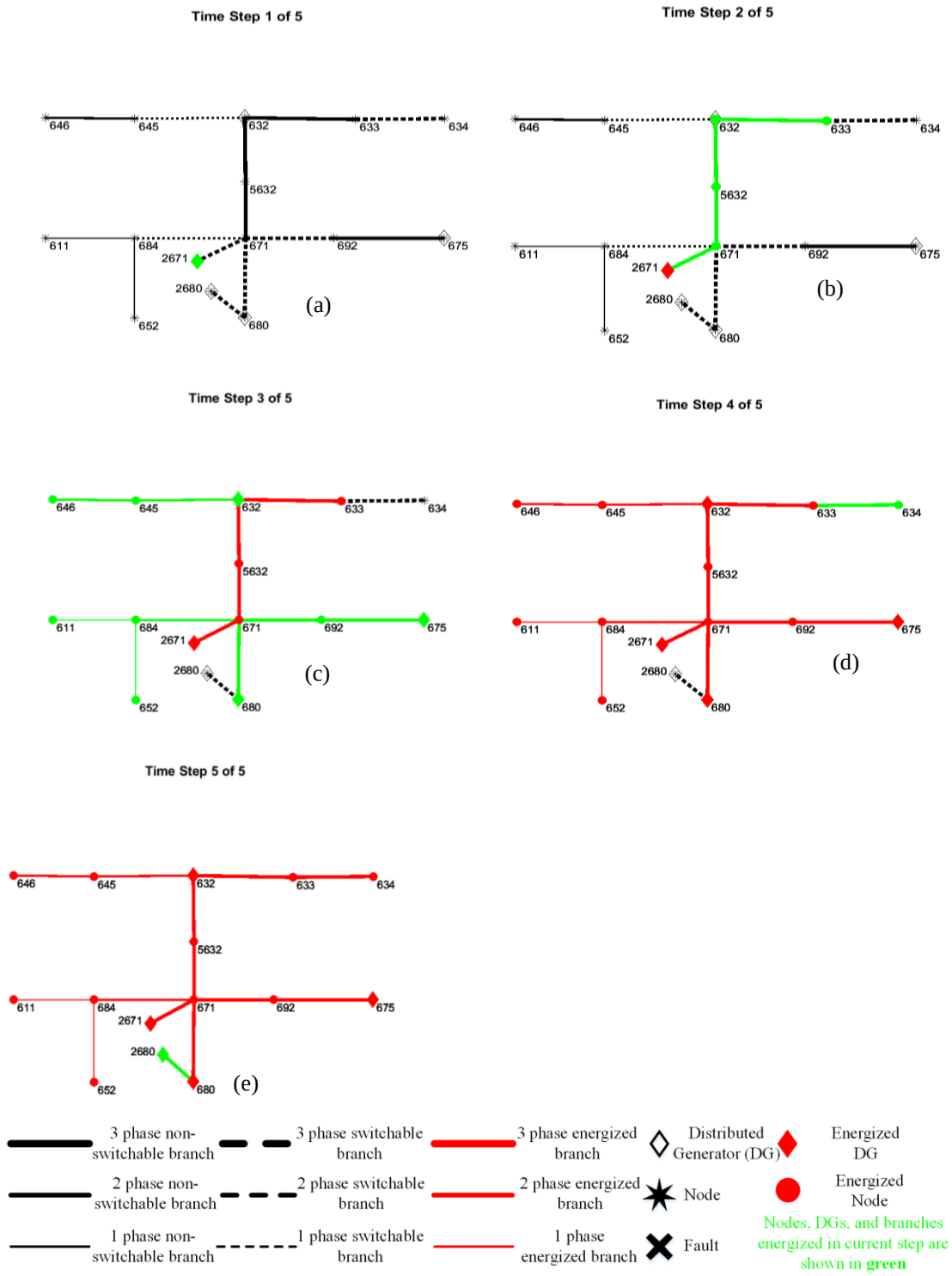

Figure 7.18 Restoration Sequence for Case 1 Scenario 3.1

Just like in the previous scenario, the topology and sequencing features of the microgrid followed the expected sequence across the restoration steps. The restoration graph of the derivative scenarios, that is scenarios 3.2 to 3.6, have been omitted.

7.4.4.5. Load Restoration Results

The load details and restoration steps for each load across scenarios 3.1 to 3.6 are shown in Table 7.9. All loads are assumed to be switchable and restorable. As expected, Table 7.9 shows that generally under the same condition, that higher DG capacity leads to more loads being restored.

Table 7.9 Load Details and Restoration Steps for Case 1 Scenario 3.1 to 3.6

Node	Config	P(a/B/C) KW	Q(A/B/C) KVAR	Turn-On Step, Scenario 3.1 (Base Case)	Turn-On Step, Scenario 3.2 (DG Cap Factor: $\times 0.33$)	Turn-On Step, Scenario 3.3 (DG Cap Factor: $\times 0.67$)	Turn-On Step, Scenario 3.4 (DG Cap Factor: $\times 1.33$)	Turn-On Step, Scenario 3.5 (DG Cap Factor: $\times 1.67$)	Turn-On Step, Scenario 3.6 (DG Cap Factor: $\times 2$)
611	Y	0/0/85	0/0/40	Off	Off	4	4	3	4
634	Y	90/60/30	55/45/15	Off	Off	Off	4	4	3
645	Y	0/82/0	0/62.5/0	4	Off	4	3	3	3
646	D	0/115/0	0/66/0	4	Off	Off	3	3	3
652	Y	100/0/0	55/0/0	4	Off	4	3	3	4
671	D	110/90/90	60/50/50	3	Off	3	4	3	3
671	Y	7/11/25	3/7/15	4	Off	Off	3	3	3
675	Y	100/50/70	45/30/40	3	5	Off	3	3	3
692	D	0/0/85	0/0/75.5	Off	Off	Off	3	4	3
5632	Y	9/22/39	4/14/20	4	3	3	3	4	3

The DG capacity factor in Table 7.9 for the derivative case is a factor that was used to multiply the DG capacities of the base case to get the DG capacities for that particular derivative case.

7.4.4.6. DG Dispatch Result and Capacity Limit Validation

The three-phase power reference settings of the two droop-controlled DGs and power setpoints of the PQ DGs for the base case of scenario 3.1 are shown in Figure 7.19

and Figure 7.20, respectively. The second droop-controlled DG at node 2680 that was synchronized at step 5 (compare with Figure 7.18 e), connected to the microgrid at zero dispatch reference setting according to the synchronization enhancing constraints of section 6.3.4. Recall there was an additional "must connect" optional constraint for all droop-controlled DG under case studies 1; setting this optional constraint to true improves the resilience of the restored microgrid by ensuring that the restoration solution energizes and connects all the master droop-controlled DGs by the last time step. This optional constraint was set to true in Table 7.1 under the option field: "Options.connectGFDGs".

Though the DGs did not all hit their capacity limit, not all loads were restored in the base case as seen in Table 7.9. Ramp rate constraints play a part in the underutilization of the DG capacities. If the number of steps parameter was increased, more loads could be restored. As expected, none of the DGs exceeded their capacity limit; this was also the case for the derivative cases.

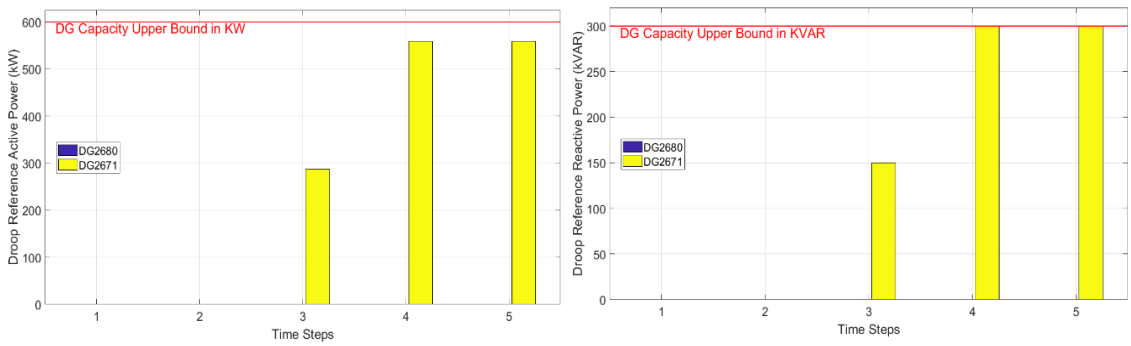

(a) (b)

Figure 7.19 (a) Droop Three-Phase Active Power Reference (b) Droop Three-Phase Reactive Power Reference for the Base Case

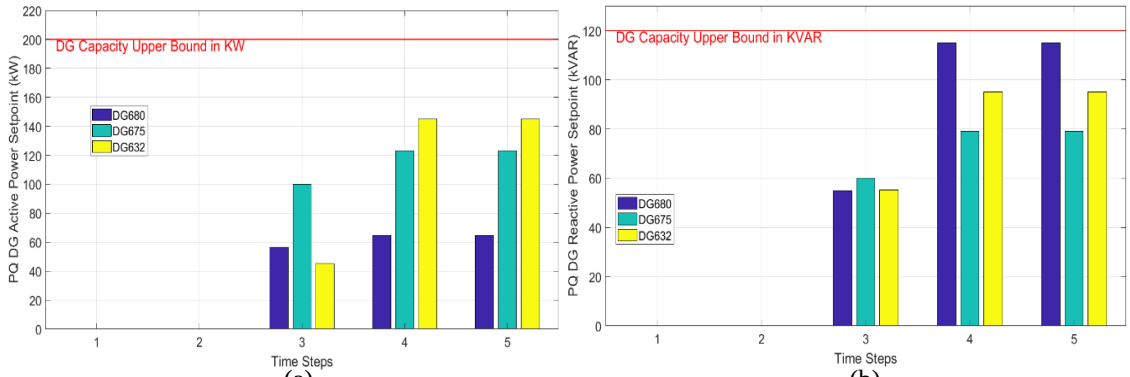

Figure 7.20 (a) PQ DG Active Power Setpoint (b) PQ DG Reactive Power Setpoint for the Base Case

7.4.4.7. Voltage Magnitude Plot at Last Step

The method ensured that the voltage lies within the limits set according to the voltage limit constraints. Only the last step of the base case is shown in Figure 7.21.

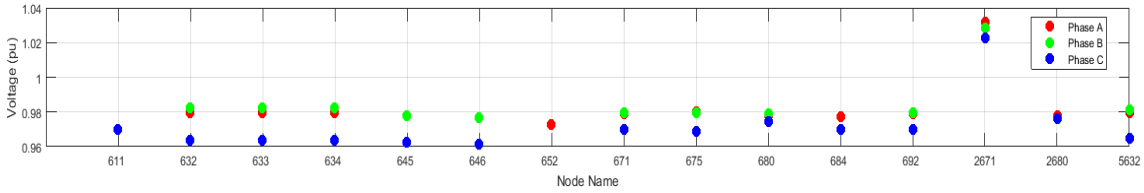

Figure 7.21 Voltage Magnitude across all Nodes for Case 1 Scenario 3 Base Case at Last Step

7.4.4.8. Summary of Case 1 Scenario 3 Results

Table 7.10 shows a summary of the cases run in this scenario. Similarly like in the previous scenario, we can see that as the DG capacities are increased, more loads can be restored as expected.

Table 7.10 Summary of Case 1 Scenario 3.1 to 3.6 Results

	Total Number of Restored Load	Sum of Nominal Active Power of Loads Restored (KW)	Solver Time (Sec)	Objective Value (KW-Steps)	Best Bound (KW-Steps)	Optimality Gap (%)
Scenario 3.1 (base case)	7 out of 10 loads	920	939	(-)2,350	(-)2,350	0
Scenario 3.2 (DG Cap Factor: × 0.33)	2 out of 10 loads	290	857	(-)430	(-)430	0
Scenario 3.3 (DG Cap Factor: × 0.67)	5 out of 10 loads	627	579	(-)1,614	(-)1,614	0
Scenario 3.4 (DG Cap Factor: × 1.33)	10 out of 10 loads	1,270	62	(-)3,255	(-)3,255	0
Scenario 3.5 (DG Cap Factor: × 1.67)	10 out of 10 loads	1,270	19	(-)3,475	(-)3,475	0
Scenario 3.6 (DG Cap Factor: × 2)	10 out of 10 loads	1,270	93.52	(-)3,625	(-)3,625	0

7.4.5. Scenario 4: case studies for validating the effects of different loading conditions

7.4.5.1. Description of Test System

This scenario has the same base case as the previous scenario, that is scenario 3. Under this scenario, there is a total of 6 cases run numbered scenario 4.1, 4.2, to 4.6 of which scenario 4.1 is considered the base case. Scenario 4.2 to 4.6 is derived from 4.1 by multiplying the nominal load values of 4.1 with a factor of 0.33, 0.67, 1.33, 1.67, and 2 respectively. The purpose of these cases is to evaluate the effects/validation of the load capacity on the black restoration model. Details of the initial system topology, DG information as well as restoration sequence result for the base case can be found in the previous scenario in section 7.4.4.

7.4.5.2. Load Restoration Results

The load details and restoration steps for each load across scenarios 4.1 to 4.6 are shown in Table 7.11. As expected, Table 7.11 shows that generally under the same condition, that higher load capacity leads to a smaller number of aggregate loads being restored.

Table 7.11 Load Details and Restoration Steps for Case 1 Scenario 4.1 to 4.6

Node	Config	P(a/B/C) KW	Q(A/B/C) KVAR	Turn-On Step 4.1 (Base Case)	Turn-On Step, Scenario 4.2 (Load Value Factor: $\times 0.33$)	Turn-On Step, Scenario 4.3 (Load Value Factor: $\times 0.67$)	Turn-On Step, Scenario 4.4 (Load Value Factor: $\times 1.33$)	Turn-On Step, Scenario 4.5 (Load Value Factor: $\times 1.67$)	Turn-On Step, Scenario 4.6 (Load Value Factor: $\times 2$)
611	Y	0/0/85	0/0/40	Off	3	3	3	Off	Off
634	Y	90/60/30	55/45/15	Off	3	3	Off	Off	Off
645	Y	0/82/0	0/62.5/0	4	3	4	3	Off	Off
646	D	0/115/0	0/66/0	4	3	4	Off	Off	Off
652	Y	100/0/0	55/0/0	4	3	4	3	Off	Off
671	D	110/90/90	60/50/50	3	3	3	4	3	5
671	Y	7/11/25	3/7/15	4	3	3	3	Off	Off
675	Y	100/50/70	45/30/40	3	3	3	Off	4	3
692	D	0/0/85	0/0/75.5	Off	3	4	Off	Off	Off
5632	Y	9/22/39	4/14/20	4	3	4	3	4	5

The load value factor in Table 7.11 for the derivative case is a factor that was used to multiply the nominal load values of the base case to get the nominal load values for that particular derivative case.

7.4.5.3. Summary of Case 1 Scenario 4 Results

Table 7.12 shows a summary of all the cases run in this scenario. As expected, as the nominal load values are increased, it can decrease the number of aggregate loads restored.

Table 7.12 Summary of Case 1 Scenario 4.1 to 4.6 Results

	Total Number of Restored Load	Sum of Nominal Active Power of Loads Restored (KW)	Solver Time (Sec)	Objective Value (KW-Steps)	Best Bound (KW-Steps)	Optimality Gap (%)
Scenario 4.1 (base case)	7 out of 10 loads	920	936	(-)2,350	(-)2,350	0
Scenario 4.2 (Load Value Factor: × 0.33)	10 out of 10 loads	419	2	(-)1,257.3	(-)1,257.3	0
Scenario 4.3 (Load Value Factor: × 0.67)	10 out of 10 loads	850.9	56	(-)2,249.9	(-)2,249.9	0
Scenario 4.4 (Load Value Factor: × 1.33)	6 out of 10 loads	891.1	273	(-)2,287.6	(-)2,287.6	0
Scenario 4.5 (Load Value Factor: × 1.67)	3 out of 10 loads	968.6	538	(-)2,421.5	(-)2,421.5	0
Scenario 4.6 (Load Value Factor: × 2)	3 out of 10 loads	1,160	508	(-)2,040	(-)2,040	0

7.4.6. Scenario 5: Power Flow Verification with PSCAD Simulation as a Benchmark

The base cases of scenario 1 to scenario 3 were set up for time-domain simulation in PSCAD. Recall that in the power flow constraints section (section 6.3.5), the power injection (output) for each droop DG has been set to be its reference active and reactive power. Setting the output power to equal its reference power was called droop reference active and reactive power constraints in sections 5.8.2 and 5.8.3, respectively. These two constraints ensure that each droop-controlled DG has an output voltage magnitude and frequency equal to its reference voltage and reference frequency respectively according to the droop equations. Also, these droop reference constraints eliminate the droop co-efficient from its power injection expression since its output powers track their reference power setting.

It is more realistic that the reference powers of the droop-controlled DGs are not always accurately tracked considering both physical and analytical concerns. Physical concerns are related to changing load profiles with time and power losses which can lead to a power mismatch between the droop reference power settings and its output power. Analytical concerns are related to errors (such as linearization errors) in modeling the system which could lead to power mismatch. Because of this power mismatch, the droop co-efficient plays a role in deciding how this mismatched power is shared among the droop-controlled DGs [96]. Also, the droop coefficient plays a role in determining the stability of the system [102] and is thus an important parameter that affects the stable transition from one restoration step to the next. For all the PSCAD simulation run in this section, the frequency droop coefficient was fixed to 0.0667 Hz per unit power and voltage droop co-efficient to 0.00667 per unit power. Both coefficients are expressed using the per phase power base of 1 MVA. The time interval between steps was fixed to 6 seconds for the first simulation and 3 seconds for the second and third simulations. Determining threshold values for the droop coefficient settings and the time interval between any two adjacent steps for stable transition would be an interesting area for future work.

The metrics used for comparing results obtained from solving the restoration model with equivalent steady-state PSCAD results is the relative error. The relative error, ε_x, of calculated quantity gotten from solving the restoration model, x, with respect to its reference PSCAD value (this PSCAD value is read when the transients have decayed/reached steady-state for each restoration step), x_{ref}, is defined as,

$$\varepsilon_x = \frac{|x - x_{ref}|}{|x_{ref}|} \times 100\% \tag{7.6}$$

The mean relative error, $\bar{\varepsilon}_x$, of a set of calculated quantities is the mean of the relative errors of each element of the set.

7.4.6.1. Power Flow Verification for Scenario 1.1 Using PSCAD as Benchmark

A zoomed out PSCAD setup of the scenario 2.1 is shown in Figure 7.22. Each subsystem in Figure 7.22 has a detailed model of its controller. Recall that scenario 2.1 was solved using a generous time step of 6. Assuming a time interval of 6 seconds between two adjacent time steps gives a total simulation time of 36 seconds. The PSCAD setup was run for a simulation time of 36 seconds. The power setpoint of the PQ DGs, droop reference power settings, load values and ZIP parameters, turn-on times for branches, loads, and DGs were set in the PSCAD according to the results obtained from the black start restoration of scenario 1.1.

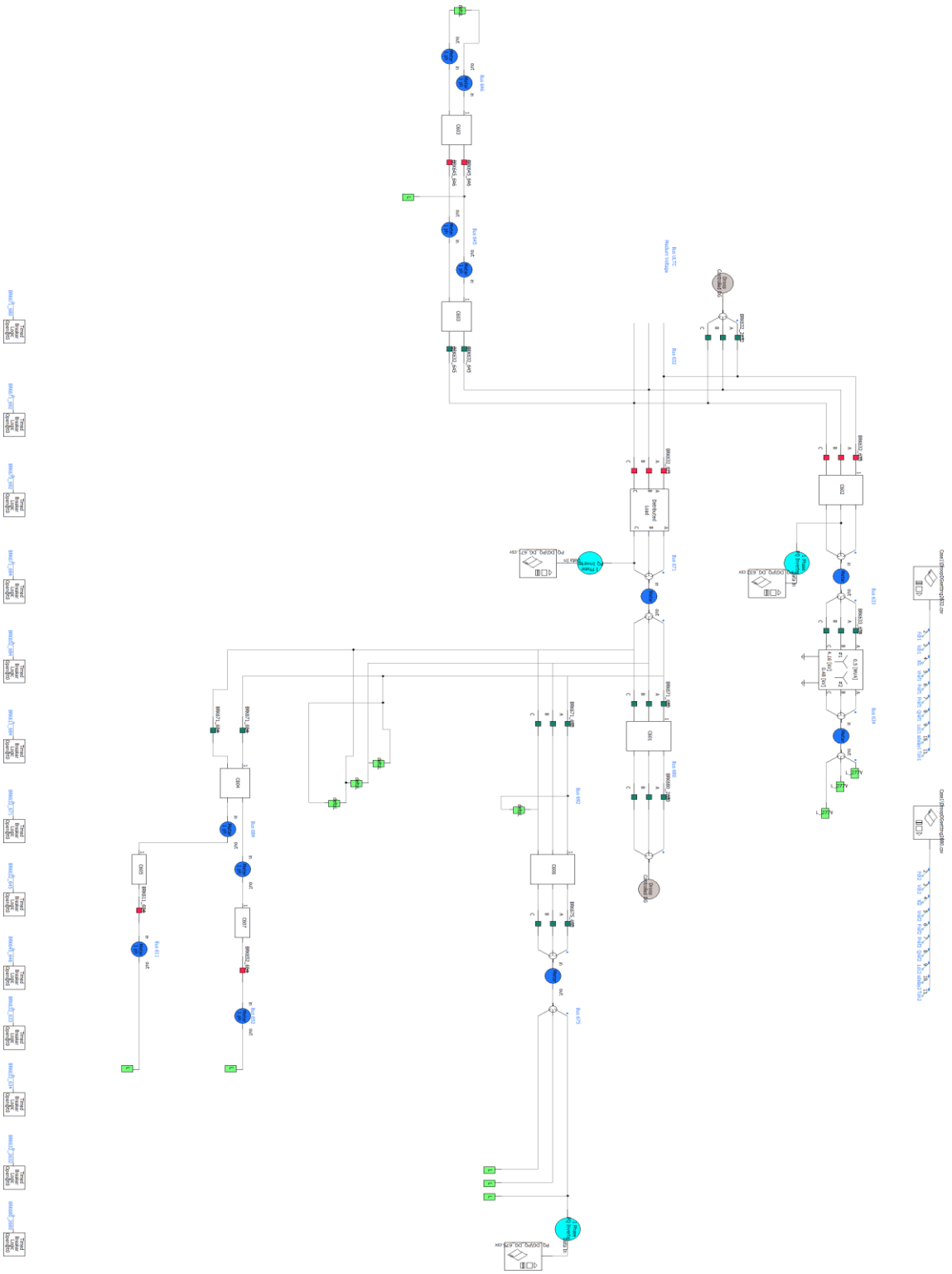

Figure 7.22 PSCAD setup for Case 1 Scenario 1.1

Figure 7.23 shows the droop reference active power for the two droop-controlled DGs. DG at node 2680 was synchronized to the microgrid at 30 seconds using the proposed zero-dispatch synchronization method. Notice that the synchronization is smooth with very short-lived transients that are barely noticeable. By visually inspecting Figure 7.23, notice that the power mismatch between the reference and output power is minimal at the last step. This is because the piecewise linearization utilized for the last step is expected to be more accurate than the alternative method (described in Appendix C) which is used for the inner steps. The red vertical lines are used to denote the time steps: T1, T2, etc.

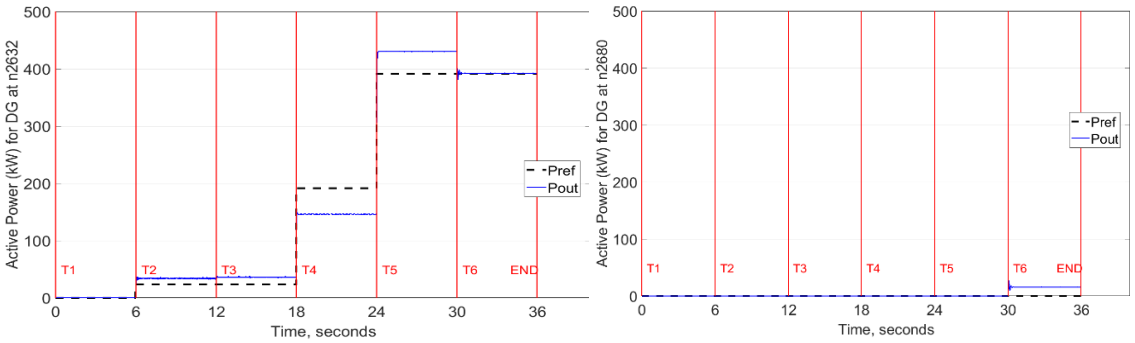

(a) (b)

Figure 7.23 Droop Reference Active Power and Output Active Power for DG at Nodes (a) 2632 and (b) 2680 as obtained from PSCAD simulation of scenario 1.1

Figure 7.24 shows the droop frequency for the two droop-controlled DGs. Notice that they are regulated to approximately 60 Hz as desired. Also, DG at node 2680 has a pretty smooth synchronization to the microgrid at 30 seconds.

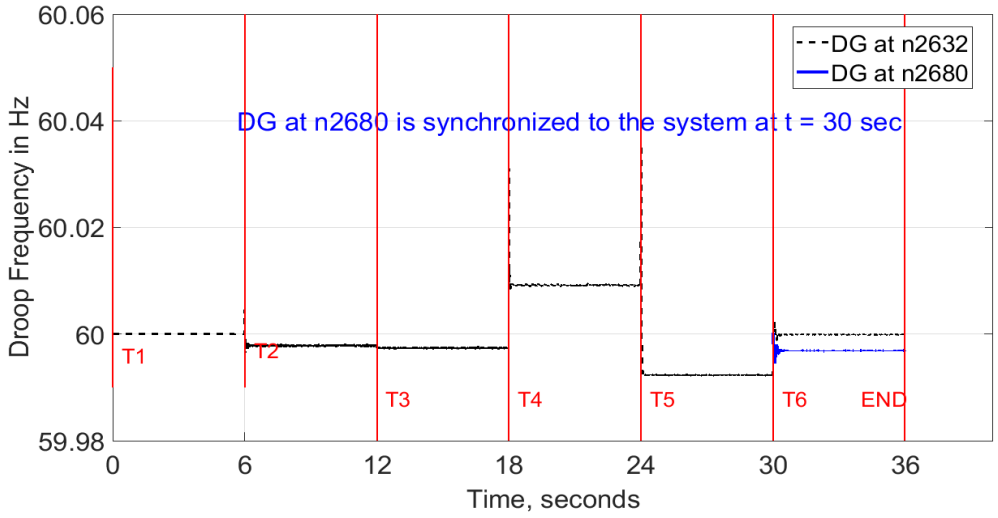

Figure 7.24 Droop Frequency for DGs at Nodes 2632 and 2680 as obtained from PSCAD Simulation of Scenario 1.1

Figure 7.25 shows the droop reference reactive power for the two droop-controlled DGs. Also observe that the reactive power output of the droop-controlled DGs tracked their set reference reactive power closely as desired.

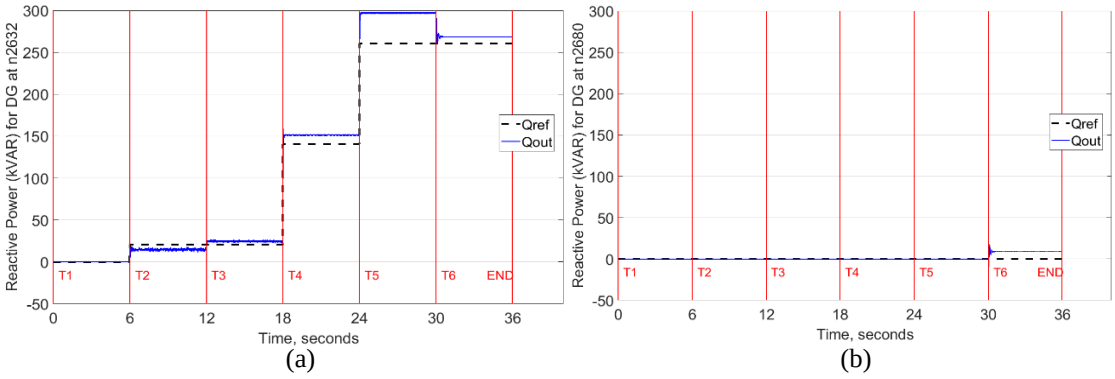

Figure 7.25 Droop Reference Reactive Power and Output Reactive Power for DG at Nodes (a) 2632 and (b) 2680 as obtained from PSCAD Simulation of Scenario 1.1

Figure 7.26 shows the percentage relative error of the nodal voltage magnitude at each node as obtained from the restoration solution of scenario 1.1 compared with steady-state PSCAD nodal voltages for the last time step. The steady-state PSCAD results are read for each step after its transients have decayed and just before the start of the next restoration step. The mean error across all the phase nodes is 1.4147% which can be considered fairly good. This means that on average the nodal voltage error is in the order of ± 0.014 per unit of the actual voltage magnitude.

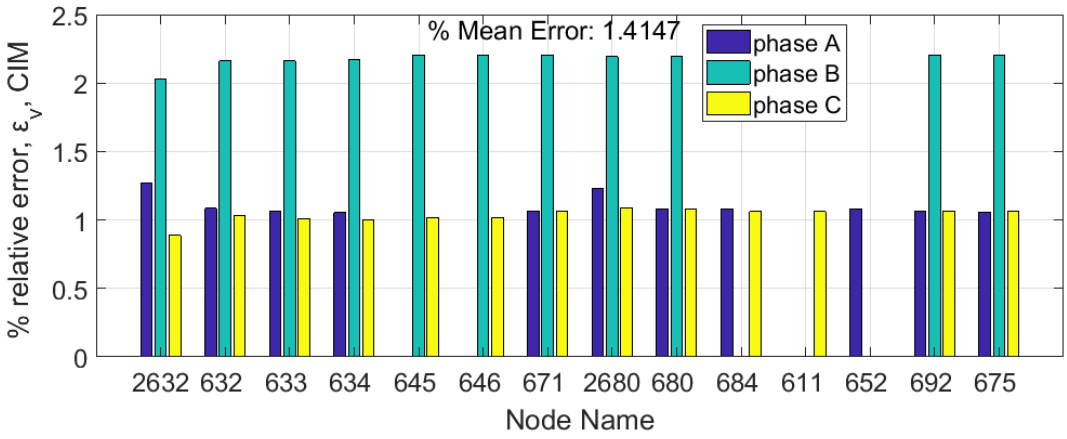

Figure 7.26 Percentage Relative Error of Voltage from Power Flow Result of Scenario 1.1 using Equivalent PSCAD Quantity as a Benchmark

The three-phase droop-controlled DGs used here are three-phase controlled; therefore, unbalance current/power dispatch from the droop-controlled DG can manifest as an unbalanced offset in three-phase terminal voltage magnitude. Even though an effort has been made to compensate for the load unbalance system-wide, any small unbalance in dispatch would affect how droop DGs control their terminal voltage due to differences in

the voltage drop across the three phases of the inverter filter. According to Ohm's law, this unbalanced voltage drop across the three-phase filters is linear and is propagated linearly down the branches to other sink nodes. Phase(s) with the greatest voltage drop deviation from the mean voltage drop across the three-phase filters are likely to have greatest relative errors; an example is phase B from Figure 7.26. To eliminate the effect of this unbalanced voltage due to differences in the voltage drop across the filter, we take the average of the voltage magnitudes across every three-phase node before calculating the relative error and the mean error. This averaging of voltage magnitude across the three phases gives the approximate value of the magnitude of the positive sequence voltage for a three-phase voltage that is not overly unbalanced. It is this positive sequence voltage that yields DC signals in the DQ frame which the inverter uses to control its internal voltage. Figure 7.27 shows the relative error of the average three-phase voltage for only three-phase nodes; notice that the mean error has reduced tremendously to 0.021% compared to 1.41% when we considered the error using individual phase nodes. This implies that much of the mean errors come from the effects of system unbalance on the filter and inverter controller rather than from the power flow equations of the restoration model. These unbalance effects on filter and inverter controllers were not accounted for in the restoration model formulation. A negative sequence compensator built into the inverter controller can help to eliminate these unwanted effects.

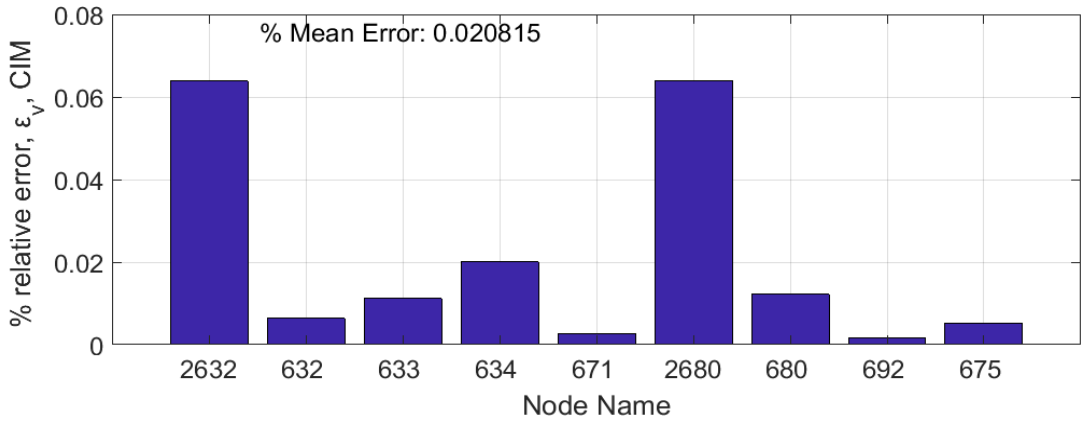

Figure 7.27 Percentage Relative Error of Average Three-Phase Voltage from Power Flow Result of Scenario 1.1 using Equivalent PSCAD Quantity as a Benchmark

Figure 7.28 shows the active and reactive power dispatch tracking of the PQ DG at node 633. Since the PQ DGs are grid-following, they do not contribute to forming the voltage reference for the system and thus would track their dispatch setting accurately if their local controllers are robustly tuned. The other PQ DGs output power have not been shown, however, the PQ DGs all tracked their dispatch power settings accurately.

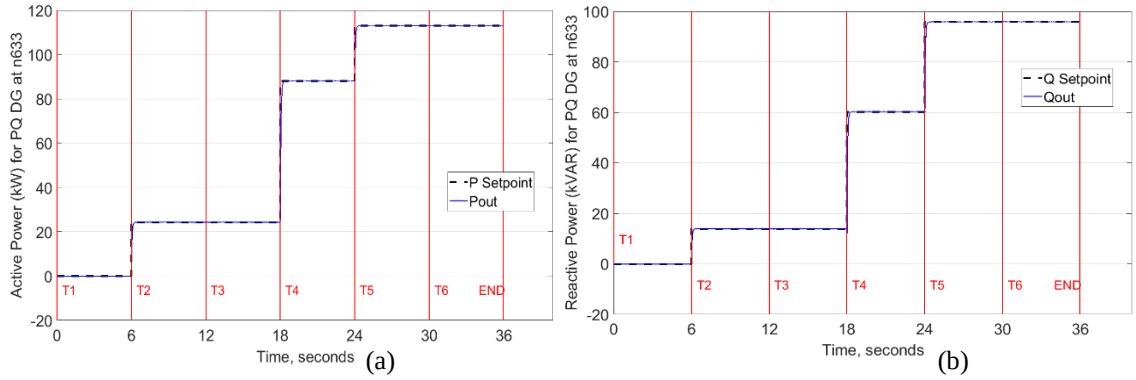

Figure 7.28 Dispatch Tracking of PQ DG at Node 633 for (a) Active Power (b) Reactive Power

7.4.6.2. Power Flow Verification For Scenario 2.1 Using PSCAD as Benchmark

Just like in section 7.4.6.1, a PSCAD setup of scenario 2.1 was also developed. Similar results to that of section 7.4.6.1 were obtained and the graphs are summarized in Figure 7.29 to Figure 7.33 below.

Figure 7.29 shows the droop reference active power for the two droop-controlled DGs. DG at node 2632 was synchronized to the microgrid at 6 seconds using the proposed zero-dispatch synchronization method. Notice that the synchronization is smooth just like the previous PSCAD simulation study. There is a sustained oscillation at the start of step 4. This sustained oscillation is mostly a function of the controller parameters. Readjusting these parameters to realize an exponentially stable step will involve detailed controller analysis and could be a focus for future study. By the start of step 5, the system became exponentially stable once again. The red vertical lines are used to denote the time steps: T1, T2, etc.

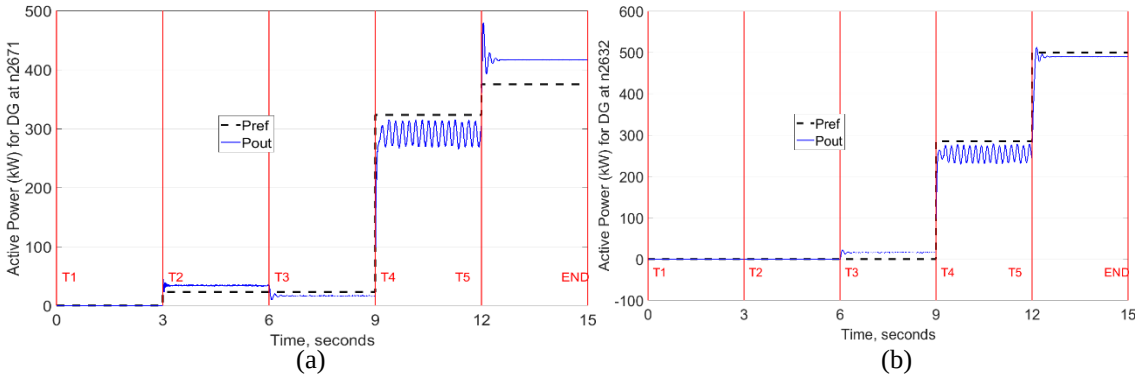

Figure 7.29 Droop Reference Active Power and Output Active Power for DG at Nodes (a) 2671 and (b) 2632 as obtained from PSCAD Simulation of Scenario 2.1

Figure 7.30 shows the droop frequency for the two droop-controlled DGs at nodes 2671 and 2632. Notice that they are regulated to approximately 60 Hz as desired. Also, DG at node 2632 has a pretty smooth synchronization to the microgrid at 6 seconds.

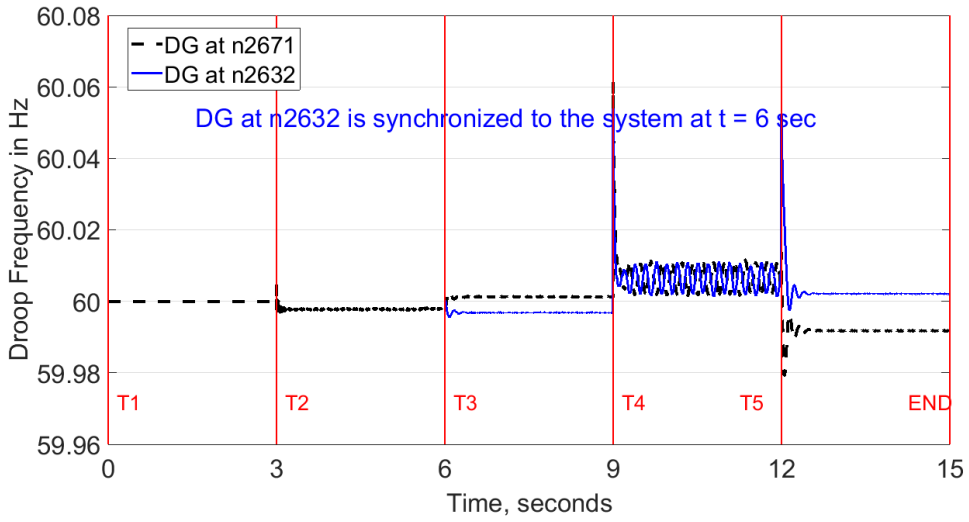

Figure 7.30 Droop Frequency for DGs at Nodes 2671 and 2632 as obtained from PSCAD Simulation of Scenario 2.1

Figure 7.31 shows the droop reference reactive power for the two droop-controlled DGs. Notice that there is a sustained oscillation at the start of step 4 just like in the active power and frequency plot of Figure 7.29 and Figure 7.30. This is because of the coupling between these parameters as a sustained oscillation will manifest in several quantities at the same time.

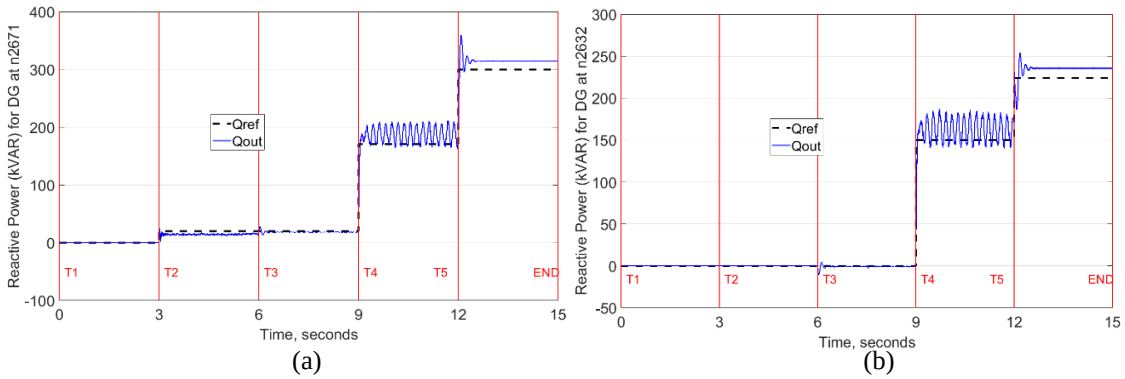

Figure 7.31 Droop Reference Reactive Power and Output Reactive Power for DG at Nodes (a) 2671 and (b) 2632 as obtained from PSCAD Simulation of Scenario 2.1

Figure 7.32 shows the percentage relative error of the nodal voltage magnitude at each node as obtained from the restoration solution of scenario 2.1 compared with steady-state PSCAD nodal voltages for the last time step. The mean error across all the phase nodes is 1.4025%. This means that on average the nodal voltage error is in the order of ±0.014 per unit of the actual voltage magnitude.

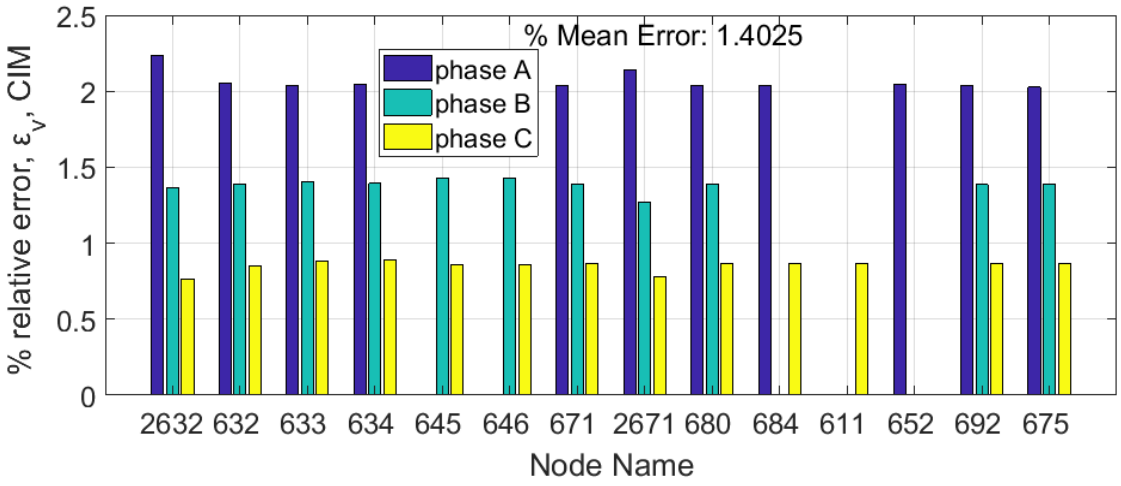

Figure 7.32 Percentage Relative Error of Voltage from Power Flow Result of Scenario 2.1 using Equivalent PSCAD Quantity as a Benchmark

Figure 7.33 shows the reduction in mean error to 0.058% by averaging out the unbalanced voltage effect due to filters and DGs' controller response to unbalanced operation.

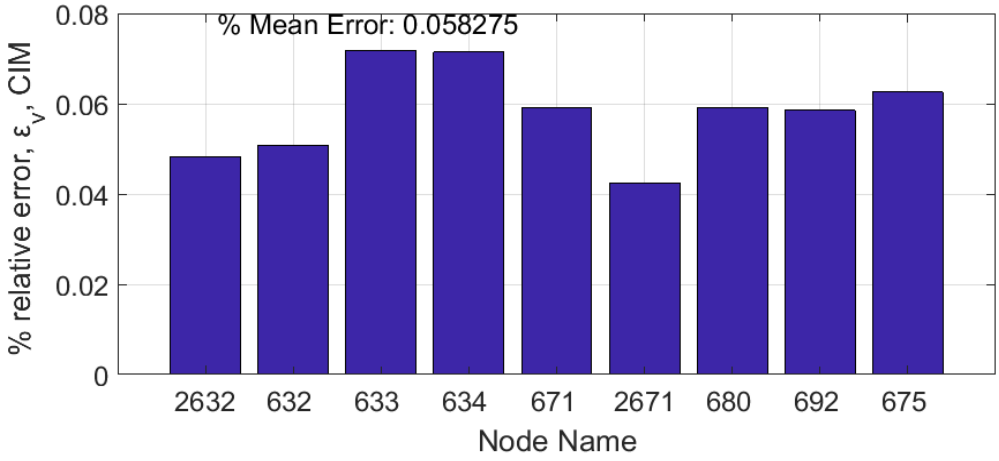

Figure 7.33 Percentage Relative Error of Average Three-Phase Voltage from Power Flow Result of Scenario 2.1 using Equivalent PSCAD Quantity as a Benchmark

7.4.6.3. Power Flow Verification for Scenario 3.1/4.1 Using PSCAD as Benchmark

Just like in section 7.4.6.1, a PSCAD setup of scenario 3.1 was also developed. Similar results to that of section 7.4.6.1 were obtained and the graphs are summarized in Figure 7.34 to Figure 7.38 below.

Figure 7.34 shows the droop reference active power for the two droop-controlled DGs. DG at node 2680 was synchronized to the microgrid at 12 seconds using the proposed zero-dispatch synchronization method. Notice that the synchronization is

smooth just like the previous PSCAD simulation study. Figure 7.34 shows that the reference active power was closely tracked for the two droop DGs.

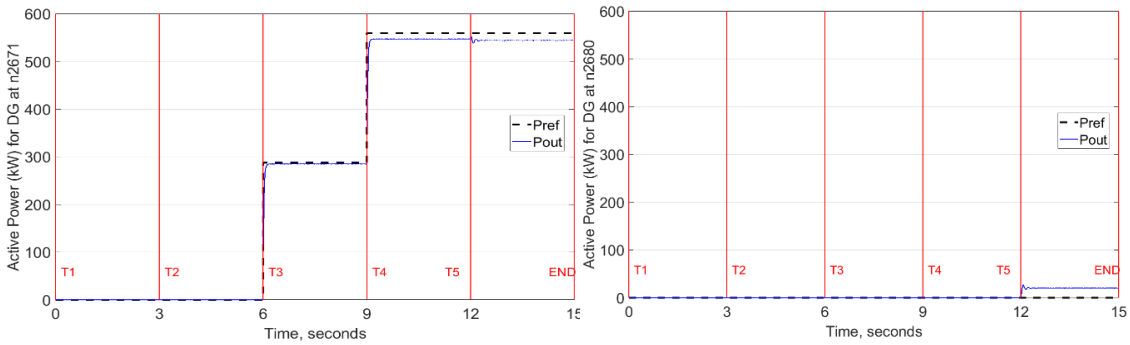

Figure 7.34 Droop Reference Active Power and Output Active Power for DG at Nodes (a) 2671 and (b) 2680 as obtained from PSCAD Simulation of Scenario 3.1

Figure 7.35 shows the droop frequency for the two droop-controlled DGs at nodes 2671 and 2680. Notice that they are regulated to approximately 60 Hz as desired. Also, DG at node 2680 has a pretty smooth synchronization to the microgrid at 12 seconds.

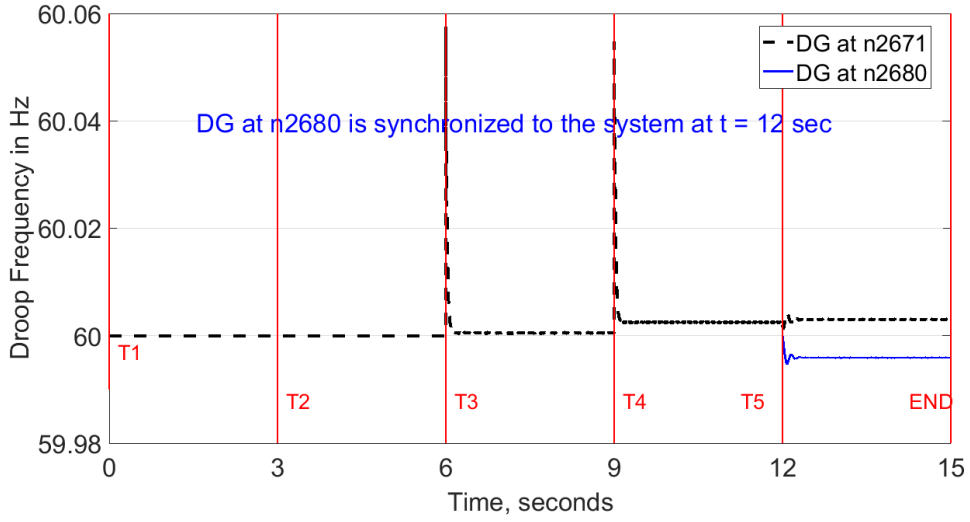

Figure 7.35 Droop Frequency for DGs at Nodes 2671 and 2632 as obtained from PSCAD Simulation of Scenario 3.1

Figure 7.36 shows the droop reference reactive power for the two droop-controlled DGs. Figure 7.36 shows that the reference reactive power was closely tracked for the two droop DGs as desired.

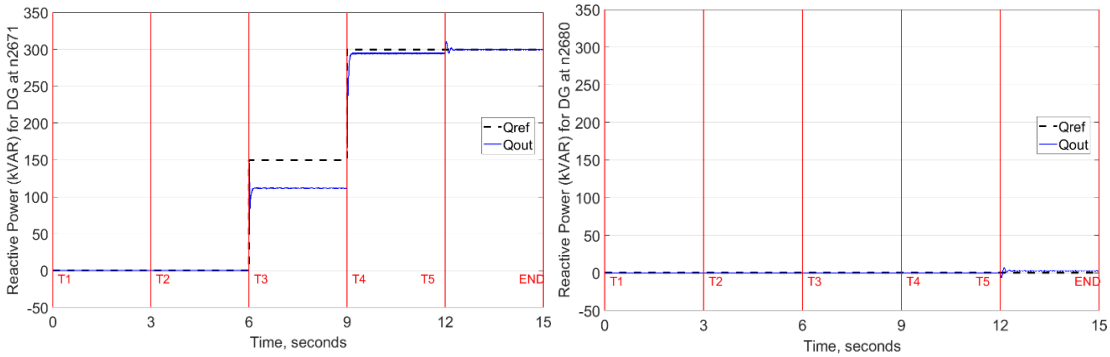

(a) (b)

Figure 7.36 Droop Reference Reactive Power and Output Reactive Power for DG at Nodes (a) 2671 and (b) 2632 as obtained from PSCAD Simulation of Scenario 3.1

Figure 7.37 shows the percentage relative error of the nodal voltage magnitude at each node as obtained from the restoration solution of scenario 2.1 compared with steady-state PSCAD nodal voltages for the last time step. The mean error across all the phase nodes is 1.3737%. This means that on average the nodal voltage error is in the order of ±0.0137 per unit of the actual voltage magnitude.

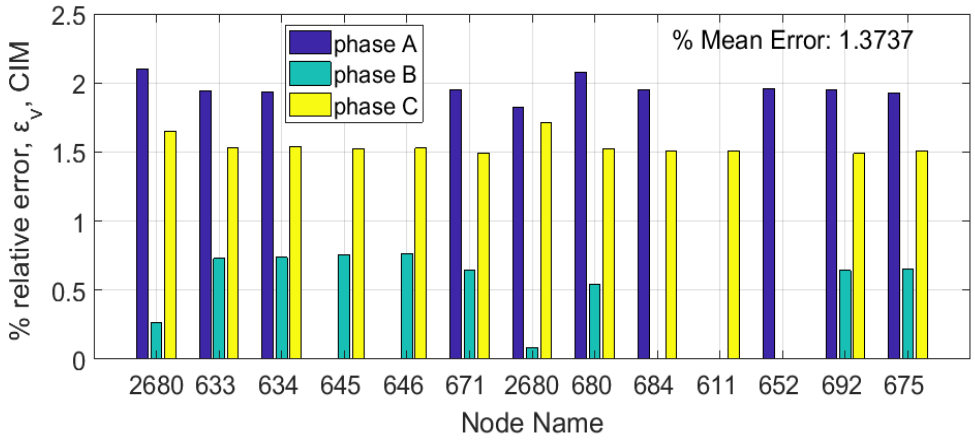

Figure 7.37 Percentage Relative Error of Voltage from Power Flow Result of Scenario 3.1 using Equivalent PSCAD Quantity as a Benchmark

Figure 7.38 shows the reduction in mean error to 0.061% by averaging out the unbalanced voltage effect due to filter and DG's controller response to unbalanced operation.

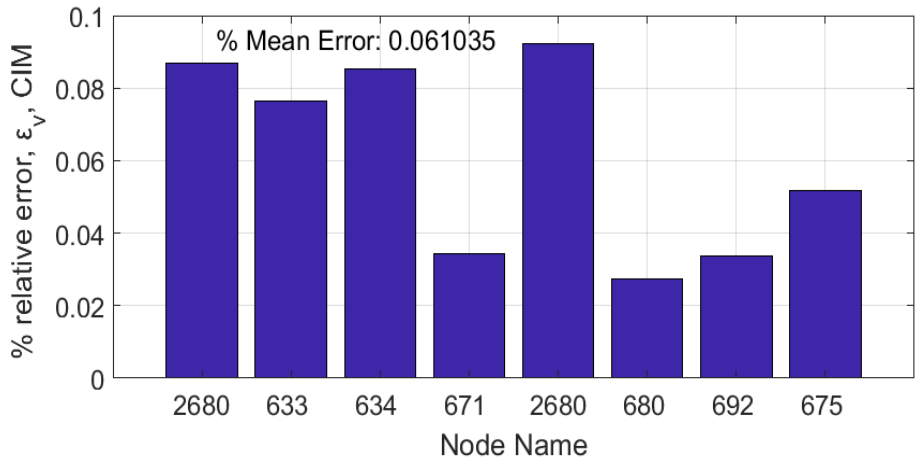

Figure 7.38 Percentage Relative Error of Average Three-Phase Voltage from Power Flow Result of Scenario 3.1 using Equivalent PSCAD Quantity as a Benchmark

7.4.6.4. Summary of Case 1 Scenario 5 Results

From the PSCAD simulation, we observed that the actual power output of the droop DGs tracked their reference power setting. The mismatch between the droop reference power and actual output was minimal at the last step which uses the piecewise linearization approach. We have also shown that the frequency was well regulated throughout the restoration steps and that the zero-dispatch synchronization approach results in smooth, low-transient synchronization of grid-supporting DGs to the microgrid. Another thing worth noting is the effect of unbalanced power dispatch on the droop-controlled DGs' filters and controllers. These effects are difficult to fully incorporate as constraints in the restoration model. Without accounting for this filter and controller unbalance effects, the nodal voltages had a mean error in the range of 1.3 to 1.5 %. After averaging out the filter and controller unbalance effects, the nodal voltages had a mean error in the range of about 0.02 to 0.06 %. This suggests that despite the system-wide

unbalance compensation that the proposed restoration method handles, additional negative sequence compensation at the three-phase controlled DGs are necessary to maintain a fairly balanced voltage across all nodes in the microgrid.

7.5. Case Studies 2: Effects of PQ DGs and Loads with Demand Response Capability

Case 2 is focused on studying the effect of including PQ DGs and loads with demand response capability. The island systems used for the case studies under this section were adapted from the IEEE 123 node test feeder. The case studies under this section are subdivided into two scenarios:

- Scenario 1: case studies for comparative performance studies of islanded microgrids with PQ DGs and demand response capability
- Scenario 2: case studies for highlighting the compensating effect of PQ DGs and how the phase choice of PQ DGs affects the restoration solution

The computation options for all cases categorized under case studies 2 are outlined in Table 7.13 below. Without loss of generality, the ZIP load co-efficient for every load in case studies 2 has been set to 0.4, 0.3, and 0.3 for constant impedance, current, and power components, respectively.

Table 7.13 Computation Settings for Case Studies 2

Options	Choice
Options.connectGFDGs	False
Options.skipPWL	True
Options.ignoreShuntAdmittance	True
Options.includeShuntAdmittanceForLastStepOnly	NA
Options.MIPGap	2%
Conservative/Generous Time Step Estimate	Varies with case

For all cases under case studies 2, the active and reactive power difference between any two phases of a three-phase droop-controlled DG has been constrained to be no more than 0.2% of the values of P_{max} and Q_{max} of the DG. Also, the nominal system load

unbalance index (NSLUI) for the active and reactive power load have been constrained and compensated to be no more than 6%.

7.5.1. Scenario 1

7.5.1.1. Description of Test System

A one-line diagram of the base test system is shown in Figure 7.39. In the base case, there was no load with demand response capability. The system is assumed to have experienced a blackout due to an unforeseen emergency. Two droop-controlled DGs are present at nodes 2054 and 2063. Details of the line information can be found in Appendix E.

Figure 7.39 One Line Diagram for Case 2 Scenario 1 Base Case

7.5.1.2. DGs' Information

The two DGs' details present in Figure 7.39 are summarized in Table 7.14. The DGs have a total active power capacity of 4900 KW and a total reactive power capacity of 2600 KVAR.

Table 7.14 DGs' Information for the Base Case

Label	Node	Type	f^{ref} (Hz)	Per phase BaseMVA	per phase baseKV	pu coupling X	Pmax (KW)	Pmin (KW)	Qmax (KVAR)	Qmin (KVAR)	Phase	Status	Blackstart	Ramp Rate %
DG1	2054	Droop	60	1	2.4018	0.3	2450	0	1300	-260	ABC	1	1	60
DG2	2063	Droop	60	1	2.4018	0.3	2450	0	1300	-260	ABC	1	1	60

7.5.1.3. Load Details

There is a total of 81 loads in this case study and the details are shown in Table 7.15. All loads are assumed to be switchable and restorable. The "total" row in Table 7.15 was obtained by first transforming the delta connected loads to equivalent wye connected loads before summing the load values of each phase of all wye connected loads. This transformation is performed for all subsequent tables with delta connected loads before they are summed to get the "total" row.

7.5.1.4. Choice of Time Steps

By graphically analyzing the one-line diagram of Figure 7.39, the conservative and generous time steps were estimated to be 6 and 7, respectively. The conservative time was chosen to solve for the black start restoration of the base case as well as the derivative cases which are introduced later.

Table 7.15 Load Details for the Base Case

Node	Config	P(A/B/C) KW	Q(A/B/C) KVAR	Node	Config	P(A/B/C) KW	Q(A/B/C) KVAR	Node	Config	P(A/B/C) KW	Q(A/B/C) KVAR
1	Y	40/0/0	20/0/0	43	Y	0/40/0	0/20/0	77	Y	0/40/0	0/20/0
2	Y	0/20/0	0/10/0	45	Y	20/0/0	10/0/0	79	Y	40/0/0	20/0/0
4	Y	0/0/40	0/0/20	46	Y	20/0/0	10/0/0	80	Y	0/40/0	0/20/0
5	Y	0/0/20	0/0/10	47	Y	35/35/35	25/25/25	82	Y	40/0/0	20/0/0
6	Y	0/0/40	0/0/20	48	Y	70/70/70	50/50/50	83	Y	0/0/20	0/0/10
7	Y	20/0/0	10/0/0	49	Y	35/70/35	25/50/20	84	Y	0/0/20	0/0/10
10	Y	20/0/0	10/0/0	50	Y	0/0/40	0/0/20	85	Y	0/0/40	0/0/20
11	Y	40/0/0	20/0/0	51	Y	20/0/0	10/0/0	86	Y	0/20/0	0/10/0
12	Y	0/20/0	0/10/0	52	Y	40/0/0	20/0/0	87	Y	0/40/0	0/20/0
16	Y	0/0/40	0/0/20	53	Y	40/0/0	20/0/0	88	Y	40/0/0	20/0/0
17	Y	0/0/20	0/0/10	55	Y	20/0/0	10/0/0	90	Y	0/40/0	0/20/0
19	Y	20/0/0	10/0/0	56	Y	0/60/0	0/40/0	92	Y	0/0/40	0/0/20
20	Y	20/0/0	10/0/0	58	Y	0/20/0	0/10/0	94	Y	40/0/0	20/0/0
22	Y	0/40/0	0/20/0	59	Y	0/20/0	0/10/0	95	Y	0/20/0	0/10/0
24	Y	0/0/40	0/0/20	60	Y	20/0/0	10/0/0	96	Y	0/20/0	0/10/0
28	Y	40/0/0	20/0/0	62	Y	0/0/70	0/0/50	98	Y	40/0/0	20/0/0
29	Y	40/0/0	20/0/0	63	Y	40/0/0	20/0/0	99	Y	0/40/0	0/20/0
30	Y	0/0/40	0/0/20	64	Y	0/75/0	0/35/0	100	Y	0/0/40	0/0/20
31	Y	0/0/20	0/0/10	65	D	35/35/70	25/25/50	102	Y	0/0/20	0/0/10
32	Y	0/0/20	0/0/10	66	Y	0/0/75	0/0/35	103	Y	0/0/40	0/0/20
33	Y	40/0/0	20/0/0	68	Y	20/0/0	10/0/0	104	Y	0/0/40	0/0/20
34	Y	0/0/40	0/0/20	69	Y	40/0/0	20/0/0	106	Y	0/60/0	0/30/0
35	D	40/0/0	20/0/0	70	Y	20/0/0	10/0/0	107	Y	0/60/0	0/30/0
37	Y	40/0/0	20/0/0	71	Y	40/0/0	20/0/0	111	Y	20/0/0	10/0/0
38	Y	0/20/0	0/10/0	73	Y	0/0/40	0/0/20	114	Y	20/0/0	10/0/0
39	Y	0/20/0	0/10/0	74	Y	0/0/40	0/0/20				
41	Y	0/0/20	0/0/10	75	Y	0/0/40	0/0/20	Total		1201/1009/1175	656/587/637
42	Y	20/0/0	10/0/0	76	D	70/70/70	50/50/50				

7.5.1.5. Restoration Sequence Graph

The one-line diagram of the restoration sequence for the base is shown in Figure 7.40 (a) to Figure 7.40 (f). Line thickness, as shown in the legend, has been used to denote single, double, and three-phase branches.

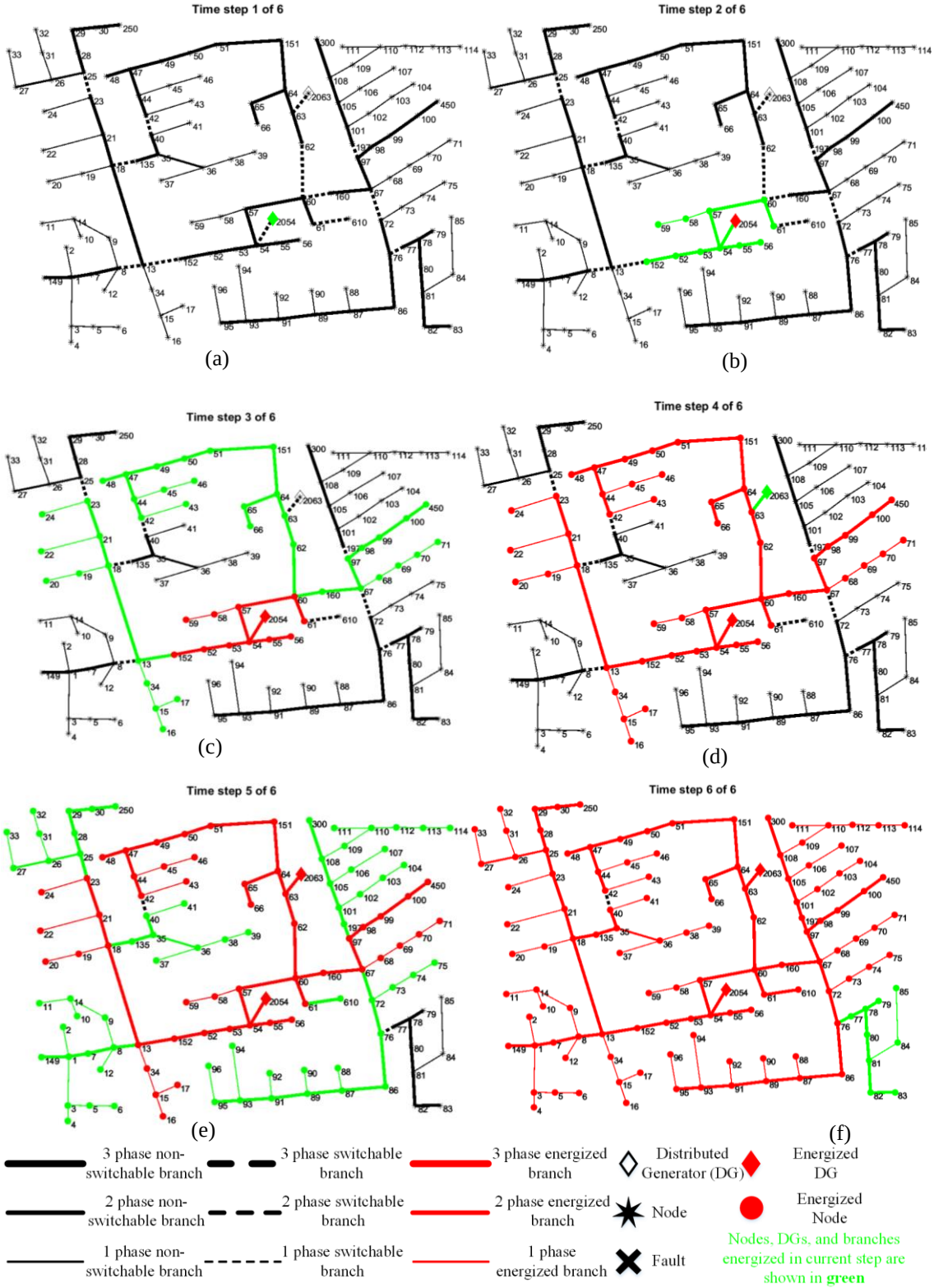

Figure 7.40 Restoration Sequence for Case 2 Base Case

7.5.1.6. Load Restoration Results

The load restoration with the restoration step of each load is shown in Table 7.16. Due to the freeze during step 4 synchronization of the grid-supporting DG as shown in Figure 7.40 (d), there was no load restored at step 4.

Table 7.16 Load Restoration Result with Energization Step for the Base Case

Node	Turn-On Step	Config	P(A/B/C) KW	Q(A/B/C) KVAR	Node	Turn-On Step	Config	P(A/B/C) KW	Q(A/B/C) KVAR	Node	Turn-On Step	Config	P(A/B/C) KW	Q(A/B/C) KVAR
16	3	Y	0/0/40	0/0/20	5	5	Y	0/0/20	0/0/10	96	5	Y	0/20/0	0/10/0
19	3	Y	20/0/0	10/0/0	6	5	Y	0/0/40	0/0/20	102	5	Y	0/0/20	0/0/10
20	3	Y	20/0/0	10/0/0	12	5	Y	0/20/0	0/10/0	103	5	Y	0/0/40	0/0/20
22	3	Y	0/40/0	0/20/0	17	5	Y	0/0/20	0/0/10	104	5	Y	0/0/40	0/0/20
24	3	Y	0/0/40	0/0/20	28	5	Y	40/0/0	20/0/0	106	5	Y	0/60/0	0/30/0
34	3	Y	0/0/40	0/0/20	29	5	Y	40/0/0	20/0/0	107	5	Y	0/60/0	0/30/0
42	3	Y	20/0/0	10/0/0	33	5	Y	40/0/0	20/0/0	111	5	Y	20/0/0	10/0/0
43	3	Y	0/40/0	0/20/0	35	5	D	40/0/0	20/0/0	114	5	Y	20/0/0	10/0/0
45	3	Y	20/0/0	10/0/0	37	5	Y	40/0/0	20/0/0	32	6	Y	0/0/20	0/0/10
47	3	Y	35/35/35	25/25/25	38	5	Y	0/20/0	0/10/0	77	6	Y	0/40/0	0/20/0
48	3	Y	70/70/70	50/50/50	39	5	Y	0/20/0	0/10/0	79	6	Y	40/0/0	20/0/0
50	3	Y	0/0/40	0/0/20	41	5	Y	0/0/20	0/0/10	80	6	Y	0/40/0	0/20/0
53	3	Y	40/0/0	20/0/0	46	5	Y	20/0/0	10/0/0	82	6	Y	40/0/0	20/0/0
55	3	Y	20/0/0	10/0/0	49	5	Y	35/70/35	25/50/20	84	6	Y	0/0/20	0/0/10
56	3	Y	0/60/0	0/40/0	60	5	Y	20/0/0	10/0/0	85	6	Y	0/0/40	0/0/20
58	3	Y	0/20/0	0/10/0	63	5	Y	40/0/0	20/0/0	1	Off	Y	40/0/0	20/0/0
59	3	Y	0/20/0	0/10/0	70	5	Y	20/0/0	10/0/0	7	Off	Y	20/0/0	10/0/0
64	3	Y	0/75/0	0/35/0	73	5	Y	0/0/40	0/0/20	10	Off	Y	20/0/0	10/0/0
65	3	D	35/35/70	25/25/50	74	5	Y	0/0/40	0/0/20	11	Off	Y	40/0/0	20/0/0
66	3	Y	0/0/75	0/0/35	75	5	Y	0/0/40	0/0/20	30	Off	Y	0/0/40	0/0/20
68	3	Y	20/0/0	10/0/0	76	5	D	70/70/70	50/50/50	31	Off	Y	0/0/20	0/0/10
69	3	Y	40/0/0	20/0/0	86	5	Y	0/20/0	0/10/0	51	Off	Y	20/0/0	10/0/0
71	3	Y	40/0/0	20/0/0	87	5	Y	0/40/0	0/20/0	52	Off	Y	40/0/0	20/0/0
98	3	Y	40/0/0	20/0/0	88	5	Y	40/0/0	20/0/0	62	Off	Y	0/0/70	0/0/50
99	3	Y	0/40/0	0/20/0	90	5	Y	0/40/0	0/20/0	83	Off	Y	0/0/20	0/0/10
100	3	Y	0/0/40	0/0/20	92	5	Y	0/0/40	0/0/20					
2	5	Y	0/20/0	0/10/0	94	5	Y	40/0/0	20/0/0	Total Restored			1021/1009/1025	566/587/547
4	5	Y	0/0/40	0/0/20	95	5	Y	0/20/0	0/10/0					

7.5.1.7. Derivative Cases with Demand Response Loads

Four cases derived from the base case are discussed in this section. These cases are called scenarios 1.2, 1.3, 1.4, and 1.5. The derivative cases were formed by converting the ZIP loads at nodes 43, 56, 62, 63, and 37 to loads with demand response (DR)

capability. Each DR load is assumed to have a direct load control (DLC) from the microgrid central controller (MGCC). To study the effect of DR, the lower limit (minimum) of load for each demand response load was set to 75%, 50%, 25%, and 0% of the current load capacity for scenarios 1.2, 1.3, 1.4, and 1.5, respectively. The upper limit (maximum) of the DR loads was set to their respective load capacities as in the base case.

Table 7.17 shows the details of the demand response loads. The phase column is the phase in which the demand response load is connected. The status column is used to indicate whether a given DR load is restorable (that is in good condition), which is denoted by a '1' or damaged, which is denoted by a '0'. The MLS column means 'maximum load step' and is used to denote how much of the load can change per step, e.g., an MLS of 100% means that the load can change by up to 100% of its nominal value per restoration step.

Table 7.17 Details of Demand Response Loads for the Derivative Cases

Label	Node	Type	Pmax (KW)	Pmin (KW)	Qmax (KVAR)	Qmin (KVAR)	Phase	Status	MLS %
L43	43	DLC	40	varies	20	varies	B	1	100
L56	56	DLC	60	varies	40	varies	B	1	100
L62	62	DLC	70	varies	50	varies	C	1	100
L63	63	DLC	40	varies	20	varies	A	1	100
L37	37	DLC	40	varies	20	varies	A	1	100

Table 7.18 shows a summary of the results for the base case (scenario 1.1) and the four derivative cases with DR loads (scenario 1.2 to 1.5). Notice from the shaded columns that as the lower limit is reduced, the sum of nominal active power loads restored and objective magnitude improve (i.e. increase) or do not get worse. The magnitude of the best bound gives an upper bound of what the best objective magnitude could be while the

optimality gap gives the difference between the objective value and the best bound expressed in percentage of the objective value. Both the best bound and the optimality gap give us an idea of how close we are to proving optimality. An optimality gap of under 2% can be considered as near-optimal.

Table 7.18 Summary of Results of Base Case and the Four Derivative Cases with Demand Response Loads

	Total Number of Restored Load	Sum of Nominal Active Power of Loads Restored (KW)	Solver Time (Sec)	Objective Value (KW-Steps)	Best Bound (KW-Steps)	Optimality Gap (%)
Base Case (no DR loads), scenario 1.1	71 out of 81 loads	3,055.0	37,956	(-)8,480.0	(-)8,645.0	1.95
(75% lower limit for DR loads) , scenario 1.2	72 out of 81 loads	3,078.4	1,500	(-)8,710.2	(-)8,773.7	0.73
Case 2 (50% lower limit for DR loads), scenario 1.3	71 out of 81 loads	3,080.7	3,289	(-)8,717.8	(-)8,891.5	1.99
Case 3 (25% lower limit for DR loads), scenario 1.4	73 out of 81 loads	3,083.2	1,876	(-)8,724.0	(-)8,844.2	1.38
Case 4 (0% lower limit for DR loads), scenario 1.5	72 out of 81 loads	3,083.2	1,500	(-)8,723.9	(-)8,869.1	1.66

Given that there is an enormous unique combination of loads (possibly tending towards infinite combination!) to be restored out of 81 loads, the total number of restored loads is not a reliable metric to evaluate which solution is better especially when their numbers are quite close. For instance, observe from scenarios 1.2 and 1.3 rows, that even though scenario 1.2 restored more aggregate loads by integer count, scenario 1.3 has a greater sum of nominal active power loads restored and better objective magnitude. Recall

that the aggregate loads are not all equal in value, so the case with a higher integer count of restored load is not always the better solution.

Notice that the solver time becomes considerably reduced with the addition of DR loads. The DR loads likely help the solver to discover better search nodes earlier than when there is no DR load.

7.5.1.8. Derivative Cases with PQ DGs

Three cases derived from the base case are discussed in this section. These cases are numbered as scenario 1.6, 1.7, and 1.8. Just like in scenario 1.1 (base case), the DGs have a total active power capacity of 4900 KW and total reactive power capacity of 2600 KVAR except that some of this capacity comes from the single-phase PQ DGs in these cases. The droop DG nodes remain the same as those in the base case. Observing the PQ DG nodes by considering the node locations of Figure 7.39, we can see that for scenario 1.6 (with the PQ DG nodes are at nodes 4, 33, and 107), the bus block of these PQ DGs were farthest from the droop DG nodes. As seen in Table 7.19, the PQ DG nodes (34, 19, and 67) of scenario 1.7 were less far from the droop DG nodes compared with those of scenario 1.6. PQ DG nodes of scenario 1.8 were the least distance from the droop DG nodes.

Table 7.19 DGs' Information for Derivative Cases of Case Studies 1 Scenario 1 with PQ DGs

Label	DG Node for S1.6	DG Node for S1.7	DG Node for S1.8	Type	f^{ref} (Hz)	Per phase BaseMVA	per phase baseKV	pu coupling X	Pmax (KW)	Pmin (KW)	Qmax (KVAR)	Qmin (KVAR)	Phase	Status	Blackstart	Ramp Rate %
DG1	2054	2054	2054	Droop	60	1	2.4018	0.3	2000	0	1000	-200	ABC	1	1	60
DG2	2063	2063	2063	Droop	60	1	2.4018	0.3	2000	0	1000	-200	ABC	1	1	60

Table 7.19 Continued

Label	DG Node for S1.6	DG Node for S1.7	DG Node for S1.8	Type	f^{ref} (Hz)	Per phase BaseMVA	per phase baseKV	pu coupling X	Pmax (KW)	Pmin (KW)	Qmax (KVAR)	Qmin (KVAR)	Phase	Status	Blackstart	Ramp Rate %
DG3	4	34	60	PQ	NA	NA	2.4018	NA	300	0	200	-40	C	1	0	60
DG4	33	19	152	PQ	NA	NA	2.4018	NA	450	0	300	-60	A	1	0	60
DG5	107	67	59	PQ	NA	NA	2.4018	NA	150	0	100	-20	B	1	0	60

Table 7.20 shows a summary of the results for the base case (scenario 1.1) and the three derivative cases with PQ DGs (scenario 1.6 to 1.8). Notice from the shaded column for the total number of loads restored, the derivative cases with PQ DGs restored all the loads while the base case restored 71 loads even though it has the same total DG capacity as the derivative cases.

In the derivative cases, the presence of single-phase PQ DGs acted as an unbalance load compensator for the microgrid and enhanced the restoration of more loads. Notice that the objective function of scenario 1.8 is the greatest in magnitude followed by 1.7 and then 1.6. Because the PQ DGs of scenario 1.8 is closest to the droop DG bus block, they are utilized in earlier restoration steps for unbalance compensation and earlier load pick up than those of 1.7 and 1.6. For this reason, scenario 1.8 has the greatest objective magnitude, which is analogous to having the greatest energy restored (most loads restored sooner than the other derived cases) in the considered restoration steps. Likewise, because the PQ DGs of scenario 1.7 is closer to the droop DG bus blocks than those of scenario 1.6, the objective magnitude of 1.7 is greater than those of 1.6. The magnitude of the best bound also follows the same trend as the objective magnitude, with scenario 1.8 having the greatest magnitude followed by 1.7 and lastly 1.6. The optimality gaps were all under

2% and show that the solutions are near-optimal. Just like in the previous subsection with DR loads, the addition of PQ DGs reduced the solver time considerably.

Table 7.20 Summary of Results of Base Case and the Four Derivative Cases with Demand Response Loads

	Total Number of Restored Load	Sum of Nominal Active Power of Loads Restored (KW)	Solver Time (Sec)	Objective Value (KW-Steps)	Best Bound (KW-Steps)	Optimality Gap (%)
Base Case (no DR loads, no PQ DGs), scenario 1.1	71 out of 81 loads	3,055.0	37,956	(-)8,480.0	(-)8,645.0	1.95
scenario 1.6 (with PQ DGs)	81 out of 81 loads	3,385.0	662	(-)9,385.0	(-)9,555.0	1.81
scenario 1.7 (with PQ DGs)	81 out of 81 loads	3,385.0	132	(-)10,530.0	(-)10,730.0	1.90
scenario 1.8 (with PQ DGs)	81 out of 81 loads	3,385.0	210	(-)10,770.0	(-)10,950.0	1.38

7.5.1.9. Derivative Cases with PQ DGs and DR loads

The three derivative cases with PQ DGs from the previous section, that is, scenarios 1.6, 1.7, and 1.8 were further modified to include loads with demand response capability to create scenarios 1.9, 1.10, and 1.11 respectively. The five loads converted to DR loads in section 7.5.1.7 were converted to have DR capability with 0% allowable lower limit for each load (this is the maximum possible controllability range for the DR loads) for each of scenarios 1.9, 1.10, and 1.11.

Table 7.21 shows the performance metric values for the derivative cases with both PQ DGs and loads with DR capability. Compared to Table 7.20, notice that there is no change in the sum of nominal loads restored. However, there is a slight improvement in the objective function for scenarios 1.9, 1.10, 1.11 compared with scenarios 1.6, 1.7, and 1.8 of Table 7.20. The improvement in the objective function values means that more loads

are restored sooner or in other words, more energy was restored in the restoration steps solved for.

Table 7.21 Summary of Results of Base Case and the Three Derivative Cases with both PQ DGs and Demand Response Loads

	Total Number of Restored Load	Sum of Nominal Active Power of Loads Restored (KW)	Solver Time (Sec)	Objective Value (KW-Steps)	Objective Value from Table 7.20, without DR loads (KW-Steps)	Best Bound (KW-Steps)	Optimality Gap (%)
Base Case (no DR loads, no PQ DGs), scenario 1.1	71 out of 81 loads	3,055.0	37,956	(-)8,480.0	(-)8,480.0	(-)8,645.0	1.95
S1.9 (with PQ DGs and DR loads added to S1.6)	81 out of 81 loads	3,385.0	161	(-)9,508.7	(-)9,385.0	(-)9,548.9	0.42
S1.10 (with PQ DGs and DR loads added to S1.7)	81 out of 81 loads	3,385.0	59	(-)10,588.8	(-)10,530.0	(-)10,749.5	1.52
S1.11 (with PQ DGs and DR loads added to S1.8)	81 out of 81 loads	3,385.0	55	(-)10,810.3	(-)10,770.0	(-)10,986.9	1.63

7.5.2. Scenario 2

There is a total of 9 case studies in this scenario. The purpose of these cases is to study the compensating effect of PQ DGs and how the choice of PQ DG phase affects the restoration solution.

7.5.2.1. Description of Test System

A one-line diagram of the base test system is shown in Figure 7.41. The system is assumed to have experienced a blackout due to an unforeseen emergency. Two droop-controlled DGs are present at nodes 2054 and 2063. A single-phase PQ DG is present at nodes 47 and 57, respectively. These PQ DG nodes are three-phase nodes and therefore, the PQ DG can connect to any of the phases in these nodes. For the base case, the PQ DG at nodes 47 and 57 connect to phases A and B, respectively. Details of the line information can be found in Appendix E.

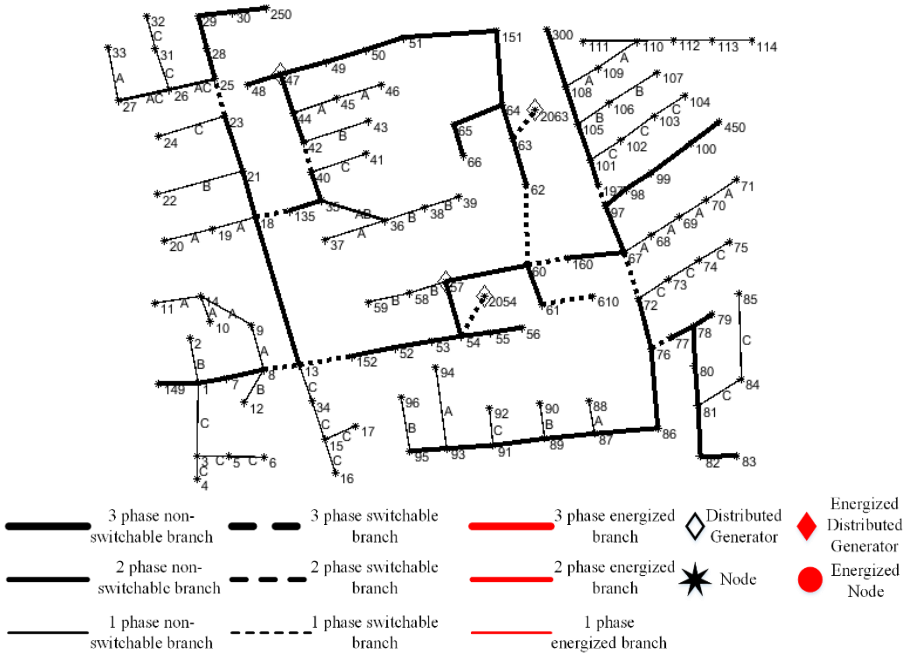

Figure 7.41 One Line Diagram for Case studies 2 scenario 2 Base Case

7.5.2.2. DGs' Information and Details of the Derivative Cases

The four DGs' details present in Figure 7.41 are summarized in Table 7.22. The phases of the PQ DGs for the base case are at phases A and B for DGs at nodes 47 and 57, respectively. The DGs have a total active power capacity of 4500 KW and a total reactive power capacity of 2320 KVAR.

Table 7.22 DGs' Information for the Base Case of Case Studies 2 Scenario 2

Label	Node	Type	f^{ref} (Hz)	Per phase BaseMVA	per phase baseKV	pu coupling X	Pmax (KW)	Pmin (KW)	Qmax (KVAR)	Qmin (KVAR)	Phase	Status	Blackstart	Ramp Rate %
DG1	2054	Droop	60	1	2.4018	0.3	2000	0	1000	-200	ABC	1	1	60
DG2	2063	Droop	60	1	2.4018	0.3	2000	0	1000	-200	ABC	1	1	60
DG3	47	PQ	NA	NA	2.4018	NA	300	0	200	-60	A	1	0	60
DG4	57	PQ	NA	NA	2.4018	NA	200	0	120	-20	B	1	0	60

To generate the derivative cases, the phases of the PQ DGs were modified to realize 8 derivative cases numbered scenarios 2.2, 2.3, to 2.9 where scenario 2.1 is the base case. Table 7.23 outlines the phases of the PQ DGs for the derivative cases studied under this scenario.

Table 7.23 Phases of the PQ DGs for the Derivative Cases of Case Studies 2 Scenario 2

	S2.1 (base)	S2.2	S2.3	S2.4	S2.5	S2.6	S2.7	S2.8	S2.9
PQ DG at node 47	A	A	B	B	C	C	A	B	C
PQ DG at node 57	B	C	A	C	A	B	A	B	C

7.5.2.3. Load Details and Unbalance Indices

There is a total of 81 loads in this case study and the details are shown in Table 7.24. The loads are configured as either wye or delta connected. All loads are assumed to be switchable and restorable.

By transforming the delta connected load into equivalent Y connected load and summing the nominal power for the loads gives: the sum of nominal active power load is 1,201.1 KW, 1,009.2 KW, and 1,174.7 KW for phases A, B, and C respectively. The sum of the nominal reactive power load is 656.1 KVAR, 586.5 KVAR, and 637.4 KVAR for phases A, B, and C respectively. Notice that phases A and C are more loaded than phase B, and therefore, phases A and C would probably need more load compensation in the form of PQ DGs than phase B.

Table 7.24 Load Details for the Base Case

Node	Config	P(A/B/C) KW	Q(A/B/C) KVAR	Node	Config	P(A/B/C) KW	Q(A/B/C) KVAR	Node	Config	P(A/B/C) KW	Q(A/B/C) KVAR
1	Y	40/0/0	20/0/0	43	Y	0/40/0	0/20/0	77	Y	0/40/0	0/20/0
2	Y	0/20/0	0/10/0	45	Y	20/0/0	10/0/0	79	Y	40/0/0	20/0/0
4	Y	0/0/40	0/0/20	46	Y	20/0/0	10/0/0	80	Y	0/40/0	0/20/0
5	Y	0/0/20	0/0/10	47	Y	35/35/35	25/25/25	82	Y	40/0/0	20/0/0
6	Y	0/0/40	0/0/20	48	Y	70/70/70	50/50/50	83	Y	0/0/20	0/0/10
7	Y	20/0/0	10/0/0	49	Y	35/70/35	25/50/20	84	Y	0/0/20	0/0/10
10	Y	20/0/0	10/0/0	50	Y	0/0/40	0/0/20	85	Y	0/0/40	0/0/20
11	Y	40/0/0	20/0/0	51	Y	20/0/0	10/0/0	86	Y	0/20/0	0/10/0
12	Y	0/20/0	0/10/0	52	Y	40/0/0	20/0/0	87	Y	0/40/0	0/20/0
16	Y	0/0/40	0/0/20	53	Y	40/0/0	20/0/0	88	Y	40/0/0	20/0/0
17	Y	0/0/20	0/0/10	55	Y	20/0/0	10/0/0	90	Y	0/40/0	0/20/0
19	Y	20/0/0	10/0/0	56	Y	0/60/0	0/40/0	92	Y	0/0/40	0/0/20
20	Y	20/0/0	10/0/0	58	Y	0/20/0	0/10/0	94	Y	40/0/0	20/0/0
22	Y	0/40/0	0/20/0	59	Y	0/20/0	0/10/0	95	Y	0/20/0	0/10/0
24	Y	0/0/40	0/0/20	60	Y	20/0/0	10/0/0	96	Y	0/20/0	0/10/0
28	Y	40/0/0	20/0/0	62	Y	0/0/70	0/0/50	98	Y	40/0/0	20/0/0
29	Y	40/0/0	20/0/0	63	Y	40/0/0	20/0/0	99	Y	0/40/0	0/20/0
30	Y	0/0/40	0/0/20	64	Y	0/75/0	0/35/0	100	Y	0/0/40	0/0/20
31	Y	0/0/20	0/0/10	65	D	35/35/70	25/25/50	102	Y	0/0/20	0/0/10
32	Y	0/0/20	0/0/10	66	Y	0/0/75	0/0/35	103	Y	0/0/40	0/0/20
33	Y	40/0/0	20/0/0	68	Y	20/0/0	10/0/0	104	Y	0/0/40	0/0/20
34	Y	0/0/40	0/0/20	69	Y	40/0/0	20/0/0	106	Y	0/60/0	0/30/0
35	D	40/0/0	20/0/0	70	Y	20/0/0	10/0/0	107	Y	0/60/0	0/30/0
37	Y	40/0/0	20/0/0	71	Y	40/0/0	20/0/0	111	Y	20/0/0	10/0/0
38	Y	0/20/0	0/10/0	73	Y	0/0/40	0/0/20	114	Y	20/0/0	10/0/0
39	Y	0/20/0	0/10/0	74	Y	0/0/40	0/0/20				
41	Y	0/0/20	0/0/10	75	Y	0/0/40	0/0/20	Total		1201/1009/1175	656/587/637
42	Y	20/0/0	10/0/0	76	D	70/70/70	50/50/50				

7.5.2.4. Choice of Time Steps

By graphically analyzing the one-line diagram of Figure 7.41, the conservative and generous time steps were estimated to be 6 and 7, respectively. The generous time step of 7 was chosen to solve for the black start restoration of the base case as well as the derivative cases.

7.5.2.5. Restoration Sequence Graph

The one-line diagram of the restoration sequence is shown in Figure 7.42 (a) to (g). Line thickness, as shown in the legend, has been used to denote single, double, and three-phase branches.

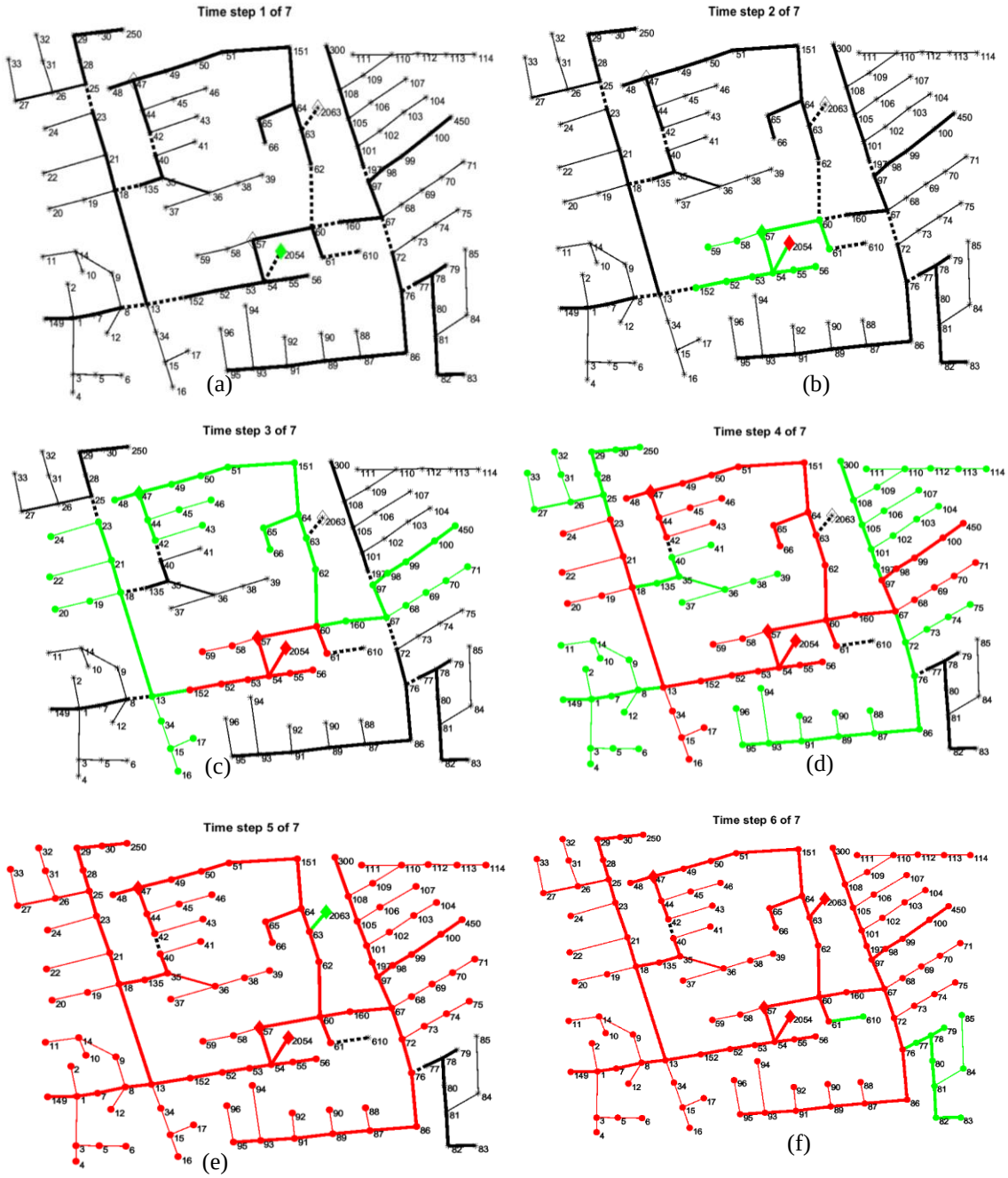

Figure 7.42 Restoration Sequence for Case Studies 2 Scenario 2 Base Case

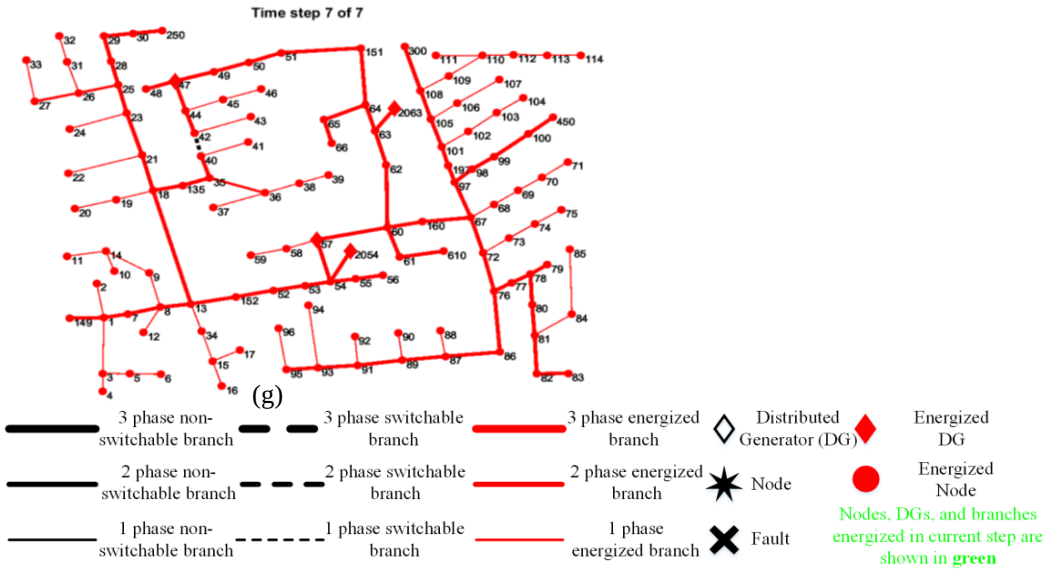

Figure 7.42 Continued

7.5.2.6. Summary of Scenario 2 results

Table 7.25 shows a summary of the cases performed for scenario 2. Notice that scenario 2.2 and 2.5 with a PQ DG connected to phase A and C, restored all the loads. This is because, as calculated in the load details subsection 7.5.2.3, phases A and C are the phases with more nominal load value and thus, in more need of PQ DG for compensation.

Another observation is that for the last three cases (scenarios 2.7, 2.8, and 2.9), the solver time reached the upper time limit set for this scenario, which was set to 10,000 seconds. It appears that failure in selecting the most suitable phases to connect the PQ DGs negatively affects the integer programming optimal/near-optimal solution search (the solver output shows that the optimality gap for these three cases was barely moving after a few thousand seconds).

Table 7.25 Summary of Results of Base Case and the 8 derivative Cases for Case Studies 2 scenario 2

	Total Number of Restored Load	Sum of Nominal Active Power of Loads Restored (KW)	Solver Time (Sec)	Objective Value (KW-Steps)	Best Bound (KW-Steps)	Optimality Gap (%)
S2.1 Base Case (PQ DGs at phases A&B)	78 out of 81 loads	3,255.0	1920	(-)12,515.0	(-)12,745.0	1.84
S2.2 (PQ DGs at phases A&C)	81 out of 81 loads	3,385.0	2720	(-)12,765.0	(-)13,020.0	2.00
S2.3 (PQ DGs at phases B&A)	78 out of 81 loads	3,265.0	1902	(-)12,455.0	(-)12,695.0	1.93
S2.4 (PQ DGs at phases B&C)	76 out of 81 loads	3,225.0	10,000	(-)12,115.0	(-)12,470.0	2.93
S2.5 (PQ DGs at phases C&A)	81 out of 81 loads	3,385.0	1178	(-)12,925.0	(-)13,180.0	1.97
S2.6 (PQ DGs at phases C&B)	76 out of 81 loads	3,225.0	10,000	(-)12,335.0	(-)12,615.0	2.27
S2.7 (PQ DGs at phases A&A)	77 out of 81 loads	3,235.0	10,000	(-)12,165.0	(-)12,500.0	2.75
S2.8 (PQ DGs at phases B&B)	72 out of 81 loads	3,085.0	10,000	(-)11,210.0	(-)11,880.0	5.98
S2.9 (PQ DGs at phases C&C)	76 out of 81 loads	3,205.0	10,000	(-)11,855.0	(-)12,265.0	2.93

A plot of the optimality gap trajectory against solver time for select cases (scenarios 2.1, 2.2, 2.5, 2.7, 2.8, and 2.9) is shown in Figure 7.43. The optimality gap, which is a measure of the difference between the objective function and the best bound, is above 2% for the cells shaded in yellow in Table 7.25; these cells correspond to the cases that were not well compensated based on the choices of the PQ DG phases. These above 2% optimality gaps show that the solutions of the least compensated cases are not as near-optimal as the well-compensated ones.

These results suggest that given the choice of phases to connect PQ DGs, the phases with more load capacity should be given priority.

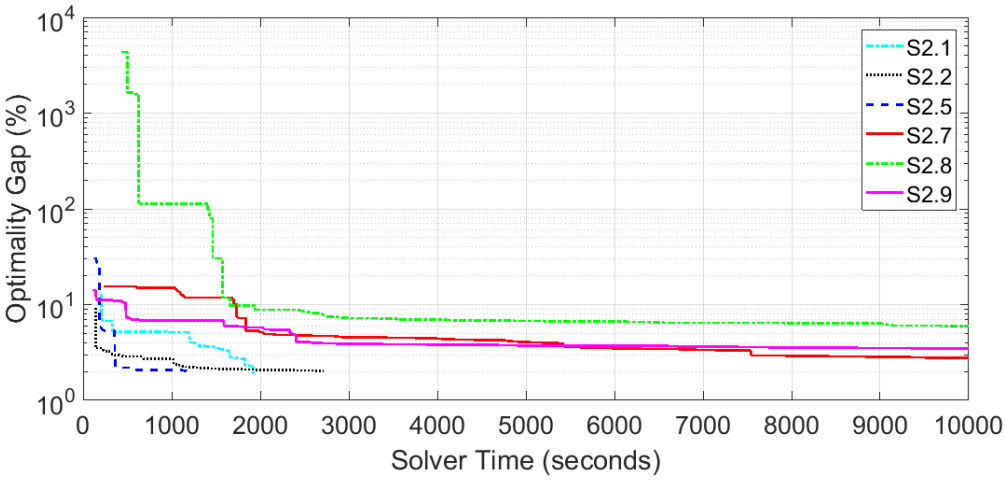

Figure 7.43 Plot of Optimality Gap for Select Cases of Case Studies 2 Scenario 2

7.6. Case Studies 3: Effects of Different Initial System Conditions

Case studies 3 is the performance of the restoration method under different initial system conditions such as choice of branches/loads that are switchable, whether there are damaged lines and loads in the system, and choice of restoration step. The island system used for the case studies under this section is adapted from the IEEE 123 node test feeder. The case studies under this section are subdivided into four scenarios:

- Scenario 1: case studies for studying the impact of the choice of droop-controlled DG node
- Scenario 2: case studies for highlighting the effect of the choice of switchable lines/loads
- Scenario 3: case studies for highlighting the effect of damaged lines and loads
- Scenario 4: case studies for studying the impact of the choice of restoration time step

The computation options for all scenarios categorized under case studies 3 sections are outlined in Table 7.26 below.

Table 7.26 Computation Settings for Case Studies 3

Options	Choice
Options.connectGFDGs	False
Options.skipPWL	True
Options.ignoreShuntAdmittance	True
Options.includeShuntAdmittanceForLastStepOnly	NA
Options.MIPGap	2%
Conservative/Generous Time Step Estimate	Varies with case

7.6.1. Scenario 1

7.6.1.1. Description of Test System

A one-line diagram of the base test system is shown in Figure 7.44. One droop-controlled DG is present at node 2001 (for the droop-controlled DG node, we have used a naming convention in which its name is gotten by adding 2000 to the next adjacent node). Three PQ DGs are present at nodes 4, 33, and 107. Note that the branch adjacent to a droop-controlled DG node is the coupling inductor.

Figure 7.44 One Line Diagram for Case Studies 3 Scenario 1 Base Case

7.6.1.2. DG Information

The DGs' details present in Figure 7.44 are summarized in Table 7.27. The DGs have a total active power capacity of 4900 KW and a total reactive power capacity of 2600 KVAR.

Table 7.27 DGs' information for case studies 3 scenario 1 base case

Label	Node	Type	f^{ref} (Hz)	Per phase BaseMVA	per phase baseKV	pu coupling X	Pmax (KW)	Pmin (KW)	Qmax (KVAR)	Qmin (KVAR)	Phase	Status	Blackstart	Ramp Rate %
DG1	2001	Droop	60	1	2.4018	0.3	4000	0	2000	-200	ABC	1	1	60
DG2	4	PQ	NA	NA	NA	NA	300	0	200	-40	C	1	0	60
DG3	33	PQ	NA	NA	NA	NA	450	0	300	-60	A	1	0	60
DG4	107	PQ	NA	NA	NA	NA	150	0	100	-20	B	1	0	60

7.6.1.3. Derivative Cases

There are two derivative cases numbered 1.2 and 1.3, with the base case numbered 1.1. Notice that the droop-controlled DG of the base case is situated closer to the peripheral of the system. To create the derivative cases, we move the droop DG to a node near the center of the system. As seen in Figure 7.45, the droop DG for scenario 1.2 is located at node 2013. As seen in Figure 7.46, the droop DG for scenario 1.3 is located at node 2054 which is located more centered than both scenarios 1.1 and 1.2.

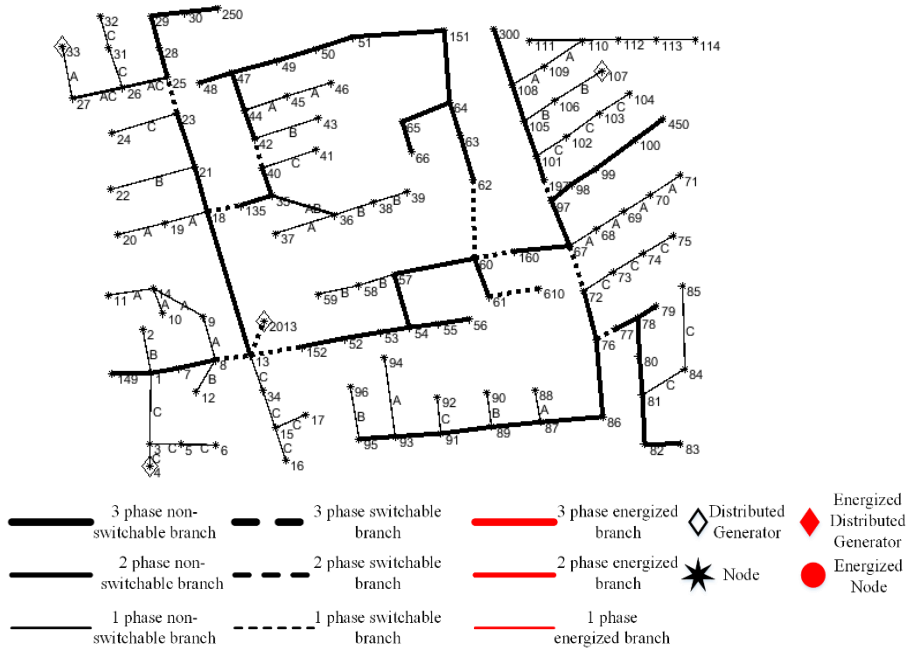

Figure 7.45 One Line Diagram for Case Studies 3 Scenario 1.2

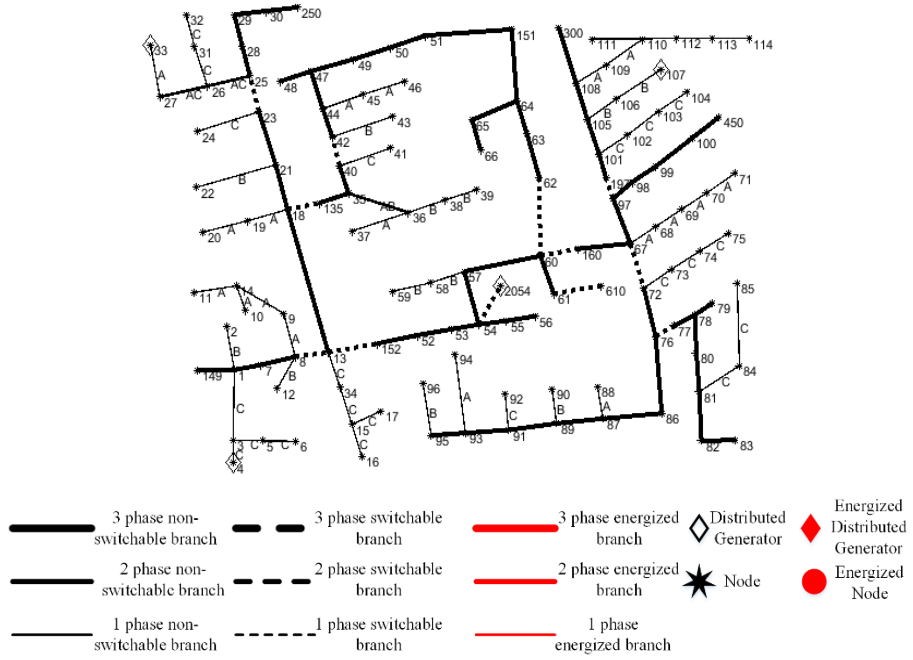

Figure 7.46 One Line Diagram for Case Studies 3 Scenario 1.3

7.6.1.4. Load Details

There is a total of 81 loads in this case study and the details are shown in Table 7.28. All loads are assumed to be switchable and restorable.

Table 7.28 Load Details for Case Studies 3 Scenario 1

Node	Config	P(A/B/C) KW	Q(A/B/C) KVAR	Node	Config	P(A/B/C) KW	Q(A/B/C) KVAR	Node	Config	P(A/B/C) KW	Q(A/B/C) KVAR
1	Y	40/0/0	20/0/0	43	Y	0/40/0	0/20/0	77	Y	0/40/0	0/20/0
2	Y	0/20/0	0/10/0	45	Y	20/0/0	10/0/0	79	Y	40/0/0	20/0/0
4	Y	0/0/40	0/0/20	46	Y	20/0/0	10/0/0	80	Y	0/40/0	0/20/0
5	Y	0/0/20	0/0/10	47	Y	35/35/35	25/25/25	82	Y	40/0/0	20/0/0
6	Y	0/0/40	0/0/20	48	Y	70/70/70	50/50/50	83	Y	0/0/20	0/0/10
7	Y	20/0/0	10/0/0	49	Y	35/70/35	25/50/20	84	Y	0/0/20	0/0/10
10	Y	20/0/0	10/0/0	50	Y	0/0/40	0/0/20	85	Y	0/0/40	0/0/20
11	Y	40/0/0	20/0/0	51	Y	20/0/0	10/0/0	86	Y	0/20/0	0/10/0
12	Y	0/20/0	0/10/0	52	Y	40/0/0	20/0/0	87	Y	0/40/0	0/20/0
16	Y	0/0/40	0/0/20	53	Y	40/0/0	20/0/0	88	Y	40/0/0	20/0/0
17	Y	0/0/20	0/0/10	55	Y	20/0/0	10/0/0	90	Y	0/40/0	0/20/0
19	Y	20/0/0	10/0/0	56	Y	0/60/0	0/40/0	92	Y	0/0/40	0/0/20
20	Y	20/0/0	10/0/0	58	Y	0/20/0	0/10/0	94	Y	40/0/0	20/0/0
22	Y	0/40/0	0/20/0	59	Y	0/20/0	0/10/0	95	Y	0/20/0	0/10/0
24	Y	0/0/40	0/0/20	60	Y	20/0/0	10/0/0	96	Y	0/20/0	0/10/0
28	Y	40/0/0	20/0/0	62	Y	0/0/70	0/0/50	98	Y	40/0/0	20/0/0
29	Y	40/0/0	20/0/0	63	Y	40/0/0	20/0/0	99	Y	0/40/0	0/20/0
30	Y	0/0/40	0/0/20	64	Y	0/75/0	0/35/0	100	Y	0/0/40	0/0/20
31	Y	0/0/20	0/0/10	65	D	35/35/70	25/25/50	102	Y	0/0/20	0/0/10
32	Y	0/0/20	0/0/10	66	Y	0/0/75	0/0/35	103	Y	0/0/40	0/0/20
33	Y	40/0/0	20/0/0	68	Y	20/0/0	10/0/0	104	Y	0/0/40	0/0/20
34	Y	0/0/40	0/0/20	69	Y	40/0/0	20/0/0	106	Y	0/60/0	0/30/0
35	D	40/0/0	20/0/0	70	Y	20/0/0	10/0/0	107	Y	0/60/0	0/30/0
37	Y	40/0/0	20/0/0	71	Y	40/0/0	20/0/0	111	Y	20/0/0	10/0/0
38	Y	0/20/0	0/10/0	73	Y	0/0/40	0/0/20	114	Y	20/0/0	10/0/0
39	Y	0/20/0	0/10/0	74	Y	0/0/40	0/0/20				
41	Y	0/0/20	0/0/10	75	Y	0/0/40	0/0/20		Total	1201/1009/1175	656/587/637
42	Y	20/0/0	10/0/0	76	D	70/70/70	50/50/50				

7.6.1.5. Choice of Time Steps

By graphically analyzing the one-line diagram of Figure 7.44 to Figure 7.46, the conservative and generous time steps were estimated for scenarios 1.1, 1.2, and 1.3 as shown in Table 7.29. A solution time step of 5 was chosen to solve for the restoration of all three cases.

Table 7.29 Choice of Time Step and Time Step Estimation for Case Studies 3 Scenario 1

	Scenario 1.1	Scenario 1.2	Scenario 1.3
Conservative/Generous Steps	7/7	6/6	5/5
Choice of Steps	5	5	5

Notice that the more centered scenario 1.3 has smaller time steps estimation followed by scenario 1.2 and then the base case which is scenario 1.1.

7.6.1.6. Restoration Sequence Graph

The one-line diagram of the restoration sequence for the base case (scenario 1.1) is shown in Figure 7.47 (a) to (e). Notice that by the end of the restoration step in Figure 7.47 (e), 3 major bus blocks in the system on the east side of the system have not been restored.

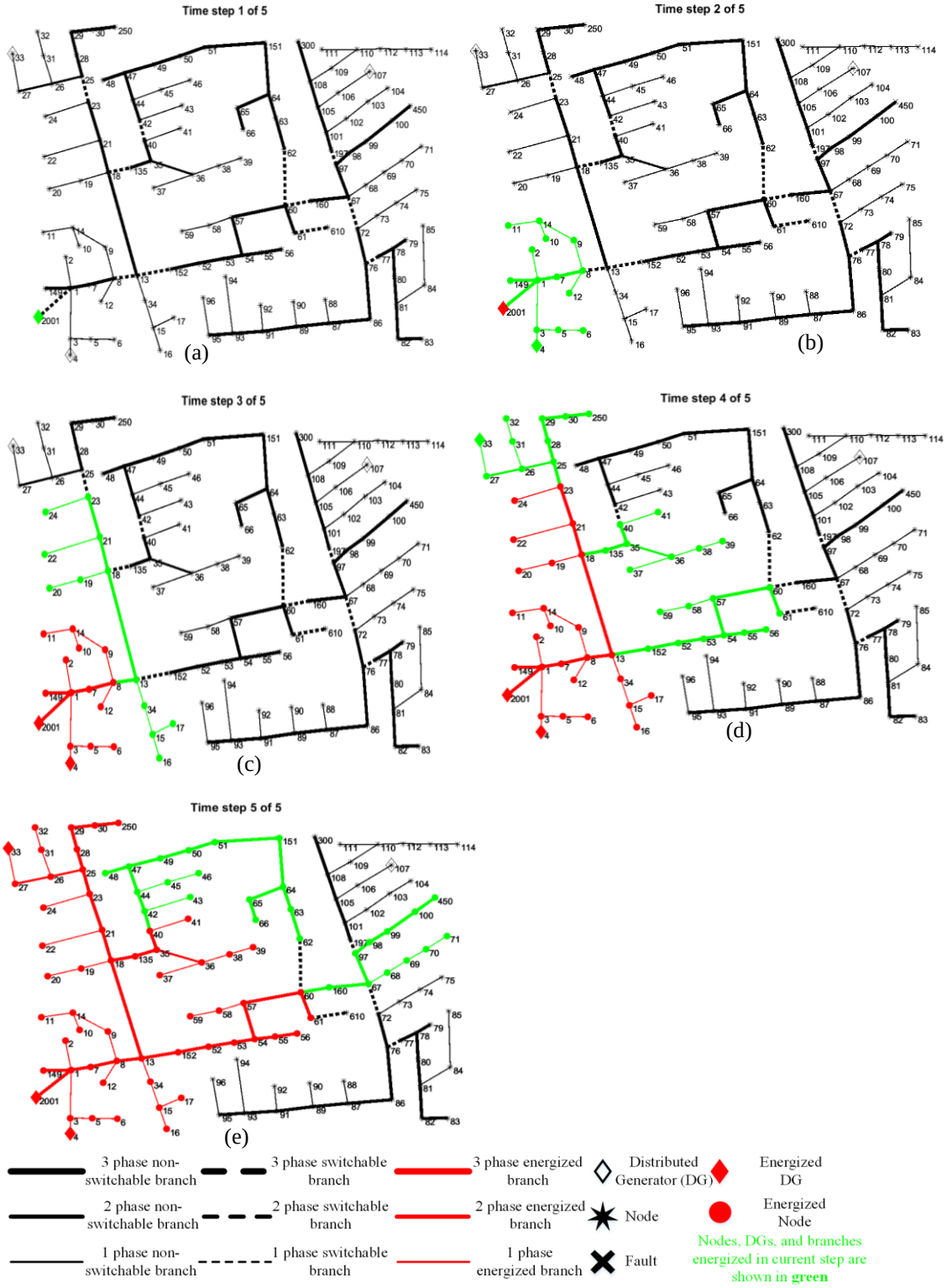

Figure 7.47 Restoration Sequence for Case Studies 3 Scenario 1.1 (Base Case)

The one-line diagram of the restoration sequence for scenario 1.2 is shown in Figure 7.48 (a) to (e). Notice that by the end of the restoration step in Figure 7.48 (e), one major bus block on the southeast side of the system has not been restored.

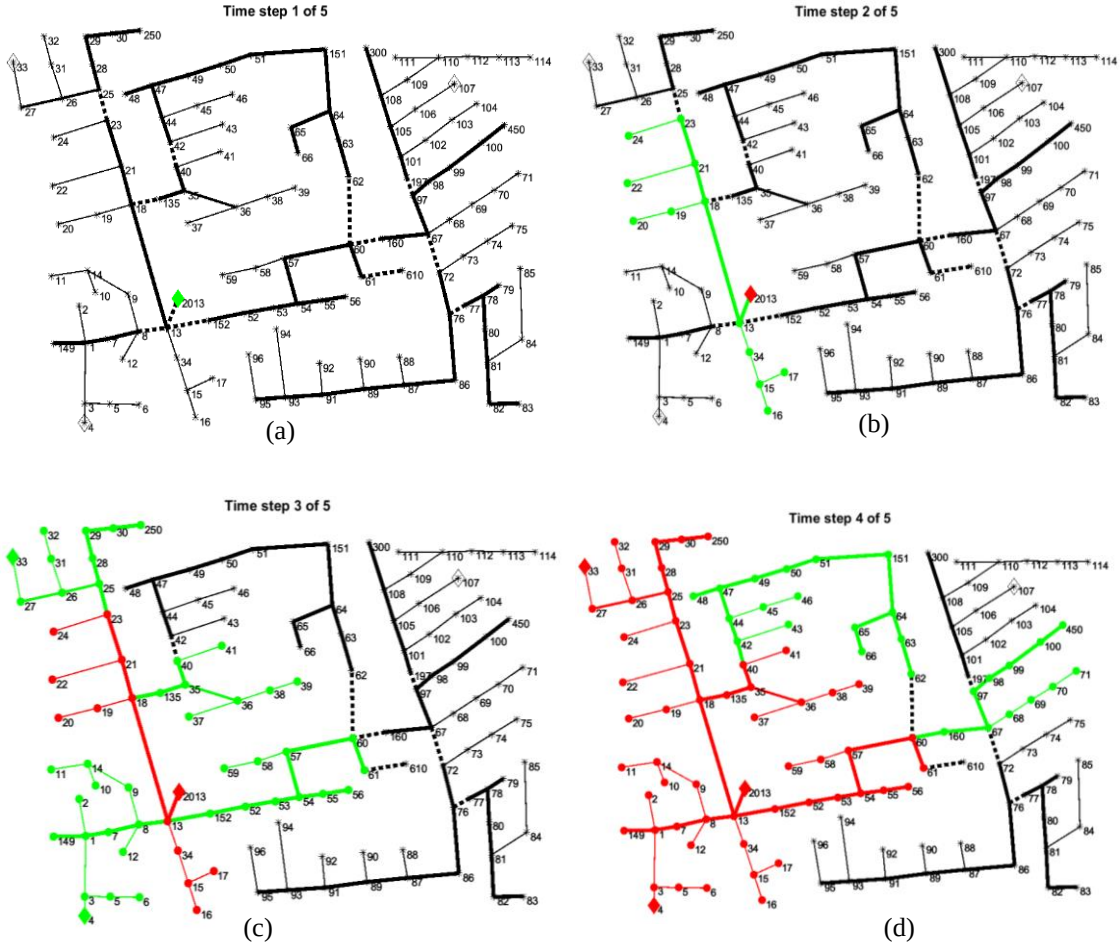

Figure 7.48 Restoration Sequence for Case Studies 3 Scenario 1.2

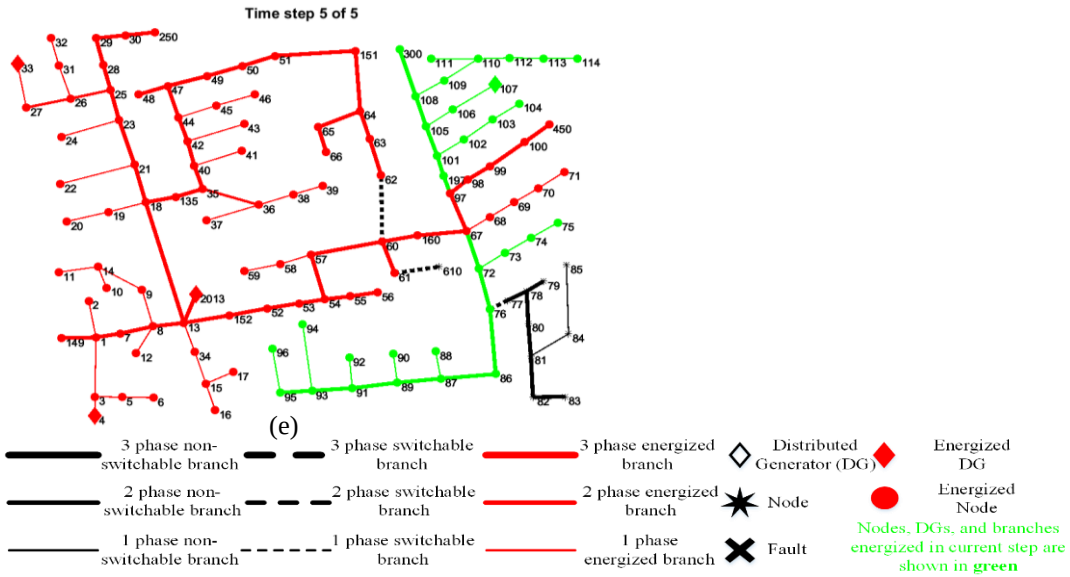

Figure 7.48 Continued

The one-line diagram of the restoration sequence for scenario 1.3 is shown in Figure 7.49 (a) to (e). By the end of the restoration step in Figure 7.49 (e), all of the major bus blocks in the system have been restored. This case has the most centered droop-controlled DG node and reached every corner of the system faster than those of scenarios 1.1 and 1.2. For any given aggregate load to be restored, its node must be energized. Expectedly, scenario 1.3, which restored the most nodes has the potential to restore more loads than scenarios 1.1 and 1.2. The next subsection looks at the numerical results of the three cases in this scenario for comparison.

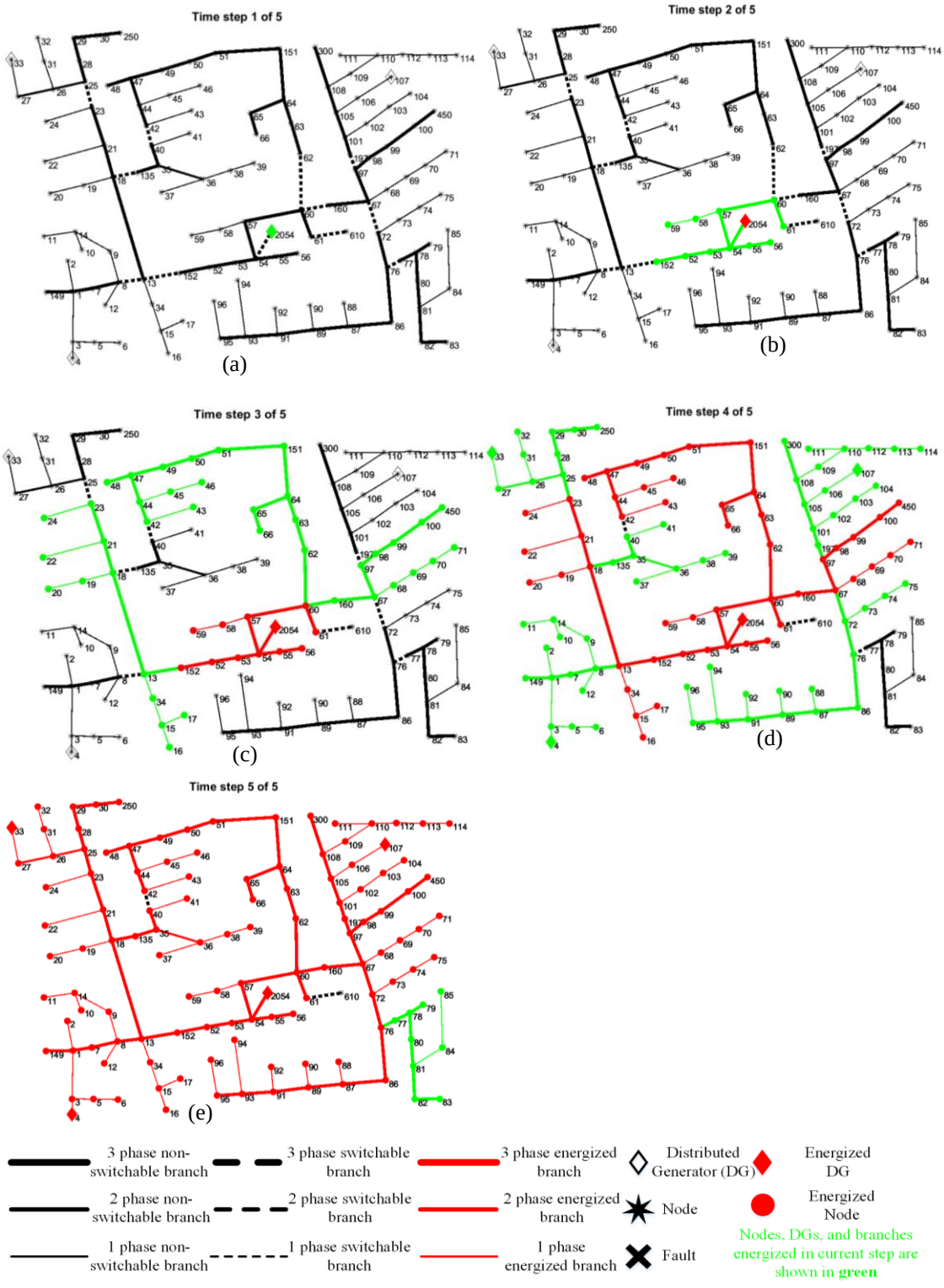

Figure 7.49 Restoration Sequence for Case Studies 3 Scenario 1.3

7.6.1.7. Summary of Scenario 1 results

Table 7.30 shows a summary of the three cases run in this scenario. Notice that scenario 1.3 restored the most loads, followed by 1.2 and lastly 1.1 (base case). Scenario 1.3 has a more centered droop DG node (which will be selected as build-up/black start node) and this enables it to reach other nodes in the microgrid better than scenarios 1.2 and 1.1. This shows that a more centered node would likely be the best choice of nodes to install a droop-controlled black start DG during planning.

Table 7.30 Summary of Results of Base Case and the Two Derivative Cases for Case Studies 3 Scenario 1

	Total Number of Restored Load	Sum of Nominal Active Power of Loads Restored (KW)	Solver Time (Sec)	Objective Value (KW-Steps)	Best Bound (KW-Steps)	Optimality Gap (%)
Scenario 1.1 (base case)	54 out of 81 loads	2,255.0	4.17	(-)3,875.0	(-)3,890.0	0.39
Scenario 1.2	64 out of 81 loads	2,785.0	8.90	(-)6,240.0	(-)6,360.0	1.92
Scenario 1.3	69 out of 81 loads	2,945.0	471.95	(-)7,055.0	(-)7,195.0	1.98

7.6.2. Scenario 2

There is a total of 3 case studies in this scenario. The purpose is to study the effects and performance of the restoration method to switchable/non-switchable lines/loads.

7.6.2.1. Description of Test System

A one-line diagram of the base test system is shown in Figure 7.50. One droop-controlled DGs is present at node 2054. Three PQ DGs are present at nodes 34, 45, and 67.

Figure 7.50 One Line Diagram for Case Studies 3 Scenario 2 Base Case

7.6.2.2. DGs' Information and Details of the Derivative Cases

The DGs' details present in Figure 7.50 are summarized in Table 7.31. The DG columns remain the same as previously described.

Table 7.31 DGs' Information for Case Studies 3 Scenario 2 Base Case

Label	Node	Type	f^{ref} (Hz)	Per phase BaseMVA	per phase baseKV	pu coupling X	Pmax (KW)	Pmin (KW)	Qmax (KVAR)	Qmin (KVAR)	Phase	Status	Blackstart	Ramp Rate %
DG1	2054	Droop	60	1	2.4018	0.3	4000	0	2000	-400	ABC	1	1	50
DG2	34	PQ	NA	NA	NA	NA	300	0	200	-40	C	1	0	50
DG3	45	PQ	NA	NA	NA	NA	450	0	300	-60	A	1	0	50
DG4	67	PQ	NA	NA	NA	NA	150	0	100	-20	B	1	0	50

7.6.2.3. Load Details

The load details of the base case in this scenario are the same as those of scenario 1 which is given in Table 7.28. All loads are assumed to be switchable and restorable except for scenarios 3.2 and 3.3 where two of the loads are assumed to be non-switchable. For the derivative scenario, a modification on the controllability of two loads is made. This modification is described in the next subsection.

7.6.2.4. Derivative Cases

There are two derivative cases numbered 2.2 and 2.3, with the base case numbered 2.1.

In the first derivative case, scenario 2.2, two aggregate loads at nodes 59 and 58 are converted from switchable to non-switchable loads as shown in Figure 7.51. In Figure 7.51, only non-switchable loads are shown; there are 79 other switchable loads which are not shown for emphasis sake. A switchable load can be energized at the same step or a later restoration step to when its node became energized – this leads to better controllability for a switchable load. For non-switchable loads, they are automatically energized whenever their node becomes energized.

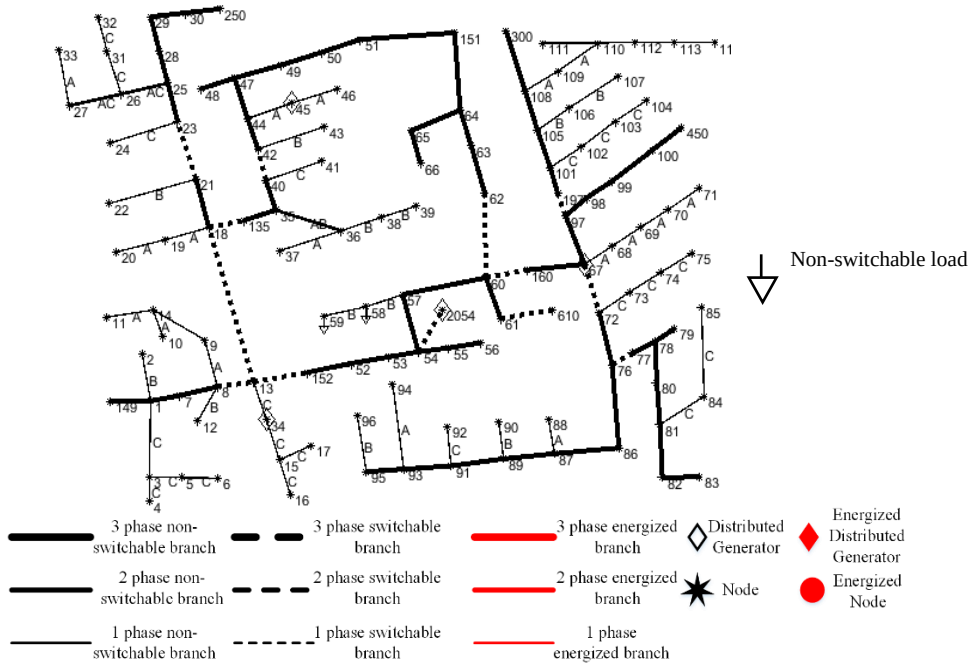

Figure 7.51 One Line Diagram for Case Studies 3 Scenario 2.2 (Loads at Nodes 58 and 59 are made Non-switchable)

In the second derivative case, the branch between nodes 58 and 57 is converted from non-switchable to switchable branch as shown in Figure 7.52. The loads at nodes 58 and 59 are still maintained as non-switchable just like in scenario 2.2. Converting the branch between nodes 58 and 57 to become switchable improves the controllability of the two non-switchable loads as we will see soon.

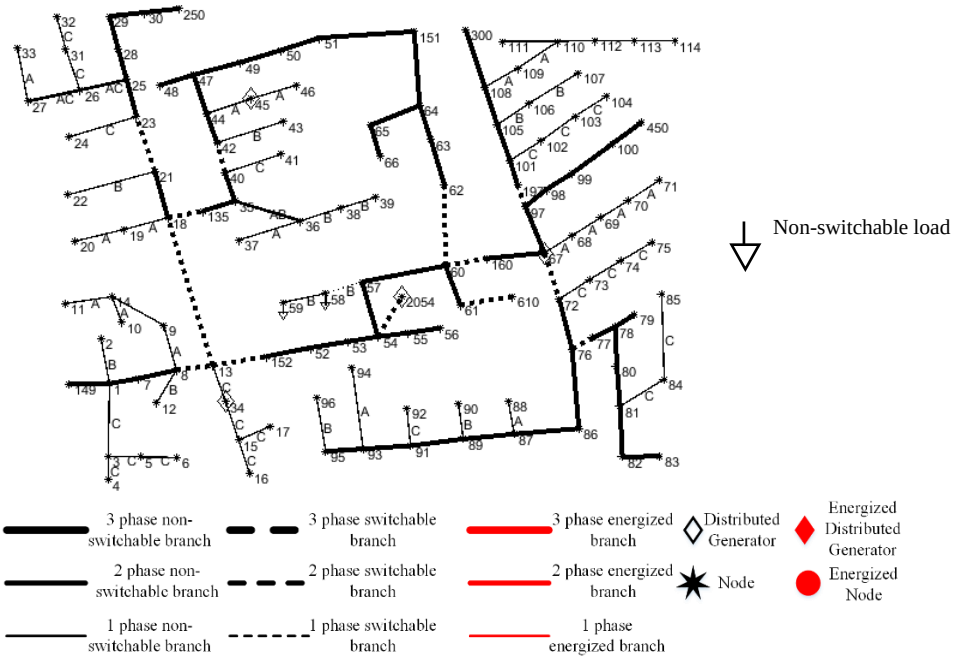

Figure 7.52 One Line Diagram for Case Studies 3 Scenario 2.3 (Branch between Nodes 57 and 58 is made Switchable)

7.6.2.5. Choice of Time Steps

By graphically analyzing the one-line diagram of Figure 7.50 to Figure 7.52, the conservative and generous time steps were estimated for all three cases to be 5, and a restoration time step of 5 was used to solve for all the cases under this scenario.

7.6.2.6. Restoration Sequence Graph for Scenario 2.1

The one-line diagram of the restoration sequence for the base case (scenario 2.1) is shown in Figure 7.53 (a) to (e). Observe that by the end of the restoration step in Figure 7.53 (e), all nodes have been restored.

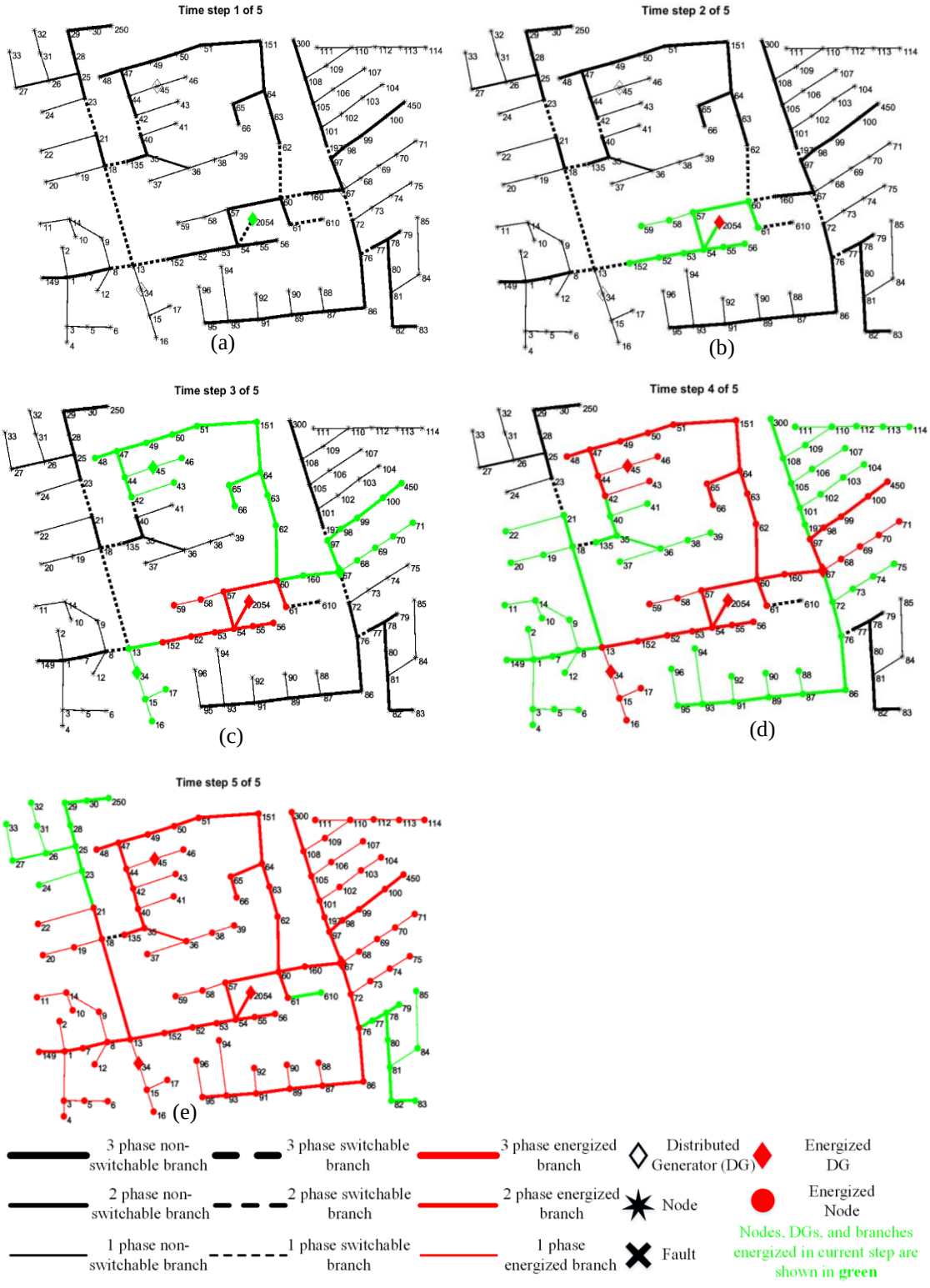

Figure 7.53 Restoration Sequence for Case Studies 3 Scenario 2.1 (Base Case)

The system is restored as desired. Note that all the loads are switchable. Something interesting happens when the loads at nodes 58 and 59 are converted to become non-switchable. This is explained in the next subsection which covers the restoration sequence for scenario 2.2.

7.6.2.7. Restoration Sequence Graph for Scenario 2.2

The one-line diagram of the restoration sequence for scenario 2.2 is shown in Figure 7.54 (a) and (b). Figure 7.54 (a) and (b) show only the first and the last restoration step since all the steps have the same topology. Figure 7.54 (a) shows the first step of the restoration with the droop DG at node 2054 energized. To energize the next set of nodes adjacent to node 2054, the branch between nodes 2054 and 54 has to be closed. It was not possible to close this branch because of the non-switchable loads at nodes 58 and 59 which would automatically be energized if this branch was closed. Energizing these loads would lead to unbalance power demand from the droop DG since none of the other switchable loads in this adjacent bus block could balance these two loads. Also, there is no PQ DG in this adjacent bus block that can help to compensate for the load unbalance.

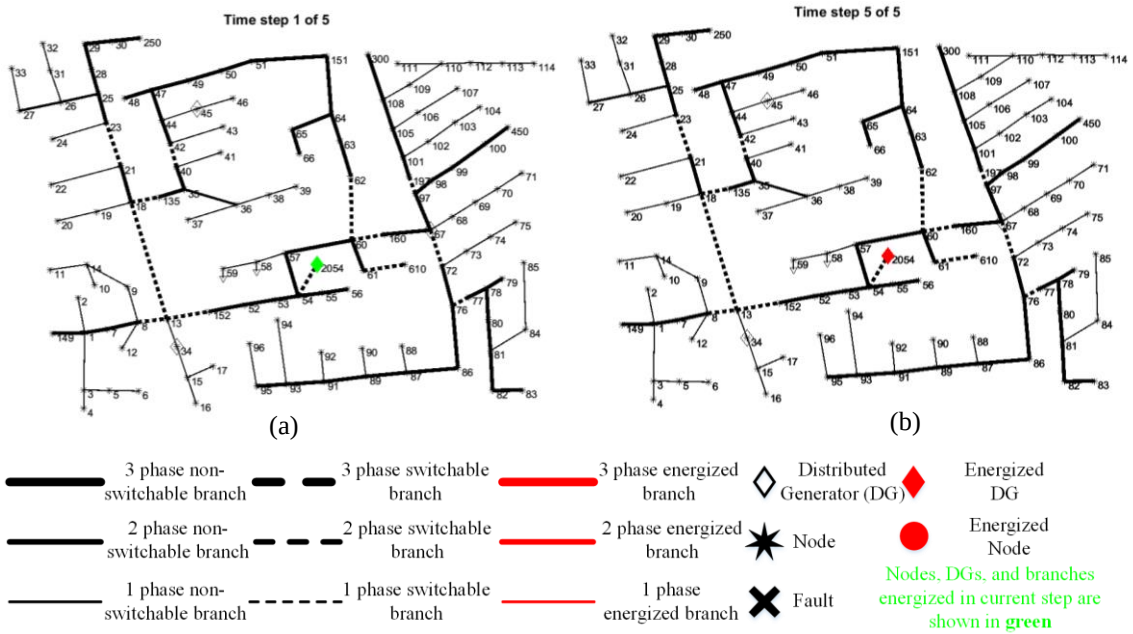

Figure 7.54 Restoration Sequence for Case Studies 3 Scenario 2.2

To improve the controllability of the system, the branch between nodes 57 and 58 is made switchable. This improved controllability is studied in scenario 2.3 which is explained in the next subsection.

7.6.2.8. Restoration Sequence Graph for Scenario 2.3

The one-line diagram of the restoration sequence for scenario 2.3 is shown in Figure 7.55 (a) to (e). Unlike in scenario 2.2, Figure 7.55 (b) shows that the branch between nodes 2054 and 54 was energized in the second step and this was possible because of the switchable branch between nodes 57 and 58 which isolates the two non-switchable loads at nodes 58 and 59 in the second step. This isolation ensures that the droop DG maintains its power unbalance constraint in the second step of the restoration. These two non-switchable loads are eventually energized in step 3. This case, in comparison to scenario 2.2, shows that for the restoration to reach most parts of the system, it is necessary

to maintain controllability of the elements, especially those closer to the black start nodes. However, improving controllability by increasing the number of switchable branches can increase the number of restoration time steps needed to solve the system.

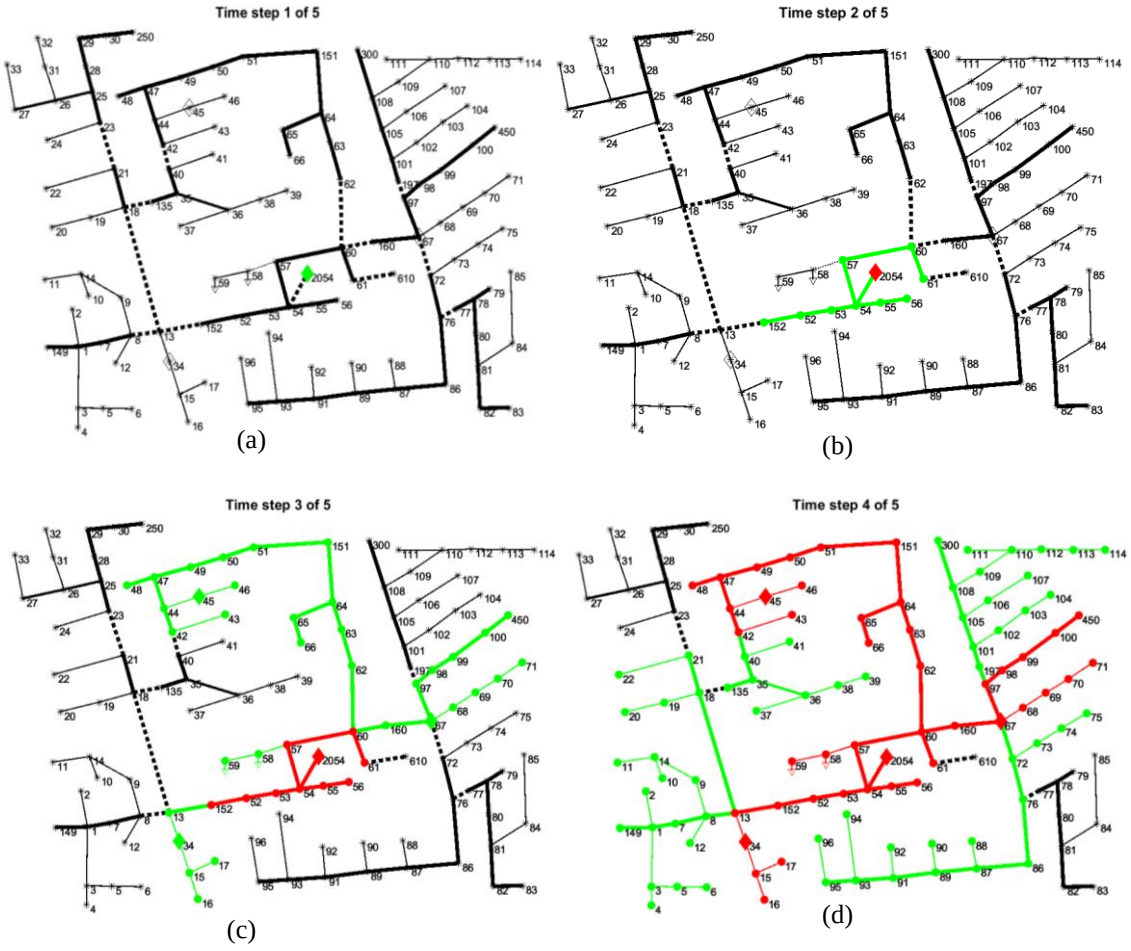

Figure 7.55 Restoration Sequence for Case Studies 3 Scenario 2.3

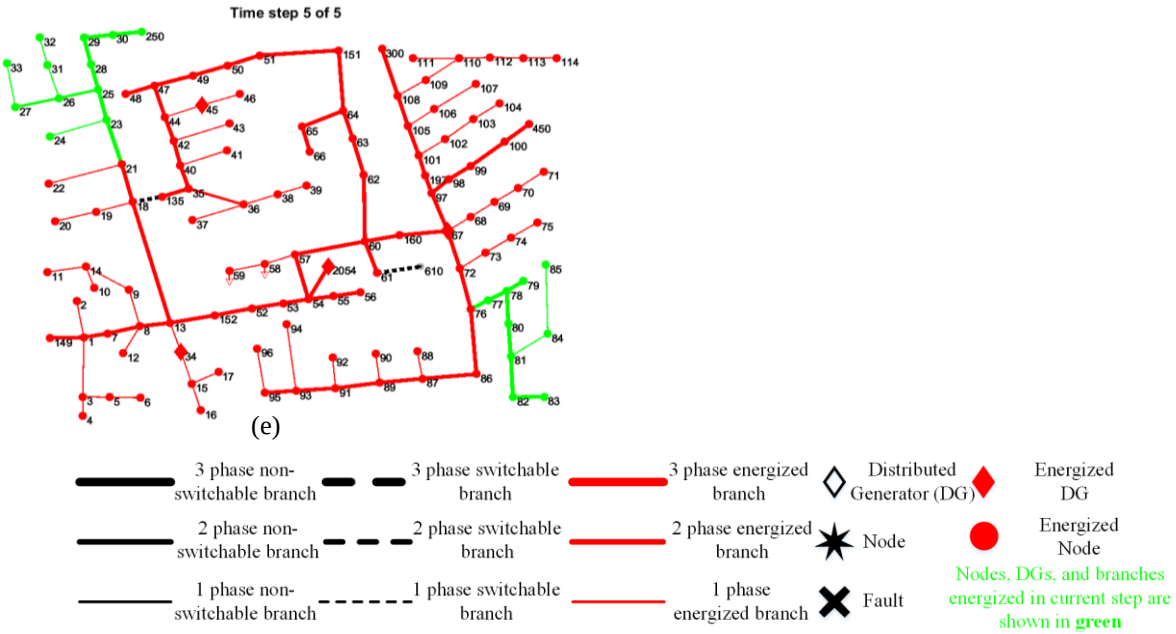

Figure 7.55 Continued

7.6.2.9. Summary of Scenario 2 results

Table 7.32 shows a summary of the three cases run in this scenario. Scenario 2.3 restored more loads and has a bit more objective magnitude than scenario 2.1. Scenario 2.2 did not restore any load; just as it was highlighted in Figure 7.54 (a) and (b), only the droop DG node was energized.

Table 7.32 Summary of Results of Base Case and the Two Derivative Cases for Case Studies 3 Scenario 2

	Total Number of Restored Load	Sum of Nominal Active Power of Loads Restored (KW)	Solver Time (Sec)	Objective Value (KW-Steps)	Best Bound (KW-Steps)	Optimality Gap (%)
Scenario 2.1 (base case)	61 out of 81 loads	2,805.0	26.68	(-)6,985.0	(-)7,105.0	1.72
Scenario 2.2	0 out of 81 loads	0.0	0.90	(-)0.0	(-)0.0	0.00
Scenario 2.3	64 out of 81 loads	2,825.0	23.21	(-)7,025.0	(-)7,130.0	1.49

7.6.3. Scenario 3

There is a total of 4 case studies in this scenario. The purpose is to study the effects and performance of the restoration method to damaged lines and loads.

7.6.3.1. Description of Test System

Each of the cases in this scenario is derived from the base case of scenario 2. Just like in scenario 2, one droop-controlled DG is present at node 2054. Three PQ DGs are present at nodes 34, 45, and 67. The one-line diagram of the first case, scenario 3.1, is shown in Figure 7.56. The main change here is that the branch between nodes 9 and 14 is assumed to be damaged.

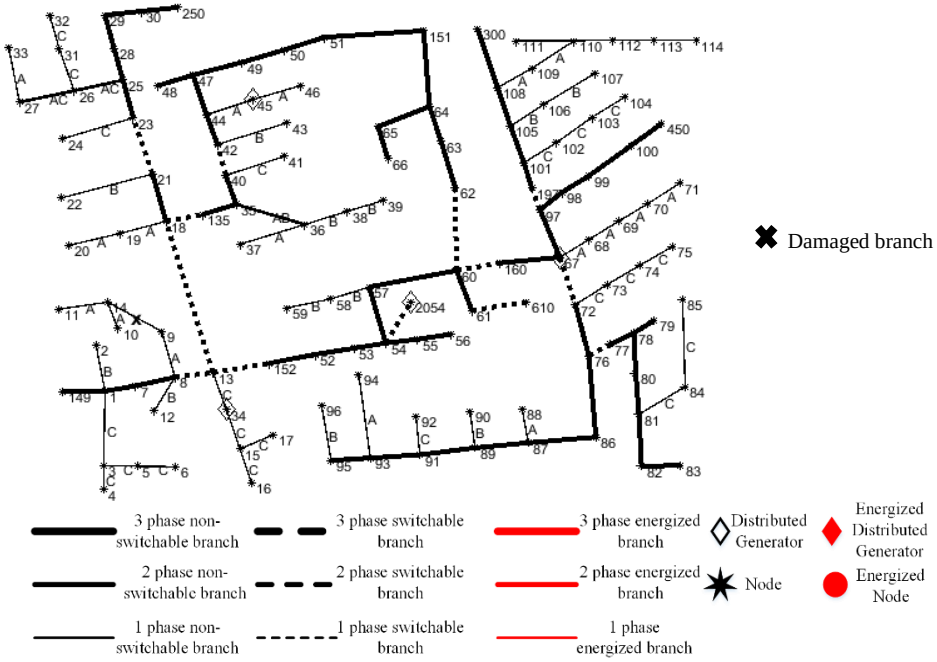

Figure 7.56 One Line Diagram for Case Studies 3 Scenario 3.1

In scenario 3.2, the branch between nodes 8 and 9 is converted to a switchable branch as shown in Figure 7.57. This switchable branch is expected to assist in better isolation of the damaged branch.

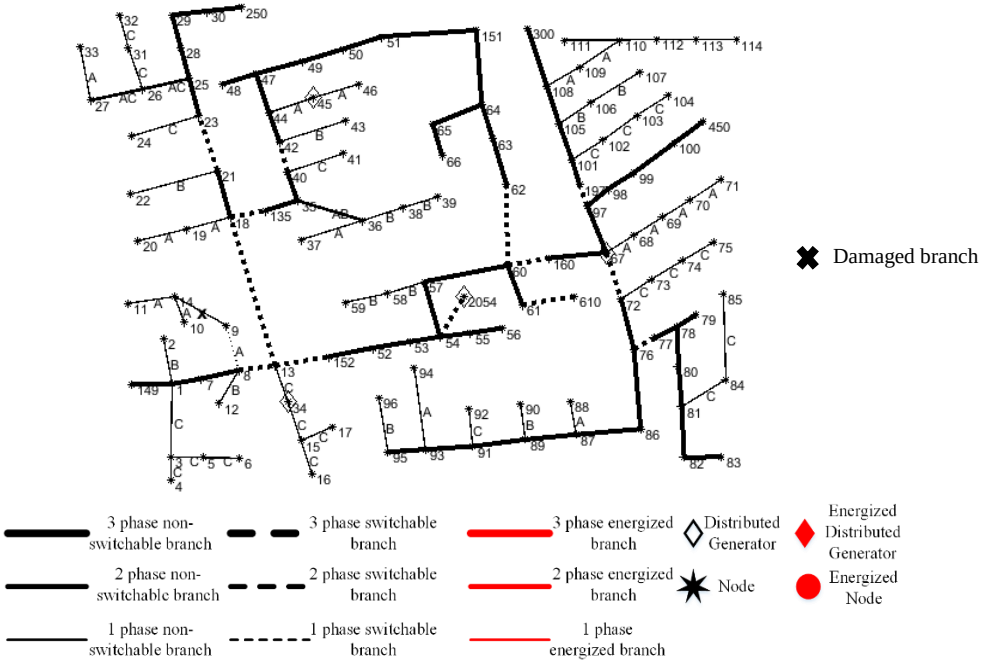

Figure 7.57 One Line Diagram for Case Studies 3 Scenario 3.2

For scenario 3.3, the modifications to scenarios 3.1 and 3.2 are reversed, and the two loads at nodes 111 and 114 are modified to damaged non-switchable load as shown in Figure 7.58. Note that out of all the loads in the system, only the damaged non-switchable loads are shown for emphasis sake.

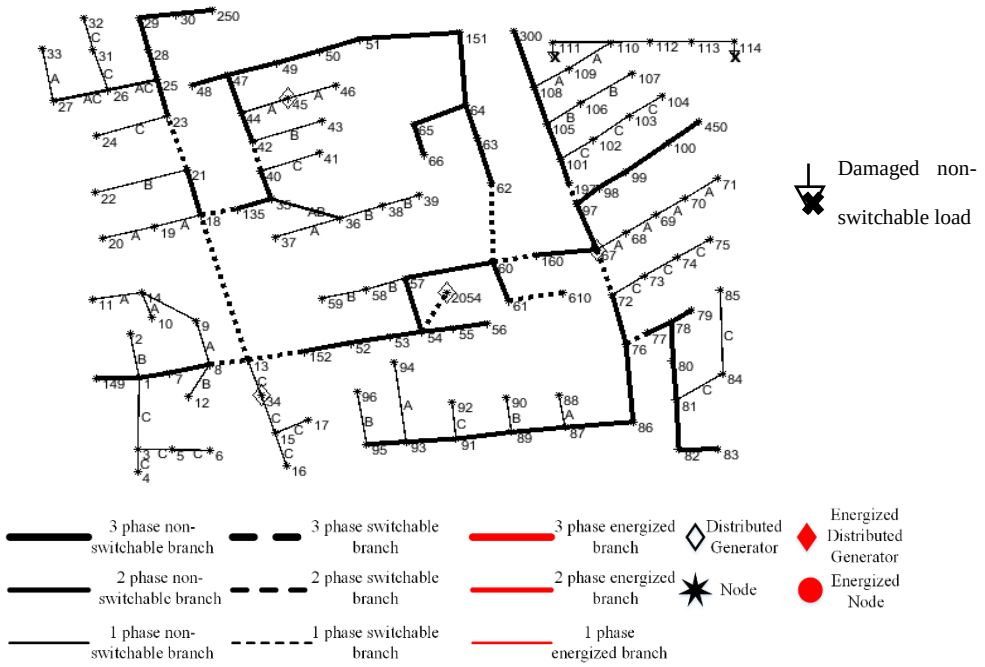

Figure 7.58 One Line Diagram for Case Studies 3 Scenario 3.3

In scenario 3.4, the branch between nodes 105 and 108 is modified to a switchable branch to assist in better isolation of the damaged non-switchable loads at nodes 111 and 114 as shown in Figure 7.59.

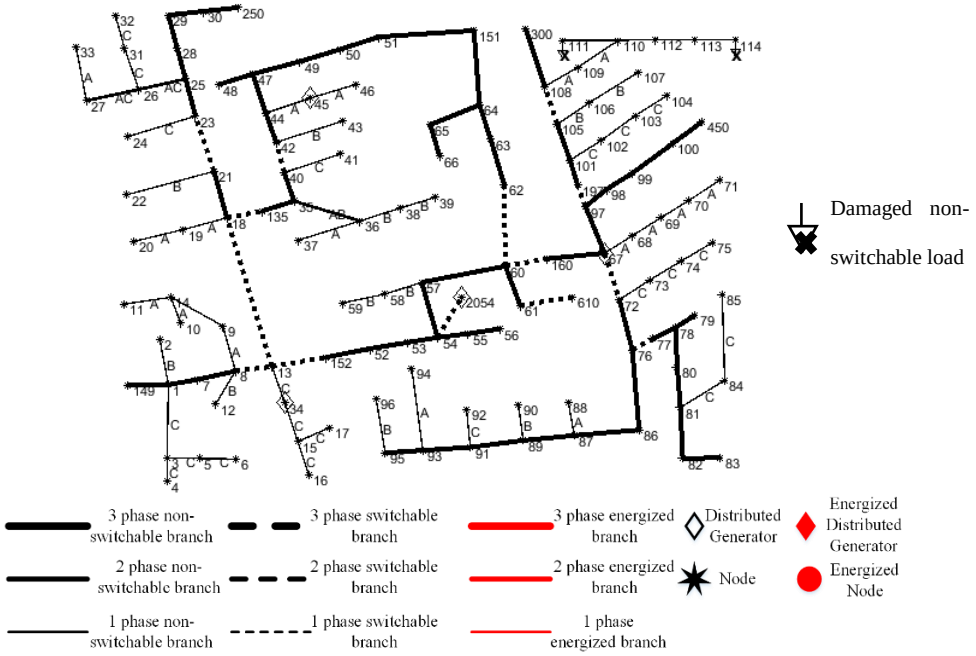

Figure 7.59 One Line Diagram for Case Studies 3 Scenario 3.4

7.6.3.2. DG Information and Details of the Derivative Cases

The DGs' details present in Figure 7.56 to Figure 7.59 are summarized in Table 7.33. All the cases under this scenario use the same DG parameters of Table 7.33. The DG columns remain the same as previously described.

Table 7.33 DGs' Information for Case Studies 3 Scenario 3

Label	Node	Type	f^{ref} (Hz)	Per phase BaseMVA	per phase baseKV	pu coupling X	Pmax (KW)	Pmin (KW)	Qmax (KVAR)	Qmin (KVAR)	Phase	Status	Blackstart	Ramp Rate %
DG1	2054	Droop	60	1	2.4018	0.3	4000	0	2000	-400	ABC	1	1	50
DG2	34	PQ	NA	NA	NA	NA	300	0	200	-40	C	1	0	50
DG3	45	PQ	NA	NA	NA	NA	450	0	300	-60	A	1	0	50
DG4	67	PQ	NA	NA	NA	NA	150	0	100	-20	B	1	0	50

7.6.3.3. Load Details

The load details of the base case in this scenario are the same as those of scenario 1 which is given in Table 7.28. All loads are assumed to be switchable and restorable except for scenarios 3.3 and 3.4, where two of the loads are assumed to be damaged and non-switchable.

7.6.3.4. Choice of Time Steps

By graphically analyzing the one-line diagram of Figure 7.56 to Figure 7.59, the conservative and generous time steps were estimated for all four cases to be 5, and time step of 5 was used to solve for all the cases under this scenario.

7.6.3.5. Restoration Sequence Graph for Scenarios 3.1 & 3.2

The one-line diagram of the restoration sequence for scenarios 3.1 is shown in Figure 7.60 (a) to (e). Notice that by the end of the restoration step in Figure 7.60 (e), none of the nodes in the bus block of which the damaged line is part of was restored.

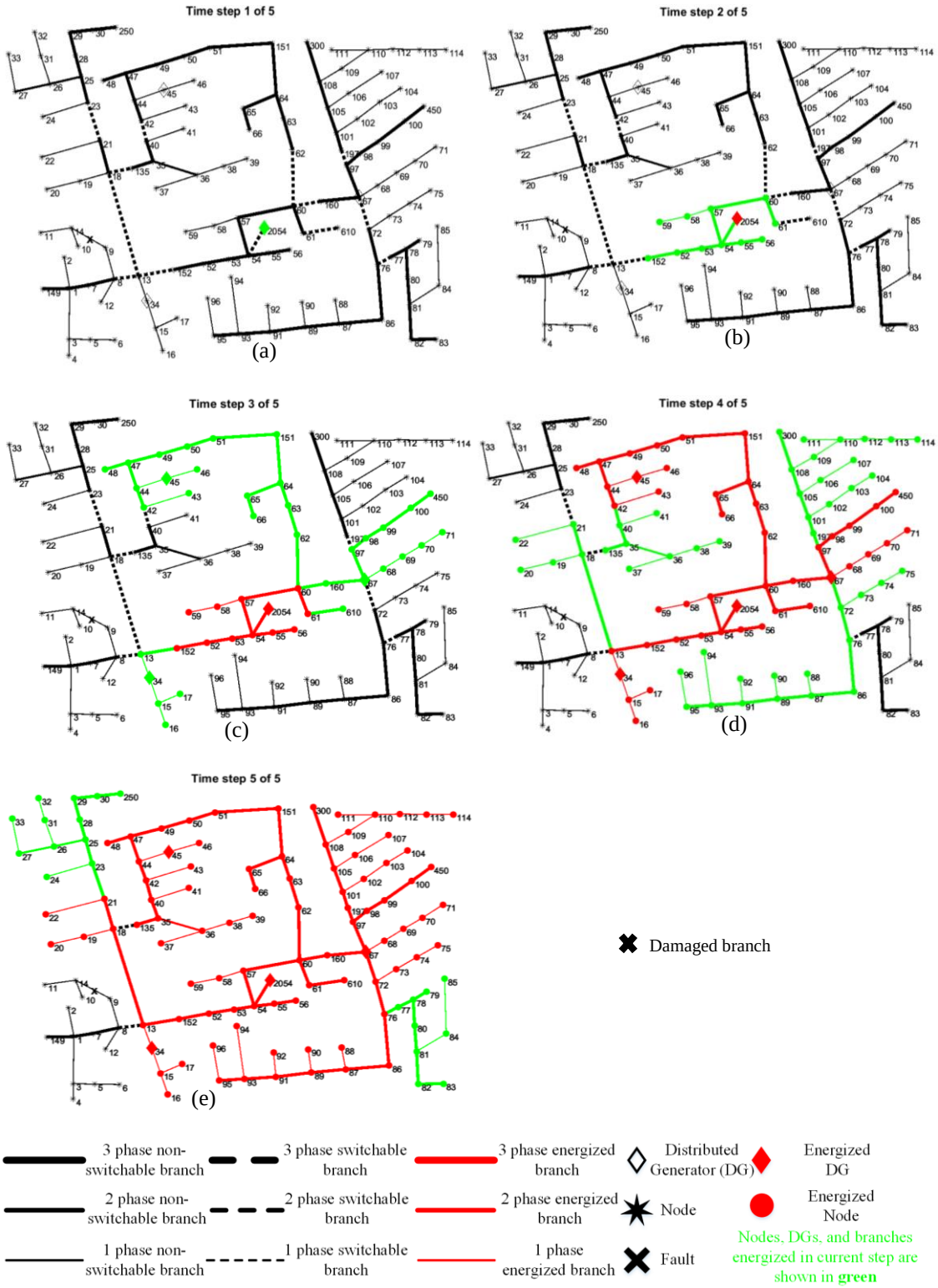

Figure 7.60 Restoration Sequence for Case Studies 3 Scenario 3.1

Scenario 3.2 is derived from 3.1 and shows how the restoration method can help in restoring more nodes if there are switchable branches adjacent to a damaged branch. The one-line diagram of the restoration sequence for this scenario is shown in Figure 7.61 (a) to (e). Notice that by the end of the restoration step in Figure 7.61 (e), when compared to Figure 7.60 (e), more nodes are restored. A numerical comparison of the loads restored is made in the summary subsection.

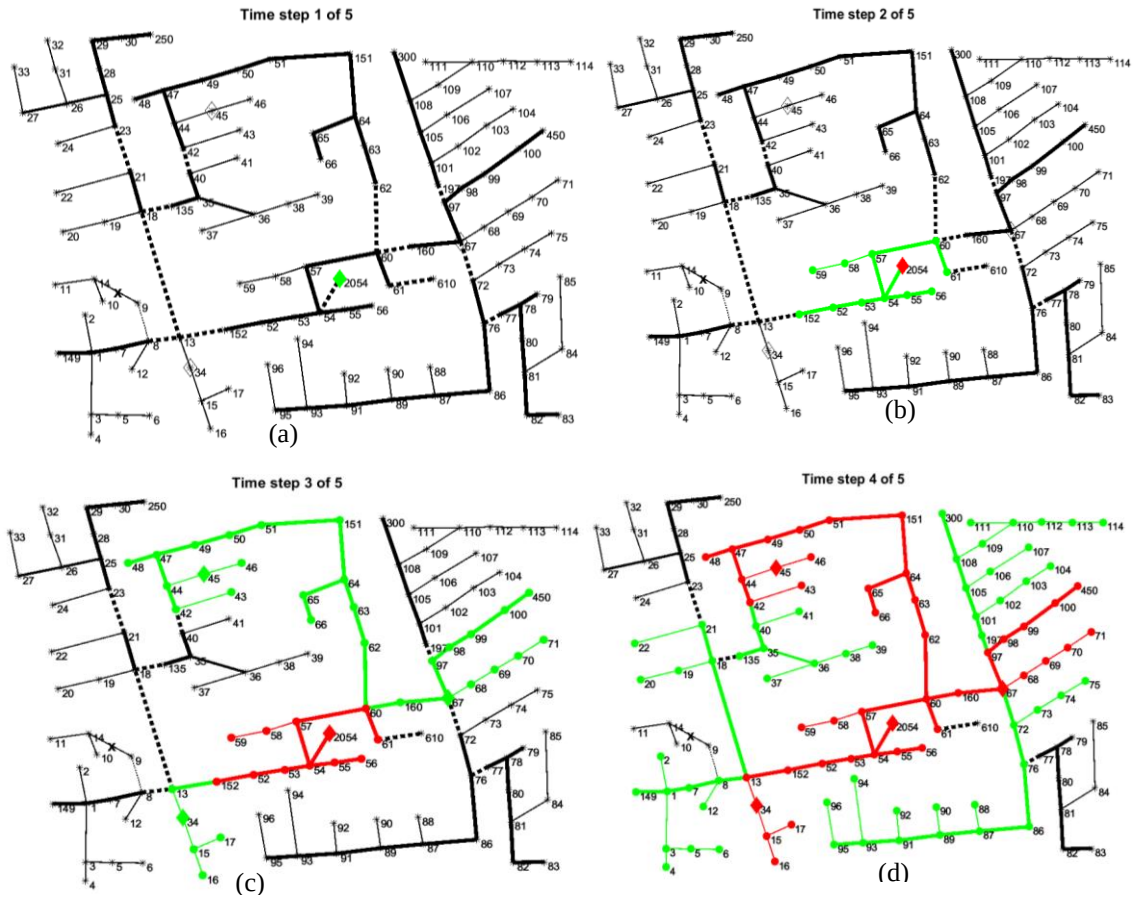

Figure 7.61 Restoration Sequence for Case Studies 3 Scenario 3.2

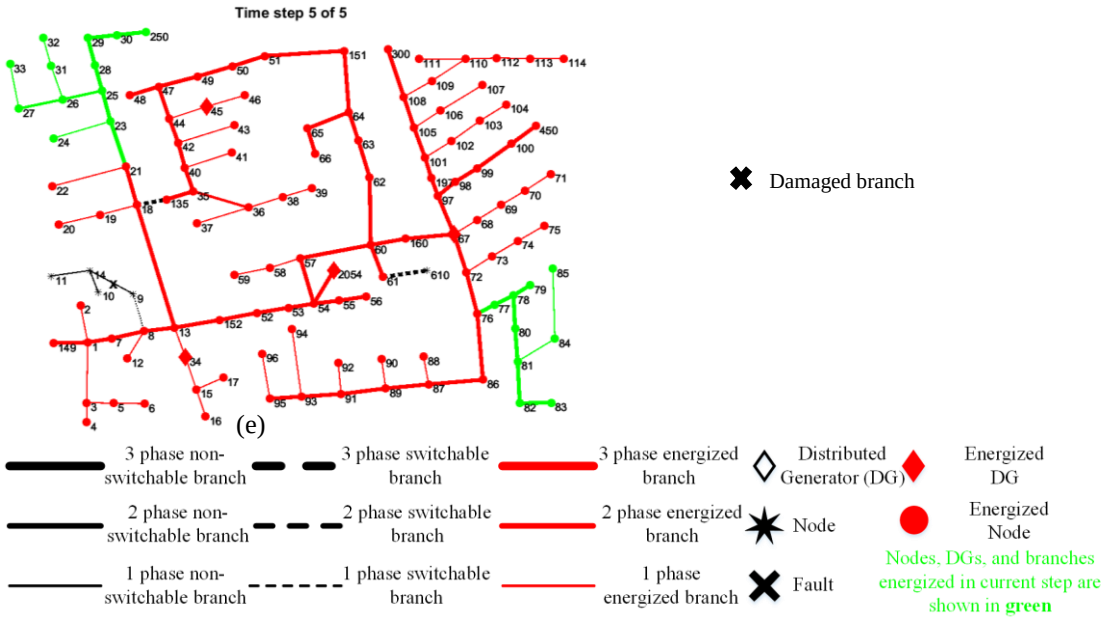

Figure 7.61 Continued

7.6.3.6. Restoration Sequence Graph for Scenarios 3.3 & 3.4

The one-line diagram of the restoration sequence for scenarios 3.3 is shown in Figure 7.62 (a) to (e). Observe that by the end of the restoration step in Figure 7.62 (e), none of the nodes in the bus block of which the damaged load is part of was restored.

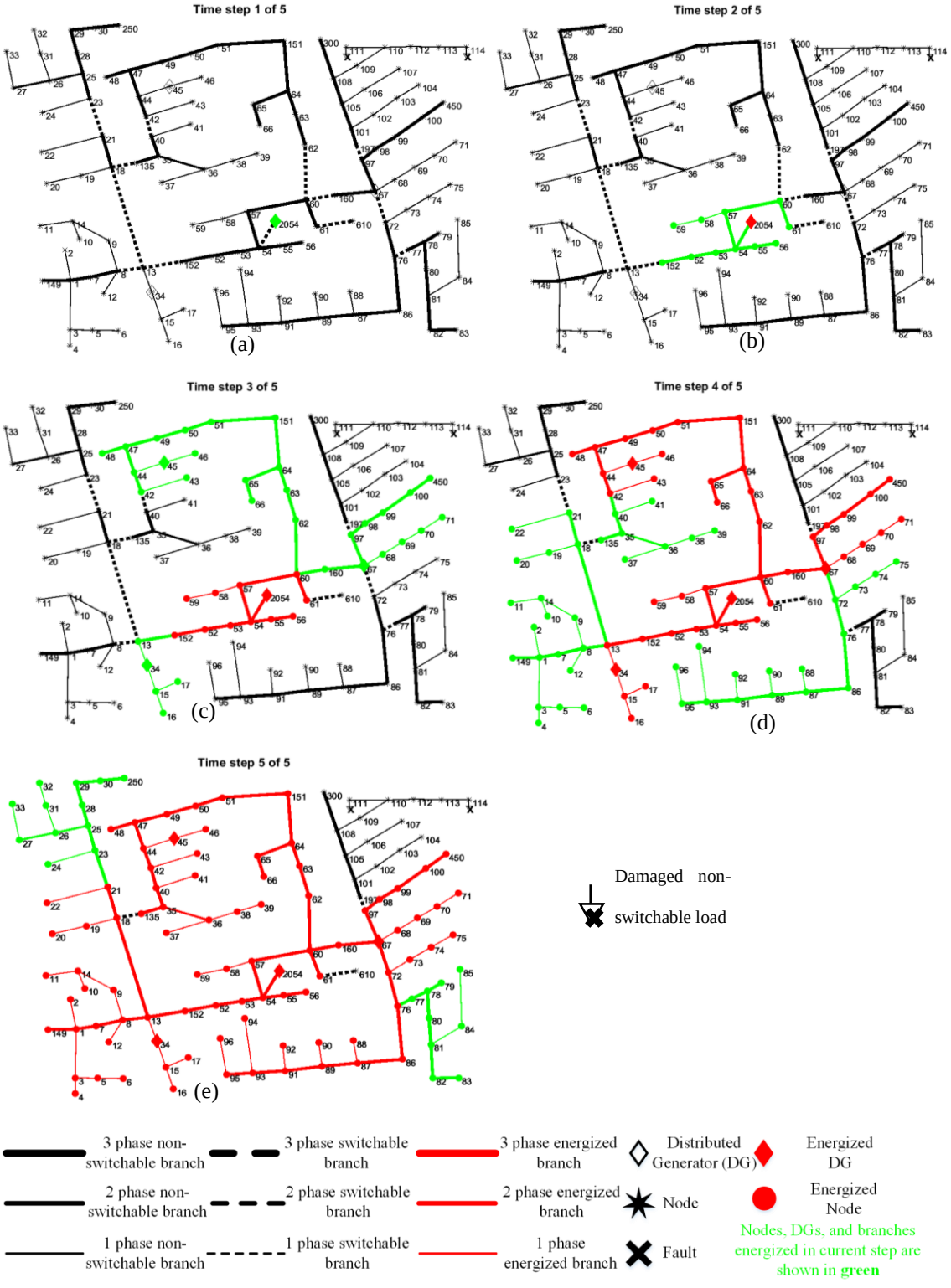

Figure 7.62 Restoration Sequence for Case Studies 3 Scenario 3.3

Scenario 3.4 is derived from 3.3 and shows how the restoration method can help in restoring more nodes if there is/are switchable branches closer to the node with damaged non-switchable loads. The one-line diagram of the restoration sequence for this scenario is shown in Figure 7.63 (a) to (e). Observe that by the end of the restoration step in Figure 7.63 (e), when compared to Figure 7.62 (e), more nodes are restored. A numerical comparison of the loads restored is made in the summary subsection.

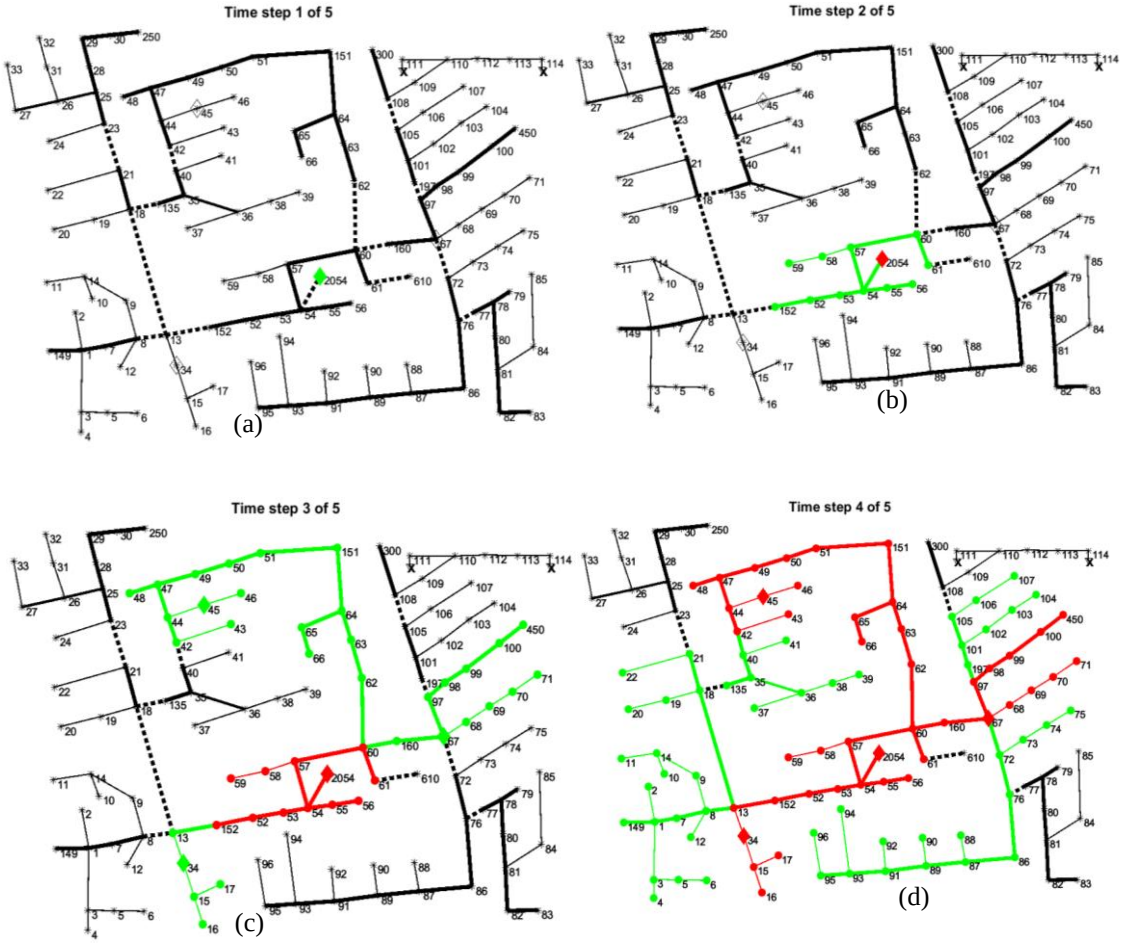

Figure 7.63 Restoration Sequence for Case Studies 3 Scenario 3.4

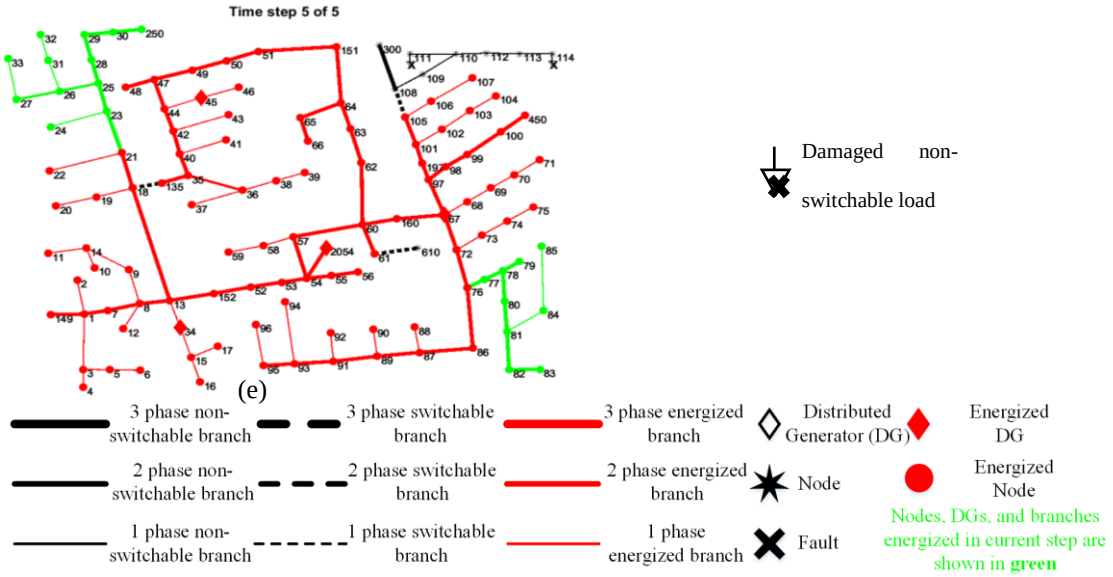

Figure 7.63 Continued

7.6.3.7. Summary of Scenario 3 results

Table 7.34 shows a summary of the four cases run in this scenario. From the magnitude of the objective value, which represents the total energy restored, scenarios 3.2 and 3.4 performed better than scenarios 3.1 and 3.3 respectively because 3.2 and 3.4 have better controllability that aid in better isolation of damaged elements. The cases under this scenario also demonstrate the method's ability to isolate faulty regions during black start.

Table 7.34 Summary of Results of Four Cases for Case Studies 3 Scenario 3

	Total Number of Restored Load	Sum of Nominal Active Power of Loads Restored (KW)	Solver Time (Sec)	Objective Value (KW-Steps)	Best Bound (KW-Steps)	Optimality Gap (%)
Scenario 3.1 (with damaged line)	59 out of 81 loads	2,745.0	592.12	(-)6,745.0	(-)6,870.0	1.85
Scenario 3.2 (with damaged line and better isolation path)	60 out of 81 loads	2,785.0	29.64	(-)6,945.0	(-)7,055.0	1.58
Scenario 3.3 (with damaged loads)	62 out of 81 loads	2,765.0	49.64	(-)6,825.0	(-)6,950.0	1.83
Scenario 3.4 (with damaged loads and better isolation path)	60 out of 81 loads	2,785.0	23.34	(-)6,945.0	(-)7,070.0	1.80

7.6.4. Scenario 4

There is a total of four cases in this scenario. The purpose of the case studies in this scenario is to study the performance of the restoration method under different choices of the restoration time step.

7.6.4.1. Description of Test System

A one-line diagram of the base test system is shown in Figure 7.64. Two droop-controlled DGs are present at nodes 2054 and 2063. Three PQ DGs are present at nodes 34, 59, and 46. Details of the line information can be found in Appendix E.

Figure 7.64 One Line Diagram for Case Studies 3 Scenario 4

7.6.4.2. DGs' Information

The DGs' details present in Figure 7.64 are summarized in Table 7.35.

Table 7.35 DGs' Information for Case Studies 3 Scenario 4

Label	Node	Type	f^{ref} (Hz)	Per phase BaseMVA	per phase baseKV	pu coupling X	Pmax (KW)	Pmin (KW)	Qmax (KVAR)	Qmin (KVAR)	Phase	Status	Blackstart	Ramp Rate %
DG1	2054	Droop	60	1	2.4018	0.3	1700	0	800	-100	ABC	1	1	50
DG2	2063	Droop	60	1	2.4018	0.3	1700	0	800	-100	ABC	1	1	50
DG2	34	PQ	NA	NA	NA	NA	250	0	150	-30	C	1	0	50
DG3	46	PQ	NA	NA	NA	NA	400	0	250	-40	A	1	0	50
DG4	59	PQ	NA	NA	NA	NA	150	0	100	-20	B	1	0	50

7.6.4.3. Load Details

The load details for each case in this scenario are the same as those of scenario 1 which is given in Table 7.28. All loads are assumed to be switchable and restorable.

7.6.4.4. Choice of Time Steps and Cases

By graphically analyzing the one-line diagram of Figure 7.64, the conservative and generous time steps were estimated as time steps of 6 and 7 respectively. Four cases are run based on these time step estimates. These are scenarios 4.1, 4.2, 4.3, and 4.4 with solution time steps of 5, 6, 7, and 8 steps, respectively.

7.6.4.5. Restoration Sequence Graph

The one-line diagram of the restoration sequence for scenario 4.1 with the restoration step set to be one less than the conservative steps estimate (that is set to 5) is shown in Figure 7.65 (a) to (e). Notice from Figure 7.65 (e) that the chosen restoration step was not sufficient to reach every node in the system.

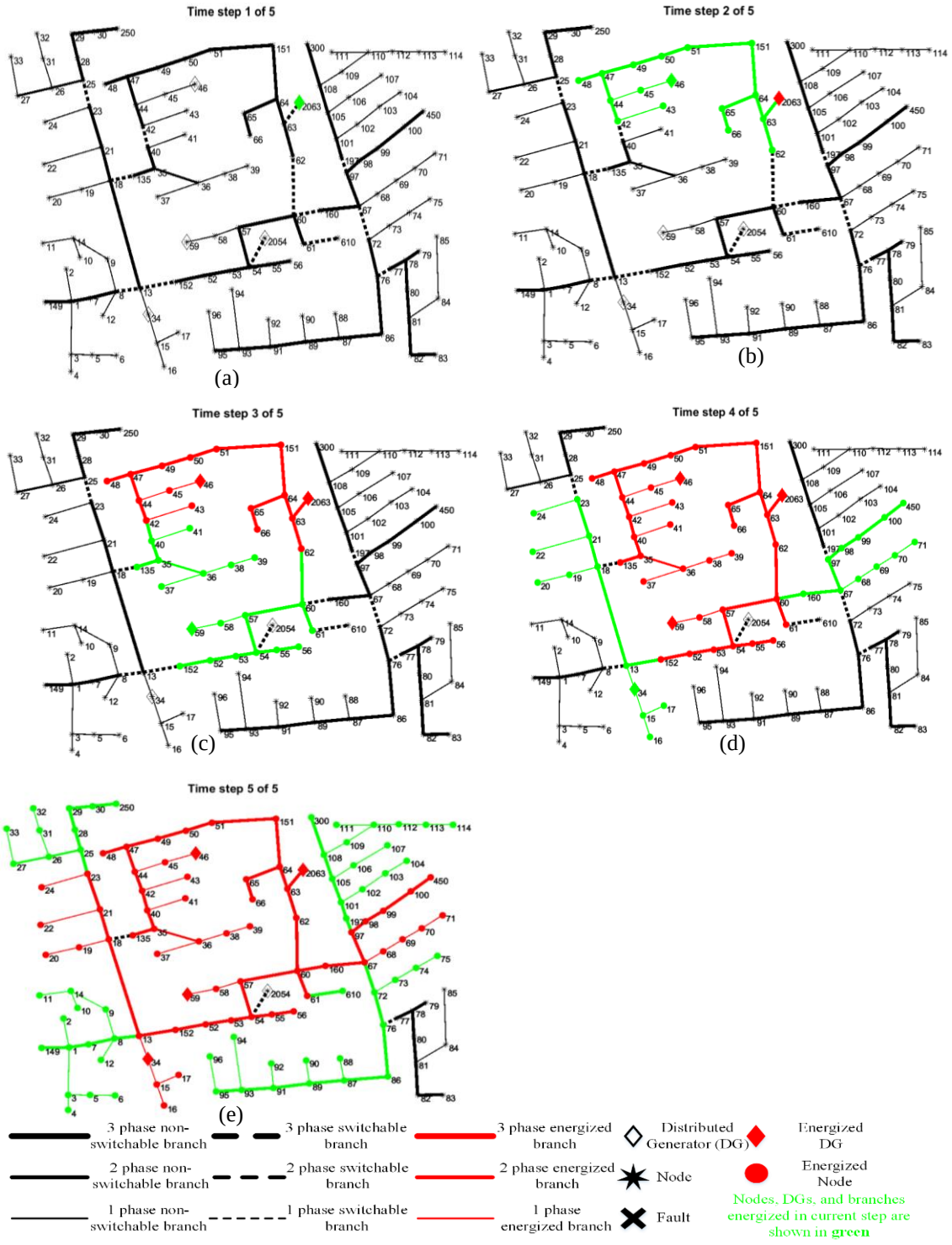

Figure 7.65 Restoration Sequence for Case Studies 3 Scenario 4.1

The one-line diagram of the restoration sequence (showing only first and last step) for scenario 4.2 with the restoration step set to be equal to the conservative steps estimate (that is set to 6) is shown in Figure 7.66 (a) and (b). Notice from Figure 7.66 (b) that this choice of steps was sufficient to restore every node in the system. It is difficult to tell if this choice was sufficient for all DGs to ramp up until we look at the load restoration results and results of scenarios 4.3 and 4.4 which have greater restoration steps. Sequence graph of scenarios 4.3 and 4.4 have been omitted since by their last step, all the nodes have been restored as well.

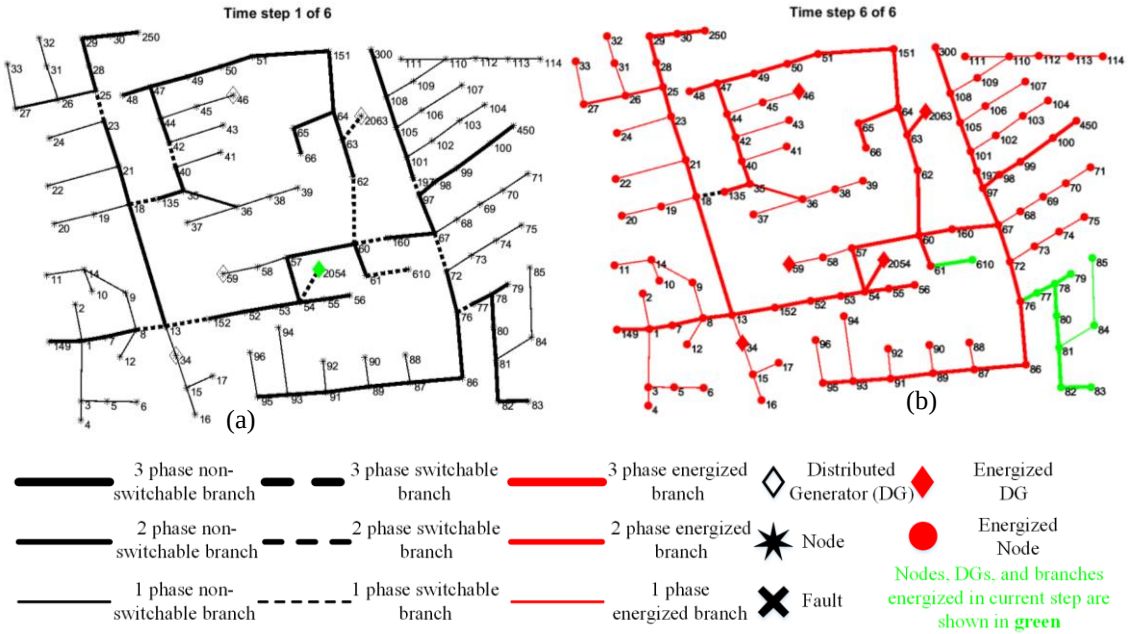

Figure 7.66 Restoration Sequence for Case Studies 3 Scenario 4.2

7.6.4.6. Summary of Scenario 4 results

Table 7.36 shows a summary of the four cases run in this scenario. Since scenario 4.1 could not restore all the load nodes, it is no surprise that it did not restore all the loads.

Scenario 4.2, on the other hand, was solved using the conservative time step estimate. This scenario restored all the load nodes but did not restore all the loads. A factor that is at play here is the DG ramp rate – if the ramp rate factor was higher, scenario 4.2 may restore all the loads. Scenario 4.3 was solved using the generous time step and was sufficient enough step to restore all the loads. Scenario 4.4 was solved with a time step greater than the other scenario and it restored all the loads as expected. Also, observe that the solver time did not always increase as the solution time step increases. Increasing solution time step will increase the number of variables and constraints, however, in mixed-integer programming, there are known factors likeness tightness [117] and even unknown ones that play out to determine speed of calculation. In summary, the choice of solution time steps is an important consideration in how good a solution can be: increasing the solution time steps can improve the solution at the cost of a potential increase (could also be a decrease) in computational burden but not make worse.

Table 7.36 Summary of Results of four Cases for Case Studies 3 Scenario 4

	Total Number of Restored Load	Sum of Nominal Active Power of Loads Restored (KW)	Solver Time (Sec)	Objective Value (KW-Steps)	Best Bound (KW-Steps)	Optimality Gap (%)
Scenario 4.1 (Solved with time step of 5)	58 out of 81 loads	2,395.0	245.53	(-)6,330.0	(-)6,430.0	1.57
Scenario 4.2 (Solved with time step of 6, which is the conservative time step estimate)	72 out of 81 loads	3,095.0	2030.66	(-)9,085.0	(-)9,255.0	1.87
Scenario 4.3 (Solved with time step of 7, which is the generous time step estimate)	81 out of 81 loads	3,385.0	1920.69	(-)12,415.0	(-)12,645.0	1.85
Scenario 4.4 (Solved with time step of 8)	81 out of 81 loads	3,385.0	1961.96	(-)15,780.0	(-)16,055.0	1.74

7.7. Case Studies 4: Impacts of Non-Dispatchable Renewable DGs

Case studies 4 is the performance of the restoration method when non-dispatchable renewable DGs are available in the system. The island system used for the case studies under this section is adapted from the IEEE 123 node test feeder. The case studies under this section are subdivided into three scenarios:

- Scenario 1: case studies highlighting the impact of having/not having "must connect" constraints for the non-dispatchable renewable DG
- Scenario 2: case studies for highlighting the effect of the phase of non-dispatchable renewable DGs
- Scenario 3: case studies for highlighting the effect of non-dispatchable renewable DG capacity

In some of the cases, additional "must connect" constraints are enforced for the non-dispatchable DGs to ensure utilization of the renewable sources which are expected to be more environmentally friendly. These additional constraints ensure that by the last step of the restoration, the non-dispatchable DG are energized and connected to the restored system. While enforcing the connection of renewable DGs may reduce operation cost and unwanted emission, the resulting solution could be farther from the optimal solution (or solution may not exist) than when these additional constraints are not included.

The computation options for all cases categorized under the case studies 4 section is outlined in Table 7.37.

Table 7.37 Computation Settings for Case Studies 4

Options	Choice
Options.connectGFDGs	False
Options.skipPWL	True
Options.ignoreShuntAdmittance	True
Options.includeShuntAdmittanceForLastStepOnly	NA
Options.MIPGap	2%
Conservative/Generous Time Step Estimate	Varies with case

7.7.1. Scenario 1

This scenario studies the performance of the restoration method under the condition of having/not having "must connect" constraints for the non-dispatchable renewable DG.

7.7.1.1. Description of Test System

A one-line diagram of the base test system is shown in Figure 7.67. One droop-controlled DGs is present at node 2063. Three PQ dispatchable DGs are present at nodes 34, 46, and 59. A non-dispatchable PQ DG is present at node 85.

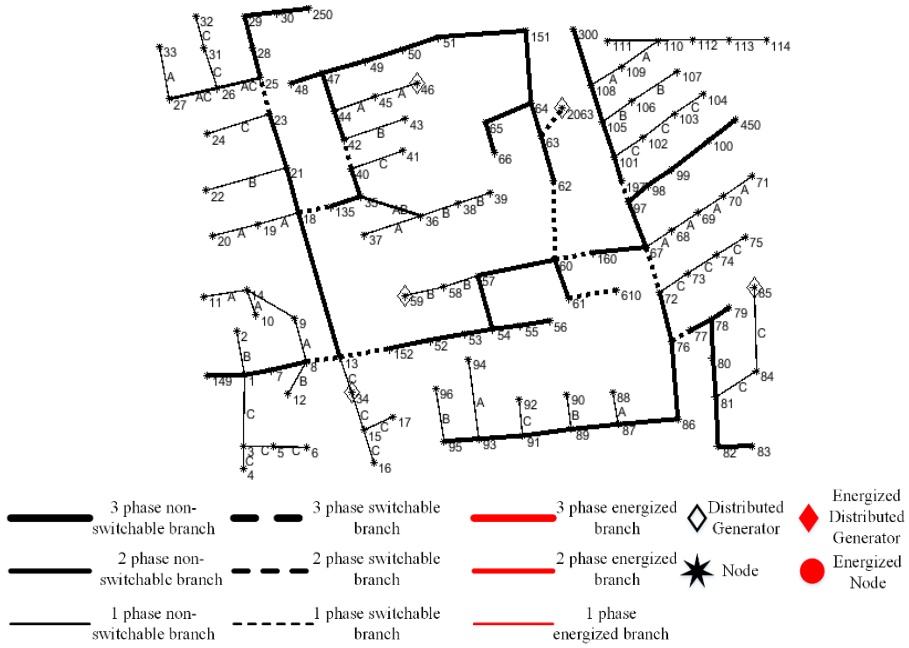

Figure 7.67 One Line Diagram for case studies 4 scenario 1

7.7.1.2. DGs' Information

The DGs' details present in Figure 7.67 are summarized in Table 7.38.

Table 7.38 DGs' Information for Case Studies 4 Scenario 1

Label	Node	Type	f^{ref} (Hz)	Per phase BaseMVA	per phase baseKV	pu coupling X	Pmax (KW)	Pmin (KW)	Qmax (KVAR)	Qmin (KVAR)	Phase	Status	Blackstart	Ramp Rate %
DG1	2063	Droop	60	1	2.4018	0.3	2800	0	1600	-150	ABC	1	1	50
DG2	34	PQ	NA	NA	NA	NA	100	0	50	-10	C	1	0	50
DG3	46	PQ	NA	NA	NA	NA	100	0	50	-10	A	1	0	50
DG4	59	PQ	NA	NA	NA	NA	100	0	50	-10	B	1	0	50
DG5	85	PQ-NonDisp	NA	NA	NA	NA	350	350	220	220	C	1	0	100

7.7.1.3. Derivative Cases

There are two cases in this scenario numbered 1.1 and 1.2. Scenario 1.1 does not have the additional "must connect" constraints for the non-dispatchable renewable DGs, while scenario 2.1 does. This is the only difference between these two cases.

7.7.1.4. Load Details

There is a total of 81 loads in this case study and the details are shown in Table 7.39. All loads are assumed to be switchable and restorable.

Table 7.39 Load Details for Case Studies 4 Scenario 1

Node	Config	P(A/B/C) KW	Q(A/B/C) KVAR	Node	Config	P(A/B/C) KW	Q(A/B/C) KVAR	Node	Config	P(A/B/C) KW	Q(A/B/C) KVAR
1	Y	40/0/0	20/0/0	43	Y	0/40/0	0/20/0	77	Y	0/40/0	0/20/0
2	Y	0/20/0	0/10/0	45	Y	20/0/0	10/0/0	79	Y	40/0/0	20/0/0
4	Y	0/0/40	0/0/20	46	Y	20/0/0	10/0/0	80	Y	0/40/0	0/20/0
5	Y	0/0/20	0/0/10	47	Y	35/35/35	25/25/25	82	Y	40/0/0	20/0/0
6	Y	0/0/40	0/0/20	48	Y	70/70/70	50/50/50	83	Y	0/0/20	0/0/10
7	Y	20/0/0	10/0/0	49	Y	35/70/35	25/30/20	84	Y	0/0/20	0/0/10
10	Y	20/0/0	10/0/0	50	Y	0/0/40	0/0/20	85	Y	0/0/40	0/0/20
11	Y	40/0/0	20/0/0	51	Y	20/0/0	10/0/0	86	Y	0/20/0	0/10/0
12	Y	0/20/0	0/10/0	52	Y	40/0/0	20/0/0	87	Y	0/40/0	0/20/0
16	Y	0/0/40	0/0/20	53	Y	40/0/0	20/0/0	88	Y	40/0/0	20/0/0
17	Y	0/0/20	0/0/10	55	Y	20/0/0	10/0/0	90	Y	0/40/0	0/20/0
19	Y	20/0/0	10/0/0	56	Y	0/60/0	0/40/0	92	Y	0/0/40	0/0/20
20	Y	20/0/0	10/0/0	58	Y	0/20/0	0/10/0	94	Y	40/0/0	20/0/0
22	Y	0/60/0	0/30/0	59	Y	0/20/0	0/10/0	95	Y	0/40/0	0/20/0
24	Y	0/0/40	0/0/20	60	Y	20/0/0	10/0/0	96	Y	0/40/0	0/20/0
28	Y	40/0/0	20/0/0	62	Y	0/0/20	0/0/10	98	Y	40/0/0	20/0/0
29	Y	40/0/0	20/0/0	63	Y	40/0/0	20/0/0	99	Y	0/70/0	0/40/0
30	Y	0/0/40	0/0/20	64	Y	0/75/0	0/25/0	100	Y	0/0/40	0/0/20
31	Y	0/0/20	0/0/10	65	D	35/35/70	25/25/50	102	Y	0/0/20	0/0/10
32	Y	0/0/20	0/0/10	66	Y	0/0/30	0/0/20	103	Y	0/0/40	0/0/20
33	Y	40/0/0	20/0/0	68	Y	20/0/0	10/0/0	104	Y	0/0/40	0/0/20
34	Y	0/0/40	0/0/20	69	Y	40/0/0	20/0/0	106	Y	0/60/0	0/30/0
35	D	40/0/0	20/0/0	70	Y	20/0/0	10/0/0	107	Y	0/60/0	0/30/0
37	Y	60/0/0	40/0/0	71	Y	40/0/0	20/0/0	111	Y	20/0/0	10/0/0
38	Y	0/70/0	0/35/0	73	Y	0/0/40	0/0/20	114	Y	30/0/0	15/0/0
39	Y	0/40/0	0/20/0	74	Y	0/0/40	0/0/20				
41	Y	0/0/20	0/0/10	75	Y	0/0/40	0/0/20		Total	1231/1169/1080	681/642/582
42	Y	20/0/0	10/0/0	76	D	70/70/70	50/50/50				

7.7.1.5. Choice of Time Steps

The restoration time step is set to 6 which is the same as the conservative/generous time estimate for the topology of this scenario presented in Figure 7.67.

7.7.1.6. Restoration Sequence Graph

The one-line diagram of the restoration sequence for scenario 1.1 is shown in Figure 7.68 (a) to (f). Notice from the last step in Figure 7.68 (f) that even though node 85 has been energized, the non-dispatchable DG at this node has not been connected to the system and energized. Recall that in scenario 1.1, the connection of non-dispatchable DG is not enforced with an additional constraint.

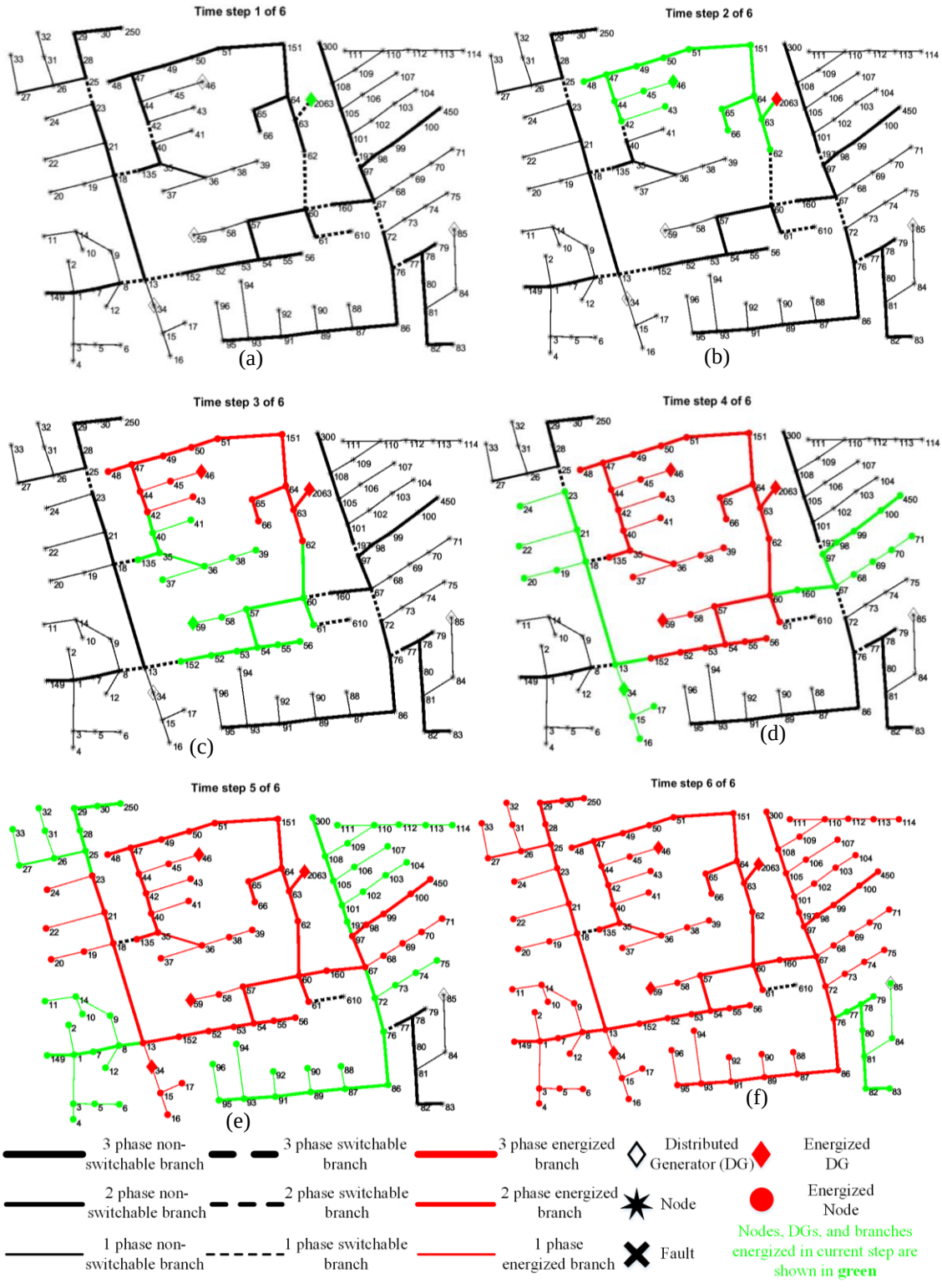

Figure 7.68 Restoration Sequence for Case Studies 4 Scenario 1.1

The one-line diagram of the restoration sequence for scenario 1.2 is shown in Figure 7.69 (a) to (f). Notice from the last step in Figure 7.69 (f) that the non-dispatchable DG at node 85 is energized and connected to the restored system. Recall that in scenario 1.2, the connection of non-dispatchable DG is enforced with an additional constraint.

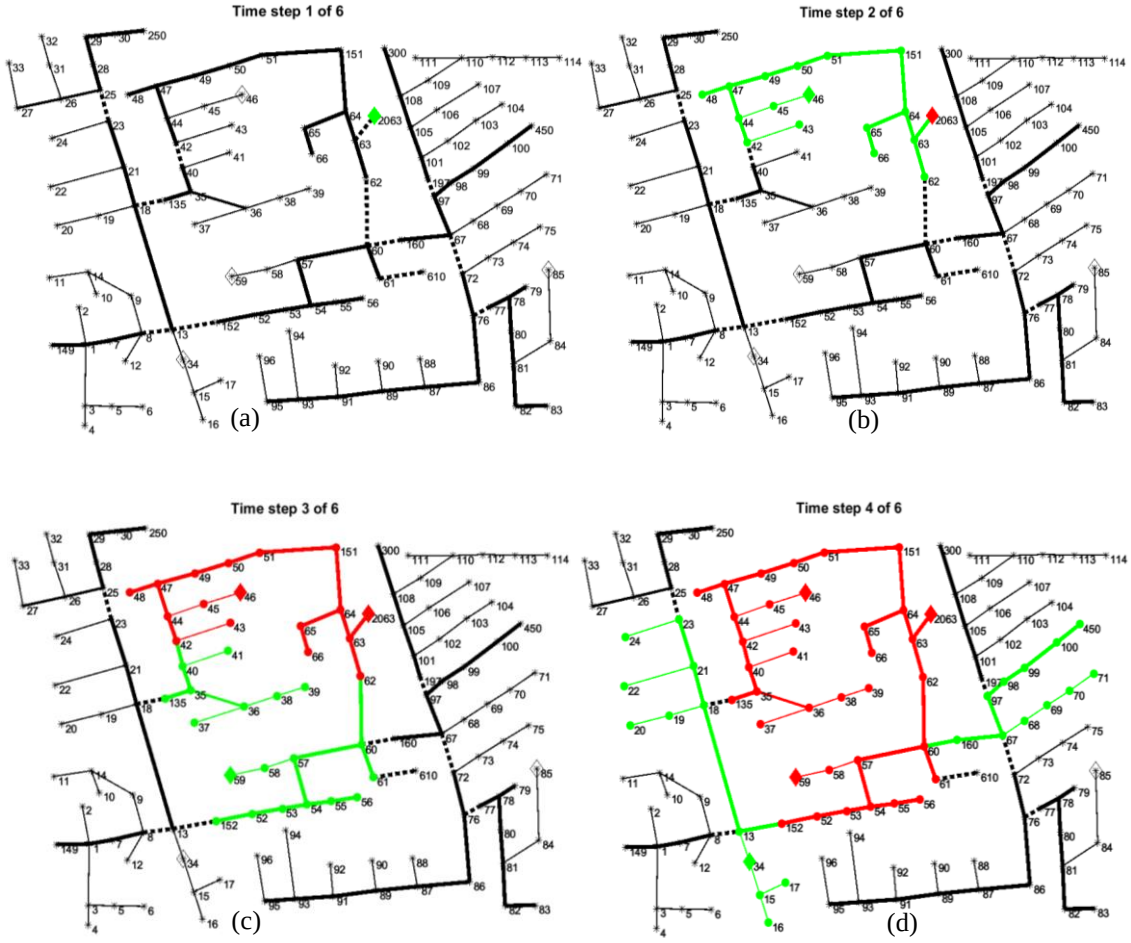

Figure 7.69 Restoration Sequence for Case Studies 4 Scenario 1.2

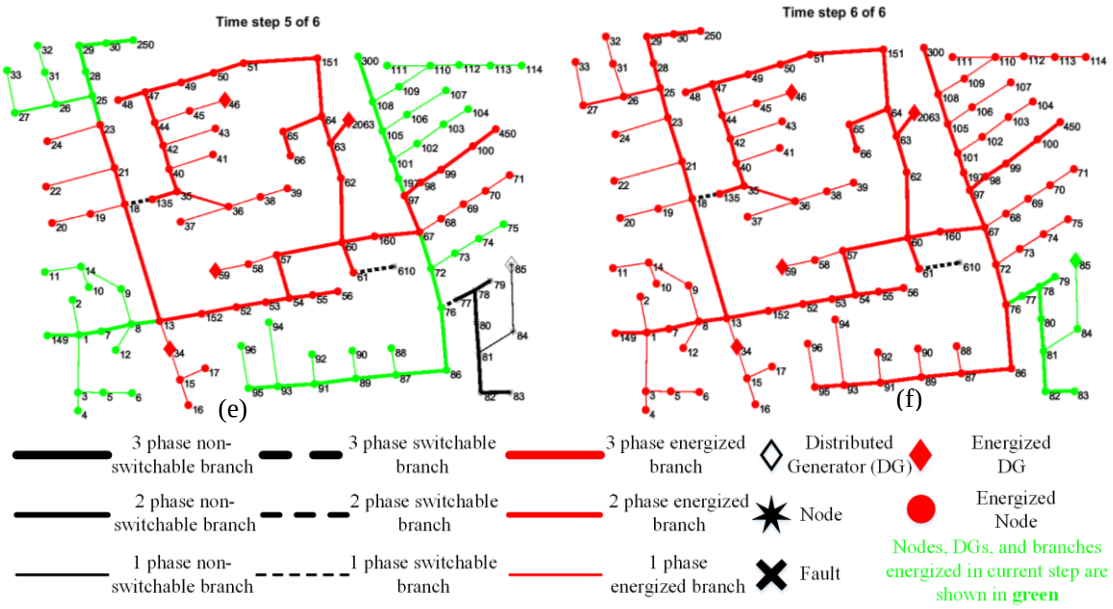

Figure 7.69 Continued

7.7.1.7. Summary of Scenario 1 results

Table 7.40 shows a summary of the two cases run in this scenario. Recall that it is scenario 1.2 that has the additional "must connect" constraints for the non-dispatchable DG. Scenario 1.1 has a greater objective magnitude than 1.2 because 1.1 can be seen as a slightly relaxed form of 1.2 due to the additional constraint of 1.2 (relaxed problems will always have a better or same objective magnitude as the non-relaxed one if optimality is proved because the solution space of the non-relaxed one is a subset of the relaxed one). The "sum of the nominal load" and the "total number of loads restored" columns produced counterintuitive results. Despite that the objective magnitude (energy restored in the restoration steps) of 1.1 is greater than 1.2, 1.2 has a greater sum of nominal active power loads than 1.1. This means that scenario 1.1 restored more loads sooner while scenario 1.2 restored the most load by the last time steps. Notice from the "total number of restored

load" column, that though 1.2 has a greater sum of nominal active loads restored, it has a lesser total number of loads restored. This goes to show that the total number of loads restored does not tell the full story as the aggregate loads do not all have the same nominal value. In general, when optimality is proved or nearly proved, cases with the additional "must connect" constraints for the non-dispatchable will tend to have lesser or equal objective magnitude compared with the equivalent case without the "must connect" constraints.

Table 7.40 Summary of Results of Case Studies 4 Scenario 1

	Total Number of Restored Load	Sum of Nominal Active Power of Loads Restored (KW)	Sum of Nominal active load restored by phases A/B/C	Solver Time (Sec)	Objective Value (KW-Steps)	Best Bound (KW-Steps)	Optimality Gap (%)
Scenario 1.1	60 out of 81 loads	2,520.0	841.1/829.2/849.7	1214.51	(-)8,490.0	(-)8,655.0	1.94
Scenario 1.2	59 out of 81 loads	2,640.0	781.1/779.2/1079.7	436.50	(-)8,470.0	(-)8,630.0	1.89

Also observe from Table 7.40, under the "sum of nominal active load restored by phases" column, that the loads restored in scenario 1.1 are fairly balanced, while for scenario 1.2, all loads in phase C are restored (recall from Table 7.39 that phase C has a total nominal active power load of 1080 to the nearest whole number) . The method restored all of phase C loads in scenario 1.2 for power balancing reason because the non-dispatchable DG (with details in Table 7.38) is connected to phase C.

7.7.2. Scenario 2

This scenario highlights the effect of the phase of non-dispatchable renewable DGs.

7.7.2.1. Description of Test System

A one-line diagram of the base test system is shown in Figure 7.70. One droop-controlled DGs is present at node 2063. Three PQ dispatchable DGs are present at nodes 34, 46, and 59. A non-dispatchable DG is present at node 81.

Figure 7.70 One Line Diagram for Case Studies 4 Scenario 2

7.7.2.2. DG Information

The DGs' details present in Figure 7.70 are summarized in Table 7.41.

Table 7.41 DGs' Information for Case Studies 4 Scenario 2

Label	Node	Type	f^{ref} (Hz)	Per phase BaseMVA	per phase baseKV	pu coupling X	Pmax (KW)	Pmin (KW)	Qmax (KVAR)	Qmin (KVAR)	Phase	Status	Blackstart	Ramp Rate %
DG1	2063	Droop	60	1	2.4018	0.3	2800	0	1600	-150	ABC	1	1	50
DG2	34	PQ	NA	NA	NA	NA	100	0	50	-10	C	1	0	50
DG3	46	PQ	NA	NA	NA	NA	100	0	50	-10	A	1	0	50
DG4	59	PQ	NA	NA	NA	NA	100	0	50	-10	B	1	0	50
DG5	81	PQ-NonDisp	NA	NA	NA	NA	350	350	220	220	C	1	0	100

7.7.2.3. Derivative Cases

There are six cases in this scenario numbered 2.1A, 2.1B, 2.2A, 2.2B, 2.3A, and 2.3B. The cases with "A" appended to their name do not have enforced connection of non-dispatchable DG while the ones with "B" appended to their name do. Scenarios 2.1A and 2.1B have their non-dispatchable DG connected to phase A, 2.2 A and 2.2B are connected to phase B, while 2.3A and 2.3B are connected to phase C. These details are summarized in Table 7.42. The restoration time step is set to 6 which is same as the conservative/generous time estimate for the topology of the scenario presented in Figure 7.70.

Table 7.42. Phases and Connection Requirement of the non-dispatchable DGs for Case Studies 4 Scenario 2

	S2.1A	S2.1B	S2.2A	S2.2B	S2.3A	S2.3B
Phase	A	A	B	B	C	C
Connection enforced for non-dispatchable DG?	No	Yes	No	Yes	No	Yes

7.7.2.4. Load Details

The load details for each case in this scenario are the same as those of scenario 1 which is given in Table 7.39. All loads are assumed to be switchable and restorable.

By transforming the delta connected load into equivalent Y connected load and summing the nominal power for the loads gives: the sum of nominal active power load is 1,231.1 KW, 1,169.2 KW, and 1,079.7 KW for phases A, B, and C respectively. The sum of the nominal reactive power load is 681.1 KVAR, 641.5 KVAR, and 582.4 KVAR for phases A, B, and C, respectively. Notice that phase A has a greater total nominal load

value to be restored, followed by phase B and then phase C. We will refer to these loading conditions in the next subsection.

7.7.2.5. Performance Summary of Scenario 2

A summary of the six cases is shown in Table 7.43. Notice that scenarios 2.1 A&B have the greatest objective magnitude, followed by scenarios 2.2 A&B, and lastly scenarios 2.3 A&B. For scenarios 2.1 A&B, the non-dispatchable DG is connected to phase A which is the most loaded and therefore is the best phase in which its connection would provide the greatest load balancing. Similarly, for scenarios 2.2 A&B, the non-dispatchable DG is connected to phase B which has greater loading than phase C and thus provide greater load balancing than those of phase C.

In scenarios 2.3A, the non-dispatchable DG connected to phase C was not energized in 2.3 A because it is the least loaded phase and did not provide any helpful load balancing. However, in scenario 2.3B, the non-dispatchable was energized since this case has an additional constraint to enforce its energization.

Table 7.43 Summary of Results of Six Cases for Case Studies 4 Scenario 2

	Total Number of Restored Load	Sum of Nominal Active Power of Loads Restored (KW)	Solver Time (Sec)	Objective Value (KW-Steps)	Best Bound (KW-Steps)	Optimality Gap (%)	Non-dispatchable DG connection enforced?	Non-dispatchable DG Phase	Non-dispatchable DG Energized?
Scenario 2.1A	66 out of 81 loads	2,760.0	2926.23	(-)8,680.0	(-)8,850.0	1.96	No	A	Yes
Scenario 2.1B	65 out of 81 loads	2,760.0	1120.36	(-)8,680.0	(-)8,850.0	1.96	Yes	A	Yes
Scenario 2.2A	59 out of 81 loads	2,730.0	754.91	(-)8,580.0	(-)8,750.0	1.98	No	B	Yes
Scenario 2.2B	60 out of 81 loads	2,720.0	521.58	(-)8,575.0	(-)8,745.0	1.98	Yes	B	Yes
Scenario 2.3A	60 out of 81 loads	2,520.0	1298.16	(-)8,490.0	(-)8,655.0	1.94	No	C	No
Scenario 2.3B	59 out of 81 loads	2,640.0	221.08	(-)8,470.0	(-)8,635.0	1.95	Yes	C	Yes

7.7.3. Scenario 3

This scenario studies the impact of non-dispatchable renewable DG capacity.

7.7.3.1. Description of Test System

A one-line diagram of the test system is shown in Figure 7.71. One droop-controlled DG is present at node 2063. Three PQ dispatchable DGs are present at nodes 34, 46, and 59. Two non-dispatchable DGs are present at nodes 19 and 81.

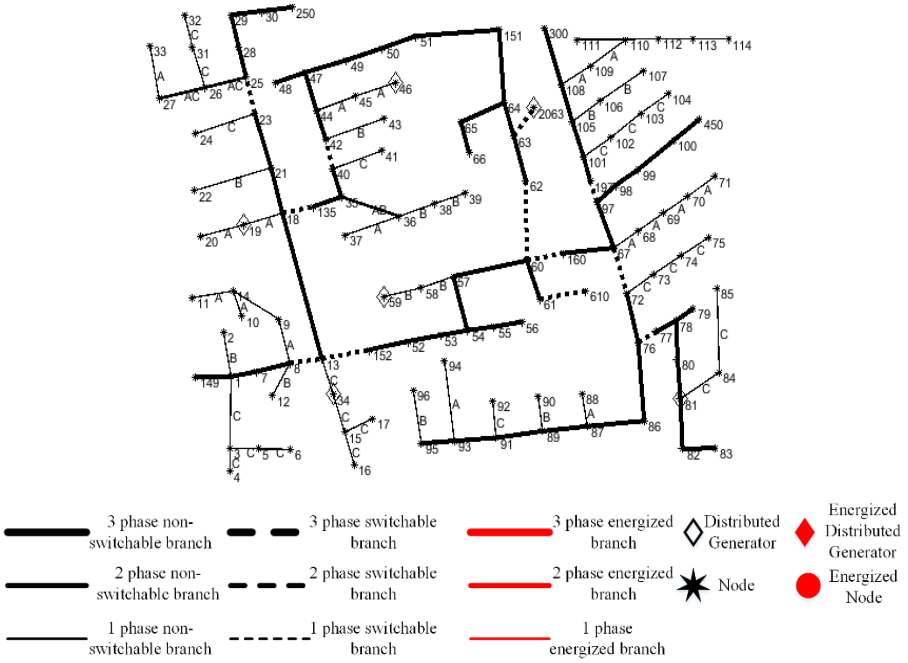

Figure 7.71 One Line Diagram for Case Studies 4 scenario 3

7.7.3.2. DGs' Information

The DGs' details present in Figure 7.71 are summarized in Table 7.44.

Table 7.44. DGs' Information for Case Studies 4 Scenario 3

Label	Node	Type	f^{ref} (Hz)	Per phase BaseMVA	per phase baseKV	pu coupling X	Pmax (KW)	Pmin (KW)	Qmax (KVAR)	Qmin (KVAR)	Phase	Status	Blackstart	Ramp Rate %
DG1	2063	Droop	60	1	2.4018	0.3	2800	0	1600	-150	ABC	1	1	50
DG2	34	PQ	NA	NA	NA	NA	100	0	50	-10	C	1	0	50
DG3	46	PQ	NA	NA	NA	NA	100	0	50	-10	A	1	0	50
DG4	59	PQ	NA	NA	NA	NA	100	0	50	-10	B	1	0	50
DG5	81	PQ-NonDisp	NA	NA	NA	NA	120	120	70	70	B	1	0	100
DG6	19	PQ-NonDisp	NA	NA	NA	NA	200	200	110	110	A	1	0	100

7.7.3.3. Derivative Cases

There are twelve cases in this scenario numbered 2.1A, 2.1B, 2.2A, 2.2B, to 2.6A, and 2.6B. The cases with “A” appended to their name do not have enforced connection of non-dispatchable DG while the ones with “B” appended to their name do. Scenarios 2.1 A&B, 2.2 A&B, to 2.6 A&B have their non-dispatchable DG capacities multiplied by a factor of 0.5, 0.75, 1, 2, 4, and 6 respectively. The restoration time step is set to 6 which is the same as the conservative/generous time estimate for the topology of the scenario presented in Figure 7.71.

7.7.3.4. Load Details

The load details for each case in this scenario are the same as those of scenario 1 which is given in Table 7.39. All loads are assumed to be switchable and restorable.

7.7.3.5. Performance Summary of Scenario 3

A summary of the ten cases is shown in Table 7.45. Notice that as the non-dispatchable DG capacity factor is increased (that is its output value is multiplied by a factor), the objective magnitude (which is the energy restored) increases until a certain capacity factor threshold. Scenarios 3.5 A&B has a non-dispatchable DGs capacity factor

of 4 and it is seen in Table 7.45 that these two cases did not improve their objective magnitude compared to the first eight cases. At a capacity factor of 4, the non-dispatchable DGs are no longer beneficent since it poses balancing issues for the other DGs in the system.

Table 7.45 Summary of Results of Six Cases for Case Studies 4 Scenario 3

	Total Number of Restored Load	Sum of Nominal Active Power of Loads Restored (KW)	Solver Time (Sec)	Objective Value (KW-Steps)	Best Bound (KW-Steps)	Optimality Gap (%)	Non-dispatchable DG connection enforced?	Non-dispatchable DG Energized?	Non-dispatchable DGs capacity factor
Scenario 3.1A	64 out of 81 loads	2,680.0	389.98	(-)8,850.0	(-)9,020.0	1.92	No	DG5 & DG6	0.5
Scenario 3.1B	64 out of 81 loads	2,660.0	239.78	(-)8,830.0	(-)9,005.0	1.98	Yes	DG5 & DG6	0.5
Scenario 3.2A	66 out of 81 loads	2,780.0	259.00	(-)9,015.0	(-)9,190.0	1.94	No	DG5 & DG6	0.75
Scenario 3.2B	65 out of 81 loads	2,760.0	154.03	(-)9,030.0	(-)9,210.0	1.99	Yes	DG5 & DG6	0.75
Scenario 3.3A	69 out of 81 loads	2,840.0	324.42	(-)9,115.0	(-)9,295.0	1.97	No	DG5 & DG6	1
Scenario 3.3B	69 out of 81 loads	2,850.0	220.38	(-)9,150.0	(-)9,265.0	1.26	Yes	DG5 & DG6	1
Scenario 3.4A	69 out of 81 loads	3,090.0	511.37	(-)9,290.0	(-)9,470.0	1.94	No	DG5 & DG6	2
Scenario 3.4B	69 out of 81 loads	3,090.0	235.20	(-)9,290.0	(-)9,475.0	1.99	Yes	DG5 & DG6	2
Scenario 3.5A	60 out of 81 loads	2,520.0	895.44	(-)8,490.0	(-)8,655.0	1.94	No	None	4
Scenario 3.5B	60 out of 81 loads	2,770.0	209.31	(-)7,695.0	(-)7,825.0	1.69	Yes	DG5 & DG6	4
Scenario 3.6A	57 out of 81 loads	2,520.0	414.18	(-)8,490.0	(-)8,655.0	1.94	No	None	6
Scenario 3.6B	Infeasible	Infeasible	0.08	Infeasible	Infeasible	Infeasible	Yes	Infeasible	6

In scenario 3.6A, none of the non-dispatchable DGs were connected to the system and thus this case has the same objective magnitude as 3.5A which could not connect to any as well. In scenario 3.6B, the connection of non-dispatchable DGs is enforced and it returned an infeasible solution. At a capacity factor of 6, enforcing connection of the non-dispatchable DGs resulted in an infeasible solution. A look at the load profile in Table 7.39 and DGs details in Table 7.44 can provide more insight on this factor of 6. The second

non-dispatchable DG, DG6, has a larger output compared to the first one, and has a forecasted output of 200KW/110KVAR (connected to phase A). Multiplying by a capacity factor of 6 gives 1200KW/660KVAR. The nominal sum of the total restorable load on phase A is 1231KW/681KVAR. We can infer that once the capacity of these non-dispatchable DGs approaches the nominal sum of restorable loads for any phase, then it can become infeasible to enforce its connection. This makes more sense considering that some of these loads are double-phase and three-phase loads, and restoring any phase enforces the restoration of the other phases.

This study suggests that the balancing threshold for a microgrid should be properly considered when determining whether a non-dispatchable DG should be connected and incorporating output curtailment for relatively large non-dispatchable DG sources may help in making its connection feasible and beneficial.

7.8. Case Studies 5: Performance Under Different Loading Conditions

The purpose of case studies 5 is to check the performance of the developed method under different loading situations. The island system used for the case studies under this section is adapted from the IEEE 123 node test feeder. The case studies under this section are subdivided into two scenarios:

- Scenario 1: case studies highlighting the impact of different nominal loading conditions ranging from lightly loaded to heavily loaded
- Scenario 2: case studies highlighting the impact of different unbalance load conditions using nominal system load unbalance index (NSLUI)

The computation options for all cases categorized under the case studies 5 section is outlined in Table 7.46 below.

Table 7.46 Computation Settings for Case Studies 5

Options	Choice
Options.connectGFDGs	False
Options.skipPWL	True
Options.ignoreShuntAdmittance	True
Options.includeShuntAdmittanceForLastStepOnly	NA
Options.MIPGap	2%
Conservative/Generous Time Step Estimate	Varies with case

7.8.1. Scenario 1

This scenario studies the impact of different nominal loading conditions ranging from lightly loaded to heavily loaded.

7.8.1.1. Description of Test System

A one-line diagram of the test system is shown in Figure 7.72. One droop-controlled DG is present at node 2063. Three PQ DGs are present at nodes 34, 46, and 59.

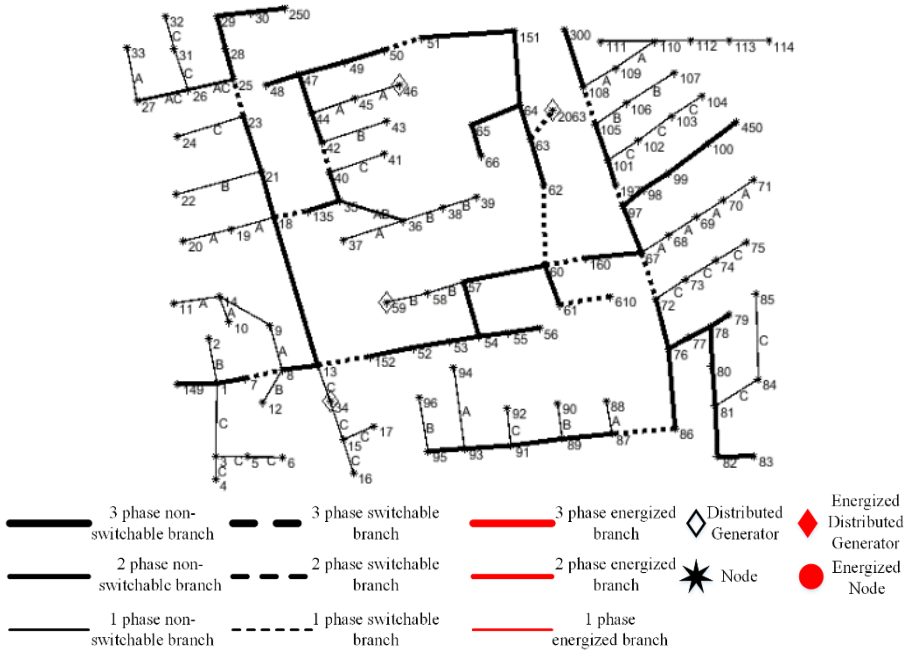

Figure 7.72 One Line Diagram for Case Studies 5 Scenario 1

7.8.1.2. DG Information

The DGs' details present in Figure 7.72 are summarized in Table 7.47.

Table 7.47 DGs' Information for Case Studies 5 Scenario 1

Label	Node	Type	f^{ref} (Hz)	Per phase BaseMVA	per phase baseKV	pu coupling X	Pmax (KW)	Pmin (KW)	Qmax (KVAR)	Qmin (KVAR)	Phase	Status	Blackstart	Ramp Rate %
DG1	2063	Droop	60	1	2.4018	0.3	2800	0	1600	-150	ABC	1	1	50
DG2	34	PQ	NA	NA	NA	NA	250	0	150	-20	C	1	0	50
DG3	46	PQ	NA	NA	NA	NA	250	0	150	-20	A	1	0	50
DG4	59	PQ	NA	NA	NA	NA	250	0	150	-20	B	1	0	50

7.8.1.3. Load Details

There is a total of 81 loads in this case study and the details are shown in Table 7.48. All loads are assumed to be switchable and restorable.

Table 7.48 Load details for case studies 5 scenario 1

NODE	CONFIG	P(A/B/C) KW	Q(A/B/C) KVAR	NODE	CONFIG	P(A/B/C) KW	Q(A/B/C) KVAR	NODE	CONFIG	P(A/B/C) KW	Q(A/B/C) KVAR
1	Y	40/0/0	20/0/0	43	Y	0/40/0	0/20/0	77	Y	0/40/0	0/20/0
2	Y	0/20/0	0/10/0	45	Y	20/0/0	10/0/0	79	Y	40/0/0	20/0/0
4	Y	0/0/40	0/0/20	46	Y	20/0/0	10/0/0	80	Y	0/40/0	0/20/0
5	Y	0/0/20	0/0/10	47	Y	35/35/35	25/25/25	82	Y	40/0/0	20/0/0
6	Y	0/0/40	0/0/20	48	Y	70/70/70	50/50/50	83	Y	0/0/20	0/0/10
7	Y	20/0/0	10/0/0	49	Y	35/70/35	25/30/20	84	Y	0/0/20	0/0/10
10	Y	20/0/0	10/0/0	50	Y	0/0/40	0/0/20	85	Y	0/0/40	0/0/20
11	Y	40/0/0	20/0/0	51	Y	20/0/0	10/0/0	86	Y	0/20/0	0/10/0
12	Y	0/20/0	0/10/0	52	Y	40/0/0	20/0/0	87	Y	0/40/0	0/20/0
16	Y	0/0/40	0/0/20	53	Y	40/0/0	20/0/0	88	Y	40/0/0	20/0/0
17	Y	0/0/20	0/0/10	55	Y	20/0/0	10/0/0	90	Y	0/40/0	0/20/0
19	Y	20/0/0	10/0/0	56	Y	0/60/0	0/40/0	92	Y	0/0/40	0/0/20
20	Y	20/0/0	10/0/0	58	Y	0/20/0	0/10/0	94	Y	40/0/0	20/0/0
22	Y	0/60/0	0/30/0	59	Y	0/20/0	0/10/0	95	Y	0/40/0	0/20/0
24	Y	0/0/40	0/0/20	60	Y	20/0/0	10/0/0	96	Y	0/40/0	0/20/0
28	Y	40/0/0	20/0/0	62	Y	0/0/20	0/0/10	98	Y	40/0/0	20/0/0
29	Y	40/0/0	20/0/0	63	Y	40/0/0	20/0/0	99	Y	0/70/0	0/40/0
30	Y	0/0/40	0/0/20	64	Y	0/75/0	0/25/0	100	Y	0/0/40	0/0/20
31	Y	0/0/20	0/0/10	65	Y	35/35/70	25/25/50	102	Y	0/0/20	0/0/10
32	Y	0/0/20	0/0/10	66	Y	0/0/30	0/0/20	103	Y	0/0/40	0/0/20
33	Y	40/0/0	20/0/0	68	Y	20/0/0	10/0/0	104	Y	0/0/40	0/0/20
34	Y	0/0/40	0/0/20	69	Y	40/0/0	20/0/0	106	Y	0/60/0	0/30/0
35	Y	40/0/0	20/0/0	70	Y	20/0/0	10/0/0	107	Y	0/60/0	0/30/0
37	Y	60/0/0	40/0/0	71	Y	40/0/0	20/0/0	111	Y	20/0/0	10/0/0
38	Y	0/70/0	0/35/0	73	Y	0/0/40	0/0/20	114	Y	30/0/0	15/0/0
39	Y	0/40/0	0/20/0	74	Y	0/0/40	0/0/20				
41	Y	0/0/20	0/0/10	75	Y	0/0/40	0/0/20		TOTAL	1235/1155/1090	680/620/605
42	Y	20/0/0	10/0/0	76	Y	70/70/70	50/50/50				

7.8.1.4. Derivative Cases

There are six cases in this scenario numbered scenarios 2.1, 2.2 to 2.6. These six cases, scenarios 2.1, 2.2 to 2.6, are derived by multiplying the nominal load values of Table 7.48 by a factor of 0.33, 0.67, 1, 1.33, 1.67, and 2 respectively. The restoration time

step for each case is set to 6 which is the same as the conservative/generous time estimate for the topology of the scenario presented in Figure 7.72.

7.8.1.5. Performance Summary of Scenario 1

A summary of the six cases run in this scenario is shown in Table 7.49. Table 7.49 shows that as the load factor is increased, a lesser number of aggregate loads are restored even though the objective magnitude and the sum of nominal active power increases. Notice that as the load factor increases, it becomes more difficult to close in on 0% optimality gap (in other words get the objective value to match the best bound) and the solver time increases as well.

Table 7.49 Summary of Results of Six Cases for Case Studies 5 Scenario 1

	Total Number of Restored Load	Sum of Nominal Active Power of Loads Restored (KW)	Solver Time (Sec)	Objective Value (KW-Steps)	Best Bound (KW-Steps)	Optimality Gap (%)	Load Factor
Scenario 1.1	81 out of 81 loads	1,148.4	4.67	(-)3,210.9	(-)3,210.9	0.00	0.33
Scenario 1.2	81 out of 81 loads	2,331.6	4.84	(-)6,519.1	(-)6,519.1	0.00	0.67
Scenario 1.3	66 out of 81 loads	2,890.0	67.23	(-)8,720.0	(-)8,880.0	1.83	1
Scenario 1.4	50 out of 81 loads	2,939.3	614.76	(-)9,615.9	(-)9,802.1	1.94	1.33
Scenario 1.5	40 out of 81 loads	2,981.0	4000.10	(-)10,070.1	(-)10,395.8	3.23	1.67
Scenario 1.6	37 out of 81 loads	3,000.0	4000.06	(-)10,220.0	(-)10,710.0	4.79	2

7.8.2. Scenario 2

This scenario studies the performance of the restoration method under different unbalance load condition using nominal system load unbalance index (NSLUI).

7.8.2.1. Description of Test System

A one-line diagram of the test system is shown in Figure 7.73. One droop-controlled DG is present at node 2063. Three PQ DGs are present at nodes 34, 46, and 59.

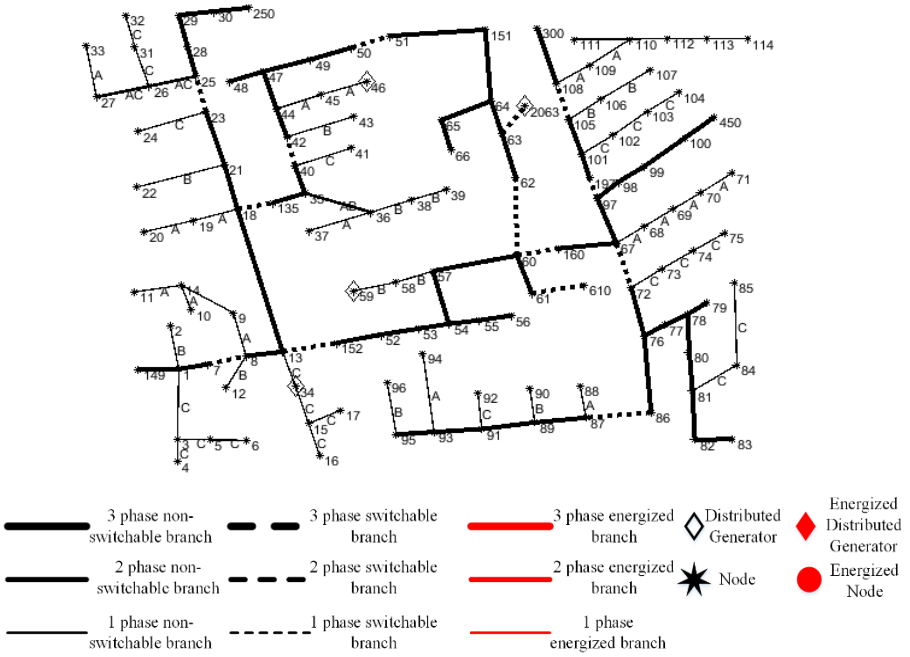

Figure 7.73 One Line Diagram for Case Studies 5 Scenario 2

7.8.2.2. DG Information

The DGs' details present in Figure 7.73 are summarized in Table 7.50.

Table 7.50 DGs' Information for Case Studies 5 Scenario 2

Label	Node	Type	f^{ref} (Hz)	Per phase BaseMVA	per phase baseKV	pu coupling X	Pmax (KW)	Pmin (KW)	Qmax (KVAR)	Qmin (KVAR)	Phase	Status	Blackstart	Ramp Rate %
DG1	2063	Droop	60	1	2.4018	0.3	2800	0	1600	-150	ABC	1	1	50
DG2	34	PQ	NA	NA	NA	NA	250	0	150	-20	C	1	0	50
DG3	46	PQ	NA	NA	NA	NA	250	0	150	-20	A	1	0	50
DG4	59	PQ	NA	NA	NA	NA	250	0	150	-20	B	1	0	50

7.8.2.3. Load Details

There is a total of 81 loads in this case study and the details of the aggregate loads for the first case, scenario 2.1, are shown in Table 7.51. All loads are assumed to be switchable and restorable. The sum of the nominal active power load is 1180 KW, each phase, while the sum of the nominal reactive power load is 660 KVAR for phase. This results in a nominal system load unbalance index of 0% for both the active and reactive power loads.

Table 7.51 Load Details for Case Studies 5 Scenario 2.1

Node	Config	P(A/B/C) KW	Q(A/B/C) KVAR	Node	Config	P(A/B/C) KW	Q(A/B/C) KVAR	Node	Config	P(A/B/C) KW	Q(A/B/C) KVAR
1	Y	20/0/0	10/0/0	43	Y	0/40/0	0/20/0	77	Y	0/40/0	0/20/0
2	Y	0/20/0	0/10/0	45	Y	20/0/0	10/0/0	79	Y	40/0/0	20/0/0
4	Y	0/0/40	0/0/20	46	Y	20/0/0	10/0/0	80	Y	0/40/0	0/20/0
5	Y	0/0/20	0/0/10	47	Y	35/35/35	25/25/25	82	Y	40/0/0	20/0/0
6	Y	0/0/40	0/0/20	48	Y	70/70/70	50/50/50	83	Y	0/0/20	0/0/10
7	Y	20/0/0	10/0/0	49	Y	35/70/35	25/30/20	84	Y	0/0/20	0/0/10
10	Y	20/0/0	10/0/0	50	Y	0/0/40	0/0/20	85	Y	0/0/40	0/0/20
11	Y	40/0/0	20/0/0	51	Y	20/0/0	10/0/0	86	Y	0/20/0	0/10/0
12	Y	0/20/0	0/10/0	52	Y	40/0/0	20/0/0	87	Y	0/40/0	0/20/0
16	Y	0/0/40	0/0/20	53	Y	40/0/0	20/0/0	88	Y	25/0/0	15/0/0
17	Y	0/0/20	0/0/10	55	Y	20/0/0	10/0/0	90	Y	0/40/0	0/20/0
19	Y	20/0/0	10/0/0	56	Y	0/60/0	0/40/0	92	Y	0/0/40	0/0/20
20	Y	20/0/0	10/0/0	58	Y	0/20/0	0/10/0	94	Y	40/0/0	20/0/0
22	Y	0/60/0	0/30/0	59	Y	0/20/0	0/10/0	95	Y	0/50/0	0/30/0
24	Y	0/0/40	0/0/20	60	Y	20/0/0	10/0/0	96	Y	0/55/0	0/30/0
28	Y	40/0/0	20/0/0	62	Y	0/0/20	0/0/10	98	Y	40/0/0	25/0/0
29	Y	20/0/0	10/0/0	63	Y	40/0/0	20/0/0	99	Y	0/70/0	0/40/0
30	Y	0/0/40	0/0/20	64	Y	0/75/0	0/45/0	100	Y	0/0/40	0/0/20
31	Y	0/0/20	0/0/10	65	Y	35/35/70	25/25/50	102	Y	0/0/30	0/0/15
32	Y	0/0/20	0/0/10	66	Y	0/0/30	0/0/20	103	Y	0/0/50	0/0/30
33	Y	40/0/0	20/0/0	68	Y	20/0/0	10/0/0	104	Y	0/0/50	0/0/30
34	Y	0/0/40	0/0/20	69	Y	40/0/0	20/0/0	106	Y	0/60/0	0/30/0
35	Y	40/0/0	20/0/0	70	Y	20/0/0	10/0/0	107	Y	0/60/0	0/30/0
37	Y	60/0/0	40/0/0	71	Y	40/0/0	20/0/0	111	Y	20/0/0	10/0/0
38	Y	0/70/0	0/35/0	73	Y	0/0/60	0/0/30	114	Y	30/0/0	15/0/0
39	Y	0/40/0	0/20/0	74	Y	0/0/60	0/0/30				
41	Y	0/0/20	0/0/10	75	Y	0/0/60	0/0/30		Total	1180/1180/1180	660/660/660
42	Y	20/0/0	10/0/0	76	Y	70/70/70	50/50/50				

7.8.2.4. Derivative Cases

There are five derivative cases in this scenario numbered scenarios 2.2 to 2.6. The load profile of scenarios 2.2, 2.3 to 2.6 are adjusted from the load profile of Table 7.51 by moving a fraction of the load values from phase B to phase C to get NSLUI of 10%, 20%, 30%, 40%, and 50% respectively.

7.8.2.5. Performance Summary of Scenario 2

A summary of the six cases run in this scenario is shown in Table 7.52. Table 7.52 shows as the NSLUI of the loads increase, lesser objective magnitude and the sum of nominal active power of loads restored will be realized.

Table 7.52 Summary of Results of Six Cases for Case Studies 5 Scenario 2

	Total Number of Restored Load	Sum of Nominal Active Power of Loads Restored (KW)	Solver Time (Sec)	Objective Value (KW-Steps)	Best Bound (KW-Steps)	Optimality Gap (%)	NSLUI (%)
Scenario 2.1	68 out of 81 loads	2,870.0	125.09	(-)8,640.0	(-)8,800.0	1.85	0
Scenario 2.2	65 out of 81 loads	2,878.0	94.96	(-)8,608.5	(-)8,773.0	1.91	10
Scenario 2.3	63 out of 81 loads	2,857.0	136.68	(-)8,500.0	(-)8,616.0	1.36	20
Scenario 2.4	63 out of 81 loads	2,758.0	86.60	(-)8,158.5	(-)8,305.0	1.80	30
Scenario 2.5	62 out of 81 loads	2,629.0	52.84	(-)7,395.0	(-)7,519.0	1.68	40
Scenario 2.6	55 out of 81 loads	2,275.0	46.00	(-)6,360.0	(-)6,470.0	1.73	50

Figure 7.74 shows a plot of the DG utilization in percentage at the last restoration step on the y-axis for all DGs versus all the cases in this scenario on the x-axis. Notice from Figure 7.74 that the reduction in overall load restoration and DG utilization is mostly due to poor utilization of the PQ dispatchable DG on phase B. This is because some loads

were moved from phase B to phase C to increase the load NSLUI. On the other hand, the PQ dispatchable DG on phase C got to maximum utilization of 100%.

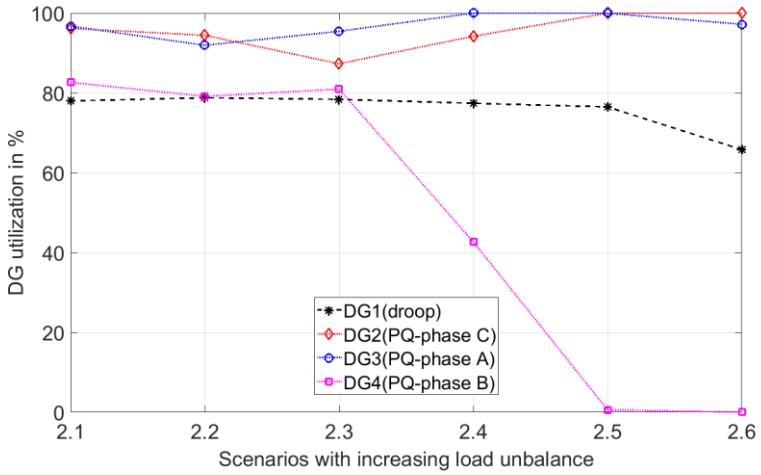

Figure 7.74 DG Utilization at the Last Step for all Cases in Scenario 2

7.9. Section Summary

In this section, the BSR formulation developed in section 6 for the MMO microgrids has been used in extensive cases studies for validation and performance analysis. Six performance metrics were used to evaluate the cases: total energy restored (absolute value of the objective function), sum of nominal active loads restored, total number of restored aggregate loads (integer count), best bound, and computation/solver time. A set of case studies grouped as case studies 1 to 5 were performed. Each of the case studies 1 to 5 has several scenarios that were focused toward evaluating and studying a particular feature of the new restoration method.

Case studies 1 was focused on validating and verifying the functionality of the MMO restoration method. These cases were grouped under five scenarios. Scenarios 1 to

4 of case studies 1 focused on validating the functionalities, such as ensuring that the restored systems follow the expected sequence and maintain tree topology, DGs operate as expected, and that loads are restored in the expected manner. Scenario 5 of case studies was focused on verifying that the restoration solution is accurate by using detailed PSCAD simulation of the system as benchmark. Without accounting for converter's filter and controller unbalance effects, the power flow results from the restoration method had a mean nodal voltage error in the range of 1.3 to 1.5%. After averaging out these filter and controller unbalance effects, the nodal voltages had a mean error in the range of about 0.02 to 0.06%.

Case studies 2 was focused on studying the effects of PQ DGs and loads with demand response capability. The demand response loads were assumed to have a direct load control (DLC) scheme which are implemented by microgrid central controller (MGCC). These studies show that, in general, including PQ DGs and loads with demand response capability improve the restoration results (that is, increase in energy restored) by helping to balance the loads in the system. Increasing the controllability range of the demand response loads can lead to a better solution but no worse solution. Scenario 2 of case studies 2 indicates that the method works better when the system's loading is well compensated through proper choice of phases to locate single phase PQ DGs. Well planned and compensated systems were solved several times faster than poorly compensated systems.

In case studies 3, the performance of the system under different system initial conditions was evaluated. Some of the initial system conditions considered include

performance of the restoration method under different choice of the droop-controlled DG node (mostly planning related), effect of switchable/non-switchable lines and loads on the controllability of the method, performance under the presence of damaged lines and loads, and lastly, the impact of restoration time steps. Under the above-mentioned conditions, the restoration method was able to generate good solutions and isolate faulty elements. The restoration method generally gave better solutions when the bus block of the droop-controlled DGs were well centered.

In case studies 4, the impact of non-dispatchable DGs were studied. The main take away from these cases is that the non-dispatchable DG capacity can be beneficial if properly sized. Due to its non-dispatchable nature (which reduces controllability), an increase in output power may require some curtailment if its connection is to be beneficial or even feasible. The studies showed that above a given output threshold, enforcing connection of non-dispatchable DGs to the restored system will worsen the restoration result or even lead to an infeasible solution.

Case studies 5 is focused on the performance of the restoration method under different loading conditions. Two scenarios were considered: the first was on the performance of the system under different loading conditions from lightly loaded to heavily loaded, and the second is under different unbalance conditions. In the second scenario, we highlighted how increases in load unbalance conditions can negatively affect the utilization of certain DGs.

Some general observations were made about the performance of the method. The piecewise linearization approach (Appendix B) can increase the computational burden

tremendously because of the numerous variables and constraints that it introduces especially for larger systems such as the IEEE 123 node test system. To get around this, an alternative to the piecewise linearization was presented in Appendix C. Also, another observation was the numerical issues that can sometime result from including the shunt admittance. This is mostly because of the relatively small value of the shunt admittance which can increase numerical instability for systems as large as the IEEE 123 node test feeder. Because distribution lines are relatively shorter compared to bulk power system transmission lines, the shunt admittance can be ignored without incurring significant errors just like it is done in the DistFlow equations [64, 65]. More details about these computation related observations are discussed in section 7.2.7.

In all, the new restoration method conveyed robustness through the quality solutions that it returned in the studied cases.

8. CONCLUSIONS AND FUTURE WORK

8.1. Summary and Conclusions

The goals and contributions of this dissertation are summarized as follows:

1. Formulated sequential black start restoration (BSR) for islanded single master microgrids with considerations of operational and dynamic stability constraints.
2. Proposed linear and optimal power flow formulations for multi-master microgrids with droop-control.
3. Formulated sequential BSR for islanded multi-master microgrids with considerations of droop control, operational and dynamic constraints.

In this dissertation, control of islanded microgrids for black start restoration (BSR) has been studied with considerations of primary control. Two microgrid control architectures were considered based on primary control: the single master operation (SMO) and the multi-master operation (MMO) microgrids.

For the SMO BSR, a sequential BSR was proposed that integrates frequency response and settling time characterization into the BSR formulation. The settling time characterization enables finding the exact switching times for the remote controlled switches (RCS). Novel and existing linearization approaches were utilized to formulate a mixed-integer linear programming (MILP) problem. The BSR method was verified through transient simulation in PSCAD and can ensure that the operating constraints are satisfied while minimizing the total restoration time and maximizing the energy restored.

The MMO microgrids studied in this dissertation were assumed to be droop controlled. Due to the difficulty of incorporating existing linear power flow (LPF) methods into islanded droop-controlled microgrids, we first derived two novel LPF approximations for the islanded droop-controlled microgrids before developing BSR formulation for the MMO microgrids. The first LPF approximation is a derivative of the current injection method (CIM) and the second is a derivative of the DistFlow. To show their applicability, the two LPF approximations were extended to develop two OPF problems which were formulated as a quadratic programming (QP) and a mixed-integer quadratic programming (MIQP) problem to minimize operating cost.

Finally, we developed a novel sequential BSR formulation with considerations of droop as the primary control for the MMO microgrids. The power flow constraint for this formulation is based on the current injection LPF derived in this dissertation. Several operational constraints were modeled and linearized using existing and novel methods to realize a MILP formulation. Extensive case studies for validation and performance analysis were conducted. The BSR method was verified using detailed transient simulation in PSCAD. It was observed that the PQ DGs and loads with demand response can aid in improving restoration results by balancing the loads in the system. For the use of non-dispatchable renewable DGs during restoration, an increase in output power may require some curtailment if its connection is to be beneficial or even feasible. In general, the BSR method returned quality solutions in all the cases studied.

8.2. Future Work

For the SMO microgrid, the primary control of the master DG is controlled isochronously and its governor integrates frequency error to zero following step changes in system loading. On the other hand, the MMO microgrid requires more coordination owing to the effects of droop and ensuring that the power is shared in the desired proportion. Unlike the SMO microgrids where we characterized the dynamics of its frequency response with few equations, characterizing the dynamics of the frequency response for the MMO will require more complicated controller analysis. Future work will focus on detailed controller analysis for the MMO microgrid to characterize its frequency response, estimate settling time, and stability region.

In this dissertation, we have studied the MMO microgrid control using conventional droop for BSR. In the literature, there are different variants of droop control of islanded microgrids. Evaluating the use of other forms of droop for BSR will be an interesting area to explore in the future. Also, developing linear power flow (LPF) approximations considering different forms of droop will be of interest.

REFERENCES

[1] D. T. Ton and M. A. Smith, "The U.S. Department of Energy's Microgrid Initiative," *The Electricity Journal*, vol. 25, no. 8, pp. 84-94, 2012/10/01/ 2012.

[2] A. Kaur, J. Kaushal, and P. Basak, "A review on microgrid central controller," *Renewable and Sustainable Energy Reviews*, vol. 55, pp. 338-345, 2016/03/01/ 2016.

[3] A. Hussain, V.-H. Bui, and H.-M. Kim, "Microgrids as a resilience resource and strategies used by microgrids for enhancing resilience," *Applied Energy*, vol. 240, pp. 56-72, 2019/04/15/ 2019.

[4] L. Cohn. (2020). *California Microgrids Flex Their Skills During Blackouts*. Available: https://microgridknowledge.com/california-blackouts-microgrids-flexible-load/

[5] E. F. Merchant. (2018, 4/6/2018). *As Hurricane Season Approaches, More Microgrids Crop Up in Puerto Rico*. Available: https://www.greentechmedia.com/articles/read/as-hurricane-season-approaches-more-microgrids-cropping-up-in-puerto-rico

[6] L. Cohn. (2017, November 29). *Microgrid Kept Power On Even as the California Wildfires Caused Outages*. Available: https://microgridknowledge.com/islanded-microgrid-fires/

[7] A. Peters. (2020). *New microgrids are helping Australia get power back after the fires*. Available: https://www.fastcompany.com/90465605/new-microgrids-are-helping-australia-get-power-back-after-the-fires

[8] M. Farrokhabadi *et al.*, "Microgrid Stability Definitions, Analysis, and Examples," *IEEE Transactions on Power Systems*, vol. 35, no. 1, pp. 13-29, 2020.

[9] N. Gil and J. A. Lopes, *Exploiting automated demand response, generation and storage capabilities for hierarchical frequency control in islanded multi-microgrids*. 2008.

[10] N. J. Gil and J. A. P. Lopes, "Hierarchical Frequency Control Scheme for Islanded Multi-Microgrids Operation," in *2007 IEEE Lausanne Power Tech*, 2007, pp. 473-478.

[11] T. L. Vandoorn, J. C. Vasquez, J. D. Kooning, J. M. Guerrero, and L. Vandevelde, "Microgrids: Hierarchical Control and an Overview of the Control and Reserve

Management Strategies," *IEEE Industrial Electronics Magazine,* vol. 7, no. 4, pp. 42-55, 2013.

[12] J. Driesen and F. Katiraei, "Design for distributed energy resources," *IEEE Power and Energy Magazine,* vol. 6, no. 3, pp. 30-40, 2008.

[13] "IEEE Guide for Design, Operation, and Integration of Distributed Resource Island Systems with Electric Power Systems," *IEEE Std 1547.4-2011,* pp. 1-54, 2011.

[14] J. A. P. Lopes, C. L. Moreira, and A. G. Madureira, "Defining control strategies for MicroGrids islanded operation," *IEEE Transactions on Power Systems,* vol. 21, no. 2, pp. 916-924, 2006.

[15] K. L. Butler-Purry and N. D. R. Sarma, "Self-healing reconfiguration for restoration of naval shipboard power systems," *IEEE Transactions on Power Systems,* vol. 19, no. 2, pp. 754-762, 2004.

[16] K. L. Butler, N. D. R. Sarma, and V. R. Prasad, "Network reconfiguration for service restoration in shipboard power distribution systems," *IEEE Transactions on Power Systems,* vol. 16, no. 4, pp. 653-661, 2001.

[17] K. L. Butler, N. D. R. Sarma, and V. R. Prasad, "A new method of network reconfiguration for service restoration in shipboard power systems," in *1999 IEEE Transmission and Distribution Conference (Cat. No. 99CH36333)*, 1999, vol. 2, pp. 658-662 vol.2.

[18] H. Zhai, M. Yang, B. Chen, and N. Kang, "Dynamic reconfiguration of three-phase unbalanced distribution networks," *International Journal of Electrical Power & Energy Systems,* vol. 99, pp. 1-10, 2018.

[19] Z. Qin, D. Shirmohammadi, and W. H. E. Liu, "Distribution feeder reconfiguration for service restoration and load balancing," *IEEE Transactions on Power Systems,* vol. 12, no. 2, pp. 724-729, 1997.

[20] Y. Xiaodan, J. Hongjie, W. Chengshan, W. Wei, Z. Yuan, and Z. Jinli, "Network reconfiguration for distribution system with micro-grids," in *2009 International Conference on Sustainable Power Generation and Supply*, 2009, pp. 1-4.

[21] S. Tan, J. X. Xu, and S. K. Panda, "Optimization of Distribution Network Incorporating Distributed Generators: An Integrated Approach," *IEEE Transactions on Power Systems,* vol. 28, no. 3, pp. 2421-2432, 2013.

[22] S. Toune, H. Fudo, T. Genji, Y. Fukuyama, and Y. Nakanishi, "Comparative study of modern heuristic algorithms to service restoration in distribution systems," *IEEE Transactions on Power Delivery,* vol. 17, no. 1, pp. 173-181, 2002.

[23] R. Perez-Guerrero, G. T. Heydt, N. J. Jack, B. K. Keel, and A. R. Castelhano, "Optimal Restoration of Distribution Systems Using Dynamic Programming," *IEEE Transactions on Power Delivery,* vol. 23, no. 3, pp. 1589-1596, 2008.

[24] Y. Fukuyama and C. Hsaio-Dong, "A parallel genetic algorithm for service restoration in electric power distribution systems," in *Proceedings of 1995 IEEE International Conference on Fuzzy Systems.*, 1995, vol. 1, pp. 275-282 vol.1.

[25] I. Watanabe, I. Kurihara, and Y. Nakachi, "A Hybrid Genetic Algorithm for Service Restoration Problems in Power Distribution Systems," in *2006 IEEE International Conference on Evolutionary Computation*, 2006, pp. 3250-3257.

[26] I. Watanabe and M. Nodu, "A genetic algorithm for optimizing switching sequence of service restoration in distribution systems," in *Proceedings of the 2004 Congress on Evolutionary Computation (IEEE Cat. No.04TH8753)*, 2004, vol. 2, pp. 1683-1690 Vol.2.

[27] Z. Wang and J. Wang, "Self-Healing Resilient Distribution Systems Based on Sectionalization Into Microgrids," *IEEE Transactions on Power Systems,* vol. 30, no. 6, pp. 3139-3149, 2015.

[28] C. Chen, J. Wang, F. Qiu, and D. Zhao, "Resilient Distribution System by Microgrids Formation After Natural Disasters," *IEEE Transactions on Smart Grid,* vol. 7, no. 2, pp. 958-966, 2016.

[29] B. Chen, C. Chen, J. Wang, and K. L. Butler-Purry, "Sequential Service Restoration for Unbalanced Distribution Systems and Microgrids," *IEEE Transactions on Power Systems,* vol. 33, no. 2, pp. 1507-1520, 2018.

[30] B. Chen, C. Chen, J. Wang, and K. L. Butler-Purry, "Multi-Time Step Service Restoration for Advanced Distribution Systems and Microgrids," *IEEE Transactions on Smart Grid,* vol. 9, no. 6, pp. 6793-6805, 2018.

[31] B. Chen, Z. Ye, C. Chen, and J. Wang, "Toward a MILP Modeling Framework for Distribution System Restoration," *IEEE Transactions on Power Systems,* vol. 34, no. 3, pp. 1749-1760, 2019.

[32] B. Chen, Z. Ye, C. Chen, J. Wang, T. Ding, and Z. Bie, "Toward a Synthetic Model for Distribution System Restoration and Crew Dispatch," *IEEE Transactions on Power Systems,* vol. 34, no. 3, pp. 2228-2239, 2019.

[33] L. Yang, Y. Zhao, C. Wang, P. Gao, and J. Hao, "Resilience-Oriented Hierarchical Service Restoration in Distribution System Considering Microgrids," *IEEE Access*, vol. 7, pp. 152729-152743, 2019.

[34] Z. Ye, C. Chen, B. Chen, and K. Wu, "Resilient Service Restoration for Unbalanced Distribution Systems with DERs by Leveraging Mobile Generators," *IEEE Transactions on Industrial Informatics*, pp. 1-1, 2020.

[35] S. Poudel, A. Dubey, and K. P. Schneider, "A Generalized Framework for Service Restoration in a Resilient Power Distribution System," *IEEE Systems Journal*, pp. 1-13, 2020.

[36] M. A. Gilani, A. Kazemi, and M. Ghasemi, "Distribution system resilience enhancement by microgrid formation considering distributed energy resources," *Energy*, vol. 191, p. 116442, 2020/01/15/ 2020.

[37] L. Fu, B. Liu, K. Meng, and Z. Y. Dong, "Optimal Restoration of An Unbalanced Distribution System into Multiple Microgrids Considering Three-Phase Demand-Side Management," *IEEE Transactions on Power Systems*, pp. 1-1, 2020.

[38] Y. Wang *et al.*, "Coordinating Multiple Sources for Service Restoration to Enhance Resilience of Distribution Systems," *IEEE Transactions on Smart Grid*, 2019.

[39] J. A. P. Lopes, C. L. Moreira, and A. G. Madureira, "Microgrids black start and islanded operation," presented at the Proc. 15th Power System Computation Conference, Liege, Belgium, 2005.

[40] J. A. P. Lopes *et al.*, "Control strategies for microgrids emergency operation," in *2005 International Conference on Future Power Systems*, 2005, pp. 6 pp.-6.

[41] F. Katiraei, M. R. Iravani, and P. W. Lehn, "Micro-grid autonomous operation during and subsequent to islanding process," *IEEE Transactions on Power Delivery*, vol. 20, no. 1, pp. 248-257, 2005.

[42] L. Che, M. Khodayar, and M. Shahidehpour, "Only Connect: Microgrids for Distribution System Restoration," *IEEE Power and Energy Magazine*, vol. 12, no. 1, pp. 70-81, 2014.

[43] M. Nuschke, "Development of a microgrid controller for black start procedure and islanding operation," in *2017 IEEE 15th International Conference on Industrial Informatics (INDIN)*, 2017, pp. 439-444.

[44] F. Katiraei, R. Iravani, N. Hatziargyriou, and A. Dimeas, "Microgrids management," *IEEE Power and Energy Magazine*, vol. 6, no. 3, pp. 54-65, 2008.

[45] N. Pogaku, M. Prodanovic, and T. C. Green, "Modeling, Analysis and Testing of Autonomous Operation of an Inverter-Based Microgrid," *IEEE Transactions on Power Electronics*, vol. 22, no. 2, pp. 613-625, 2007.

[46] R. Majumder, "Modeling, stability analysis and control of microgrid," Queensland university of technology, 2010.

[47] R. Majumder, "Some aspects of stability in microgrids," *IEEE Transactions on power systems*, vol. 28, no. 3, pp. 3243-3252, 2013.

[48] J. W. Simpson-Porco, F. Dörfler, and F. Bullo, "Droop-controlled inverters are Kuramoto oscillators," in *IFAC Workshop on Distributed Estimation and Control in Networked Systems*, 2012, pp. 264-269.

[49] J. W. Simpson-Porco, F. Dörfler, and F. Bullo, "Synchronization and power sharing for droop-controlled inverters in islanded microgrids," *Automatica*, vol. 49, no. 9, pp. 2603-2611, 2013/09/01/ 2013.

[50] Y. Kuramoto, "Self-entrainment of a population of coupled non-linear oscillators," in *International symposium on mathematical problems in theoretical physics*, 1975, pp. 420-422: Springer.

[51] M. Kabalan, P. Singh, and D. Niebur, "Large Signal Lyapunov-Based Stability Studies in Microgrids: A Review," *IEEE Transactions on Smart Grid*, vol. 8, no. 5, pp. 2287-2295, 2017.

[52] M. Kabalan, P. Singh, and D. Niebur, "A Design and Optimization Tool for Inverter-Based Microgrids Using Large-Signal Nonlinear Analysis," *IEEE Transactions on Smart Grid*, vol. 10, no. 4, pp. 4566-4576, 2019.

[53] E. Chun and M. Kabalan, "Effects of Controller Saturation on Domain of Attraction Estimation of Droop-Controlled Inverter," in *2019 North American Power Symposium (NAPS)*, 2019, pp. 1-6.

[54] M. Kabalan, P. Singh, and D. Niebur, "Nonlinear Lyapunov Stability Analysis of Seven Models of a DC/AC Droop Controlled Inverter Connected to an Infinite Bus," *IEEE Transactions on Smart Grid*, vol. 10, no. 1, pp. 772-781, 2019.

[55] O. Ajala, "A hierarchy of microgrid models with some applications," University of Illinois at Urbana-Champaign, 2018.

[56] O. Ajala, A. D. Domínguez-García, and P. W. Sauer, "A hierarchy of models for inverter-based microgrids," in *Energy Markets and Responsive Grids*: Springer, 2018, pp. 307-332.

[57] "Distributed Energy Resources: Connection Modeling and Reliability Considerations," North American Electric Reliability Corporation (NERC)Feb. 2017, Available: https://www.nerc.com/comm/Other/essntlrlbltysrvcstskfrcDL/Distributed_Energy_Resources_Report.pdf.

[58] "Bulk Electric System Definition Reference Document," North American Electric Reliability Corporation (NERC)April 2014, Available: https://www.nerc.com/pa/RAPA/BES%20DL/bes_phase2_reference_document_20140325_final_clean.pdf.

[59] N. Y. ISO. A Review of Distributed Energy Resources [Online]. Available: www.nyiso.com

[60] N. Y. DPS. Reforming the Energy Vision [Online]. Available: http://www3.dps.ny.gov/

[61] J. Rocabert, A. Luna, F. Blaabjerg, and P. Rodríguez, "Control of Power Converters in AC Microgrids," *IEEE Transactions on Power Electronics*, vol. 27, no. 11, pp. 4734-4749, 2012.

[62] W. Guo and L. Mu, "Control principles of micro-source inverters used in microgrid," *Protection and Control of Modern Power Systems*, vol. 1, no. 1, p. 5, 2016.

[63] J. T. Bialasiewicz, "Renewable Energy Systems With Photovoltaic Power Generators: Operation and Modeling," *IEEE Transactions on Industrial Electronics*, vol. 55, no. 7, pp. 2752-2758, 2008.

[64] M. E. Baran and F. F. Wu, "Network reconfiguration in distribution systems for loss reduction and load balancing," *IEEE Transactions on Power Delivery*, vol. 4, no. 2, pp. 1401-1407, 1989.

[65] L. Gan and S. H. Low, "Convex relaxations and linear approximation for optimal power flow in multiphase radial networks," in *2014 Power Systems Computation Conference*, 2014, pp. 1-9.

[66] "IEEE Standard for Interconnection and Interoperability of Distributed Energy Resources with Associated Electric Power Systems Interfaces," *IEEE Std 1547-2018 (Revision of IEEE Std 1547-2003)*, pp. 1-138, 2018.

[67] K. P. Schneider *et al.*, "Improving Primary Frequency Response to Support Networked Microgrid Operations," *IEEE Transactions on Power Systems*, vol. 34, no. 1, pp. 659-667, 2019.

[68] K. P. Schneider *et al.*, "Enabling Resiliency Operations Across Multiple Microgrids With Grid Friendly Appliance Controllers," *IEEE Transactions on Smart Grid*, vol. 9, no. 5, pp. 4755-4764, 2018.

[69] O. Bassey, B. Chen, and K. L. Butler-Purry, "Sequential service restoration in distribution systems and microgrids integrating frequency response and varying switching interval," in *2018 IEEE Texas Power and Energy Conference (TPEC)*, 2018, pp. 1-6.

[70] P. W. Sauer and M. A. Pai, *Power System Dynamics and Stability*. Prentice-Hall, Inc., 1998.

[71] A. J. Wood and B. F. Wollenberg, *Power Generation, Operation, and Control*. 1996.

[72] L. Moysis, M. Tsiaousis, N. Charalampidis, M. Eliadou, and I. Kafetzis, "An Introduction to Control Theory Applications with Matlab," *2015. DOI: 10.13140/RG. 2.1*, vol. 3926, 2015.

[73] D. Georgakis, S. Papathanassiou, N. Hatziargyriou, A. Engler, and C. Hardt, "Operation of a prototype microgrid system based on micro-sources quipped with fast-acting power electronics interfaces," in *2004 IEEE 35th Annual Power Electronics Specialists Conference (IEEE Cat. No.04CH37551)*, 2004, vol. 4, pp. 2521-2526 Vol.4.

[74] S. Barsali, M. Ceraolo, P. Pelacchi, and D. Poli, "Control techniques of Dispersed Generators to improve the continuity of electricity supply," in *2002 IEEE Power Engineering Society Winter Meeting. Conference Proceedings (Cat. No.02CH37309)*, 2002, vol. 2, pp. 789-794 vol.2.

[75] L. Peng, D. Bai, Y. Kang, and J. Chen, "Research on three-phase inverter with unbalanced load," in *Applied Power Electronics Conference and Exposition, 2004. APEC '04. Nineteenth Annual IEEE*, 2004, vol. 1, pp. 128-133 Vol.1.

[76] O. Bassey and K. L. Butler-Purry, "Modeling Single-Phase PQ Inverter for Unbalanced Power Dispatch in Islanded Microgrid," in *2019 IEEE Texas Power and Energy Conference (TPEC)*, 2019, pp. 1-6.

[77] B. Crowhurst, E. F. El-Saadany, L. E. Chaar, and L. A. Lamont, "Single-phase grid-tie inverter control using DQ transform for active and reactive load power compensation," in *2010 IEEE International Conference on Power and Energy*, 2010, pp. 489-494.

[78] A. M. Mnider, D. J. Atkinson, M. Dahidah, and M. Armstrong, "A simplified DQ controller for single-phase grid-connected PV inverters," in *2016 7th International Renewable Energy Congress (IREC)*, 2016, pp. 1-6.

[79] F. E. Aamri, H. Maker, A. Mouhsen, and M. Harmouchi, "A new strategy to control the active and reactive power for single phase grid-connected PV inverter," in *2015 3rd International Renewable and Sustainable Energy Conference (IRSEC)*, 2015, pp. 1-6.

[80] S. Golestan, M. Monfared, J. M. Guerrero, and M. Joorabian, "A D-Q synchronous frame controller for single-phase inverters," in *2011 2nd Power Electronics, Drive Systems and Technologies Conference*, 2011, pp. 317-323.

[81] A. Roshan, R. Burgos, A. C. Baisden, F. Wang, and D. Boroyevich, "A D-Q Frame Controller for a Full-Bridge Single Phase Inverter Used in Small Distributed Power Generation Systems," in *APEC 07 - Twenty-Second Annual IEEE Applied Power Electronics Conference and Exposition*, 2007, pp. 641-647.

[82] O. Bassey. Single-Phase PQ Inverter Model and Application to Unbalance Compensation in Islanded Microgrids (PSCAD Simulation) [Online]. Available: http://hdl.handle.net/1969.1/174294

[83] H. Ahmadi and J. R. Martı´, "Linear Current Flow Equations With Application to Distribution Systems Reconfiguration," *IEEE Transactions on Power Systems*, vol. 30, no. 4, pp. 2073-2080, 2015.

[84] (2019). *PES Test Feeder*. Available: http://sites.ieee.org/pes-testfeeders/resources/

[85] J. Lofberg, "YALMIP : a toolbox for modeling and optimization in MATLAB," in *2004 IEEE International Conference on Robotics and Automation (IEEE Cat. No.04CH37508)*, 2004, pp. 284-289.

[86] Gurobi Optimization [Online]. Available: http://www.gurobi.com/

[87] M. M. A. Abdelaziz, H. E. Farag, E. F. El-Saadany, and Y. A. I. Mohamed, "A Novel and Generalized Three-Phase Power Flow Algorithm for Islanded Microgrids Using a Newton Trust Region Method," *IEEE Transactions on Power Systems*, vol. 28, no. 1, pp. 190-201, 2013.

[88] M. A. Allam, A. A. Hamad, and M. Kazerani, "A Generic Modeling and Power-Flow Analysis Approach for Isochronous and Droop-Controlled Microgrids," *IEEE Transactions on Power Systems*, vol. 33, no. 5, pp. 5657-5670, 2018.

[89] F. Mumtaz, M. H. Syed, M. A. Hosani, and H. H. Zeineldin, "A Novel Approach to Solve Power Flow for Islanded Microgrids Using Modified Newton Raphson

With Droop Control of DG," *IEEE Transactions on Sustainable Energy,* vol. 7, no. 2, pp. 493-503, 2016.

[90] G. C. Kryonidis, E. O. Kontis, A. I. Chrysochos, K. O. Oureilidis, C. S. Demoulias, and G. K. Papagiannis, "Power Flow of Islanded AC Microgrids: Revisited," *IEEE Transactions on Smart Grid,* vol. 9, no. 4, pp. 3903-3905, 2018.

[91] G. Díaz, J. Gómez-Aleixandre, and J. Coto, "Direct Backward/Forward Sweep Algorithm for Solving Load Power Flows in AC Droop-Regulated Microgrids," *IEEE Transactions on Smart Grid,* vol. 7, no. 5, pp. 2208-2217, 2016.

[92] H. Ahmadi, J. R. Martı´, and A. v. Meier, "A Linear Power Flow Formulation for Three-Phase Distribution Systems," *IEEE Transactions on Power Systems,* vol. 31, no. 6, pp. 5012-5021, 2016.

[93] J. R. Martí, H. Ahmadi, and L. Bashualdo, "Linear Power-Flow Formulation Based on a Voltage-Dependent Load Model," *IEEE Transactions on Power Delivery,* vol. 28, no. 3, pp. 1682-1690, 2013.

[94] H. Ahmadi and J. R. Martí, "Distribution System Optimization Based on a Linear Power-Flow Formulation," *IEEE Transactions on Power Delivery,* vol. 30, no. 1, pp. 25-33, 2015.

[95] H. Chou and K. L. Butler-Purry, "Investigation of voltage stability in unbalanced distribution systems with DG using three-phase current injection based CPF," in *2014 IEEE PES General Meeting | Conference & Exposition*, 2014, pp. 1-5.

[96] O. Bassey, K. L. Butler-Purry, and B. Chen, "Active and Reactive Power Sharing in Inverter Based Droop-Controlled Microgrids," in *2019 IEEE Power & Energy Society General Meeting (PESGM)*, Atlanta, GA, USA, 2019, pp. 1-5.

[97] H. Saadat, *Power System Analysis McGraw-Hill Series in Electrical Computer Engineering*. 1999.

[98] K. D. Brabandere, B. Bolsens, J. V. d. Keybus, A. Woyte, J. Driesen, and R. Belmans, "A Voltage and Frequency Droop Control Method for Parallel Inverters," *IEEE Transactions on Power Electronics,* vol. 22, no. 4, pp. 1107-1115, 2007.

[99] M. C. Chandorkar, D. M. Divan, and R. Adapa, "Control of parallel connected inverters in standalone AC supply systems," *IEEE Transactions on Industry Applications,* vol. 29, no. 1, pp. 136-143, 1993.

[100] K. Jung-Won, C. Hang-Seok, and C. Bo Hyung, "A novel droop method for converter parallel operation," *IEEE Transactions on Power Electronics*, vol. 17, no. 1, pp. 25-32, 2002.

[101] A. Haddadi, A. Shojaei, and B. Boulet, "Enabling high droop gain for improvement of reactive power sharing accuracy in an electronically-interfaced autonomous microgrid," in *2011 IEEE Energy Conversion Congress and Exposition*, 2011, pp. 673-679.

[102] E. Barklund, N. Pogaku, M. Prodanovic, C. Hernandez-Aramburo, and T. C. Green, "Energy Management in Autonomous Microgrid Using Stability-Constrained Droop Control of Inverters," *IEEE Transactions on Power Electronics*, vol. 23, no. 5, pp. 2346-2352, 2008.

[103] I. U. Nutkani, P. C. Loh, and F. Blaabjerg, "Droop Scheme With Consideration of Operating Costs," *IEEE Transactions on Power Electronics*, vol. 29, no. 3, pp. 1047-1052, 2014.

[104] H. P. Williams, *Model building in mathematical programming*. John Wiley & Sons, 2013.

[105] M. J. Thompson, "Fundamentals and advancements in generator synchronizing systems," in *2012 65th Annual Conference for Protective Relay Engineers*, 2012, pp. 203-214.

[106] O. Ajala, A. D. Dominguez-Garcìa, and D. Liberzon, "An Approach to Robust Synchronization of Electric Power Generators," in *2018 IEEE Conference on Decision and Control (CDC)*, 2018, pp. 1586-1591.

[107] H. Renmu, J. Ma, and D. J. Hill, "Composite load modeling via measurement approach," *IEEE Transactions on Power Systems*, vol. 21, no. 2, pp. 663-672, 2006.

[108] "IEEE Standard Test Procedure for Polyphase Induction Motors and Generators," *IEEE Std 112-2017 (Revision of IEEE Std 112-2004)*, pp. 1-115, 2018.

[109] P. Pillay and M. Manyage, "Definitions of voltage unbalance," *IEEE Power Engineering Review*, vol. 21, no. 5, pp. 50-51, 2001.

[110] J. S. Vardakas, N. Zorba, and C. V. Verikoukis, "A Survey on Demand Response Programs in Smart Grids: Pricing Methods and Optimization Algorithms," *IEEE Communications Surveys & Tutorials*, vol. 17, no. 1, pp. 152-178, 2015.

[111] P. Palensky and D. Dietrich, "Demand Side Management: Demand Response, Intelligent Energy Systems, and Smart Loads," *IEEE Transactions on Industrial Informatics,* vol. 7, no. 3, pp. 381-388, 2011.

[112] M. Adibi *et al.*, "Power System Restoration - A Task Force Report," *IEEE Transactions on Power Systems,* vol. 2, no. 2, pp. 271-277, 1987.

[113] M. Lavorato, J. F. Franco, M. J. Rider, and R. Romero, "Imposing Radiality Constraints in Distribution System Optimization Problems," *IEEE Transactions on Power Systems,* vol. 27, no. 1, pp. 172-180, 2012.

[114] D. A. Marcus, *Graph Theory : A Problem Oriented Approach*. Washington, UNITED STATES: American Mathematical Society, 2008.

[115] S. Herke. Graph Theory: 51. Eccentricity, Radius & Diameter [Online]. Available: https://www.youtube.com/watch?v=YbCn8d4Enos

[116] *Mixed-Integer Programming (MIP) – A Primer on the Basics*. Available: https://www.gurobi.com/resource/mip-basics/

[117] G. Morales-España, J. M. Latorre, and A. Ramos, "Tight and Compact MILP Formulation of Start-Up and Shut-Down Ramping in Unit Commitment," *IEEE Transactions on Power Systems,* vol. 28, no. 2, pp. 1288-1296, 2013.

APPENDIX A

LINEARIZATION OF BILINEAR TERMS

Given the product of a binary variable, b, and a continuous variable, x, where x is bounded below and above by x_{min} and x_{max}, respectively. Introduce and replace this product with a new variable $z = bx$ wherever it is found in the model. We can linearize this product as follows by including (A.1) and (A.2) into the model.

$$x_{min} \leq x \leq x_{max} \tag{A.1}$$

$$x_{min} b \leq z \leq x_{max} b, x_{min}(1 - b) \leq x - z \leq x_{max}(1 - b) \tag{A.2}$$

APPENDIX B

LINEARIZATION OF THE PRODUCT OF TWO CONTINUOUS BOUNDED VARIABLES

Separable Function Realization and Piecewise Linearization

The technique of linearizing the product of two continuous variables is covered in chapter 7 of [104] and is adapted as follows. Consider the product of two bounded continuous variables x and y, $z = xy$, with bounds $x_{min} \leq x \leq x_{max}$, $y_{min} \leq y \leq y_{max}$. It is desired that this product be linearized. This product can also be written in this form.

$$z = xy = \frac{1}{4}[(x+y)(x+y) - (x-y)(x-y)] \tag{A.3}$$

Rewrite (A.3) using the following auxiliary variable $X = (x+y)$ and $Y = x - y$, then,

$$z = xy = \frac{1}{4}(X^2 - Y^2) \tag{A.4}$$

Which is now in a separable form. The auxiliary variables have the following bounds,

$$x_{min} + y_{min} \leq X \leq x_{max} + y_{max} \tag{A.5}$$

$$x_{min} - y_{max} \leq Y \leq x_{max} - y_{min} \tag{A.6}$$

Define, $z_1 = X^2, z_2 = Y^2$. The square convex functions z_1, z_2 can then be linearized independently using a piecewise approach. Figure A-1 shows a piecewise linearization of the square function with n breakpoints. Breakpoints are the points on the figure where the square function is evaluated.

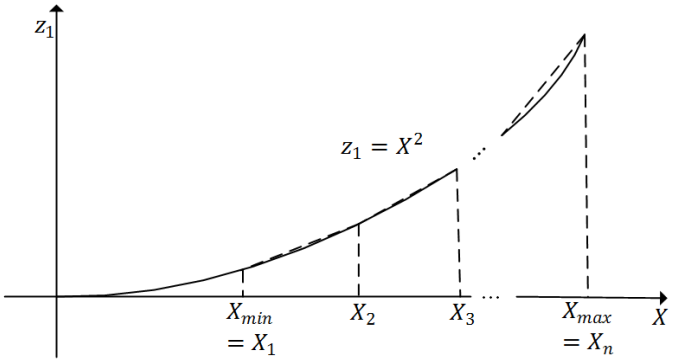

Figure A-1 Piecewise Linearization of a Square Function using n Breakpoints

The piecewise linearization equations for $z_1 = X^2$ can then be written as follows.

$$X = \lambda_1 X_1 + \lambda_2 X_2 + \cdots + \lambda_n X_n \tag{A.7}$$

$$z_1 = \lambda_1 X_1^2 + \lambda_2 X_2^2 + \cdots + \lambda_n X_n^2 \tag{A.8}$$

where $\lambda_1, \lambda_2, \ldots, \lambda_n$ are auxiliary variables that denote weights for the function evaluations at the breakpoints. To ensure that the weights are properly selected and that at most two adjacent breakpoints are activated, the following additional constraints are introduced.

$$\lambda_1 + \lambda_2 + \cdots + \lambda_n = 1, \lambda_i \geq 0, i \in \{1,2, \ldots, n\} \tag{A.9}$$

$$SOS2(\{\lambda_1, \lambda_2, \ldots, \lambda_n\}) \tag{A.10}$$

Where (A.10) imposes that the set of λ is a special ordered set of type 2 (SOS2). This constraint ensures that at most two adjacent breakpoints are activated and can be realized with auxiliary integer constraints manipulation.

Error Minimization of the Piecewise Linearization Approach

The next question worth exploring is: at what points on the x-axis should the breakpoint be chosen for linearization error minimization? The error can be characterized

as the area between the piecewise linear approximation and the square function and can be written as a function of the inner breakpoints since the outer breakpoints are known.

$$Error, e = f(X_2, X_3, \dots, X_{n-1}) \tag{A.11}$$

Define, $X_{i+1} - X_i = \Delta X_i, \forall i \in \{1,2, \dots, n-1\}$

The minimization problem then becomes:

$$\begin{gathered} min\, f(X_2, X_3, \dots, X_{n-1}) \\ \text{Subject to } \Delta X_i \geq 0, \forall i \in \{1,2, \dots, n-1\} \end{gathered} \tag{A.12}$$

Since the function to be linearized is convex, we can see geometrically that none of the inequality constraints is active at the minimal point. Therefore, we can ignore the Lagrange multipliers typically used for the inequality constraints and simply solve for the minimum of the objective function by unconstrained gradient method which gives the following nice results.

$$\frac{\partial f}{\partial X_1} = 0, \rightarrow \Delta X_1 = \Delta X_2 \tag{A.13}$$

$$\frac{\partial f}{\partial X_2} = 0, \rightarrow \Delta X_2 = \Delta X_3 \tag{A.14}$$

And so on to $\Delta X_{n-2} = \Delta X_{n-1}$. This means that equal intervals for the breakpoints will give minimal error. In the optimal power flow linearization, 5 breakpoints were used for each piecewise linearization task.

APPENDIX C

AN ALTERNATIVE TO PIECEWISE LINEARIZATION BY APPROXIMATING VOLTAGE VARIABLE AS A CONSTANT

In section 6.3.5.2 where we derived the expression for the current injection of the droop-controlled DG and PQ DG nodes, several products of two continuous variables were realized. These products consist of a power injection variable and a rectangular voltage variable. The piecewise linearization approach of Appendix B introduces several variables and constraints which can slow down the solver especially for larger systems. The approach presented in this appendix presents less computational burden.

Let the power injection variables be $p \in P_{set} = \{\hat{P}_{a,k,t}, \hat{P}_{b,k,t}, \hat{P}_{c,k,t}, \hat{Q}_{a,k,t}, \hat{Q}_{b,k,t}, \hat{Q}_{c,k,t}\}$, where $\hat{P}_{a,k,t}, \hat{P}_{b,k,t}$, and $\hat{P}_{c,k,t}$ represent the active power injection variables for phases a, b, and c, respectively, and $\hat{Q}_{a,k,t}, \hat{Q}_{b,k,t}$, and $\hat{Q}_{c,k,t}$ represent the reactive power injection variables for phases a, b, and c, respectively, at an arbitrary node, k, at time step t.

Let the rectangular voltage variables be $v \in V_{set} = \{\hat{V}_{k,t}^{re,a}, \hat{V}_{k,t}^{re,b}, \hat{V}_{k,t}^{re,c}, \hat{V}_{k,t}^{im,a}, \hat{V}_{k,t}^{im,b}, \hat{V}_{k,t}^{im,c}\}$, where $\hat{V}_{k,t}^{re,a}, \hat{V}_{k,t}^{re,b}$, and $\hat{V}_{k,t}^{re,c}$ represent the real part of complex nodal voltages at phases a, b, and c, respectively, and $\hat{V}_{k,t}^{im,a}, \hat{V}_{k,t}^{im,b}$, and $\hat{V}_{k,t}^{im,c}$ represent the imaginary part of nodal voltages at phases a, b, and c, respectively at an arbitrary node, k, at time step t.

Then the product of the voltage and power can be expressed as,

$$z = v.p, \quad p \in P_{set}, v \in V_{set} \tag{A.15}$$

The magnitude of the nodal voltage for an energized node is within less than ±10% or ±0.1 pu from the voltage magnitude of 1 pu. Therefore, we can approximate

$$z = k_n.p, \quad p \in P_{set}, k_n \in \{k_1, k_2, \dots, k_6\} \tag{A.16}$$

Where k_n is constant set equal to the nominal rectangular voltage, and k_1, k_2, and k_3 are constants used for approximating $\hat{V}_{k,t}^{re,a}, \hat{V}_{k,t}^{re,b}$, and $\hat{V}_{k,t}^{re,c}$ respectively, and k_4, k_5, and k_6 are constants used for approximating $\hat{V}_{k,t}^{im,a}, \hat{V}_{k,t}^{im,b}$, and $\hat{V}_{k,t}^{im,c}$ respectively. The nominal rectangular voltages are expressed as follows noting that phases a, b, and c are assumed to have phasor angle of 0˚, -120˚, and 120˚, respectively:

$$\begin{bmatrix} k_1 \\ k_2 \\ k_3 \end{bmatrix} = |V_{nom}| * \begin{bmatrix} 1 \\ -\sin(30°) \\ -\sin(30°) \end{bmatrix}, \qquad \begin{bmatrix} k_4 \\ k_5 \\ k_6 \end{bmatrix} = |V_{nom}| * \begin{bmatrix} 0 \\ -\cos(30°) \\ \cos(30°) \end{bmatrix} \tag{A.17}$$

where $|V_{nom}|$ is a constant that represent the nominal voltage magnitude in pu, and is set equal to 1.03 for the droop DG node and 0.98 for other nodes. The droop DG nodes are set at a higher 1.03 pu because the inductor coupling of the droop DG drops the voltage transmitted to its adjacent node.

APPENDIX D

SOME DETAILS OF THE MODIFIED IEEE 13 NODE TEST FEEDER

The original IEEE 13 node test feeder can be found here [84]. The key details and the modifications are summarized as follows. The one line diagram of the original and modified feeder are shown in Figure A-2.

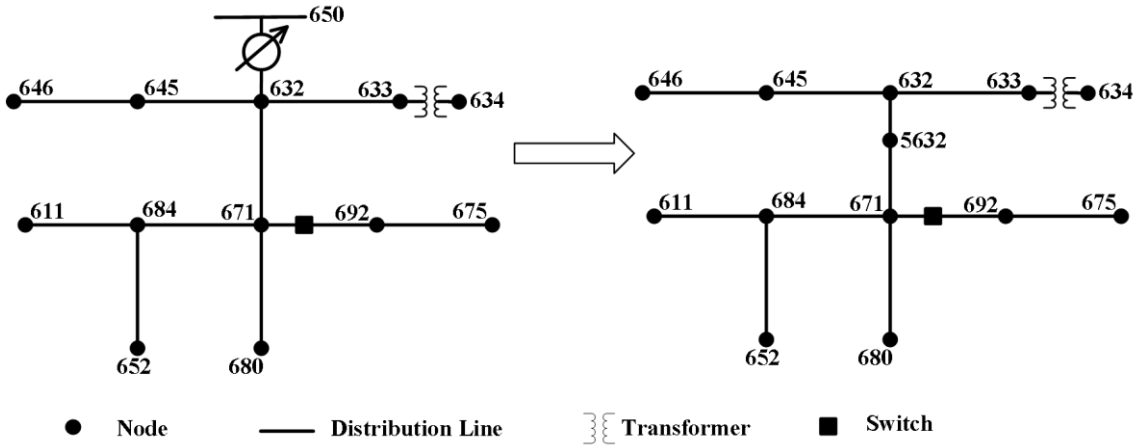

Figure A-2 IEEE Original and Modified 13 node Test Feeder

In the original system, the substation is at node 650. The system is assumed to be islanded and therefore modified by eliminating node 650 and its voltage regulator. An additional node, 5632, was added between nodes 632 and 671. In cases with droop-controlled DG, an additional node is added to account for the inductor coupling of the droop-controlled. In cases with PQ DG, the PQ DG are connected directed its node without inductor coupling. An example from section 5.8.9, which is the optimal power flow example case, with droop-controlled DGs and PQ DGs is shown in Figure A-3.

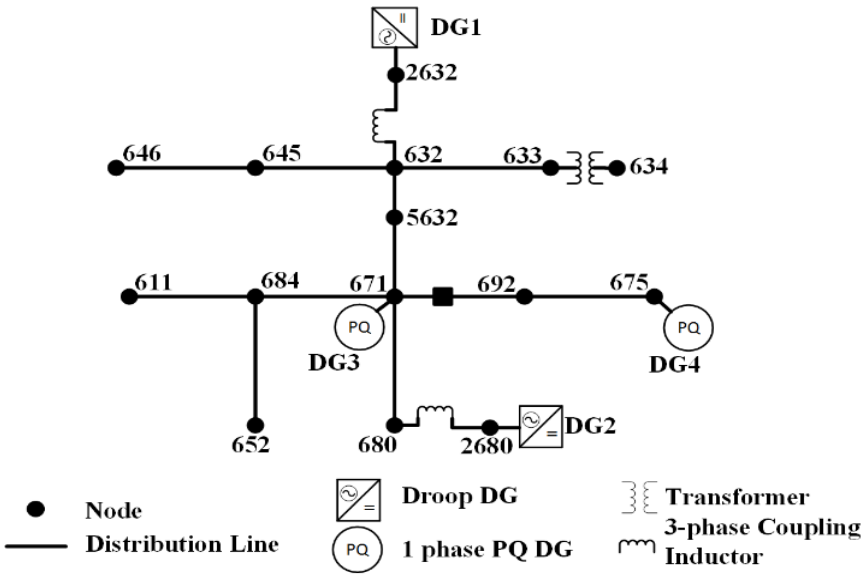

Figure A-3 Modified IEEE 13 Node Test Feeder with Droop-Controlled and PQ DGs

Notice the convention we use in naming the additional nodes of Figure A-3 due to the inductor coupling: we add "2000" to the adjacent node number to get the droop internal node number. For instance, consider the inductor coupled to node 680, its droop node is called 2680. We use this naming convention throughout for all cases including those of modified IEEE 123 node test feeder presented in Appendix E.

The line segment data, line configuration and transformer data are summarized as shown Table A-1, Table A-2, and Table A-3 below,

Table A-1 Line Segment Details of Modified IEEE 13 Node Test Feeder

Node A	Node B	Length(ft.)	Config.	Node A	Node B	Length(ft.)	Config.
632	645	500	603	671	5632	1500	601
632	633	500	602	671	684	300	604
633	634	0	XFM-1	671	680	1000	601
645	646	300	603	671	692	0	Switch

Table A-1 Continued

Node A	Node B	Length(ft.)	Config.	Node A	Node B	Length(ft.)	Config.
650	632	2000	601	684	611	300	605
684	652	800	607	692	675	500	606
632	5632	500	601				

Table A-2 Line Configuration of IEEE 13 Node Test Feeder

Config	Z (R +jX) in ohms per mile	B in micro Siemens per mile
601	[0.3465+1i*1.0179 0.1560 + 1i*0.5017 0.1580 + 1i*0.4236; 0.1560+1i*0.5017 0.3375 + 1i*1.0478 0.1535 + 1i*0.3849; 0.1580 + 1i*0.4236 0.1535 + 1i*0.3849 0.3414 + 1i*1.0348]	[6.2998 -1.9958 -1.2595; -1.9958 5.9597 -0.7417; -1.2595 -0.7417 5.6386]
602	[0.7526 + 1i*1.1814 0.1580+1i*0.4236 0.1560+1i*0.5017; 0.1580+1i*0.4236 0.7475 + 1i*1.1983 0.1535+1i*0.3849; 0.1560+1i*0.5017 0.1535+1i*0.3849 0.7436 + 1i*1.2112]	[5.6990 -1.0817 -1.6905; -1.0817 5.1795 -0.6588; -1.6905 -0.6588 5.4246]
603	[0.0000+1i*0.0000 0.0000+1i*0.0000 0.0000+1i*0.0000; 0.0000+1i*0.0000 1.3294+1i*1.3471 0.2066+1i*0.4591; 0.0000+1i*0.0000 0.2066+1i*0.4591 1.3238+1i*1.3569]	[0.0000 0.0000 0.0000; 0.0000 4.7097 -0.8999; 0.0000 -0.8999 4.6658]
604	[1.3238+1i*1.3569 0.0000+1i*0.0000 0.2066+1i*0.4591; 0.0000+1i*0.0000 0.0000+1i*0.0000 0.0000+1i*0.0000; 0.2066+1i*0.4591 0.0000+1i*0.0000 1.3294+1i*1.3471]	[4.6658 0.0000 -0.8999; 0.0000 0.0000 0.0000; -0.8999 0.0000 4.7097]
605	[0.0000+1i*0.0000 0.0000+1i*0.0000 0.0000+1i*0.0000; 0.0000+1i*0.0000 0.0000+1i*0.0000 0.0000+1i*0.0000; 0.0000+1i*0.0000 0.0000+1i*0.0000 1.3292+1i*1.3475]	[0.0000 0.0000 0.0000; 0.0000 0.0000 0.0000; 0.0000 0.0000 4.5193]
606	[0.7982+1i*0.4463 0.3192+1i*0.0328 0.2849+1i*0.0143; 0.3192+1i*0.0328 0.7891+1i*0.4041 0.3192+1i*0.0328; 0.2849+1i*0.0143 0.3192+1i*0.0328 0.7982+1i*0.4463]	[96.8897 0.0000 0.0000; 0.0000 96.8897 0.0000; 0.0000 0.0000 96.8897]
607	[1.3425+1i* 0.5124 0.0000+1i*0.0000 0.0000+1i*0.0000; 0.0000+1i*0.0000 0.0000+1i*0.0000 0.0000+1i*0.0000; 0.0000+1i*0.0000 0.0000+1i*0.0000 0.0000+1i*0.0000]	[88.9912 0.0000 0.0000; 0.0000 0.0000 0.0000; 0.0000 0.0000 0.0000]

Table A-3 Data for the Transformer between Nodes 633 and 634

	kVA	kV-high	kV-low	R - %	X - %
XFM -1	500	4.16 – Gr.W	0.48 – Gr.W	1.1	2

More details can be found in the original IEEE 13 node test feeder document [84].

APPENDIX E

SOME DETAILS OF THE MODIFIED IEEE 123 NODE TEST FEEDER

The original IEEE 123 node test feeder can be found here [84]. The key details and the modifications are summarized as follows. The one line diagram of the original 123 node test feeder is shown in Figure A-4.

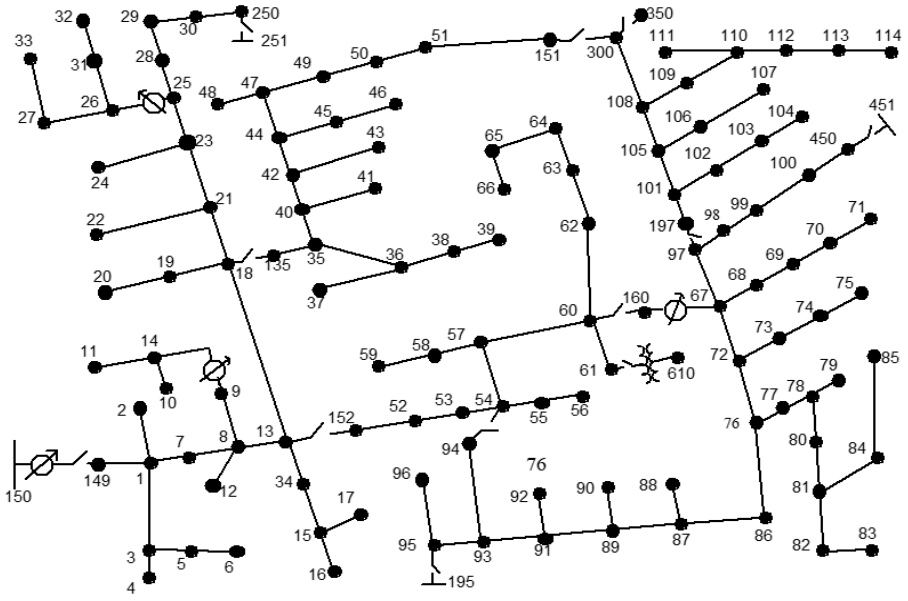

Figure A-4 Original IEEE 123 Node Test Feeder

The system is modified to an islanded system by removing the substation nodes at nodes 150, 251, and 451. Also, the voltage regulators are removed. A typical one line diagram of the modified 123 node test feeder is shown in Figure A-5. Figure A-5 is the one-line diagram of the islanded system from section 7.5.1, which is the base case of case studies #2 scenario 1 of section 7. The droop node in Figure A-5 is at nodes 2063 and 2054

(same naming convention for the droop nodes with those of IEEE 13 node test feeder presented in Appendix D).

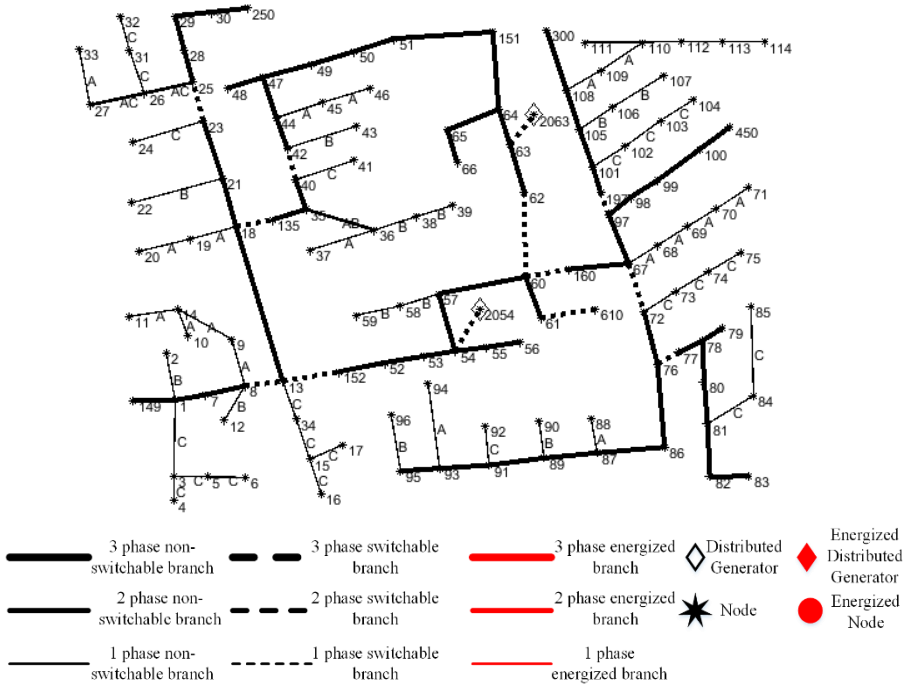

Figure A-5 Modified IEEE 123 Node Test Feeder

Other cases derived from the IEEE 123 node test feeder have the same line impedance configuration as those of Figure A-5 except that the DG nodes, the coupling inductance, and which line is switchable/non-switchable might differ.

The line segment data, line configuration and transformer data are summarized as shown Table A-4, Table A-5, and Table A-6 below,

Table A-4 Line Segment Details of Modified IEEE 123 Node Test Feeder

Node A	Node B	Length(ft.)	Config.	Node A	Node B	Length(ft.)	Config.	Node A	Node B	Length(ft.)	Config.	Node A	Node B	Length(ft.)	Config.
1	2	175	L10	30	250	200	L2	63	64	350	L12	93	95	300	L6
1	3	250	L11	31	32	300	L11	64	65	425	L12	95	96	200	L10
1	7	300	L1	34	15	100	L11	65	66	325	L12	97	98	275	L3
3	4	200	L11	35	36	650	L8	67	68	200	L9	98	99	550	L3
3	5	325	L11	35	40	250	L1	67	72	275	L3	99	100	300	L3
5	6	250	L11	36	37	300	L9	67	97	250	L3	100	450	800	L3
7	8	200	L1	36	38	250	L10	68	69	275	L9	101	102	225	L11
8	12	225	L10	38	39	325	L10	69	70	325	L9	101	105	275	L3
8	9	225	L9	40	41	325	L11	70	71	275	L9	102	103	325	L11
8	13	300	L1	40	42	250	L1	72	73	275	L11	103	104	700	L11
9	14	425	L9	42	43	500	L10	72	76	200	L3	105	106	225	L10
13	34	150	L11	42	44	200	L1	73	74	350	L11	105	108	325	L3
13	18	825	L2	44	45	200	L9	74	75	400	L11	106	107	575	L10
14	11	250	L9	44	47	250	L1	76	77	400	L6	108	109	450	L9
14	10	250	L9	45	46	300	L9	76	86	700	L3	108	300	1000	L3
15	16	375	L11	47	48	150	L4	77	78	100	L6	109	110	300	L9
15	17	350	L11	47	49	250	L4	78	79	225	L6	110	111	575	L9
18	19	250	L9	49	50	250	L4	78	80	475	L6	110	112	125	L9
18	21	300	L2	50	51	250	L4	80	81	475	L6	112	113	525	L9
19	20	325	L9	51	151	500	L4	81	82	250	L6	113	114	325	L9
21	22	525	L10	52	53	200	L1	81	84	675	L11	135	35	375	L4
21	23	250	L2	53	54	125	L1	82	83	250	L6	149	1	400	L1
23	24	550	L11	54	55	275	L1	84	85	475	L11	152	52	400	L1
23	25	275	L2	54	57	350	L3	86	87	450	L6	160	67	350	L6
25	26	350	L7	55	56	275	L1	87	88	175	L9	197	101	250	L3
25	28	200	L2	57	58	250	L10	87	89	275	L6	13	152	NA	Switch
26	27	275	L7	57	60	750	L3	89	90	225	L10	18	135	NA	Switch
26	31	225	L11	58	59	250	L10	89	91	225	L6	60	160	NA	Switch
27	33	500	L9	60	61	550	L5	91	92	300	L11	97	197	NA	Switch
28	29	300	L2	60	62	250	L12	91	93	225	L6	61	610	NA	XFM-1
29	30	350	L2	62	63	175	L12	93	94	275	L9	64	151	300	L12

Table A-5 Line Configuration of IEEE 123 Node Test Feeder

Config	Z (R +jX) in ohms per mile	B in micro Siemens per mile
L1	[0.4576+1i*1.0780 0.1560+1i*0.5017 0.1535+1i*0.3849; 0.1560+1i*0.5017 0.4666+1i*1.0482 0.1580+1i*0.4236; 0.1535+1i*0.3849 0.1580+1i*0.4236 0.4615+1i*1.0651]	[5.6765 -1.8319 -0.6982 -1.8319 5.9809 -1.1645 -0.6982 -1.1645 5.3971]
L2	[0.4666+1i*1.0482 0.1580+1i*0.4236 0.1560+1i*0.5017; 0.1580+1i*0.4236 0.4615+1i*1.0651 0.1535+1i*0.3849; 0.1560+1i*0.5017 0.1535+1i*0.3849 0.4576+1i*1.0780]	[5.9809 -1.1645 -1.8319 -1.1645 5.3971 -0.6982 -1.8319 -0.6982 5.6765]

Table A-5 Continued

Config	Z (R +jX) in ohms per mile	B in micro Siemens per mile
L3	[0.4615+1i*1.0651 0.1535+1i*0.3849 0.1580+1i*0.4236; 0.1535+1i*0.3849 0.4576+1i*1.0780 0.1560+1i*0.5017; 0.1580+1i*0.4236 0.1560+1i*0.5017 0.4666+1i*1.0482]	[5.3971 -0.6982 -1.1645 -0.6982 5.6765 -1.8319 -1.1645 -1.8319 5.9809]
L4	[0.4615+1i*1.0651 0.1580+1i*0.4236 0.1535+1i*0.3849; 0.1580+1i*0.4236 0.4666+1i*1.0482 0.1560+1i*0.5017; 0.1535+1i*0.3849 0.1560+1i*0.5017 0.4576+1i*1.0780]	[5.3971 -1.1645 -0.6982 -1.1645 5.9809 -1.8319 -0.6982 -1.8319 5.6765]
L5	[0.4666+1i*1.0482 0.1560+1i*0.5017 0.1580+1i*0.4236; 0.1560+1i*0.5017 0.4576+1i*1.0780 0.1535+1i*0.3849; 0.1580+1i*0.4236 0.1535+1i*0.3849 0.4615+1i*1.0651]	[5.9809 -1.8319 -1.1645 -1.8319 5.6765 -0.6982 -1.1645 -0.6982 5.3971]
L6	[0.4576+1i*1.0780 0.1535+1i*0.3849 0.1560+1i*0.5017; 0.1535+1i*0.3849 0.4615+1i*1.0651 0.1580+1i*0.4236; 0.1560+1i*0.5017 0.1580+1i*0.4236 0.4666+1i*1.0482]	[5.6765 -0.6982 -1.8319 -0.6982 5.3971 -1.1645 -1.8319 -1.1645 5.9809]
L7	[0.4576+1i*1.0780 0.0000+1i*0.0000 0.1535+1i*0.3849; 0.0000+1i*0.0000 0.0000+1i*0.0000 0.0000+1i*0.0000; 0.1535+1i*0.3849 0.0000+1i*0.0000 0.4615+1i*1.0651]	[5.1154 0.0 -1.0549; 0.0 0.0 0.0 ; -1.0549 0.0 5.1704]
L8	[0.4576+1i*1.0780 0.1535+1i*0.3849 0.0000+1i*0.0000; 0.1535+1i*0.3849 0.4615+1i*1.0651 0.0000+1i*0.0000; 0.0000+1i*0.0000 0.0000+1i*0.0000 0.0000+1i*0.0000]	[5.1154 -1.0549 0.0 ; -1.0549 5.1704 0.0 ; 0.0 0.0 0.0]
L9	[1.3292+1i*1.3475 0.0000+1i*0.0000 0.0000+1i*0.0000; 0.0000+1i*0.0000 0.0000+1i*0.0000 0.0000+1i*0.0000; 0.0000+1i*0.0000 0.0000+1i*0.0000 0.0000+1i*0.0000]	[4.5193 0.0 0.0 ; 0.0 0.0 0.0 ; 0.0 0.0 0.0]
L10	[0.0000+1i*0.0000 0.0000+1i*0.000 0.0000+1i*0.0000; 0.0000+1i*0.0000 1.3292+1i*1.3475 0.0000+1i*0.0000; 0.0000+1i*0.0000 0.0000+1i*0.0000 0.0000+1i*0.0000]	[0.0 0.0 0.0; 0.0 4.5193 0.0; 0.0 0.0 0.0]
L11	[0.0000+1i*0.0000 0.0000+1i*0.000 0.0000+1i*0.0000; 0.0000+1i*0.0000 0.0000+1i*0.000 0.0000+1i*0.0000; 0.0000+1i*0.0000 0.0000+1i*0.0000 1.3292+1i*1.3475]	[0.0 0.0 0.0; 0.0 0.0 0.0; 0.0 0.0 4.5193]
L12	[1.5209+1i*0.7521 0.5198+1i*0.2775 0.4924+1i*0.2157; 0.5198+1i*0.2775 1.5329+1i*0.7162 0.5198+1i*0.2775; 0.4924+1i*0.2157 0.5198+1i*0.2775 1.5209+1i*0.7521]	[67.2242 0.0 0.0; 0.0 67.2242 0.0; 0.0 0.0 67.2242]

Table A-6 Data for the Transformer between Nodes 61 and 610

	kVA	kV-high	kV-low	R - %	X - %
XFM -1	150	4.16 – D	0.48 – D	1.27	2.72

More details can be found in the original IEEE 123 node test feeder document [84].